Investigating Anti-Tumour T Cell Dynamics in Models of Primary and Metastatic Colorectal Cancer

Bethany Kennedy

A thesis submitted to the University of Birmingham for the degree of DOCTOR OF PHILOSOPHY

Institute of Immunology and Immunotherapy
College of Medical and Dental Sciences
University of Birmingham

May 2024



CANCER RESEARCH UK CLINICAL ACADEMIC TRAINING PROGRAMME



UNIVERSITY OF BIRMINGHAM

UNIVERSITY OF
BIRMINGHAM

University of Birmingham Research Archive

e-theses repository

This unpublished thesis/dissertation is copyright of the author and/or third parties. The intellectual property rights of the author or third parties in respect of this work are as defined by The Copyright Designs and Patents Act 1988 or as modified by any successor legislation.

Any use made of information contained in this thesis/dissertation must be in accordance with that legislation and must be properly acknowledged. Further distribution or reproduction in any format is prohibited without the permission of the copyright holder.

Abstract

Despite the successes of immunotherapy in the treatment of several cancer types, in metastatic proficient mismatch repair (pMMR) colorectal cancer (CRC) it has shown limited beneficial impact. In CRC, liver metastases are common and represent one of the greatest clinical challenges, both worsening prognosis and impeding the response to immunotherapy. Hence, it is essential to decipher the mechanisms by which liver metastases disrupt anti-tumour immunity and how these can be targeted therapeutically. The aim of this work was to better understand the fate of intratumoural CD8 T cells, namely how populations within the tumour interface with the peripheral immune compartment and ultimately contribute to the response to metastatic disease. To do this, novel *in vivo* primary and metastatic orthotopic CRC models that enable the temporal labelling of immune cells were developed. Across multiple models, the dynamics and migratory capacity of CD8 T cell populations were investigated.

This work, utilising both scRNA-seq and flow cytometry, identified an intratumoural TCF-1+ PD-1+ stem-like CD8 compartment. This stem-like population actively trafficked from tumours and these 'tumour experienced' T cells migrated to the dLN and beyond, circulating through lymphoid tissues. Implantation of CRC cell lines within both the colon wall and liver, modelling primary and metastatic disease respectively, showed that the location of tumour cell lines did not impact the phenotype of intratumoural CD8 populations. Finally, utilising an *in vivo* dual liver and subcutaneous tumour model allowed for the systemic suppressive effect of liver tumours on the anti-tumour immune response

to be recapitulated. This model, coupled with novel labelling of the immune compartment of liver tumours, confirmed that CD8 T cells are able to migrate between the two tumour sites; however, the migration of T cells between dual subcutaneous tumours was minimal, highlighting the importance of orthotopic models in the study of immune cell migratory dynamics. Collectively, this work has developed new tools to study the migration of immune subsets in orthotopic metastatic models of CRC and revealed new insight into the behaviour of the stem-like CD8 population in cancer.

Acknowledgements

I would like to thank Professor David Withers for the invaluable guidance, endless patience, and support. I could not have asked for a better supervisor.

Thank you to all members of the Withers group for the support and laughter throughout my time in the lab. Claire Willis, for her skills, time, and friendship, a single thank you does not cover the hundreds of hours we have spent together in the BMSU. Special thanks to Fabrina Gaspal, Suaad Idris, and Isaac Dean.

Thank you to Professor Gary Middleton for his mentorship and giving me this opportunity.

Finally, I would like to thank all my family and friends. Jan, Mark, Freddie, and Elena thank you for your lifelong support and individual wisdoms. Oliver, thank you for your partnership and constant encouragement.

Thank you to Cancer Research UK (SEBSTF-2021\100002) for funding this work. I would like to acknowledge the Biomedical Services Unit, and Flow Cytometry and Microscopy Facilities at the University of Birmingham for making this work possible.

Table of Contents

Chapter 1 ..... **1**

1.1. Introduction to Cancer Immunology *2*
1.1.1. Discovery of an immune response against cancer 3
1.1.2. Immunoediting 4
1.1.3. Evading immune destruction as a hallmark of cancer 5
1.1.4. Pro- and anti-tumourigenic immune subsets in the tumour microenvironment 6

1.2. CD8 T Cell Activation & Effector Function in Cancer *7*
1.2.1. Presentation of tumour antigen on MHC class I 8
1.2.2. T cell activation 10
1.2.3. CD8 effector functions in cancer 12

1.3. CD8 Dysfunction in Cancer - The Default State *14*
1.3.1. Discovery of 'exhausted' CD8 T cells 14
1.3.2. CD8 T cell exhaustion in cancer 17
1.3.3. Stem-like CD8 T cells sustain the exhausted compartment 19

1.4. Harnessing the Immune Response Against Cancer - Current CD8 Immunotherapies *20*
1.4.1. Types of T cell focused immunotherapy 21
1.4.2. Immune checkpoint blockade 24
1.4.3. Resistance to immune checkpoint blockade 27
1.4.4. Combination therapies 28

1.5. Systemic and Long-lived Immunity to Cancer *29*
1.5.1. Generation of CD8 memory responses 29
1.5.2. Memory CD8 T cells in cancer 30

1.6. The Immune Response to Colorectal Cancer *31*
1.6.1. The immune landscape of colorectal cancer 32
1.6.2. The importance of liver metastasis in CRC 33
1.6.3. Immunotherapy in the treatment of proficient mismatch repair colorectal cancer 34

1.7. Aims & Objectives *37*

Chapter 2 ..... **38**

2.1. Materials *39*
2.1.1. Chemicals & Reagents 39
2.1.2. Antibodies 41
2.1.3. Cell Lines 45
2.1.4. Mice 46

2.2. Cell Culture *48*
2.2.1. Thawing Cells 48
2.2.2. Cell Passage 48
2.2.3. Preparing Cells for Injection 49
2.2.4. Counting Cells 49
2.2.5. Freezing Cells 50
2.2.6. Mycoplasma Testing 50

2.3. In Vivo Procedures *51*
2.3.1. Subcutaneous Implantation of Tumour Cell Lines 51
2.3.2. Endoscopic Implantation of Tumour Cell Lines and Organoids within the Colon Wall 52
2.3.3. Intrahepatic Implantation of Tumour Cell Lines 52
2.3.4. *In Vivo* Bioluminescent Imaging using IVIS 54

2.3.5. Administration of Antibodies 54
2.3.6. Photoconversion Procedure 54
2.3.7. Intravenous CD45 Labelling 56
2.3.8. Blood Sampling 56

2.4. Tissue Processing & Cell Isolation for Flow Cytometry 57
2.4.1. Preparation of Tumour 57
2.4.2. Preparation of Lymph Nodes 58
2.4.3. Preparation of Spleen 58
2.4.4. Preparation of Liver 59
2.4.5. Preparation of Large Intestine 60
2.4.6. Preparation of Blood Samples 60

2.5. Magnetic Sorting for CD8 Enrichment 61

2.6. Flow Cytometry 62
2.6.1. Proportion of Tissues Stained for Flow Cytometry 62
2.6.2. Extracellular Staining 62
2.6.3. Intracellular Staining 63
2.6.4. Sample Processing Pre-Acquisition 63

2.7. Immunofluorescence Microscopy 64
2.7.1. Tissue Fixation, Sectioning and Preparation of Slides 64
2.7.2. Immunolabelling of Tissue Sections 64

2.8. Single-cell RNA-sequencing 65

2.9. Data Processing 66
2.9.1. Data Collection & Analyses of Flow Cytometry Data 66
2.9.2. Image Capture, Visualisation & Analysis of Microscopy Data 67
2.9.3. Data Acquisition & Analysis for IVIS Imaging Data 67

2.10. Statistical Analysis 67

Chapter 3 69

3.1. Introduction 70
3.1.1. The importance of stem-like CD8 T cells in cancer 71
3.1.2. The location and migratory potential of stem-like CD8 T cells 71
3.1.3. Tracking T cell migration in pre-clinical tumour models using Kaede transgenic mice 73
3.1.4. Aims 74

3.2. Results 76
3.2.1. Establishing subcutaneous CRC models to study the composition of the intratumoural CD8 population and how this changes over time 76
3.2.2. Examining changes in the intratumoural CD8 population over time 82
3.2.3. Studying the changes in the intratumoural stem-like population over time 89
3.2.4. Investigating the phenotype of CD8 T cells as they enter the tumour 99
3.2.5. Examining the composition of CD8 T cells that egress the tumour 103
3.2.6. Examining the dissemination of stem-like CD8 T cells 111

3.3. Summary 117
3.3.1. Identifying changes in the intratumoural stem-like CD8 population over time 117
3.3.2. Investigating the migratory potential of stem-like CD8 T cells 119

Chapter 4 122

4.1. Introduction 123
4.1.1. Limitations of pre-clinical tumour models 123
4.1.2. The importance of modelling metastatic disease 126

4.1.3. Chapter aims 127

4.2. Results *128*
4.2.1. Establishing an orthotopic model of colorectal cancer 128
4.2.2. Characterisation of the intratumoural CD8 T cell population in orthotopic colon tumours compared to subcutaneous tumours 135
4.2.3. Establishing a model to track the migration of immune cells in orthotopic colon tumours 141
4.2.4. Establishing a liver tumour model through direct injection following limited surgical exposure 143
4.2.5. Establishing a model to track the migration of immune cells in liver tumour models 149

4.3. Summary *156*
4.3.1. Immunogenicity of modified cell lines 156
4.3.2. Orthotopic and subcutaneous tumours have comparable CD8 T cell compartments 158
4.3.3. Photolabelling of orthotopic tumours 160

Chapter 5 162

5.1. Introduction *163*
5.1.1. The liver is an immune suppressive environment 163
5.1.2. Proposed mechanisms underlying the systemic suppressive effects of liver metastasis 165
5.1.3. Aims 168

5.2. Results *169*
5.2.1. Investigating the composition of intratumoural CD8 T cells in orthotopic liver models 169
5.2.2. The presence of liver tumours impedes the effects of anti-PD-L1 treatment 174
5.2.3. Liver tumours alter the anti-tumour response in peripheral tumours 178
5.2.4. Investigating immune cell traffic between liver tumours and subcutaneous tumours 186
5.2.5. Assessing which lymphocyte populations are required for anti-tumour control in the dual liver and subcutaneous model 192

5.3. Summary *199*
5.3.1. Exhaustion is rapidly established in the intratumoural CD8 population of liver tumours 200
5.3.2. Dual liver and subcutaneous tumour models can be used to investigate systemic suppression of the anti-cancer immune response 201
5.3.3. Novel *in vivo* tumour labelling can be used to assess immune trafficking between tumours 202
5.3.4. The cellular basis of systemic suppression of the anti-tumour immune response by liver tumours 204

Chapter 6 206

6.1. Overview *207*
6.1.1. The dynamics of the stem-like CD8 response in cancer 209
6.1.2. Modelling colorectal cancer and metastatic disease 212
6.1.3. Systemic suppression of anti-tumour immunity by hepatic metastases in CRC 214

6.2. Limitations & Future Work *216*
6.2.1. Defining the stem-like CD8 compartment in pre-clinical tumour models 216
6.2.2. Improving orthotopic tumour models 216
6.2.3. Investigating the systemic suppressive effect of liver metastasis 219

6.3. Concluding Remarks *222*

Papers arising from this PhD 223

References 224

Appendix Chapter 3 248

Appendix Chapter 4 ..... **258**

Appendix Chapter 5 ..... **263**

Appendix Chapter 6 ..... **269**

List of Figures

Figure 1.1. Illustration showing the spectrum of CD8 T cell exhaustion. 17
Figure 1.2. Diagram demonstrating immunotherapies that target the anti-tumour CD8 T cell response. 21
Figure 2.1. Procedure for injection of tumour cell lines subcutaneously on the flank. 51
Figure 2.2. Procedure for injection of tumour cell lines into the colon via colonoscopy. 52
Figure 2.3. Procedure for intrahepatic injection of tumour cell lines. 53
Figure 3.1. Summary of initial tumour models used to investigate immune cell trafficking in dynamic labelling models. 77
Figure 3.2. Enumerating the intratumoural CD8 T cell population by flow cytometry in subcutaneous and primary tumour models. 79
Figure 3.3. Phenotype of the total CD8 T cell intratumoural population in subcutaneous tumour models. . 80
Figure 3.4. Phenotype of the antigen-specific CD8 T cell intratumoural population in subcutaneous tumour models. 83
Figure 3.5. Using the Kaede transgenic mouse and photo-labelling of tumours to assess changes in the immune compartment over time. 85
Figure 3.6. Determining the extent to which cells within the tumour vasculature contribute to the tumour infiltrating lymphocyte analysis. 87
Figure 3.7. Examining the effect of time in the tumour on the phenotype of the CD8 population. 88
Figure 3.8. Comparison of antigen-specific CD8 T cells versus the total CD8 compartment in tumours over time. 90
Figure 3.9. Identification of intratumoural stem-like CD8 T cells using scRNA-seq analysis of MC38-OVA subcutaneous tumours. 92
Figure 3.10. Defining the intratumoural stem-like CD8 population by flow cytometry. 93
Figure 3.11. Phenotyping the intratumoural stem-like CD8 population over time. 96
Figure 3.12. Determining the expansion of the OVA+ antigen-specific CD8 population. 98
Figure 3.13. Phenotype of CD8 T cells entering the tumour within 5 hours of photoconversion. 100
Figure 3.14. Photoconversion of the tumour draining lymph node allows tracking of CD8 T cells migrating into the tumour. 102
Figure 3.15. Characterisation of Kaede red+ CD8 T cells trafficking to the tumour within 24 hours of photoconversion of the draining lymph node. 104
Figure 3.16. Identification of a stem-like population in Kaede Red+ CD8 T cells trafficking to the tumour draining lymph node on scRNA-seq. 106
Figure 3.17. A population of Kaede Red+ CD8 T cells can be found in the draining lymph node following photoconversion of the subcutaneous tumour. 107
Figure 3.18. Phenotyping the Kaede Red+ CD8 population trafficking to the draining lymph node in CT26 tumours. 109

Figure 3.19. Understanding antigen-specific CD8 T cell trafficking to the tumour draining lymph node in MC38 OVA tumours. 110
Figure 3.20. Establishing a dual flank subcutaneous tumour model to understand the migration of CD8 T cells between tumours and peripheral lymphoid tissues –CT26. 112
Figure 3.21. Using the dual flank subcutaneous tumour model to understand the migration of antigen-specific CD8 T cells beyond the draining lymph node –MC38-OVA. 115
Figure 3.22. Illustration demonstrating the proposed establishment and migration of the stem-like CD8 compartment. 121
Figure 4.1. Implantation of CT26 GFP Luciferase colorectal cancer cell line into the colon wall of BALB/c mice. 129
Figure 4.2. Monitoring the growth of CT26 GFP Luc colon tumours using IVIS. 131
Figure 4.3. Expression of GFP and luciferase renders CT26 more immunogenic. 132
Figure 4.4. Monitoring the growth of CT26 WT tumours using repeat colonoscopy. 134
Figure 4.5. Characterising the difference in the CD8 population of CT26 tumours implanted in the colon versus subcutaneously. 136
Figure 4.6. Identifying the stem-like CD8 population in CT26 tumours implanted in the colon versus subcutaneously. 138
Figure 4.7. Examining the spatial distribution of T cells in subcutaneous tumour models. 139
Figure 4.8. Examining the spatial distribution of T cells in orthotopic colon tumour models. 140
Figure 4.9. Photolabelling of colon tumours *in situ* using a UV colonoscope. 142
Figure 4.10. Studying egress of immune cells to the draining lymph node following photolabelling of colon tumours *in situ.* 144
Figure 4.11. Monitoring the growth of CT26 GFP Luc liver tumours using IVIS. 146
Figure 4.12. Monitoring the growth of CT26 GFP Luc liver tumours with different cell carriers. 147
Figure 4.13. Characterising the difference in the CD8 population of CT26 GFP Luc tumours implanted in the liver in Matrigel versus PBS. 148
Figure 4.14. Examining the spatial distribution of T cells in liver tumour models. 150
Figure 4.15. Photolabelling of liver tumours *in situ.* 151
Figure 4.16. Spatial characterisation of photolabelled T cells in transcutaneously labelled subcutaneous tumours. 153
Figure 4.17. Spatial characterisation of photolabelled T cells in liver tumours. 155
Figure 5.1. Illustration of proposed mechanisms behind the liver tumour-mediated diminished response to ICB. 167
Figure 5.2. Phenotypic comparison of CD8 T cells in CT26 tumours implanted intrahepatically versus subcutaneously. 170
Figure 5.3. Comparison of exhausted CD8 T cell populations within tumours implanted intrahepatically versus subcutaneously. 172

Figure 5.4. Comparison of exhausted CD8 T cell populations in liver tumours at day 7 and 14. 173
Figure 5.5. Intrahepatic tumour burden blunts anti-PD-L1 enhancement of the anti-tumour response. ... 175
Figure 5.6. Liver tumours do not drive overt changes in CD8 T cell phenotype but do result in altered density within the tumour. 176
Figure 5.7. Intrahepatic tumour burden influences the growth of s.c. tumours at distal sites. 179
Figure 5.8. Intrahepatic tumour burden does not influence the phenotype of intratumoural CD8 populations at distal sites. 181
Figure 5.9. The presence of tumour intrahepatically changes the phenotype of CD8 T cells within anatomically distinct lobes of the liver. 182
Figure 5.10. Setting up a model to investigate whether the systemic immune suppressive effect of liver tumours is antigen dependent. 184
Figure 5.11. The systemic immune suppressive effect of liver tumours appears volume dependent rather than antigen-specific. 185
Figure 5.12. Establishing a dual liver + flank subcutaneous tumour model to understand immune cell migration out of and into subcutaneous tumours. 187
Figure 5.13. Establishing a dual liver + flank subcutaneous tumour model to understand the migration of CD8 T cells from the subcutaneous tumour to liver tumour. 189
Figure 5.14. Establishing a dual liver + flank subcutaneous tumour model to understand the migration of CD8 T cells from liver tumour to subcutaneous tumour. 191
Figure 5.15. Stem-like CD8 T cells egress liver tumours. 193
Figure 5.16. Establishing *in vivo* depletion of CD4 and CD8 T cells. 195
Figure 5.17. Depletion of CD4 and CD8 T cells in the dual liver/s.c. tumour model- impact on tumour growth. 196
Figure 5.18. Depletion of CD4 and CD8 T cells in the dual liver/s.c. tumour model- impact on immune populations in the s.c. tumour. 198
Figure 5.19. Illustration of Chapter 5 findings. 199
Appendix 3.1. Phenotype of the CD8 T cell population in spontaneous PyMT tumour model. 249
Appendix 3.2. The tissue resident memory CD8 population is absent in implanted CT26 and MC38-OVA tumours but present in primary PyMT tumours. 250
Appendix 3.4. Validation of OVA tetramer staining. 252
Appendix 3.5. Phenotype of the total CD8 T cell intratumoural population in subcutaneous CT26 tumour models over time- further quantitation. 253
Appendix 3.6. Characterising the co-expression of inhibitory receptors on CD8 T cells in subcutaneous tumour models over time. 254
Appendix 3.7. Phenotype of the CD8 T cell intratumoural population in subcutaneous tumour models over time in MC38-OVA model. 255
Appendix 3.8. Phenotyping the intratumoural stem-like CD8 population over time. 256

Appendix 3.9. Phenotype of CD8 T cells entering the tumour within 5 hours of photoconversion. 257
Appendix 4.1. Gating strategy used to identify CD8 T cells within colon tumours. 259
Appendix 4.2. Microscopy controls for CD8 and pancytokeratin stain. 260
Appendix 4.3. Gating strategy used to identify CD8 T cells within liver tumours. 261
Appendix 4.4. Microscopy controls for photoconverted tumours. 262
Appendix 5.1. FMO and isotype controls for PD-1, CX3CR1, FOXP3, TOX, TCF-1. 264
Appendix 5.2. Comparison of exhausted CD8 T cell populations in liver tumours at day 7 and 14 -further enumeration. 265
Appendix 5.3. Comparison of CD8 T cell populations within tumours implanted intrahepatically versus subcutaneously – further enumeration. 266
Appendix 5.4. Establishing a dual liver + flank subcutaneous tumour model to understand the migration of CD8 T cells from liver tumour to subcutaneous tumour. 267
Appendix 5.5. Establishing *in vivo* depletion of CD4 and CD8 T cells –further validation using blood samples. 268
Appendix 6.1. Injection of AKPT organoids into the colon wall as a further orthotopic colorectal cancer model. 270

List of Tables

Table 1.1– Inhibitory immune checkpoints currently targeted. 25
Table 1.2- Combination therapies with anti-PD-1/PD-L1 trialled in pMMR CRC. 36
Table 2.1- Staining buffer solution used for flow cytometry. 39
Table 2.2- Staining solution used for immunofluorescence microscopy. 39
Table 2.3- Chemicals and additives used to make solutions A, B and C in Gey's red cell lysis buffer. 40
Table 2.4- List of antibodies used for flow cytometry throughout this project. 41
Table 2.5- List of primary antibodies used for immunofluorescence microscopy in this project. 44
Table 2.6- List of secondary antibodies used for immunofluorescence microscopy in this project. 44
Table 2.7- Therapeutic antibodies used for in vivo experiments. 44
Table 2.8- Murine colon adenocarcinoma and melanoma cell lines utilised throughout the project. 45
Table 2.9- Base media and additional supplements used for the culture of cancer cell lines. 45
Table 2.10- Mice used throughout this project. 47
Table 2.11- Proportions of tissues stained for flow cytometry. 62
Table 2.12- Statistical analyses used in this thesis according to the data type. 68

List of Abbreviations

ACT	Adoptive cell therapy
AKPT	$Apc^{fl/+}$ $Kras^{G12D/+}$ $P53^{fl/fl}$ $Tgfbr1^{fl/fl}$
AP-1	Activator protein 1
APC	Antigen presenting cell
Bcl-6	B-cell lymphoma 6
BLIMP1	B lymphocyte-induced maturation protein-1
BMSU	Biomedical services unit
BSA	Bovine serum albumin
BTLA	B- and T-lymphocyte attenuator
CAF	Cancer associated fibroblast
CCL	Chemokine ligand
CCR	Chemokine receptor β
CD	Cluster of differentiation
cDC	Conventional dendritic cell
CMS	Consensus molecular subtype
CRC	Colorectal cancer
CTL	Cytotoxic T lymphocyte
CTLA-4	Cytotoxic T-lymphocyte associated protein 4
CXCR	Chemokine receptor α
DAMP	Damage-associated molecular pattern
DAPI	4’,6-diamidino-2-phenylindole
DC	Dendritic cell
dLN	Draining lymph node
DMEM	Dulbecco's modified eagle medium
dMMR	Deficient mismatch repair
DMSO	Dimethylsulfoxide
DNAse	Deoxyribonuclease
DPBS	Dulbecco's phosphate-buffered saline
EDTA	Ethylenediaminetetraacetic acid
EGFR	Epidermal growth factor receptor
EOMES	Eomesodermin
FasL	Fas ligand
Fc	Fragment crystallisable
FLT3L	FMS-like tyrosine kinase 3 ligand
FMO	Fluorescence minus one
FOXP3	Forkhead box P3
GFP	Green fluorescent protein
HBSS	Hanks’ balanced salt solution
Hi-FBS	Heat-inactivated foetal bovine serum
ICB	Immune checkpoint blockade
ICD	Immunogenic cell death

ICOS	Inducible T cell costimulator
IFNγ	Interferon gamma
IgG	Immunoglobulin G
IL	Interleukin
IQR	Interquartile range
I.v.	Intravenous
KG	Kaede green
KR	Kaede red
LAG-3	Lymphocyte-activation gene 3
LCMV	Lymphocytic choriomeningitis
LN	Lymph node
LSEC	Liver sinusoidal endothelial cell
Luc	Luciferase
MAGE	Melanoma-associated antigen
MDSC	Myeloid derived suppressor cell
MFI	Median fluorescence intensity
MHCI	Major histocompatibility complex class I
N4RA1	Nuclear receptor subfamily 4 group A member 1
NFAT	Nuclear factor of activated T cells
NICE	National Institute for Health and Care Excellence
NK	Natural killer
OVA	Ovalbumin
PBS	Phosphate buffered saline
PD-1	Programmed cell death protein 1
PD-L1	Programmed death-ligand 1
PD-L2	Programmed death-ligand 2
pMMR	Proficient mismatch repair
PRR	Pattern recognition receptor
ROI	Region of interest
RPMI	Roswell Park Memorial Institute
RT	Room temperature
SA	Streptavidin
s.c.	Subcutaneous
scATAC-seq	Single-cell sequencing assay for transposase-accessible chromatin
scRNA-seq	Single-cell ribonucleic acid sequencing
SD	Standard deviation
T-bet	T-box transcription factor
Tem	T effector memory
TCF-1	T cell factor 1
Tcm	T central memory
TCR	T cell receptor
TF	Transcription factor
TGF-β	Transforming growth factor beta
Th2	Type 2 T helper
TIGIT	T cell immunoreceptor with Ig and ITIM domains

TIL	Tumour infiltrating lymphocyte
TIM-3	T cell immunoglobulin and mucin domain-containing protein 3
TMB	Tumour mutational burden
TME	Tumour microenvironment
TNF	Tumour necrosis factor
TNM	Tumour, node, metastasis
TOX	Thymocyte selection-associated HMG BOX
TP53	Tumour protein P53
Tpex	Precursor exhausted T
Treg	Regulatory T
Trm	T resident memory
UMAP	Uniform manifold approximation and projection
UV	Ultraviolet
VEGF	Vascular endothelial growth factor
VEGFR	Vascular endothelial growth factor receptor
WT	Wildtype
XCL1	Chemokine (C motif) ligand

Chapter 1

Introduction

1.1. Introduction to Cancer Immunology

The burden of cancer within the United Kingdom is substantial, with 375,000 new cases of cancer diagnosed and 167,000 deaths attributed to cancer each year.(1, 2) Globally, it is estimated that 18.1 million new cases of cancer were diagnosed and 10 million deaths were due to cancer in 2020.(3, 4) Most of the cancer-related mortality both within the UK and worldwide is attributed to metastatic disease, in which cancer cells from the initial tumour mass detach and establish deposits at an anatomically distant site.(5, 6)

The therapeutic enhancement of the anti-cancer immune response represents one of the most significant advances in the field of oncology in recent years.(7) However, there remains enormous scope to improve responses to immunotherapy, and this is especially true in the metastatic setting where immunotherapy has shown limited success.(8) Improvements in immunotherapy critically depend upon a robust understanding of the effector immune compartment and the cellular environment that facilitates or obstructs it, the so-called tumour microenvironment (TME). This is especially the case in metastatic disease, where the interactions of tissue-specific cells and the cancer appear to develop further mechanisms of immune evasion.(9, 10) Cancer-related mortality is due to increase by 64% over the next two decades, and so research into the immunology of metastases is critical.(4)

1.1.1. Discovery of an immune response against cancer

Cancer immunosurveillance refers to the capacity of the immune system to recognise tumour antigen and eliminate cancer cells accordingly. Paul Ehrlich was the first to hypothesise that most neoplastic cells were removed by the immune system before clinical presentation.(11) Evidence of an anti-tumour immune response was provided by Gross in 1943, in a series of experiments in which mice were inoculated intradermally with syngeneic tumour cells before reinoculation with the same tumour cells.(12) Gross observed a higher rate of spontaneous regression of subcutaneously implanted tumours in animals that had prior inoculation with the same syngeneic tumour lysate.(12) Spontaneous rejection of intradermally implanted tumours had been observed previously, however, Gross controlled for the possibility of genetic differences between host animal and tumour cell line by developing a syngeneic tumour cell line.(12, 13) Similar work conducted by Foley in 1953 supported this, which controlled for the possibility of mutations in the re-injected tumour cells after repeated transplantation over time.(14) Burnet, building from this work, proposed the idea of cancer immunosurveillance in 1970, theorising that tumour neo-antigens stimulate an immune response that leads to elimination of many cancers before they become clinically apparent (15):

"It is by no means inconceivable that small accumulations of tumour cells may develop and because of their possession of new antigenic potentialities provoke an effective immunological reaction with regression of the tumour and no clinical hint of its existence."

Essential advances in understanding the important link between the immune system and cancer were made using genetically engineered mice. Mice deficient in various lymphocyte subsets showed increased susceptibility to tumour development, providing strong evidence supporting the theory of immunosurveillance.(16-19) The mechanisms underlying the anti-cancer function of lymphocytes began to be uncovered in the early 2000s, with the protective role of interferon gamma (IFNγ) production by T cells and perforin.(19-21)

Much of the evidence discussed comes from utilising murine models of cancer. Clinically, some of the most compelling evidence for an immune response against cancer is the increased risk of developing cancers with no known viral aetiology observed in those immunosuppressed recipients of solid organ transplants.(22-27) Unfortunately, many cancers do lead to clinical presentation, thus evidently immune surveillance of cancer is fallible. Understanding the factors leading to the failure of immune surveillance is essential to better consider how to restore or enhance immune cell functions.

1.1.2. Immunoediting

A more nuanced way of considering the immune response to cancer, termed 'immunoediting', was introduced in Dunn *et al.'*s 2002 review.(28) Three essential phases to the immune response in the context of cancer were described, elimination, equilibrium, and finally evasion.(28) Elimination is analogous to Burnet's theory of immunosurveillance in which the immune system acts to eradicate the cancer prior to the development of symptoms.(15) Initial growth of the tumour leads to innate cell recruitment, then the

subsequent activation of infiltrating lymphocytes and production of IFNγ.(29) The IFNγ can act directly to induce tumour cell death, or indirectly through production of chemokines from the tumour as well as host tissues which have anti-angiogenic properties.(30-33) Chemokines further attract anti-tumour immune populations, such as natural killer (NK) cells, directly to the response. Death of tumour cells results in the release of tumour antigens and their uptake by DCs, which subsequently traffic to the draining lymph nodes (dLNs) and present these antigens to T cells, driving the expansion of tumour specific CD8+ and CD4+ T cells. These then home to the tumour and attempt to eliminate remaining tumour cells.(34) If successful, all the cancer cells are eradicated, however, frequently, some cells will survive the initial attack from the immune system.

Equilibrium denotes the prolonged period in which tumour growth is restrained but unable to be eliminated by the action of host immune cells.(28) During this period, the host mechanisms deployed in the elimination phase exist but exert a selection pressure, leading to outgrowth of cancer cells that are better adapted to evade immune detection and eradication. Finally, immune escape describes when a cancer has evolved the ability to resist immune detection and destruction completely. In this phase, there is outgrowth of disease and malignant spread.(28)

1.1.3. Evading immune destruction as a hallmark of cancer

In 2000 Hanahan and Weinberg suggested six unifying principles underlying the complex multi-step development of cancer, including: sustaining proliferative signalling, evading growth suppressors, activating invasion and metastasis, enabling replicative immortality,

inducing angiogenesis, and resisting cell death.(35) These hallmarks were focused on the essential capabilities normal cells acquire on their progression to a neoplastic state. This framework was updated by the authors in 2011 to include what they termed “enabling characteristics” and “emerging hallmarks”.(36) Emerging hallmarks were yet more characteristics acquired by cells on their progression to cancer, including “deregulating cellular energetics” and “avoiding immune destruction”. The enabling characteristics of “genome instability” and “tumour-promoting inflammation”, were included as they facilitate the acquisition of the original hallmarks of cancer.(36)

The 2011 review further highlighted essential elements of the TME beyond cancer cells, bringing the importance of the immune system into the picture.(36) The authors acknowledged that immune surveillance must necessitate that tumours find ways of evading detection by the immune system. Methods of immune evasion noted were secretion of immunosuppressive factors and the recruitment of inflammatory cell types that in turn have an immunosuppressive effect.(36-39) Despite work published on immune checkpoints in cancer by 2011, these were not mentioned as a mechanism of immune avoidance; and so avoiding immune destruction was confined to an “emerging” hallmark, until 2022 when Hanahan’s review included this as a core hallmark of cancer.(40-42)

1.1.4. Pro- and anti-tumourigenic immune subsets in the tumour microenvironment

Extensive analysis of the composition of the TME has revealed that an array of immune cells and subsets, both pro- and anti-tumourigenic, are present in the TME. Key cells responsible for direct tumour cell killing are NK cells initially, then later cytotoxic T

lymphocytes take over.(43, 44) This response is underpinned by cells of the innate immune compartment, including dendritic cells and certain subtypes of macrophages, as well as cells of the adaptive arm of the immune response, comprising B cells and some CD4+ T cells.(45-47) The suppressive immune populations hindering effective anti-tumour immune responses include, but are not restricted to, T regulatory (Treg) cells, inflammatory macrophages, and immune suppressive neutrophils.(48) These populations stunt effector responses via various humoral and cellular mechanisms, including the secretion of immunosuppressive cytokines, depletion of resources essential for T cell responses, and expression of inhibitory receptors.(38, 49) Beyond immune populations within the TME there are stromal populations, such as fibroblasts, that both coordinate the actions of immune cells but also display immune functions.(50-53) Both immune and stromal populations in the TME are heavily influenced by tumour site. The intricacies of the roles each of these immune subsets play in the setting of malignancy is beyond the scope of this thesis. CD8+ T cells, as the final anti-tumour effector agent in the adaptive response against cancer, will form the focus of this work.

1.2. CD8 T Cell Activation & Effector Function in Cancer

It is well-established that T cell infiltration within tumours is associated with improved prognosis.(54-57) Specifically, an enriched cytotoxic CD8+ T cell population is strongly indicative of superior outcomes in multiple cancers.(54, 55, 58-60) However, CD8+ T cells are not static and exist on a continuum of differentiation states from naïve, to effector, to

memory populations. In the model scenario in which there is clearance of the tumour and thus inciting antigen, many cytotoxic CD8+ cells will be removed by apoptosis with some differentiating to form memory cells, providing future protection.(61) If tumour clearance is not possible, then there is antigen persistence, and CD8+ T cells are pushed toward a different fate termed 'exhaustion', resulting from chronic stimulation. Both exhaustion and memory states will be covered in 1.3. and 1.5. First, it is important to consider how a robust anti-tumour CD8 T cell response is generated.

1.2.1. Presentation of tumour antigen on MHC class I

The presentation of tumour antigen represents the key initial step in the generation of a successful anti-tumour CD8 T cell response. Dendritic cells cross-present tumour antigen to naïve CD8 T cells bearing the cognate T cell receptor within the dLN, where these rare populations are concentrated to increase the likelihood of interactions.(62-66) This results in the subsequent clonal expansion of antigen-specific T cells that underlie a robust adaptive immune response. The conventional dendritic cell 1 (cDC1) subset is most effective at cross-presenting tumour antigen on major histocompatibility complex class I (MHCI) to initiate CD8 T cell responses.(64, 67) Aside from the classical model of antigen presentation described, due to the persistence of antigen in established tumours that have escaped immunological control, there exists the possibility of cross-priming by antigen presenting cells (APCs) within the TME itself.(68, 69) However, whilst the TME provides a large depot of tumour antigen, as well as populations equipped for antigen presentation, immunosuppressive populations present within tumours and lack of adequate co-stimulation may limit the extent of priming of successful T cell responses at this site.(67)

Alongside this, the typical migration of naïve T cells is through blood and lymphatic circulation, as mediated by the expression of CD62L and chemokine receptor 7 (CCR7) (70); despite evidence of naïve T cell migration into peripheral tissues, there is far less evidence of robust naïve T cell populations entering unmanipulated tumours.(71) Hence, the relative importance of this mechanism remains uncertain.

The mechanisms by which dendritic cells (DCs) are recruited into the TME and subsequently acquire antigen are important, as it has been shown that an increased number of intratumoural cDC1s is a positive prognostic marker.(72, 73) cDC1 recruitment into tumours is chemokine-mediated, important chemokines include chemokine ligand 5 (CCL5) and chemokine (C motif) ligand 1 (XCL1) produced by NK cells.(73) The population is then maintained within the TME by growth factors, such as FMS-like tyrosine kinase 3 ligand (FLT3L), again principally produced by NK cells.(74) Activation of DCs within the TME is via pattern recognition receptors (PRRs) recognising damage-associated molecular pattern (DAMPs) released from stressed or damaged cells.(75) Tumour-derived DAMPs arise from the much-increased cell turnover, damage signals are then further enhanced by conventional cancer therapies.(75, 76) Post-activation, DCs upregulate CCR7, facilitating egress through lymphatics to the dLN, where priming of naïve T cells can occur as mentioned previously.(77, 78)

In the context of cancer, there are numerous barriers to the successful presentation of tumour antigen. One of the first problems is the tumour antigens themselves. The first tumour antigen recognised by the immune system to be discovered was melanoma-

associated antigen (MAGE-1) in 1991.(79) Melanoma is an example of a cancer with a high tumour mutational burden (TMB), and therefore more tumour neoantigen which can be presented to T cells, making it more immunogenic.(80) TMB was thought to be linked to increased responsiveness to immunotherapy observed in melanoma.(81) Therefore, those cancers with a lower mutational burden, such as proficient mismatch repair (pMMR) colorectal cancer (CRC), being less 'visible' to the immune system, often induce a limited anti-tumour T cell response.(80) TMB whilst important, is not the only factor, and clearly other inhibitory mechanisms play a role. Aside from tumour antigen, another barrier worth mentioning is DC dysfunction. Mature DCs enriched in immunoregulatory molecules, or mRegDCs, was a term introduced by Miriam Merad in 2020 to describe a distinct DC subset present in tumours that might curtail the anti-tumour response via high expression of programmed death-ligand 1 (PD-L1) and 2 (PD-L2).(82) This 'mRegDC' programme was shown in both cDC1 and cDC2s following the uptake of tumour antigen, with the increase in immunoregulatory molecules ultimately reducing DC functionality.(82) More recent data indicate that this intratumoural DC population should be considered an activated DC compartment and while DC activation is associated with traffic to the dLN, dynamic labelling of tumours revealed that some activated DC are actually retained within the TME.(83) Precisely how intratumoural DCs shape the anti-tumour T cell response remains an area of intense research.

1.2.2. T cell activation

T cells originate from the bone marrow in the form of early thymic progenitors that then undergo maturation within the thymus.(84) Negative selection represents a critical step in

thymic development, involving presentation of self-peptide on MHC within the medulla. T cells binding self-peptide with high avidity are deleted and hence those exiting the thymus are not reactive to host tissues.(85-89) Upon exiting the thymus CD8+ T cells are termed naïve and require activation to become effector CD8 T cells. The initial step in CD8 T cell activation is the T cell receptor (TCR) recognising its cognate antigen, in this scenario tumour specific antigens, presented on MHCI.(90) As class I MHC is present on the surface of all nucleated cells, CD8 T cells can recognise antigen presented by DCs but also on a variety of cells, including the cancer cells themselves.(91, 92) Binding of the co-receptor CD8 to MHCI stabilises the interaction between the cell presenting antigen and the T cell, inducing conformational changes in the CD3 family of proteins resulting in phosphorylation and downstream signalling.(90)

Peptide:MHCI TCR signalling alone in the absence of other signals will not result in T cell activation, but instead anergy and eventual apoptosis; co-stimulation via interaction of CD28 on the T cell surface with CD80/B7.1 or CD86/B7.2 on other immune cells is essential for productive T cell stimulation.(93, 94) There exist a multitude of co-stimulatory, as well as co-inhibitory, receptors that contribute to determining the outcome of TCR signalling and ultimately the fate of the T cell.(95) CD8 activation requires help from innate populations as well as CD4 T cells. CD4 T cells facilitate the CD8 response through multiple mechanisms, including through CD40L binding of CD40 on DCs;(96, 97) this binding results in signalling within the DC that increases production of interleukin (IL) 12 and 15, and upregulates co-stimulatory molecules on the DC surface CD80, CD86 and CD70.(96-98) Other signals in the environment such as the presence of cytokines, can additionally

promote or inhibit the T cell response.(99) IL-12 provided by DCs, and type I interferon from DCs and macrophages, are examples of signals that enhance a CD8 effector response, promoting CD8 survival and differentiation into effector and memory subsets.(100-102) IFN*γ* production from NK cells, as well as autocrine production by CD8 T cells themselves, supports CD8 effector differentiation.(103) The absence of co-stimulation and activating signals results in reduced proliferation and diminished effector functionality.(104, 105)

The exact timing and location of CD8 T cell priming, activation and acquisition of effector functionality in cancer is still not fully resolved. A paper published by Prokhnevska *et al.* in 2023 suggested that initial priming and activation of T cell factor 1+ (TCF-1+) tumour-specific CD8 T cells occurred in the dLN, but fundamentally these cells lacked an effector phenotype.(106) It was proposed that this TCF-1+ CD8 population migrates to the tumour, where appropriate co-stimulation and cytokines are provided, resulting in acquisition of an effector phenotype. These studies relied upon phenotypic similarities and TCR overlap between cells at both sites, a direct assessment of migration was not performed.(106) However, this study highlights that subtle differences in CD8 T cell priming and activation in cancer are yet to be fully elucidated.

1.2.3. CD8 effector functions in cancer

CD8+ T cells, also termed cytotoxic T lymphocytes (CTLs), carry out essential functions protecting the host from intracellular pathogens, as well as in tumour immunosurveillance. CD8+ T cells play a major role in the anti-tumour immune response due to their ability to

directly kill cancer cells, alongside promoting tumour MHCI expression and tumour antigen presentation through IFN-γ production. Effector CD8 T cells can be identified based on expression of surface markers such as CD25, CD69 and CD95; alongside high levels of perforin, granzymes and IFN*γ*; and transcription factors (TFs) such as T-box expressed in T cells (T-bet) and eomesodermin homologue (EOMES) that drive effector functions and differentiation.(16, 107-110)

The main mechanism by which CD8+ T cells act is through the induction of target cell apoptosis, either via the directional release of cytotoxic granules or engagement of death receptors. Cytotoxic granules contain perforin, which forms pores in the membrane of the target cell, then granzymes which can travel through the perforin-pore cause apoptosis. (111, 112) Perforin-deficient mice had normal numbers of CD8 T cells but demonstrated partial defects in eradicating induced tumours.(111) Once stimulated, CD8 T cells also express Fas ligand (FasL), which can bind Fas present on the target cell, resulting in activation of the caspase cascade and subsequent apoptosis.(113) The tumouricidal activity of FasL is uncertain, as cancer cells have multiple resistance mechanisms.(114-118) Finally, most CD8 T cells release IFN-γ, alongside other cytokines, additionally boosting host immune responses. IFN-γ causes macrophage activation and the increased expression of MHCI, further assisting antigen presentation and recognition.(119, 120) However, the balance of cytokines is key, and IFN-γ exemplifies this. IFN-γ, whilst playing a role in the anti-cancer immune response, has conversely been shown to promote tumour growth through chronic inflammation and promotion of an immunosuppressive TME.(121-124) Ultimately, CD8 T cells are essential in the anti-cancer immune response, however

persistence of an effector CD8 phenotype in the face of chronic antigen exposure is not possible.

1.3. CD8 Dysfunction in Cancer - The Default State

The normal fate of CD8+ T cells following antigen clearance in the context of acute infection, is that remaining T cells undergo apoptosis with a fraction differentiating to form a pool of long-lived memory populations.(61) However, with cancer there is persistence of antigen, meaning that CD8 T cells will follow a different trajectory toward exhaustion. Persistent antigen exposure represents a different challenge for the immune response, and the exhaustion programme may represent an adaptation to enable prolonged T cell responses in this scenario. It is essential to unpick at which stage of CD8 differentiation T cells are having the greatest impact on the tumour, and which of these stages can be 'rescued' or manipulated by immunotherapeutic targeting.

1.3.1. Discovery of 'exhausted' CD8 T cells

The exhausted CD8+ T cell population represents a heterogeneous pool of cells that arise during chronic viral infections and cancer. An exhausted CD8+ T cell phenotype was first described in the context of chronic lymphocytic choriomeningitis virus (LCMV), as a population of antigen-specific CD8+ T cells that lacked the ability to produce cytokines.(125, 126) T cell exhaustion was first defined in models of chronic viral infection according to phenotypic and functional characteristics.(126, 127) High levels of co-

inhibitory receptor expression at the cell surface is an identifying feature of exhaustion.(128) For example programmed cell death protein 1 (PD-1), though present upon T cell activation, is expressed at higher levels on exhausted cells.(129-131) A 2011 review by Wherry described the hierarchical loss of function during the acquisition of an exhausted CD8 phenotype.(132) The functional changes begin with loss of *ex vivo* killing, IL-2 production and decreased proliferative potential, followed by loss of tumour necrosis factor (TNF) production.(132) Later, the ability to release cytotoxic granules and produce IFN-γ is lost.(132) More recently several TFs have been used to define the exhausted CD8+ T cell, not limited to thymocyte selection-associated high mobility group box protein (TOX), EOMES, and B lymphocyte-induced maturation protein 1 (BLIMP1). (133-137)

The main factor in the development of an exhausted CD8 T cell phenotype is prolonged antigen exposure, with the degree of exhaustion positively correlated with the amount and length of antigen exposure.(138-142) Experiments in which the amount of the LCMV-derived gp33 peptide was altered, but the viral load kept consistent, revealed that low amounts of antigen result in CD8 T cells of a phenotype found in the acute infectious setting.(141) However, low affinity TCR binding still resulted in CD8 T cell exhaustion.(141) It was also shown that depletion of CD4 T cells at the time of infection contributed to the development of exhaustion in the antigen-specific CD8 compartment, and as a result mice became lifelong LCMV carriers.(143) Finally, although proinflammatory cytokines alone are not enough to cause exhaustion, at high levels they may cause the release of regulatory cytokines that foster exhaustion. IL-10 appears to promote the development of an exhausted phenotype, and indeed several studies studying the effect of therapeutically

blocking IL-10, demonstrated that this enhanced T cell function and helped prevent exhaustion.(144-146) Transforming growth factor beta (TGF-β) is another cytokine that appears to play a role in promoting exhaustion, using a model in which TGF-β signalling was attenuated demonstrated a reduced level of PD-1 expression on virus-specific CD8 T cells.(147) Even from the two cytokines mentioned here, it is clear that the balance of cytokines has an important effect on the nature of CD8 T cell response.

T cell exhaustion exists on a gradient, from pre-exhausted to early and late exhausted, see Figure 1.1. The transition from an early dysfunctional state toward late exhaustion is characterised by a progressive increase in the expression of co-inhibitory receptors and loss of typical CD8+ effector functions, alongside changes in the expression levels of TFs.(134, 148) CD44 and PD-1 were the first markers used to show heterogeneity in the exhausted CD8 compartment, PD-1^{int} $CD44^{hi}$ were shown to retain more functionality compared to PD-1^{hi} $CD44^{int}$;(128) in addition, PD-1^{int} $CD44^{hi}$ cells still showed a degree of responsiveness to ICB.(128) Im *et al.* provided further insight into the heterogeneity in the PD-1^{int} population following PD-1 therapy in the LCMV setting.(149) Transfer of CXCR5+ TCF-1+ TIM-3- cells into infection-matched recipients were shown to mediate the response to ICB, whilst also giving rise to a more exhausted CXCR5- TCF-1- TIM-3+ population.(149) The PD-$1^{hi}$$CD44^{int}$ terminally exhausted effector population represents those CD8 T cells at the end of the exhausted spectrum, with high expression of co-inhibitory receptors, no proliferative potential and poor effector capacity.(132) The above studies are consistent with a model in which a small number of pre-exhausted or early exhausted cells giving rise to a larger exhausted or terminally exhausted population.

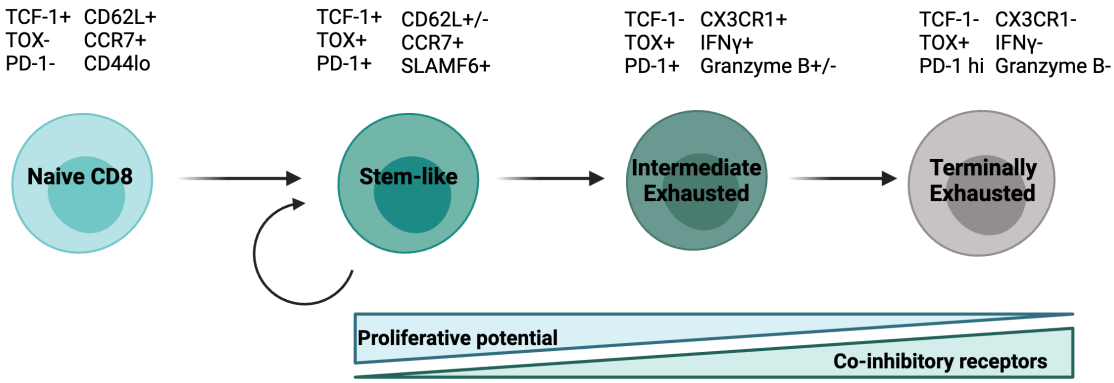


Figure 1.1. Illustration showing the spectrum of CD8 T cell exhaustion.

Transcription factors and surface markers associated with each CD8 T cell differentiation state are shown. Of note, from early to a fully exhausted state there is an increase in the expression of inhibitory receptor genes as well as loss of TCF-1. Created with Biorender.com

1.3.2. CD8 T cell exhaustion in cancer

T cell exhaustion is a defining feature of the T cell infiltrate within tumours. Some of the first evidence that demonstrated an exhausted intratumoural T cell compartment was the high expression of inhibitory receptors by tumour infiltrating lymphocytes (TILs).(150, 151) In addition, the production of effector cytokines alongside proliferative capacity is reduced in this population, as observed in T cell exhaustion in the context of chronic viral infection.(132, 151) It was demonstrated that this compartment was key in the response

to ICB, and phenotypic characterisation of the cells responding to ICB led to the realisation that there was heterogeneity in the exhausted CD8 T cell pool.(149, 152, 153)

The TF TOX was shown to underpin CD8 T cell exhaustion (133, 134). Through studying retroviral TOX expression *in vitro*, it was shown that TOX is unnecessary for the formation of effector and memory CD8 populations, but in the absence of TOX exhausted CD8 T cells did not form.(134) Single cell analysis, both scRNA-seq and scATAC-seq, and profiling of exhausted CD8 populations in tumours revealed regulatory regions important in developing an exhausted phenotype, these confirmed that they are an independent lineage from the effector population; they also highlighted that the exhaustion of T cells in both chronic viral infection and cancer are epigenetically similar.(154-156) ScATAC-seq indicated that chromosome accessibility in exhausted versus effector T cells showed fundamental differences, with exhaustion-related regions enriched for nuclear receptor subfamily 4 group A member 1 (N4RA1) and nuclear factor of activated T cells (NFAT) without adjacent activator protein 1 (AP-1) site.(154) Abdel-Hakeem *et al.* demonstrated that exhausted CD8 T cells remain epigenetically 'stuck', as upon removal of antigen there is some recovery of function, however this population is unable to regain memory capacity.(135) The evidence available supports the notion that exhaustion is a distinct state of differentiation underpinned by re-wiring of the genome.

This exhausted T cell population within tumours lacks proliferative potential, in particular in response to ICB, and so how the anti-tumour response was sustained for many years in some patients remained under debate.(157) A precursor or early exhausted population,

expressing the memory-associated transcription factor TCF-1 (encoded by *Tcf7*), provided an answer.(158, 159)

1.3.3. Stem-like CD8 T cells sustain the exhausted compartment

Stem-like CD8 T cells, or the 'precursors of exhausted' T cells (Tpex), represent an early subset on the exhaustion continuum that allows the T cell response to be sustained. Stem-like CD8 T cells have memory-like features (expression of CD62L, CCR7, CD127), lack expression of effector genes (granzyme B), but demonstrate certain features of exhaustion (including PD-1 and TOX expression).(158-160) This population express TCF-1 and preserve a high proliferative potential, meaning that stem-like cells are capable of maintaining the antigen-specific TCF-1- population whilst also undergoing self-renewal.(158) It has been suggested that high antigen load may play an important role in preventing this population from continuing along the differentiation pathway toward a fully exhausted phenotype.(141, 160)

In LCMV models, the pre-exhausted stem-like (TCF-1+ PD-1+) CD8 phenotype was linked to the proliferative burst following blockade of the PD-1/PD-L1 axis responsible for sustaining the response.(149, 158) Most of the work mentioned thus far was carried out in murine LCMV models, but Siddiqui *et al.* identified a TCF-1+ PD-1+ CD8 compartment and examined its function in both pre-clinical tumour models and the clinical setting.(148) Experiments in which TCF-1+ CD8 T cells were selectively ablated, led to reduced numbers of TCF-1- CD8 T cells and significant tumour progression.(148) Intratumoural TCF-1+ PD-1+ CD8 T cells specifically were highlighted as driving proliferation following ICB therapy, as

tumours still responded to ICB even when FTY720 was administered blocking further lymphocyte entry into the tumour.(148) Further supporting these data, transcriptomic profiling of clinical samples from melanoma patients treated with immune checkpoint blockade (ICB) revealed that a similar CD8 phenotype was essential in the response to therapy, as *Tcf7* expression by tumour infiltrating CD8 T cells correlated with an improved response to ICB.(161) The studies above emphasise the potential significance of the intratumoural stem-like CD8 compartment in the response to immunotherapy.

1.4. Harnessing the Immune Response Against Cancer - Current CD8 Immunotherapies

Over the past decade cancer immunotherapy has increasingly been recognised as an important means of treating cancer, with the Nobel Prize in Physiology or Medicine in 2018 awarded for the discovery of ICB.(7, 41, 42) Immunotherapy now forms an essential part of the treatment of some cancers, with the National Institute for Health and Care Excellence in the UK issuing recommendations for the use of ICB in multiple cancers.(162-164) There are a multitude of immunotherapies being used to target various components

of the anti-tumour immune response, however here the focus will be on the CD8 T cell response (Fig. 1.2).

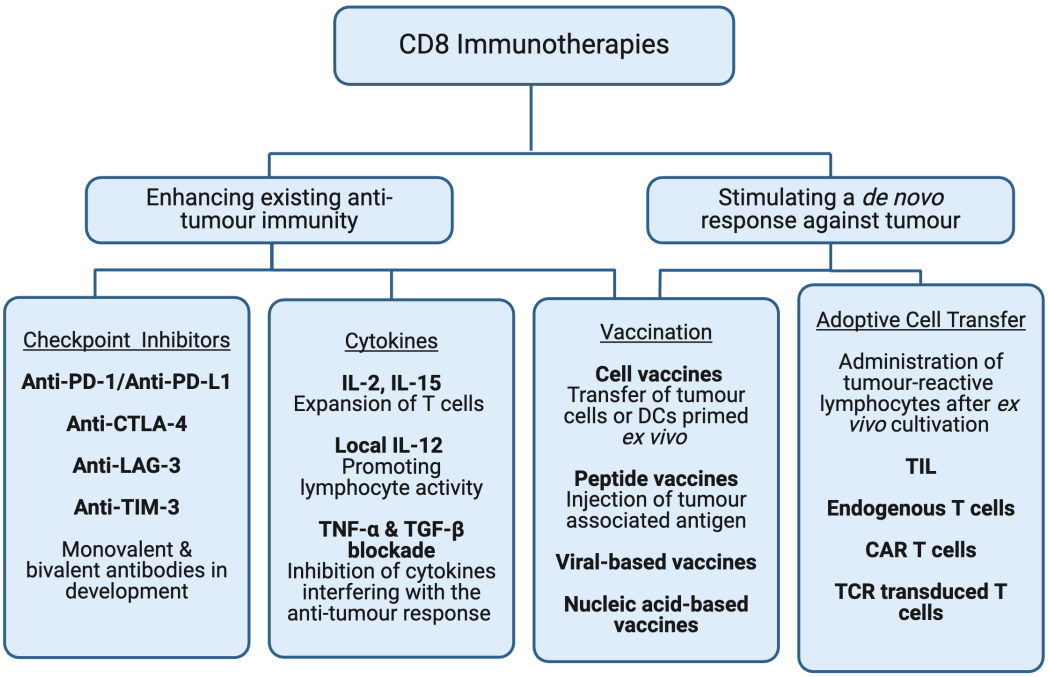


Figure 1.2. Diagram demonstrating immunotherapies that target the anti-tumour CD8 T cell response.

CD8 immunotherapies can be broadly categorised as enhancing an existing anti-tumour immune response or stimulating a new response. Types of therapies are underlined, and examples of each therapy type shown in bold. Created with Biorender.com

1.4.1. Types of T cell focused immunotherapy

T cell immunotherapies, in broad terms, can be understood as either enhancing a pre-existing anti-tumour immune response, or as generating a new response to tumour antigen, see Figure 1.2. Both checkpoint inhibitors and therapeutic cytokines, are examples

of therapies that enhance existing anti-tumour immunity. Checkpoint inhibitors are monoclonal antibodies that target immune regulatory checkpoints, allowing for the continuation of an anti-tumour immune response.(165) ICB will be covered in further detail in 1.4.2. Therapeutic cytokines have been trialled and work to support productive T cell responses, examples include: IL-2 to support T cell expansion, IL-15 through enhancement of proliferation and cytotoxicity, and locally acting IL-12 leading to IFN-γ production by T cells whilst also having anti-angiogenic properties.(166-171) Alternatively, antibodies targeting immunosuppressive cytokines such as TGF-β and TNF-α have been used in clinical trials to prolong anti-tumour T cell responses.(172-174) However, the dynamics of these cytokines in the anti-tumour response is likely to be more nuanced. TNF-α can be supportive of the immune response, but chronic TNF-α signalling within the TME can lead to activation-induced T cell death.(175, 176) Similarly, TGF-β inhibits growth of tumour cells in the initial stages of tumour development, but later on acts in an immunosuppressive fashion by recruiting immune cells of an immunoregulatory phenotype, shaping the stromal compartment, and decreasing CD8 T cell activity.(177, 178)

Stimulating a novel immune response against a patient's tumour represents another approach in cancer immunotherapy. Adoptive cell therapy (ACT) encompasses multiple techniques that involve the isolation and expansion of a patient's own T cells; once the number of tumour-specific T cells cultured has reached the therapeutic threshold, then the cells are transferred back into the patient following lymphodepletion. The three main types of ACT are tumour-infiltrating lymphocytes (TILs), genetically engineered T cell receptors,

and chimeric antigen receptor T cells. ACT has led to successful treatment of haematological malignancies in the clinic, as well as more limited successes in treating solid tumours such as melanoma.(179-182) This approach is not without its problems, including patients lacking TILs in their tumour, immunosuppressive mechanisms present in the TME, T cell exhaustion, and the time taken to produce cells for transfer.(183)

Cancer vaccination overlaps both the strategies mentioned above, with the aim of inducing tumour antigen-specific T cells capable of anti-tumour activity. Vaccine platforms are either peptide-based (containing multiple epitopes to stimulate a T cell response), cell-based (tumour cell or dendritic cell), viral-based (e.g., using adenovirus to provide tumour-shared antigen), or nucleic acid-based. Antigen selection is key to the design of vaccines, in the context of cancer these are categorised according to whether they are tumour-shared antigens or tumour-specific antigens.(184) Tumour-shared antigens include those proteins that are overexpressed in cancer, differentiated self-antigen, and viral specific proteins. The merit of this approach is that the vaccines developed can be used across patients, however these vaccines have had limited success and the nature of the antigen being non-specific means that off-target toxicities are a risk.(184, 185) Tumour-specific antigens on the other hand are expressed only by tumour cells, the off-target effects are limited with this strategy, but finding an effective neoantigen is problematic.(184, 186, 187) Currently most cancer vaccines are in clinical trial stages, and the limited benefits observed may be due to the patient groups being treated, largely those who have received all available conventional treatment and whose immune systems are depleted.(188)

1.4.2. Immune checkpoint blockade

Immune checkpoints are surface molecules, both stimulatory and inhibitory, that help regulate the magnitude of the adaptive immune response. Inhibitory immune checkpoints are key in preventing autoimmunity and regulating immune responses, so they do not cause unwanted damage to tissues. However, in the context of an anti-tumour immune response contribute to pathology by cutting short a productive T cell response and assist in immune escape of the tumour.

The discovery of ICB in enhancing the antitumour immune response, led to Allison and Honjo being jointly awarded the Nobel Prize in Physiology or Medicine in 2018.(7, 41, 42) Immune checkpoint inhibitors, also referred to as ICB, support the existing immune response by blocking receptor-ligand interactions that dampen the immune response. The PD-1/PD-L1 and CTLA-4/CD80 CD86 axis represent two of the most important pathways in the field of cancer immunotherapy. Programmed cell death 1 (PD-1) protein is present on the T cell surface post-activation and negatively regulates activity when bound by programmed cell death ligand 1 (PD-L1), expressed by both APCs in the tumour environment as well as the cancer cells themselves.(41, 189) Early work demonstrating the effect of the PD-1/PD-L1 axis in pre-clinical myeloma models demonstrated that tumour growth could be inhibited by administration of anti-PD-L1 antibodies and completely repressed in PD-1 deficient mice.(41) The second key inhibitory checkpoint, cytotoxic T lymphocyte associated protein 4 (CTLA-4), is upregulated in activated T cells and translocated to the cell surface where it can then interact with CD80/CD86 on APCs.(97) CTLA-4 binds with higher affinity and avidity than CD28 to CD80/86, where it then inhibits

T cell stimulation and cytokine production.(97, 190) Initial studies using antibodies to block CTLA-4 activity in pre-clinical cancer models resulted in the rejection of pre-established tumours.(42) Antibodies against PD-1, PD-L1, CTLA-4 and LAG-3 are currently routinely used in clinical practice (162-164, 191, 192); with many other trials using ICB targeting other checkpoints ongoing.(193) Table 1.1 summarises current therapeutically targeted inhibitory checkpoints.

Table 1.1– Inhibitory immune checkpoints currently targeted.

List of inhibitory immune checkpoints alongside their corresponding ligands and immune cell expression pattern. Current therapeutic antibodies targeting immune checkpoints and their stage of clinical development are also displayed.

Inhibitory Checkpoints	**Ligand/s**	**Pattern of Expression**	**Therapies**	**Phase of Clinical Trials**
Programmed Death-1 Receptor (PD-1)	PD-L1 PD-L2	T cells B cells	Anti-PD-1 mAb (pembrolizumab, nivolumab) Anti-PD-L1 mAb (atezolizumab)	Approved by NICE. (191, 194, 195)
Cytotoxic T-Lymphocyte Antigen 4 (CTLA-4)	CD80 CD86	T cells	Anti-CTLA-4 mAb (ipilimumab)	Approved by NICE. (164, 196)

Lymphocyte Activation Gene-3 (LAG-3)	MHCII	T cells B cells NK cells DCs	Anti-LAG-3 mAb (relatlimab) LAG3 fusion protein Bispecific LAG-3/PD-L1 Ab	Approved by NICE. (197)
T Cell Immunoreceptor with Ig and ITIM Domains (TIGIT)	CD155	T cells NK cells	Anti-TIGIT mAb (tiragolumab)	Phase III. (198)
T Cell Immunoglobulin and Mucin Domain 3 (TIM-3)	Galectin 9 CEACAM1 Phosphatidylserine	T cells B cells Cancer cells NK cells DCs Monocytes	Anti-TIM-3 mAb (sabatolimab) Bispecific TIM-3/PD-1 Ab	Phase III. (199)
NKG2A	MHCI HLA-E	T cells NK cells	Anti-NKG2A mAb (monalizumab)	Phase III. (200)
Inducible T Cell Costimulator (ICOS)	ICOSL	T cells	Anti-ICOS mAb	Phase II. (201)
B and T Lymphocyte Attenuator (BTLA)	HVEM	T cells B cells	Anti-BTLA mAb (icatolimab)	Phase I. (202)

1.4.3. Resistance to immune checkpoint blockade

Despite the successes of ICB in oncology there are still major barriers to overcome. Resistance to ICB can be either primary, in cases where the tumour is unresponsive to initial therapy, or acquired, where patients experience relapse after an original response. Tumour immunogenicity poses one of the first barriers to the generation of a productive anti-tumour immune response, with a higher TMB often correlating with improved responses to ICB.(203-206) However, TMB is an imperfect marker to predict responsiveness to ICB, this is in part due to the type of mutation not being taken into account.(81, 207, 208) Another mechanism of resistance is the downregulation of MHCI hindering the CD8 T cell response, this is described in around half of human tumours and often correlates with inferior prognosis.(92, 209-213) Finally, even when effector T cells are able to recognise tumour antigen and physically infiltrate the tumour, the TME itself is overwhelmingly immunosuppressive, harbouring immunoregulatory subtypes that foster irreversible CD8 T cell dysfunction.(150, 154, 214-216)

Differences in the response to ICB go beyond the tumour and extend to the host. It has been demonstrated that syngeneic mice, injected with the same tumour cells, treated with ICB at the same time points can have completely different responses to ICB. Host-related factors such as age, sex, and disease clearly impact the immune system at baseline, so it seems clear that these could influence response to ICB.(217, 218) Environmental factors, such as diet, microbiota and infection history, also profoundly influence the immune system of the host and thus the immune response. (219, 220) Most of the research into

the failure of the CD8 T cell response in ICB treatment focuses on the immune landscape of the tumour mass itself, neglecting to consider the role of immune cells trafficking into the cancer from elsewhere; or indeed egressing the tumour and the influence of this population on nodal disease and wider metastatic spread.

1.4.4. Combination therapies

Many patients still do not receive substantial benefit from monotherapy with ICB, and so efforts have shifted toward finding appropriate combination therapies. The use of anti-CTLA-4 with anti-PD-1 was the first ICB combination trialled in clinic, resulting in prolonged progression free survival and overall survival.(221) However, the proportion of patients reporting treatment-related adverse effects went from 86% to 96%, raising concerns over toxicity.(221) Combination therapies may combine ICB with chemotherapy, radiotherapy, targeted therapy, or other immunotherapies working on different pathways. Chemotherapy-ICB and radiation-ICB combinations are thought to work due to increased immunogenic cell death (ICD) and cancer antigen presentation following chemotherapy or radiotherapy.(222-224) Unfortunately, both chemotherapy and radiotherapy can have negative impacts on the efficacy of immunotherapy, with chemotherapy causing lymphodepletion and radiation therapy enhancing an immunosuppressive phenotype within the TME.(225, 226) With regard to targeted therapy-ICB combinations, the most promising are angiogenesis inhibitors. Like the previously mentioned strategies, ICD plays a part in the effectiveness, but in addition the VEGF-VEGFR pathway has immunomodulatory functions influencing T cell activation, regulatory populations and dendritic cells.(227, 228) Dual immunotherapy combination strategies are numerous,

including cytokines-ICB, ACT-ICB, ICB-ICB and targeting of innate immune cells alongside ICB.(229-232) Whilst these approaches are still in their infancy, several combination therapies are already approved for use in clinic.

1.5. Systemic and Long-lived Immunity to Cancer

Durable tumour regression is the desired end-state of immunotherapy. The generation of immune memory should ensure protection against future recurrence of the same cancer. Essential questions remain concerning anti-tumour immunity and memory responses, including whether true memory T cells can contribute to the immune response against cancer, and whether exhausted CD8 T cells are involved in memory responses.

1.5.1. Generation of CD8 memory responses

Memory T cells are those that have responded to antigen prior to long-term maintenance in the pool of T cells. Defining features of memory populations include a high proliferative potential, an ability to rapidly regain effector function upon antigen re-exposure, and persistence in the absence of antigen through the effects of IL-7 and IL-15.(233-235) The key memory CD8 T cell subtypes are central memory (T_{cm}), effector memory (T_{em}), and tissue resident memory (T_{rm}). T_{cm} cells are defined as CD44hi CD62L+ CCR7+ and re-circulate through secondary lymphoid tissue in search of their cognate antigen.(236) T_{cm} proliferate to produce the effector memory population.(236) T_{em} cells, CD44hi CD62L-CCR7-, circulate through non-lymphoid tissue and maintain the ability to produce effector

cytokines.(236) T_{rm} cells, CD44hi CD62L- CD69+ remain within the tissue in which they were generated, providing protection where the antigen was originally found, and produce effector cytokines.(237) Ultimately, the generation of memory CD8 T cell populations provides enhanced future protection upon re-exposure to antigen. Most of the work on CD8 memory comes from models of infection, much less is known about the role of these populations in the context of cancer.

1.5.2. Memory CD8 T cells in cancer

The vast majority of intratumoural CD8 T cells are phenotypically exhausted, and so it is essential to understand how exhaustion and the formation of memory populations fit together. Exhausted CD8+ T cells have reduced expression of CD122, forming the beta chain of the IL-15 receptor, and CD127, the alpha chain of the IL-7 receptor.(238) This means that in the absence of antigen, unlike memory cells, the remaining exhausted CD8 cells are unable to respond to IL-7 and IL-15 and are unable to be maintained.(238) However, recent data using the chronic LCMV model of exhaustion in which antigen was removed after the formation of an exhausted T cell population, showed that if epitope escape occurs early during the disease course some recovery of memory functions is possible.(135) It was found that most of the recovered exhausted cells were derived from the TCF-1+ progenitors, however this population was less capable of expansion on antigen re-exposure and preferentially gave rise to cells of an exhausted rather than effector phenotype.(135) Hence, it appears unlikely that “epigenetically scarred” exhausted populations in the tumour are contributing to systemic memory and protection against cancer, raising the question of how systemic anti-tumour memory is established.

Fundamentally, it seems that exhausted CD8 T cells within the tumour are unable to form true memory populations, and as a result poorly equipped in the instance of disease recurrence.

There is evidence that memory populations, both CD8 and CD4, form in parallel to exhausted T cells in cancer.(153, 239, 240) The presence of CD103+ CD8 T_{rm} cells has been demonstrated in several cancers, and has been associated with an improved prognosis.(241-243) Within this T_{rm} population, a PD-1+ TIM-3+ fraction was shown to be particularly responsive to treatment with a PD-1 inhibitor, transcriptionally enriched for markers of cytotoxicity and clonally expanded.(244) T_{rm} populations within lymph nodes (LNs) have been found to originate in non-lymphoid tissues, this observation is most important in the setting of nodal disease spread.(245) Beyond the tumour itself, secondary lymphoid organs and non-exhausted clones in the periphery have been shown to be essential in the response to ICB (239); with peripheral populations being the most proliferative post treatment.(239) The systemic T cell response, though often overlooked, is able to avoid the exhaustion inherent to the intratumoural CD8 pool and appears critical to a successful anti-tumour immune response.

1.6. The Immune Response to Colorectal Cancer

CRC is the fourth most common cancer in the United Kingdom, with 42,000 new diagnoses and 16,000 deaths each year.(246) The backbone of treatment for CRC is surgical resection,

chemotherapy and radiotherapy.(247) The merits of immunotherapy in the treatment of CRC are limited, and will be covered in the following pages, hence there remains enormous scope to improve efficacy in this setting.

1.6.1. The immune landscape of colorectal cancer

CRC develops from adenoma to carcinoma, adenomas form through inactivation of *APC* resulting in WNT signalling in intestinal stem cells and the resultant outgrowth of epithelial cells (248); progression to carcinoma then occurs through a combination of tumour protein P53 (TP53) inactivation and mutations in *KRAS* and *BRAF*.(248) CRC is divided up into four consensus molecular subtypes CMS1-4, however it can be roughly divided into pMMR aligning with CMS2-4, and deficient mismatch repair (dMMR) CRC, CMS1.(249) dMMR CRC is characterised by a high TMB due to the defect in mismatch repair machinery, and ICB in this setting has shown positive results in patients.(80, 250, 251) However, only around 15% of individuals with CRC have dMMR CRC, meaning that the vast majority have pMMR disease.(249, 252) pMMR CRC bears fewer mutations and has a decreased T cell infiltrate, with CMS4 containing a larger neutrophil infiltrate; in this setting the role of immunotherapy is limited, with largely disappointing results from trials in late-stage disease.(251)

The staging of CRC is based on the TNM system in which the size of the tumour, number of LNs affected, and presence of metastasis are used to provide an estimate of the extent of disease.(253) In recent years the importance of the TME has been highlighted, including the type and distribution of immune cells within this, leading to attempts to include these

factors in the classification and staging of disease. The Immunoscore was established to evaluate the risk of CRC recurrence following surgery, the scoring system incorporates CD3 and CD8 T cell density within the tumour and its margins, resulting in a score of low, intermediate or high.(254) There was a statistically significant difference between the Immunoscore assigned and the time to recurrence, with a high Immunoscore resulting in lowest risk of recurrence.(254) Taking all of the above into consideration, there is clearly an opportunity to therapeutically enhance the anti-cancer immune response in CRC; to achieve this, it is essential to first unpick the barriers to the establishment of durable and successful T cell responses in CRC.

1.6.2. The importance of liver metastasis in CRC

Primary disease can often be treated through a combination of surgical excision and chemotherapy, it is metastatic disease that kills most patients with CRC, and approximately 20% of patients have metastatic deposits at the time of presentation to clinic.(255-257) The most common sites of metastatic disease in CRC are the liver, lung and peritoneum.(258) About a third of patients diagnosed with CRC develop liver metastasis, and over half of all metastatic disease in CRC is hepatic.(258, 259) Patients with liver metastasis often have the worst prognosis, with the median survival post-diagnosis with metastatic CRC being just 9 months.(258) Some benefit of atezolizumab, an ICB agent targeting PD-L1, has been seen in those with metastatic pMMR CRC when used in combination with the chemotherapeutic drug capecitabine and anti-VEGF agent bevacizumab.(260) However, the response rate was significantly worse in those with liver metastasis (6%) versus those without (23%).(260) The reduced efficacy of ICB in the

presence of liver disease was also shown by a study comparing the combination of anti-VEGF agent regorafenib with nivolumab (targeting anti-PD-L1), with the response rates when using either drug as a monotherapy;(261) those with liver disease saw an objective response rate of 8%, versus 63% in those with lung disease.(261) Even in the setting of more immunogenic cancers that respond well to ICB, such as melanoma, those with liver metastases have much lower response rates to ICB than those without.(262-264)

The mechanisms underlying the suppressive effect of liver metastasis on systemic anti-tumour immunity are still being uncovered. One suggested mechanism is the destruction of antigen-specific T cells by macrophage populations within the liver metastases.(265) Yu *et al.* reported that monocyte-derived macrophage populations within liver tumours were able to selectively remove activated CD8+ T cells from the circulation, which depleted systemic T cell protection.(265) Regulatory T cell populations within liver tumours provide an alternative mechanism behind the observed suppression of the anti-tumour immune response.(266) Lee *et al.* demonstrated in a pre-clinical melanoma model that the antigen-specific immune suppressive effect observed when tumour antigen was present in the liver was associated with Treg activation.(266) The effect of anti-PD-1 therapy in the setting of liver disease was not observed unless Treg function was disrupted.(266)

1.6.3. Immunotherapy in the treatment of proficient mismatch repair colorectal cancer

Metastatic CRC is a disease of huge unmet therapeutic need, in particular pMMR (CMS2-4) disease. Systemic treatment for these patients is reliant on chemotherapy, however the median survival is less than two years.(267) Despite the limited beneficial impact of ICB

monotherapy in this setting, with the National Institute for Health and Care Excellence (NICE) recommending anti-PD-L1 therapy only in the setting of metastatic dMMR CRC, there are efforts to improve ICB's efficacy in the treatment of metastatic pMMR CRC;(250, 268) see Table 1.2 for some of the main anti-PD-1/PD-L1 therapeutic combination approaches currently being trialled in pMMR CRC. Combinations of ICB with both conventional and novel targets are being trialled, though many are currently in early phases. In dMMR CRC, the combination of anti-PD-1 and anti-CTLA-4 was utilised in the neoadjuvant setting, resulting in major pathological responses in over half of patients.(252) The same combination in pMMR CRC, resulted in no clinically significant differences in survival.(269) Clearly there remains enormous scope to improve immunotherapy in the treatment of CRC, particularly for those bearing liver metastasis, and to achieve this we must gain further detailed understanding of the mechanisms that limit successful immune responses.

Table 1.2- Combination therapies with anti-PD-1/PD-L1 trialled in pMMR CRC.

Therapeutic combination strategies with anti-PD-1/PD-L1, with the stage of clinical development and trial names.

	Combination	Phase of Clinical Trial	Study
Chemotherapy	Fluorouracil + oxaliplatin + anti-PD-1	II	METIMMOX.(270)
Anti-Epidermal growth factor receptor (EGFR)	Cetuximab + irinotecan + anti-PD-1	II	AVETUXIRI.(271)
Anti-VEGF	Bevacizumab + capecitabine + anti-PD-L1	II	BACCI.(272)
	Bevacizumab + FOLFOXIRI + anti-PD-L1	II	AtezoTRIBE.(273)
	Bevacizumab + fluorouracil + leucovorin + oxaliplatin + anti-PD-1	III	CheckMate9x8.(274)
Tyrosine Kinase Inhibitor	Regorafenib + anti-PD-1	Ib	REGONIVO.(261)
	Regorafenib + anti-PD-L1	II	REGOMUNE.(275)
	Levatinib + anti-PD-1	II	LEAP-005.(276)
ICB	Ipilimumab (anti-CTLA-4) + panitumumab (EGFR) + anti-PD-1	II	LCCC1632.(277)
	Favezelimab (anti-LAG-3) + anti-PD-1	II	MK-4280A.(278)

1.7. Aims & Objectives

The aim of this investigation was to understand the relationship between the CD8 compartment within primary tumours, the periphery, and secondary tumours. Much work in the field of tumour immunology has focused on changes within the intratumoural immune compartment, and yet much less is known about systemic anti-tumour immunity. Utilising the Kaede tumour photolabelling approach established within the Withers Lab, temporal labelling of host cells within tumours has enabled the study of immune cell dynamics within the tumour and subsequent migration to the periphery. Combining this photolabelling approach with primary and metastatic orthotopic models of CRC will provide new insight into how the CD8 compartments within distinct tumours interface.

The overarching aims of this investigation were to:

1. Characterise the establishment and migratory potential of the stem-like CD8 compartment in tumour models.
2. Investigate whether utilising orthotopic models of CRC alters the nature of the CD8 compartment.
3. Establish photolabelling approaches in orthotopic tumour models to enable immune cell migration in anatomically relevant models of disease to be assessed.
4. Examine how the CD8 compartment within tumours at anatomically distinct sites interact.

Chapter 2

Materials & Methods

2.1. Materials

2.1.1. Chemicals & Reagents

The staining solutions used for immunofluorescence microscopy and flow cytometry are listed in Tables 2.1 and 2.2.

Table 2.1- Staining buffer solution used for flow cytometry.

Reagent	Manufacturer	Concentration
Dulbecco's Phosphate-Buffered Saline (DPBS) + $MgCl_2$ and $CaCl_2$	Sigma-Aldrich; D8662	97.5%
Ethylenediaminetetraacetic Acid Solution (EDTA)	Sigma-Aldrich; 03690	2.5M
Heat-inactivated Foetal Bovine Serum (Hi FBS)	Sigma-Aldrich; F9665	2.0%

Table 2.2- Staining solution used for immunofluorescence microscopy.

Reagent	Manufacturer	Concentration
Phosphate-Buffered Saline (PBS)	Sigma-Aldrich; D8537	99%
Bovine Serum Albumin (BSA)	Sigma-Aldrich; A7906	1%

Gey's red cell lysis buffer is used to remove red blood cells prior to flow cytometry. Solutions A and B are made by adding the components listed in Table 2.3 to 1L of distilled

water. 50ml aliquots of Gey's buffer are then made using 35ml distilled water, 10ml solution A, 2.5ml solution B and 2.5ml solution C.

Table 2.3- Chemicals and additives used to make solutions A, B and C in Gey's red cell lysis buffer.

Solution	Component	Concentration
A	Distilled H_2O	1L
	NH_4Cl	3.5 % ($^w/_v$)
	KCl	0.185 % ($^w/_v$)
	$Na_2HPO_4.12H_2O$	0.15 % ($^w/_v$)
	KH_2PO_4	0.0119 % ($^w/_v$)
	Glucose	0.5 % ($^w/_v$)
	Gelatin	2.5 % ($^w/_v$)
	1% Phenol Red	0.15 % ($^v/_v$)
B	Distilled H_2O	1L
	$MgCl_2.6H_2O$	0.42 % ($^w/_v$)
	$MgSO_4.7H_2O$	0.14 % ($^w/_v$)
	$CaCl_2$	0.34 % ($^w/_v$)
C	Distilled H_2O	1L
	$NaHCO_5$	2.25% ($^w/_v$)

2.1.2. Antibodies

The antibodies used for flow cytometry are listed in Table 2.4.

Table 2.4- List of antibodies used for flow cytometry throughout this project.

Target Antigen	Conjugate	Clone	Manufacturer	Dilution Used
B220	PE/Dazzle^{TM}594	RA3-6B2	BioLegend	1/300
B220	BV650	RA3-6B2	BioLegend	1/100
CCR7	PE-Cy7	4B12	Invitrogen	1/100
CD103	AF700	2E7	Invitrogen	1/100
CD11b	PE/Dazzle^{TM}594	M1/70	BioLegend	1/300
CD11c	PE/Dazzle^{TM}594	N418	BioLegend	1/200
CD11c	AF700	N418	Invitrogen	1/200
CD16/32 (Fc block)	Unconjugated	2.4G2	BD Biosciences	1/200
CD3e	BUV737	145-2C11	BD Biosciences	1/200
CD39	Super Bright 600	24DMS1	Invitrogen	1/200
CD4	BUV395	GK1.5	BD Horizon	1/200
CD44	BV785	IM7	BioLegend	1/200
CD45	BUV395	104	BD Biosciences	1/400
CD45	BV785	30-F11	BioLegend	1/400
CD62L	APC	MEL-14	Invitrogen	1/200
CD62L	BV650	MEL-14	BioLegend	1/150

CD62L	BV711	MEL-14	BioLegend	1/200
CD69	BV711	H1.2F3	BioLegend	1/100
CD8	APC	53-6.7	eBioscience	1/200
CD8a	BV510	53-6.7	BioLegend	1/200
CD8a	PE-Cy7	53-6.7	BioLegend	1/200
CXCR3	BV605	CXCR3-173	BioLegend	1/100
CXCR6	Biotin	SA051D1	BioLegend	1/100
F4/80	BV605	BM8	BioLegend	1/100
FOXP3	eFluor™450	FJK-16s	Invitrogen	1/100
Isotype Control Rat IgG2a kappa	eFluor™450	eBR2a	Invitrogen	1/100
Isotype Control Rat IgG2a kappa	BV605	RTK2758	Biolegend	1/200
Isotype Control Rat IgG2a kappa	eFlour®660	eBR2a	Invitrogen	1/200
Isotype Control Rabbit IgG	PE-Cy7	DA1e	Cell Signalling Technology	1/100
LAG-3	APC	C9B7W	BioLegend	1/100

Ly6C	BV421	HK1.4	BioLegend	1/500
Ly6G	BV650	1A8	BioLegend	1/400
MHCII	APC	M5/114.15.2	BioLegend	1/500
MHCII	BV510	M5/114.15.2	BioLegend	1/500
NK1.1	BV650	PK136	BD Horizon	1/50
NKG2A	BV421	20d5	BD Biosciences	1/400
PD-1	APC	RMP1-30	eBioscience	1/200
PD-1	BV421	29F.1A12	BioLegend	1/200
PD-1	BV605	29F.1A12	BioLegend	1/200
Streptavidin (SA)	BV768		BD Horizon	1/200
TCF-1	PE-Cy7	C63D9	Cell Signalling Technology	1/100
TIM-3	BUV395	5D12	BD OptiBuild™	1/200
TIM-3	SB-645	8B.2C12	Invitrogen	1/200
TOX	eFlour®660	TXRX10	Invitrogen	1/200
XCR1	AF647	ZET	BioLegend	1/150

The antibodies used for immunofluorescence microscopy are listed in Table 2.5 and 2.6.

Table 2.5- List of primary antibodies used for immunofluorescence microscopy in this project.

Primary Antibody	Conjugate	Clone	Manufacturer	Dilution
CD3e	Biotin	eBio500A2	eBioscience	1/100
CD8	eFlour®660	53-6.7	eBioscience	1/50
Cytokeratin (pan reactive)	AlexaFluor™594	C-11	BioLegend	1/500

Table 2.6- List of secondary antibodies used for immunofluorescence microscopy in this project.

Secondary Antibody	Conjugate	Manufacturer	Dilution
Streptavidin	AlexaFluor™555	Invitrogen	1/500

Therapeutic antibodies used *in vivo* were all diluted in sterile Dulbecco's Phosphate-Buffered Saline (DPBS) without $MgCl_2$ and $CaCl_2$, the sources and concentrations are listed in Table 2.7.

Table 2.7- Therapeutic antibodies used for in vivo experiments.

Antibody	Manufacturer	Concentration (mg/ml)
Anti-PD-L1 mouse IgG1	AstraZeneca	11.2
NIP228 isotype IgG1	AstraZeneca	10.1

2.1.3. Cell Lines

Cancer cell lines utilised throughout this work are listed in Table 2.8, and the constituent elements of the culture media used listed in Table 2.9. All cell lines were cultured at 37°C and 5% CO_2. Stocks of each cell line, passage 0-1, were kept in liquid nitrogen. Cell lines were kept in the -80°C for no longer than 6 months after freezing and not passaged beyond 10 times.

Table 2.8- Murine colon adenocarcinoma and melanoma cell lines utilised throughout the project.

Cell Lines	Source	Base Culture Media
CT26	ATCC; CRL-2638™	RPMI
CT26 GFP Luciferase (CT26 GFP Luc)	GenTarget Inc; SC061-LG	RPMI
MC38	Kerafast; ENH204-FP	DMEM
MC38-OVA	AstraZeneca	DMEM
B16	ATCC; CRL-6475™	DMEM

Table 2.9- Base media and additional supplements used for the culture of cancer cell lines.

Base Media	Supplement	Concentration	Manufacturer
Roswell Park Memorial Institute-1640	Heat-inactivated Foetal Bovine Serum (Hi-FBS)	10%	Sigma-Aldrich; F9665

(RPMI-1640) (Source: Gibco)	L-glutamine	2mM	ThermoFisher; 25030081
	Penicillin-streptomycin 10000 units	Penicillin 0.1mg/ml Streptomycin 0.1mg/ml	Sigma-Aldrich; P4333
Dulbecco's Modified Eagle Medium (DMEM) (Gibco; 21875034)	Heat-inactivated Foetal Bovine Serum (Hi-FBS)	10%	Sigma-Aldrich; F9665
	L-glutamine	2mM	ThermoFisher; 25030081
	Penicillin-streptomycin 10000 units	Penicillin 0.1mg/ml Streptomycin 0.1mg/ml	Sigma-Aldrich; P4333

2.1.4. Mice

The mice used throughout this project were housed in specific pathogen-free conditions and used in accordance with Home Office guidelines at the University of Birmingham Biomedical Services Unit (BMSU) under a Project License awarded to D.R. Withers (PP3755654) and approved by the University of Birmingham Animal Welfare and Ethical Review Body (Table 2.10). Mice were housed at 21 ± 2°C, 55% humidity (±10%), with 12 h light dark/cycle in 7–7 individually ventilated caging with environmental enrichment of plastic houses plus paper bedding. Mice with subcutaneous (s.c.) tumours were injected between 6-9 weeks old, and animals with orthotopic colon or liver tumours were injected

between 10-15 weeks old. For the purposes of phenotyping experiments mice were not sex matched. However, for experiments involving immunotherapy mice were age and sex matched.

Table 2.10- Mice used throughout this project.

Strain	Formal Name	Background	Source
BALB/c	BALB/c	BALB/c	Charles River
BALB/c Kaede	C.Cg-Tg(CAG-tdKaede)15Utr	BALB/c	RIKEN BioResource Center, Experimental Animal Division and a colony is maintained in the BMSU
C57BL/6	C57BL/6J	C57BL/6	Charles River
C57BL/6 Kaede	B6.Cg-Tg(CAG-tdKaede)15Utr	C57BL/6	University of Glasgow and a colony is maintained in the BMSU
Bcl-6	*Bcl6*$^{\text{Tomato-CreERT2}}$	C57BL/6	Yohsuke Harada kindly provided these mice to the Withers Lab and a colony is maintained in the BMSU
MMTV-PyMT	FVB/N-Tg(MMTV-PyVT)634Mul/J	FVB	James Arnold Kings College London and a colony is maintained in the BMSU

2.2. Cell Culture

2.2.1. Thawing Cells

Cryovials containing the required cell line were removed from -80°C and thawed at 37°C. Cells were transferred into 20ml of pre-warmed culture media prior to centrifugation for 5 minutes at 300 RCF at 25°C. After which, the supernatant was discarded, and the cells re-suspended in 10ml of the appropriate culture media (Table 2.8) prior to transfer to a 75cm^2 cell culture flask (Corning). Cells were cultured and maintained in an incubator at 37°C 5% CO_2.

2.2.2. Cell Passage

Morphology and confluence of adherent cell lines was checked daily. At or above 70% confluency, cells were passaged. Cells were washed twice with 10ml DPBS without $CaCl_2$ or $MgCl_2$ to ensure removal of cell debris. Adherent cells were dissociated by incubating cells with 5ml TrypLE™ Express (ThermoFisher; 12605010) for 5 minutes at 37°C 5% CO_2. 15ml of pre-warmed culture media was added to the cell-trypsin solution prior to transfer to a 50ml centrifuge tube and subsequent centrifugation for 5 minutes at 300 RCF at 25°C. The supernatant was discarded, and the cells diluted 1:3, 1:5, or 1:10 as required before being placed in 10ml pre-warmed culture media in 75cm^2 cell culture flasks (Corning).

2.2.3. Preparing Cells for Injection

Cells were used for injection at approximately 70% confluency. Cells were washed twice and dissociated as per 2.2.2. 15ml of culture media was added to the cell-trypsin solution prior to transfer to a 50ml centrifuge tube and subsequent centrifugation for 5 minutes at 300 RCF at 4°C. The supernatant was discarded, and cells re-suspended in DPBS for counting as described in 2.2.4. The DPBS-cell suspension was made up to a final volume of 30ml before being centrifuged for 5 minutes at 300 RCF at 4°C. The supernatant was discarded, and cells re-suspended in the calculated volume of sterile DPBS without $CaCl_2$ or $MgCl_2$. The cells were placed on ice for transport to the BMSU for injection.

2.2.4. Counting Cells

Cell pellets were re-suspended in a volume of DPBS without $CaCl_2$ or $MgCl_2$, 10µl of the cell-DPBS suspension was then pipetted onto a haemocytometer (Biosigma Fast-Read 102®; BVS100) . The number of cells in a 4x4 grid was assessed using light microscopy, and an average of 3 separate counts taken (y); the equation for calculating the number of cells in suspension is as follows:

$$Actual\ cell\ number = (Cell\ count\ x10^4)\ x\ Volume\ of\ DPBS\ (ml)$$

The actual cell number could then be used to calculate the volume to re-suspend cells in based on the desired concentration, as follows:

$$Volume\ required\ (\mu l) = \frac{Actual\ cell\ number}{Desired\ concentration\ (cells\ per\ \mu l)}$$

2.2.5. Freezing Cells

Cells were frozen down to make stocks at approximately 80% confluency. Cells were dissociated (2.2.3.) and counted (2.2.4.). After counting, the DPBS-cell suspension was made up to a final volume of 30ml before being centrifuged for 5 minutes at 300 RCF at 4°C. The supernatant was discarded, and cells re-suspended in the calculated volume of required culture media +10% dimethylsulfoxide (DMSO), to achieve a final concentration of 1.0 x10^6 cells per 1ml. The cell-culture media-DMSO suspension was thoroughly mixed before distribution into 1ml cryovials (Greiner). Cryovials containing 1ml of 1.0 x10^6 cells were placed into the Mr. Frosty™ freezing container (ThermoFisher), this was then moved to -80°C; the Mr. Frosty™ freezing container has a chamber filled with 100% isopropyl alcohol which surrounds the cryovials, this allows cells to decrease in temperature -1°C per minute, ensuring gradual freezing of cells within the -80°C freezer.

2.2.6. Mycoplasma Testing

Cells were cultured for 48 hours prior to mycoplasma testing without antibiotics to enable alternative infections to be uncovered. The MycoStrip testing kit (Invivogen MycoStrip™; rep-mysnc-50) was routinely used for mycoplasma testing according to the manufacturer's instructions.

2.3. *In Vivo* Procedures

2.3.1. Subcutaneous Implantation of Tumour Cell Lines

Mice were weighed to ensure animals exceeded 18g before induction of anaesthesia with 5% gaseous isoflurane. Anaesthesia was then maintained with 2.5% gaseous isoflurane. The flank was shaved and cleaned with 2% chlorhexidine. Mice were injected subcutaneously with 100µl tumour cell-PBS suspension, using a 1ml syringe with 26-gauge needle (BD; 303800), then pressure applied to the site of injection (Fig. 2.1). Animals were left on oxygen and observed until recovered.

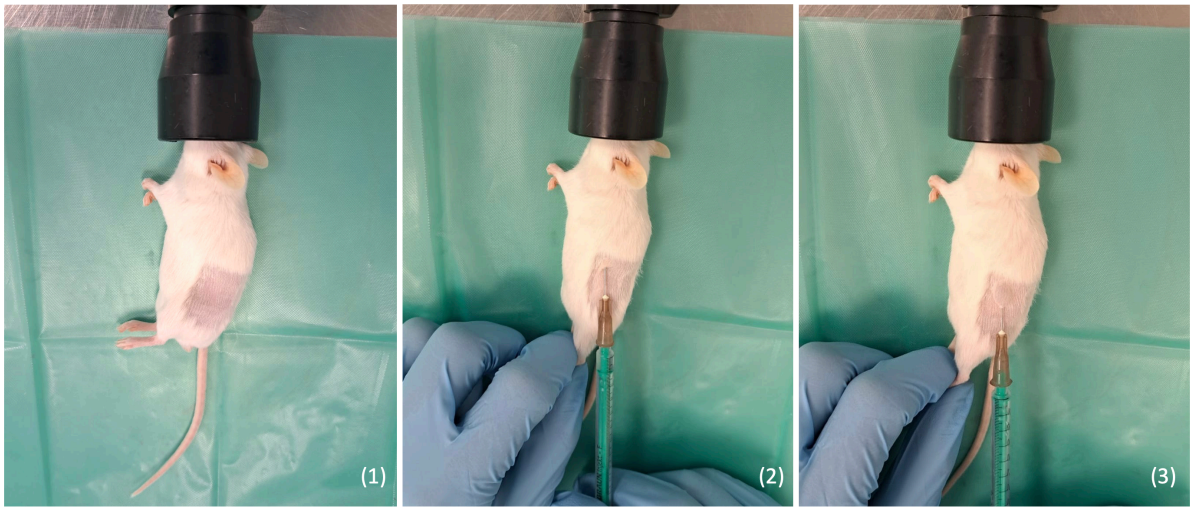


Figure 2.1. Procedure for injection of tumour cell lines subcutaneously on the flank. BALB/c Kaede mouse receiving injection of CT26 cell line shown. The images demonstrate (1) area of the flank shaved and cleaned prior to injection (2) insertion of the needle subcutaneously (3) injection site following injection of 100µl of cells.

2.3.2. Endoscopic Implantation of Tumour Cell Lines and Organoids within the Colon Wall

Mice were weighed and 0.1mg/kg buprenorphine (Temgesic®) administered. Induction of anaesthesia was achieved with 5% gaseous isoflurane before maintenance at 2.5%. Colonoscopy was performed using a Karl Storz Endoskope with a multi-purpose rigid telescope. Once the site of injection was located, 5 x10^5 tumour cells in 30% Matrigel or PBS carrier in a total volume of 30µl, were injected into the colon wall (Fig. 2.2). A 100µl Hamilton syringe with 33-gauge 180mm needle (Hamilton) was used to inject the tumour cells into the colon wall. Mice remained on oxygen and observed until recovered.

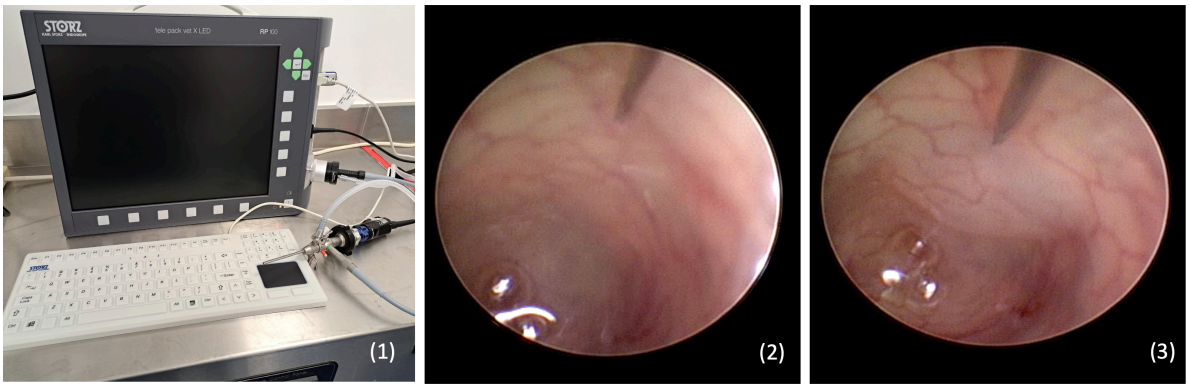


Figure 2.2. Procedure for injection of tumour cell lines into the colon via colonoscopy. BALB/c Kaede mouse receiving an injection of CT26 into the colon wall shown. The images demonstrate (1) set up of the colonoscope for the procedure (2) the colon lumen visualised by endoscopy, with needle in the top centre of the image (3) injection site in the colon wall following injection of 30µl of cells.

2.3.3. Intrahepatic Implantation of Tumour Cell Lines

Mice were weighed and 0.1mg/kg buprenorphine (Temgesic®) administered. Induction of anaesthesia was achieved with 5% gaseous isoflurane before maintenance at 2.5%. Eye

ointment (Xailin Night) was applied directly to the eyes at the start of the procedure, to ensure the eyes did not dry out. The abdomen was shaved and cleaned with 2% chlorhexidine, and the surgical area covered with sterile transparent plastic sheet. A 3cm incision was made through the skin and abdominal muscle wall to expose the larger left lobe. 2.0 x10^5 tumour cells in 30µl PBS was injected into the lower border of the left lobe using a 0.3ml 26-gauge syringe and needle (Terumo®) (Fig. 2.3). The abdominal wall was repaired using single interrupted stitches and the skin repaired using continuous intradermal suturing, both internal and external stitches were made with 13mm 1/2c Vicryl™ suture (Vicryl™; 9981). 0.5ml of 9mg/ml saline was delivered to the animals subcutaneously post-procedure. Animals were left on oxygen and observed until recovered, then placed in cages at 26°C with DietGel® and HydroGel® (ClearH_2O).

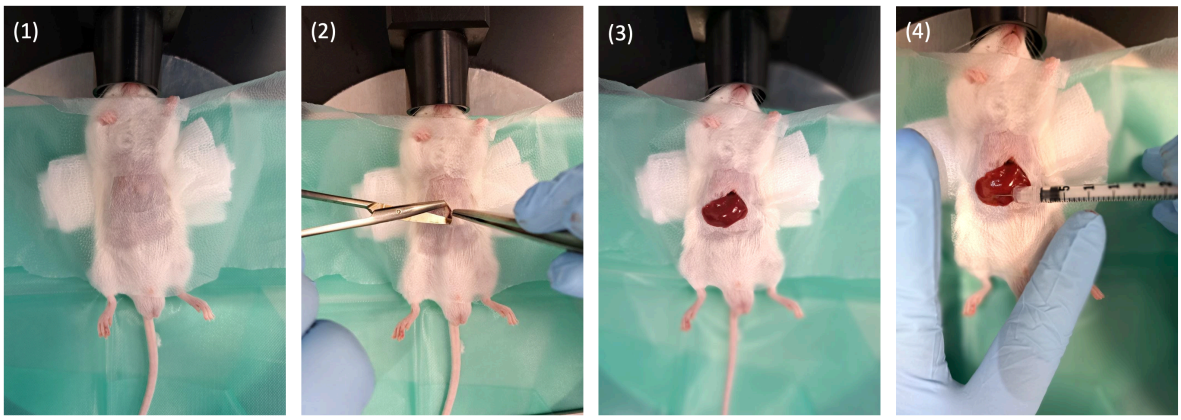


Figure 2.3. Procedure for intrahepatic injection of tumour cell lines. BALB/c Kaede mouse receiving an injection of CT26 into the left liver lobe shown. The images demonstrate: (1) positioning of the mouse for surgery (2) exposure of the surgical field, cutting through skin and muscle layers (3) liver lobe positioned outside of the abdominal cavity (4) injection of 30µl of cells in PBS into the lower border of the lobe.

2.3.4. *In Vivo* Bioluminescent Imaging using IVIS

Luciferase substrate (VivoGlo™ Luciferin, *In Vivo* Grade Cat# P1041) for *in vivo* imaging studies was reconstituted in sterile DPBS without $CaCl_2$ or $MgCl_2$, at a concentration of 15mg/ml. Luciferin was stored in 1ml aliquots at -20°C.

Animals were weighed prior to intraperitoneal injection of 10µl/g of body weight luciferase substrate, animals were left for 5 minutes before induction of anaesthesia with 5% gaseous isoflurane. Animals were then transferred to the IVIS® Spectrum *In Vivo* Imaging System (PerkinElmer) stage and anaesthesia maintained with 2.5% gaseous isoflurane. Living Image software was used for data acquisition (see 2.8.3). Mice were returned to their home cage and monitored until normal behaviour was observed. IVIS imaging was performed with a minimum of 48 hours between each session.

2.3.5. Administration of Antibodies

Antibodies were diluted, according to the concentrations listed in Table 2.7, in DPBS without $CaCl_2$ or $MgCl_2$ in sterile conditions within the lab. Mice were weighed prior to the administration of immunotherapy. All therapeutic antibodies were delivered in 200µl via intraperitoneal injection with a 1ml syringe with 26-gauge needle (BD; 303800).

2.3.6. Photoconversion Procedure

For the photoconversion of subcutaneous tumours, Kaede mice were first anaesthetised with 5% gaseous isoflurane before maintenance at 2.5% isoflurane. Any hair on the skin at the tumour site was removed. The skin over the tumour was moistened using 2%

chlorhexidine in H_2O, this was done to prevent skin damage from the photoconversion procedure. A black acrylic shield was used to protect the area of skin surrounding the tumour throughout. The tumour was exposed to light at 405nm wavelength for 9 cycles of 20 seconds, with 5 seconds in between for the re-application of 2% chlorhexidine solution. The light source used was the Dymax BlueWave QX4 system (Intertronics; DYM41572) at 50% power with an 8mm focusing lens. Animals were left on oxygen and observed until recovered. Skin condition at the site of photoconversion was regularly monitored for adverse reactions.

For the photoconversion of colon tumours, Kaede mice were first weighed and 0.1mg/kg buprenorphine (Temgesic®) administered. Induction of anaesthesia was then achieved with 5% gaseous isoflurane before maintenance at 2.5%. Colonoscopy was performed using a customised rigid telescope, with both white and ultraviolet (UV) light sources, from Zibra Corporation (commissioned March 2024). Using the white light source, the site of tumour implantation was located. The source was then switched to the UV light, and the colon tumour was exposed for 100 seconds. The endoscope was then withdrawn, and animals were left on oxygen and observed until recovered. The condition of the animal was regularly monitored until tissue collection.

For the photoconversion of liver tumours, Kaede mice were induced, and the surgical area prepared as per 2.3.3. An incision was made through the skin and abdominal muscle at the site of the previous surgery, to expose the lobe bearing the liver tumour. The liver was moistened using sterile water solution to prevent the tissue drying out during the

photoconversion procedure. A black acrylic shield was used to protect the surrounding liver and skin of the abdomen throughout. The liver tumour was exposed to light at 405nm wavelength for a varying number of cycles of 20 seconds, with 5 seconds in between for the re-application of water. The light source used for photoconversion was the Dymax BlueWave QX4 system (Intertronics; DYM41572) at 50% power with an 8mm focusing lens. The abdominal wall was repaired, and animals monitored as per 2.3.3.

2.3.7. Intravenous CD45 Labelling

The CD45 antibody (BV785 Clone 30-F11 BioLegend; 103149) was diluted to a concentration of 0.01µg/µl in sterile DPBS without $CaCl_2$ or $MgCl_2$. Mice were placed in warming containers for 10 minutes at 28°C, before being placed in restraint tubes. The anti-CD45 antibody was injected in 200µl into the tail vein of mice using a 0.3ml 26-gauge syringe and needle (Terumo®). Mice were culled 2 minutes after intravenous (i.v.) injection with anti-CD45 antibody and tissues harvested.

2.3.8. Blood Sampling

Mice were placed in warming containers for 10 minutes at 28°C, before being placed in restraint tubes. Approximately 50µl of blood was collected from the lateral saphenous vein, using a 26-gauge needle to lance the vein (BD; 303800). Droplets of blood were collected in a tube pre-coated with EDTA (Vet-Tube®E EDTA 1.3ml blood tube) and transported from the BMSU on ice.

2.4. Tissue Processing & Cell Isolation for Flow Cytometry

2.4.1. Preparation of Tumour

Subcutaneous tumours were excised from the surrounding tissue, in the case of colon and liver tumours the whole organ was dissected at BMSU; all tissues were then placed in RPMI on ice for transport from BMSU. Colon and liver tumours were excised from surrounding tissue under light microscopy.

Tumours were weighed prior to commencing tissue digestion. Individual tumours were first mechanically disrupted using scissors to divide the samples into 1-2mm pieces within an Eppendorf. 1mg/ml collagenase D (Roche; 11088858001) and 0.1mg/ml deoxyribonuclease (DNAse) I (Roche; 4536282001) reconstituted in 1ml of culture media was then added to the Eppendorf and placed in a shaking heat block (Eppendorf Thermomixer 5436) at 1000rpm 37°C for 25 minutes. After this time, tissues were filtered through a 70µm mesh using the back of a syringe plunger to mechanically disrupt the remaining tissue; RPMI was used to wash through tissue stuck to the filter to a total volume of 30ml. The tumour samples were centrifuged at 453 RCF at 4°C for 5 minutes, the supernatant discarded, and the final cell suspension resuspended in staining buffer (Table 2.1).

The above describes the standard tumour digestion protocol used for the majority of experiments in this thesis. For scRNA-seq experiments, a modified Miltenyi gentleMACS™ tumour digestion protocol was used. Tumours were weighed and mechanically disrupted

as before. Tumours were then placed into gentleMACS™ C tubes (Miltenyi; 130-093-237) and the gentleMACS™ enzyme mix added (Tumour Dissociation Kit Miltenyi; 130-096-730); the enzyme mix consisted of 12.5µl enzyme A, 10µl enzyme R, 100µl enzyme D and 2.35ml RPMI. C tubes were then placed in the gentleMACS™ Octo Dissociator (Miltenyi) with heating elements fitted and dissociated using the pre-set 37C_m_TDK1 programme. C tubes were then washed with 10ml RPMI and RPMI-tumour suspension filtered through a 70µm mesh using the back of a syringe plunger to mechanically disrupt the remaining tissue. The tumour samples were centrifuged at 453 RCF at 4°C for 5 minutes, the supernatant discarded, and the final cell suspension resuspended in the required amount of staining buffer prior to cell sorting.

2.4.2. Preparation of Lymph Nodes

Lymph nodes were dissected from the surrounding tissue, then placed in RPMI on ice for transport from BMSU. The designated tumour dLNs for subcutaneous, liver and colon tumours are the inguinal, hepatic portal and caudal lymph nodes respectively.(279, 280) Lymph nodes were placed in 200µl RPMI in a petri dish where they were cleansed of fat before being transferred to a 1.5ml Eppendorf. Preparation of tissue then continued as per the protocol stated in 2.4.1.

2.4.3. Preparation of Spleen

Spleens were dissected from the surrounding tissue, then placed in RPMI on ice for transport from BMSU. Forceps were used to remove fat and remnants of the pancreas from dissected spleens. Spleens were then crushed through a 70µm filter using the back of a

syringe plunger to mechanically disrupt the tissue, 30ml RPMI was then used to wash through residual tissue. The RPMI-spleen solution was then centrifuged at 453 RCF at 4°C for 5 minutes, the supernatant discarded, and the cell pellet resuspended in 5ml of Gey's red blood cell lysis buffer (Table 2.3); the samples were then left on ice for 5 minutes. 15ml RPMI was added to the 5ml spleen-buffer suspension, and the solution again passed through a 70µm filter before centrifugation at 453 RCF at 4°C for 5 minutes. The supernatant was discarded prior to re-suspension in the required amount of staining buffer.

2.4.4. Preparation of Liver

Livers were dissected from the surrounding tissue, then placed in RPMI on ice for transport from BMSU. Forceps were used to remove the gallbladder before the liver was mechanically disrupted through a 100µm cell strainer using the back of a syringe plunger to crush the tissue, and RPMI used to wash tissue through to a final volume of 40ml. Samples were then centrifuged at 453 RCF at 4°C for 5 minutes and the supernatant discarded. Cell pellets were resuspended in 5ml of Gey's red blood cell lysis buffer (Table 2.3) and the samples left on ice for 5 minutes. Samples were centrifuged at 453 RCF at 4°C for 5 minutes, then the supernatant discarded, and the cell pellet resuspended in 30ml RPMI. Liver suspensions were slowly layered on top of 15ml 67% OptiPrep™ density gradient medium (Sigma-Aldrich; D1556). The OptiPrep™ medium was made an hour in advance to allow it to warm to room temperature (RT). Samples were then centrifuged at 1000g 15°C for 25 minutes with no brakes. The interphase layer between the OptiPrep medium and RPMI was collected with a Pasteur pipette and transferred to a 50ml

centrifuge tube; RPMI was added to a final volume of 30ml, and samples centrifuged at 453 RCF at 4°C for 5 minutes. The supernatant was discarded, and cells resuspended in the required volume of staining buffer.

2.4.5. Preparation of Large Intestine

The colon was dissected below the caecum and the surrounding fat removed using forceps. The colon lumen was flushed twice with Hanks' Balanced Salt Solution (HBSS) (Sigma; 6648) supplemented with 2.5 FBS using a 2ml syringe with 26-gauge needle. Tissue was then brought back in HBSS + FBS on ice from the BMSU.

The colon was then cut into 0.5cm sections and incubated twice with HBSS + 2.5M EDTA in a shaking incubator for 15 min at 37°C. In between incubations the tissue was washed with HBSS. The tissue was then incubated in a shaking incubator at 37°C with the colon digestion enzyme mix (RPMI culture medium with 1mg/ml Collagenase VIII (Sigma; C0130) and 30µg/ml DNAse I (Roche; 4536282001)) for approximately 45 minutes. The cell-enzyme suspension was then passed through 100µm and 70µm strainers with RPMI to a final volume of 30ml. Samples were centrifuged at 453 RCF at 4°C for 5 minutes before re-suspension in the required volume of staining buffer.

2.4.6. Preparation of Blood Samples

Approximately 50µl of blood was collected and transferred to an Eppendorf containing 2mM EDTA to prevent clotting prior to transport from BMSU on ice. Samples were transferred to 15ml centrifuge tubes and 4ml RPMI added before centrifugation at 453 RCF

at 4°C for 5 minutes. The supernatant was discarded, then cells resuspended in 1ml of Gey's red blood cell lysis buffer (Table 2.3) and incubated on ice for 5 minutes. 4ml RPMI was added to the cell-buffer suspension before centrifugation and another incubation step with Gey's buffer. Samples were centrifuged for a final time and re-suspended in 200µl staining buffer.

2.5. Magnetic Sorting for CD8 Enrichment

A single cell suspension was made from the spleen or liver as per 2.4.3 and 2.4.4 and CD8 T cells were then enriched using the murine CD8a+ T Cell Isolation Kit (Miltenyi; 130-104-075). Single cell suspensions were counted as per 2.2.4, before incubation with CD8a (Ly-2) MicroBeads (Miltenyi; 130-117-044) for 10 minutes according to the concentration recommended by the manufacturer (10µl MicroBeads in 90µl PBS per 1 $x10^7$ cells). After 10 minutes, samples were run through LS columns (Miltenyi; 130-122-729) pre-washed with PBS and fixed to the QuadroMACS™ Separator (Miltenyi; 130-091-051). Once the sample had run through the column, the column was removed from the magnet and 2 ml of PBS plunged through the LS column to be collected in a separate centrifuge tube, this fraction contained the selected CD8+ cells.

2.6. Flow Cytometry

2.6.1. Proportion of Tissues Stained for Flow Cytometry

Samples were transferred to a 96-well plate (ThermoFisher) prior to staining. In cases where CD8 enrichment (2.4.8), allowing for analysis of the whole CD8 compartment of a tissue, was not used, a known proportion of the cell suspension was stained to enable total counts to be made (Table 2.11).

Table 2.11- Proportions of tissues stained for flow cytometry.

Tissue	Proportion Stained
Tumour	0.05g / Total weight (g)
Lymph Node	1/1
Spleen	1/1 *CD8 enrichment prior to staining*
Liver	1/1 *CD8 enrichment prior to staining*
Colon	1/3

2.6.2. Extracellular Staining

Samples were resuspended in 1/200 Fc block (Table 2.4) diluted in staining buffer and left on ice for 20 minutes, to ensure minimal non-specific Fc-binding. Where required, antibodies for cytokine receptors were diluted in culture media, and samples incubated in this mixture for 1 hour at 37°C. All other surface antibodies were diluted in staining buffer as per the concentrations listed in Table 2.4, and samples resuspended in the antibody stain and left on ice for 1 hour. Samples were resuspended in 1/1000 LIVE/DEAD™

Viability/Cytotoxicity (Invitrogen™ ThermoFisher; L34960) diluted in PBS; the viability stain was left on the samples for 20 minutes on ice. Cells, if fixed, were done so using Cytofix (BD Biosciences) on ice for 1 hour. Between each incubation step mentioned, samples were centrifuged at 453 RCF at 4°C for 5 minutes, before re-suspension with 200µl of staining buffer, and another centrifugation at the same settings.

2.6.3. Intracellular Staining

For intracellular staining, cells were permeabilised with the Forkhead box P3 (FoxP3) Transcription Factor Staining Buffer Set (Invitrogen™ ThermoFisher; 00-5523-00) following fixation and a wash step with 200µl of staining buffer. Samples were re-suspended in 100µl permeabilisation buffer (1:10 10x Permeabilisation buffer: dH_20) and incubated for 30 minutes at RT. All intracellular antibodies were diluted in permeabilization buffer solution according to the concentrations listed in Table 2.4. Intracellular staining was carried out overnight at room temperature.

2.6.4. Sample Processing Pre-Acquisition

Cells were washed twice with 200µl staining buffer in the case of extracellular staining only, or with 200µl permeabilisation buffer for intracellular staining; and centrifuged at 453 RCF at 4°C for 5 minutes between washes. For final transfer to FACS tubes, samples were re-suspended in 200µl of staining buffer. To allow for the quantitation of total cell numbers 10µl of AccuCount Blank Particles (Spherotech), containing approximately 10,000 particles, was added to the FACS tubes prior to addition of the samples. The samples were transferred to FACS tubes from the 96 well plate through a 50µm mesh to ensure minimal

cell clumping. Data was acquired using the BD LSR Fortessa™ X-20 (BD Biosciences) using FACSDiVA 8.0.2. software (BD Biosciences). FCS files were imported to FlowJo, and data analysed using FlowJo version 10 software.(281)

2.7. Immunofluorescence Microscopy

2.7.1. Tissue Fixation, Sectioning and Preparation of Slides

Murine tissues were examined under light microscopy and fat removed prior to fixation. Tissues were placed in 2% paraformaldehyde for 2 hours, then transferred to 30% sucrose for approximately 18 hours, after this time tissues were frozen on optimal cutting temperature (OCT) medium. All tissues after fixation were stored at -80°C until sectioning. Samples were cut into 7µm sections using a cryostat and placed on Superfrost™Plus Adhesion glass slides (Epredia; J1800AMNZ). Slides were air dried for 30 minutes at RT and then stored at -20°C.

2.7.2. Immunolabelling of Tissue Sections

All the following steps were carried out at RT in a humidified chamber. In between each step, excess solution was removed prior to placing sections in a PBS wash for 5 minutes, unless otherwise stated.

Slides were left to air dry for a minimum of 20 minutes prior to hydration in a PBS bath for 10 minutes. Vector Laboratories Avidin/Biotin Blocking Kit was used to block non-specific

binding as per the manufacturer's directions. Sections were incubated with 10% horse serum for 15 minutes to prevent non-specific protein binding, after which the serum was aspirated off the slide prior to the addition of primary antibody solution; no PBS wash step was required before addition of the primary antibody. Sections were incubated with primary antibodies for 45 minutes. Further incubations with antibody solutions occurred for 30 minutes. Biotinylated antibodies were detected using streptavidin-conjugated reagents, typically SA-AF555 (Table 2.6). Secondary antibodies were cross absorbed for 30 minutes in 10% mouse serum in staining solution, prior to addition to tissue sections. All antibody solutions were diluted in 1% BSA staining solution (Table 2.2).

Sections were stained with 4',6-diamidino-2-phenylindole (DAPI) for 30-60 seconds, then washed three times in PBS for 1 minute. Slides were dried before the addition of ProLong™ Gold antifade reagent (LifeTechnologies; P36930) to the tissue, on top of which cover slips were placed. The mounting media was left to partially dry, then the cover slip secured in place on the slide with clear varnish. Finally, slides were left at RT overnight in a dark container before storage at 4°C.

2.8. Single-cell RNA-sequencing

The experimental design for the scRNA-seq in this thesis involved C57BL/6 Kaede mice being injected with 2.5 x10^5 MC38-OVA cells subcutaneously between 6-9 weeks, prior to photoconversion of the subcutaneous tumour on day 13. Tumours and dLNs were collected

48 hours following photoconversion. Tissues were processed as per the gentleMACS™ method outlined in 2.4.1. Cells were stained with CD45, CD11b, Ter119, LIVE/DEAD™ Viability/Cytotoxicity. Lymphocytes (Live CD45+ TER119- Kaede+ CD11b-) were then isolated using the FACS Aria II Cell Sorter (BD) and sorted into two groups Kaede red+ (KR+) and Kaede red-. Samples were prepared by members of the Withers Lab. Analysis of scRNA-seq data was all performed by Colin Lee (Clatworthy Lab, University of Cambridge), and further details of the analysis are provided in the paper by Lee *et al.* 2023.(83)

2.9. Data Processing

2.9.1. Data Collection & Analyses of Flow Cytometry Data

Data was acquired using the BD LSR Fortessa™ X-20 (BD Biosciences) using FACSDiVA 8.0.2. software (BD Biosciences). FCS files were imported to FlowJo, and data analysed using FlowJo version 10.8 software.(281)

As a known amount of AccuCount Blank Particles (Spherotech) were added to samples prior to data acquisition, the total cell counts per sample could be calculated as follows:

$$\text{Cell Number Acquired} = \frac{\text{Cell count } (Number\ of\ cells\ acquired)}{Bead\ count\ (Number\ of\ beads\ acquired)} \times 10{,}000\ (Total\ number\ of\ beads)$$

Using the total number of cells per sample acquired, the number of cells in a given tissue could be calculated as follows:

$$\text{Cell Number per Tissue} = \frac{\text{Cell Number Acquired}}{\text{Proportion of Tissue Stained}}$$

2.9.2. Image Capture, Visualisation & Analysis of Microscopy Data

Images were acquired on the Zeiss LSM880 Confocal Microscope using ZEN Black software (Zeiss). Images were exported as CZI files and analysed using ZEN Black software (Zeiss).

2.9.3. Data Acquisition & Analysis for IVIS Imaging Data

Data was acquired using the IVIS Spectrum *In Vivo* Imaging System (PerkinElmer) using Living Image® 4.3.1. software (PerkinElmer). Bioluminescence imaging mode with open filter was used; a field of view of 23.3cm was chosen, with a subject height of 1.5cm. A time series study of 8 segments with a 1-minute delay was performed. Image files (TIFF) were imported and analysed using Living Image® 4.7.4. software (PerkinElmer). A table of peak bioluminescence was exported in Microsoft Excel for further statistical analysis.

2.10. Statistical Analysis

Statistical analyses were performed using GraphPad Prism version 9 for Mac.(282) In experiments in which the sample size was small (n <10), the decision was made not to use tests for normality as they don't have enough power to detect non-gaussian distributions.(283) In experiments in which there was an appropriately large sample size, a Shapiro-Wilk test was used to test for normality. Table 2.12 details the statistical analyses

used according to whether the data was normally distributed or not. Where a linear correlation analysis was performed, the correlation coefficient is displayed on the graph. The threshold for statistical significance was $p < 0.05$ and noted as follows: *, $p < 0.05$; **, $p < 0.01$; ***, $p < 0.001$; and ****, $p < 0.0001$. Where differences were not statistically significant, a p value was not indicated on the graph.

Table 2.12- Statistical analyses used in this thesis according to the data type.

	Two column	**Multiple column**	**Grouped**
Non-parametric	Mann-Whitney	Kruskal Wallis (Dunn's multiple comparison tests)	N/A
Parametric	Unpaired two-tailed student's *t*-test	Ordinary one-way ANOVA (Tukey's multiple comparisons test)	Two-way ANOVA (4 family comparison, Fisher's LSD test) (All means, Tukey's multiple comparisons)

Chapter 3

Investigating the Migratory Behaviour of Stem-like CD8 T cells in the Anti-Tumour Response

3.1. Introduction

A greater intratumoural CD8 T cell infiltrate is associated with improved prognosis in multiple cancer types.(54, 55, 58-60) However, CD8 T cells are not all the same, instead existing on a continuum of differentiation states from naïve, to activated, exhausted and memory.(156) In the case of acute infection, expansion of activated T cells is accompanied by a rapid contraction, leaving only a small pool of memory cells.(61) However, when there is antigen persistence, as is the case in cancer, CD8 T cells follow a different trajectory toward exhaustion.(132, 284) The concept of CD8 T cell exhaustion was first described in the context of chronic viral infection with LCMV.(132) Here, CD8 T cells were found to be both phenotypically and functionally different from the activated CD8 T cells formed in acute infection, including increased expression of co-inhibitory receptors, reduced effector function and reduced proliferative potential.(125, 132, 238) As mentioned previously, exhaustion occurs in the setting of prolonged antigen exposure, and both the length of exposure and amount of antigen correlate with the extent of exhaustion.(138, 139) High expression of multiple co-inhibitory receptors by most CD8 T cells in pre-clinical and clinical tumour samples indicates that a large proportion of these intratumoural T cells are exhausted.(151, 285, 286) Given the reduced proliferative potential of exhausted CD8 T cells, how this compartment is sustained over years in some patients treated with ICB remained a key unanswered question. The discovery of the precursor exhausted population, or stem-like CD8 T cells provides an explanation for this.(158)

3.1.1. The importance of stem-like CD8 T cells in cancer

Stem-like CD8 T cells share several features of memory populations, including retention of proliferative capacity, expression of CD127, CCR7 and TCF-1, whilst lacking effector functions such as granzyme production.(148, 149, 157, 159, 160, 287) However, unlike memory populations, stem-like CD8 T cells show some hallmarks of exhaustion, primarily increased expression of co-inhibitory receptors such as PD-1 and LAG-3, and crucially, the TF TOX.(149, 158-160) The clinical relevance of this population is that it underlies the proliferative burst in response to ICB therapy, facilitating the continuation of the CD8 response.(149) In profiling clinical melanoma samples, *Tcf7* expression within the T cell infiltrate of tumours indicated a positive response to ICB.(161) Hence, this population appears to be integral in sustaining the CD8 T cell compartment within tumours and is currently considered key to driving a productive response to treatment.

3.1.2. The location and migratory potential of stem-like CD8 T cells

Stem-like CD8 T cells have been detected within the tumour and dLN in preclinical cancer models, but the migratory potential of this population remains less clear.(148, 161, 288, 289) Murine studies of chronic viral infection observed that cDC1s support a stem-like CD8 population within the lymphoid tissue of infected animals, with some studies suggesting the T cell population is actually resident in the lymphoid tissue.(149, 290) Within the TME itself, it has been suggested that stem-like cells cluster within antigen-presenting cell niches enriched for DCs and increased MHCII expression.(288) These stem-like: APC clusters were enriched for exhausted CD8 T cells, correlated with improved tumour control, and were found in the proximity of lymphatics and vasculature.(288) Other studies

reinforced this, finding that stem-like CD8 T cells were associated with intratumoural high endothelial venules formed following antiangiogenic immunotherapies.(291) Exactly how therapeutic interventions and remodelling of the tumour environment influence the stem-like compartment, and vice versa, needs further investigation.

Whether the intratumoural stem-like compartment is sustained solely within the tumour itself or by differentiation within the dLN is debated. Anti-PD-L1 therapy dosed in a way to specifically target cells within the tumour dLN resulted in increased numbers of stem-like CD8 T cells within the LN, and a resultant decrease in tumour burden;(292) suggesting cellular traffic between the dLN and tumour, perhaps by the stem-like CD8 population. In the clinic, the same authors reported that PD-1:PD-L1 interactions in the tumour dLN, rather than in the tumour itself, dictated whether melanoma patients had a response to ICB.(292) However, stem-like CD8 T cells are clearly present within tumours and have the potential to respond within this environment. Another study using a pre-clinical model of lung adenocarcinoma compared the tumour-specific stem-like CD8 T cells within the tumour and the dLN, finding that the tumour-based stem-like population changed over time whereas the population in the dLN remained stable.(293) The authors suggested that the stem-like population in the tumour was pushed down the exhausted trajectory over time with tumour progression, yet the stem-like population within the dLN retained its phenotype and was able to then seed the tumour and sustain the response.(293) Studies of the tumour dLN from clinical samples of prostate, kidney and bladder cancer suggested a two-step maturation of stem-like CD8 T cells, showing phenotypic and TCR overlap between activated TCF-1+ CD8 T cells in the dLN and tumour; proposing that stem-like cells

in the dLN were precursors to more resident stem-like CD8 T cells that had received further co-stimulation in the TME from APCs.(106) Overall, the current understanding of tumour-specific stem-like CD8 T cells implies trafficking between the tumour and tumour dLN, in contrast to the more resident stem-like CD8 T cells found in the context of LCMV infection.(149)

3.1.3. Tracking T cell migration in pre-clinical tumour models using Kaede transgenic mice

Kaede is a protein, found in stony coral, containing a tripeptide His(62)-Tyr(63)-Gly(64) which is responsible for its green to red fluorescent shift.(294) In its base state the tripeptide contributes to a green chromophore, upon UV irradiation there is a cleavage of the peptide and formation of a double bond resulting in a red-emitting chromophore.(294) In 2008, Tomura *et al.* established a Kaede transgenic mouse model, in which expression of Kaede is under the CAG-promoter, driving ubiquitous expression of the protein.(295) Therefore, all host cells are green (termed 'Kaede green' for clarity) under normal conditions but violet light transforms the protein to a red form ('Kaede red'), enabling temporal site-specific tagging.(295) The Kaede transgenic model was initially used by Tomura *et al.* to label the skin, facilitating the study of immune cell migration between the skin and dLN.(296, 297) Within the Withers lab, site-specific photolabelling of LNs was then established by Marriott *et al.* in 2017, allowing the migration of CD4 memory T cell populations into and out of these tissues to be characterised.(298)

The Withers lab further adapted the Kaede photolabelling model to enable the study of immune cell recruitment and egress in pre-clinical tumour models.(286) In this tumour

model, syngeneic tumour cell lines are injected subcutaneously into the flank prior to selective exposure of the subcutaneous tumour to UV light, termed photoconversion. The photoconversion procedure results in near complete Kaede red labelling of the intratumoural immune compartment; meaning that Kaede green (KG) cells found within the tumour have entered during the period after photoconversion, and Kaede red cells found in the periphery were within the tumour at the time of labelling and have since egressed. Utilising this Kaede tumour model, data from our lab revealed how quickly T cells within the tumour become exhausted and that this population appear to be largely retained within the tumour and unable to egress to the dLN. Importantly, a TCF-1+ PD-1+ CD8 population labelled in the tumour and potentially a stem-like CD8 T cell population were found to have migrated to the dLN.(286) These data indicated that the intratumoural stem-like CD8 compartment is dynamic, moving between the tumour and dLN. However, detailed characterisation of the stem like compartment in the tumour, the precise nature of the migratory T cells and their fate after migration to the dLN remain poorly understood.

3.1.4. Aims

The overarching aim of this chapter was to investigate the migratory behaviour of stem-like CD8 T cells in the anti-tumour response, building on initial observations that a TCF-1+ PD-1+ CD8 T cell population egressed the tumour and was detected within the dLN. We hypothesise that the stem-like CD8 T cell compartment continually traffics from the tumour to the dLN. This behaviour would support the local expansion of exhausted CD8 T cells within the tumour whilst preserving the stem-like compartment in the face of continued antigen exposure and differentiation toward an exhausted phenotype. To

investigate this, pre-clinical tumour models grafted into Kaede transgenic mice will be used to interrogate the composition of the anti-tumour response within the tumour and dLN, combined with the direct tracking of T cells between these tissues as well as the peripheral lymphoid compartment.

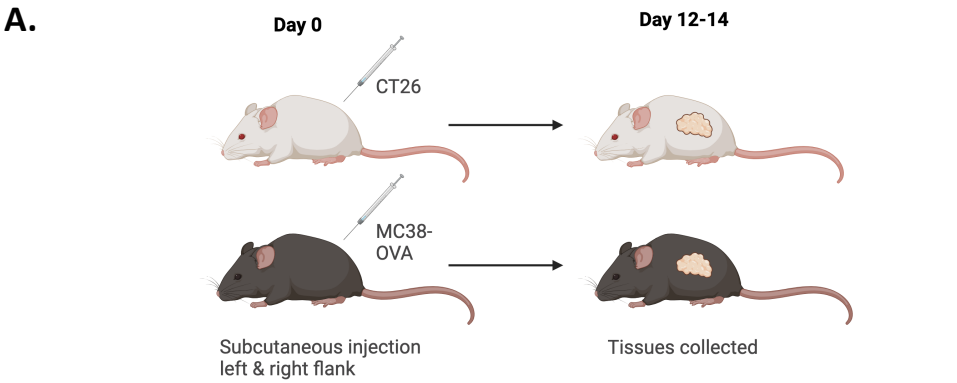
This chapter will aim to answer the following questions:

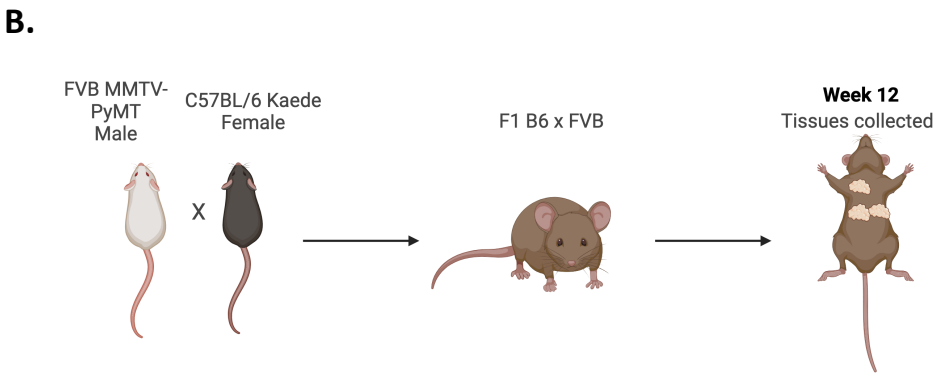
- Are stem-like CD8 T cells resident within the tumour?
- Do stem-like T cells egress the tumour, and if so, to where do they migrate?
- Are there phenotypic differences in stem-like T cell populations present in different tissues and is this dependent upon their migratory history?

3.2. Results

3.2.1. Establishing subcutaneous CRC models to study the composition of the intratumoural CD8 population and how this changes over time

To undertake detailed investigations of the CD8 T cell response in cancer, *in vivo* tumour models are required. Given that the pre-clinical model used can influence the immune environment of the tumour and hence the resulting T cell response, two different syngeneic colorectal cancer models were first compared to examine whether fundamental differences exist in the CD8 T cell compartment across mouse backgrounds. Furthermore, the use of MC38-OVA, a modified C57BL/6 CRC cell line, supported the investigation of antigen-specific CD8 T cell responses. For both CRC models, 2.5 x10^5 CT26 and MC38-OVA cells were injected into the left flank of BALB/c Kaede and C57BL/6 Kaede mice respectively, tumour growth was monitored before collection between day 12 and day 14 post-injection (Fig. 3.1A). To additionally compare with the subcutaneously implanted syngeneic cell line models, we analysed the spontaneous MMTV-PyMT breast tumour model. Here, the timing of tumour development is highly background dependent. To generate the MMTV-PyMT model on a Kaede background, F1 mice resulting from crossing PyMT+ male mice with Kaede female mice were used, in which tumours typically appeared within 11-14 weeks (Fig. 3.1B). The weight of resultant tumours from CT26 and MC38-OVA primary CRC models were between 0.025 and 0.15 grams, with tumours rapidly increasing in size between day 12 and day 14 post-injection (Fig. 3.1C-D). The weight of mammary tumours collected from PyMT mice varied substantially but were within a similar range to the CT26 and MC38-OVA tumours (Fig. 3.1E).


A.
Day 0
Day 12-14
CT26
MC38-OVA
Subcutaneous injection left & right flank
Tissues collected


B.
FVB MMTV-PyMT Male
C57BL/6 Kaede Female
X
F1 B6 x FVB
Week 12
Tissues collected

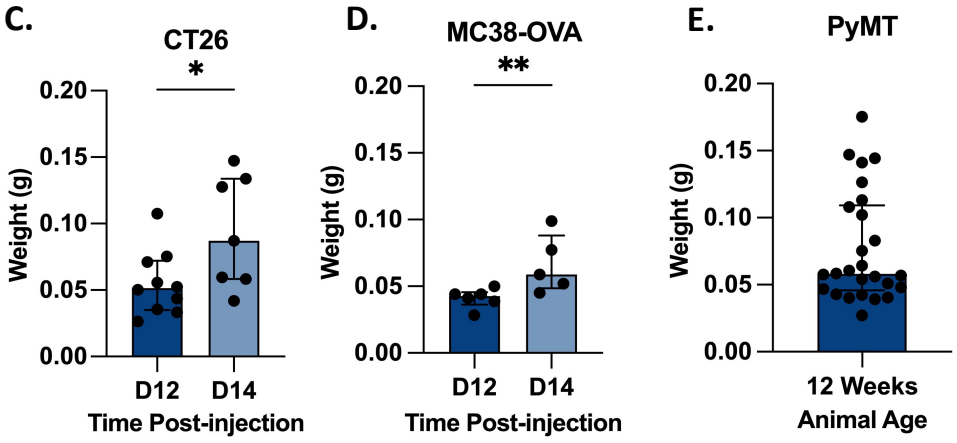

C.
CT26
*
Weight (g)
0.20
0.15
0.10
0.05
0.00
D12
D14
Time Post-injection
D.
MC38-OVA
**
Weight (g)
0.20
0.15
0.10
0.05
0.00
D12
D14
Time Post-injection
E.
PyMT
Weight (g)
0.20
0.15
0.10
0.05
0.00
12 Weeks
Animal Age

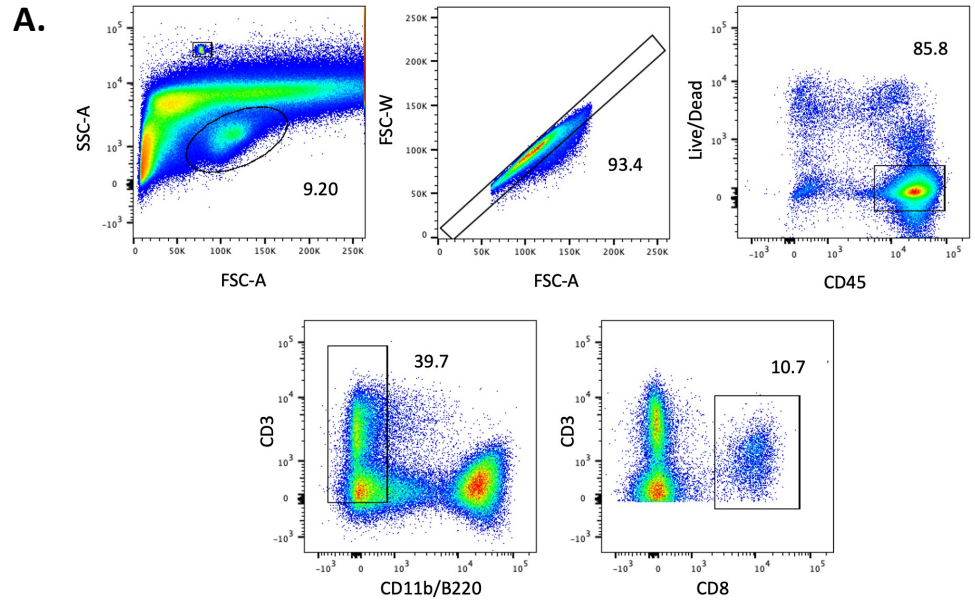
Figure 3.1. Summary of initial tumour models used to investigate immune cell trafficking in dynamic labelling models.

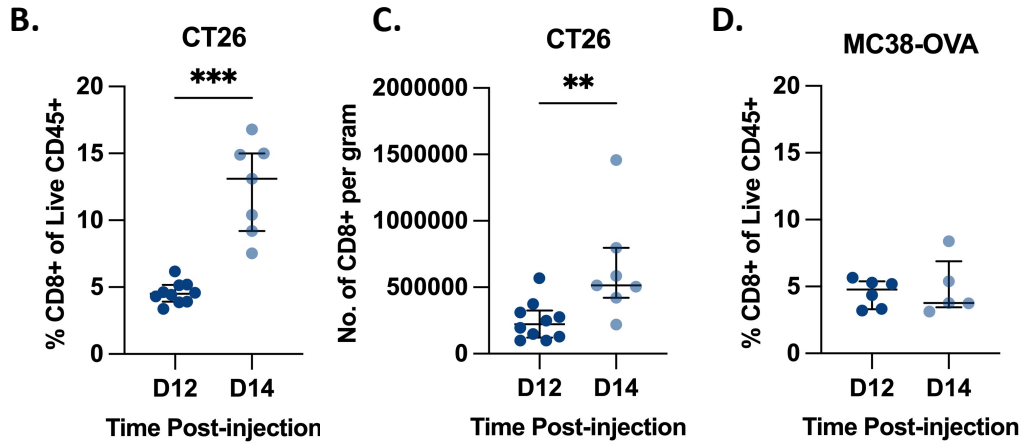
BALB/c and C57BL/6 mice (6-9 weeks) were injected with 2.5 x10^5 CT26 and MC38-OVA cells subcutaneously. To generate the MMTV-PyMT model on a Kaede background, F1 mice resulting from crossing PyMT+ male mice with Kaede female mice were used, in which tumours typically appeared within 11-14 weeks. All data shown are from two (MC38 OVA and PyMT tumours) or three (CT26) independent experiments. All graphs show the median and interquartile range (IQR). Statistical significance was determined using a Mann-Whitney test. ** = $p < 0.05$, ** = $p < 0.01$.*

A. Illustration outlining the experimental set-up of subcutaneous CRC tumour models. Created with Biorender.com.
B. Illustration demonstrating the breeding and timeline for primary PyMT breast tumour models. Created with Biorender.com.
C. The weight (g) of CT26 tumours at day 12 and day 14 post-injection.
D. The weight (g) of MC38-OVA tumours at day 12 and day 14 post-injection.
E. The weight (g) of PyMT tumours collected at 12 weeks.

Immune cells were isolated from tumours and stained with viability dye to allow immunophenotyping of live CD45+ cells by flow cytometry. Intratumoural CD8 T cells were identified by pre-gating on CD3+ CD11b- B220- cells before selecting those cells that expressed CD8 (Fig. 3.2A). After identifying intratumoural CD8 populations, the proportion of live CD45+ cells that were CD8+, as well as the number of CD8 T cells per gram of tumour were assessed. Both the proportion and infiltration of CD8 T cells in the tumour increased over time in the CT26 model, though this was not evident within the MC38-OVA tumours (Fig. 3.2B-E). Though the proportion of CD8 T cells in the live CD45+ compartment was comparable in PyMT tumours, CD8 infiltration in terms of cells per gram of tumour was significantly lower than in both CRC models (Fig. 3.2F-G). This reduced T cell infiltrate, compared with the variable tumour size and growth dynamics meant that after initial experiments, the more controlled cell line models became the focus of my studies.

To initially phenotype the CD8 T cell compartment, a panel capturing information on exhaustion, activation, and their migratory capacity was used. To identify exhausted CD8 T cells, the TF TOX, alongside PD-1 was used. In addition, expression of co-inhibitory receptor NKG2A was assessed, building on earlier studies in the lab, to explore its expression pattern on CD8 T cells.(299) CD69 and CD62L were used to indicate tissue residency versus migratory potential. The TF TCF-1 was assessed as a key marker of memory T cells, but also the stem-like compartment. Expression of these markers by CD8 T cells isolated from CT26 tumours taken at day 12 and 14 is shown in Fig. 3.3A. Most evident in this initial analysis was the robust expression of NKG2A and PD-1, which increased from day 12 to 14, alongside TOX expression, consistent with the emergence of an exhausted CD8 T cell


A.
SSC-A
FSC-A
9.20
FSC-W
FSC-A
93.4
Live/Dead
CD45
85.8
CD3
CD11b/B220
39.7
CD3
CD8
10.7


B.
CT26
***
% CD8+ of Live CD45+
D12
D14
Time Post-injection
C.
CT26
**
No. of CD8+ per gram
D12
D14
Time Post-injection
D.
MC38-OVA
% CD8+ of Live CD45+
D12
D14
Time Post-injection

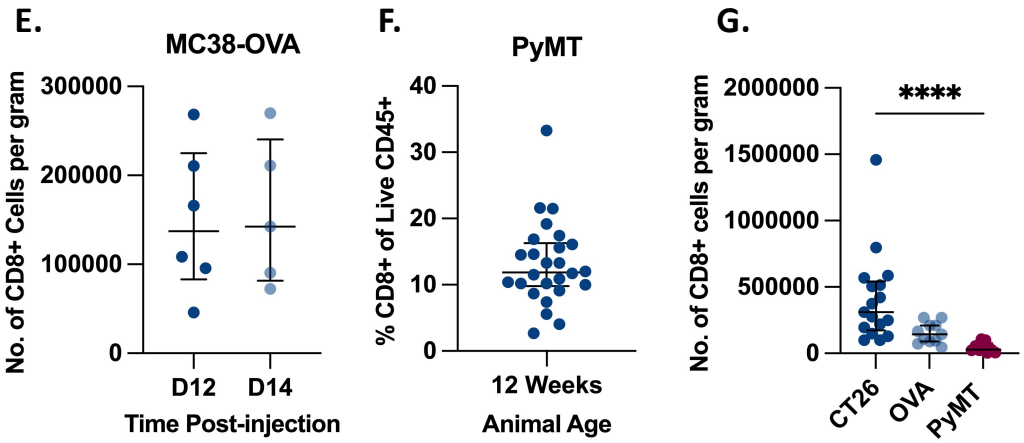

E.
MC38-OVA
No. of CD8+ Cells per gram
D12
D14
Time Post-injection
F.
PyMT
% CD8+ of Live CD45+
12 Weeks
Animal Age
G.
****
No. of CD8+ cells per gram
CT26
OVA
PyMT

Figure 3.2. Enumerating the intratumoural CD8 T cell population by flow cytometry in subcutaneous and primary tumour models.

BALB/c and C57BL/6 mice (6-9 weeks) were injected with 2.5 x10^5 CT26 and MC38-OVA cells subcutaneously. To generate the MMTV-PyMT model on a Kaede background, F1 mice resulting from crossing PyMT+ male mice with Kaede female mice were used, in which tumours typically appeared within 11-14 weeks. All data shown are from two (MC38 OVA and PyMT tumours) or three (CT26) independent experiments. All graphs show the median and IQR. In the case of two-column analysis statistical significance was determined using a Mann-Whitney test, in the case of multiple column analysis statistical significance was determined using a Kruskal-Wallis multiple comparison with Dunn's post-hoc correction performed. ** = p < 0.05, ** = p < 0.01, *** = p < 0.001, **** = p < 0.0001*

A. Gating strategy used to define the CD8+ T cell population in subcutaneous tumours. Representative flow cytometry plots shown are from a CT26 subcutaneously implanted tumour at day 12 post-injection.
B. The percentage of live CD45+ cells that are CD8+ in CT26 tumours day 12 versus day 14 post-injection.
C. The number of CD8+ cells per gram of CT26 tumour shown at day 12 and day 14 post-injection.
D. The percentage of live CD45+ cells that are CD8+ in MC38-OVA tumours day 12 versus day 14 post-injection.
E. The number of CD8+ cells per gram of MC38-OVA tumour shown at day 12 and day 14 post-injection.
F. The percentage of live CD45+ cells that are CD8+ in PyMT tumours collected when the animal was 12 weeks of age.
G. Comparison of CD8 T cell infiltration, demonstrated as CD8+ cells per gram of tumour, in three different tumour models.

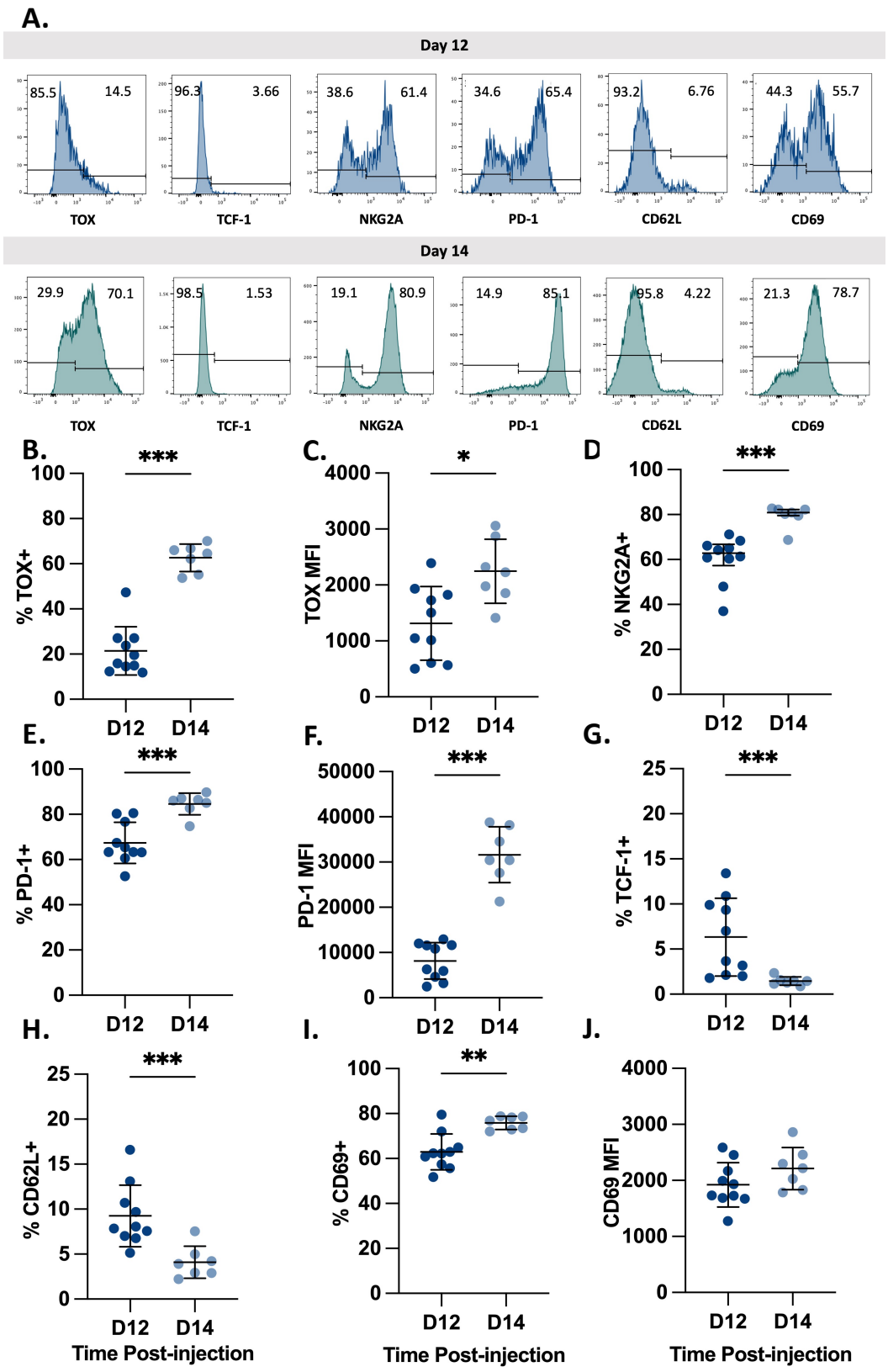

A.
Day 12
85.5
14.5
96.3
3.66
38.6
61.4
34.6
65.4
93.2
6.76
44.3
55.7
TOX
TCF-1
NKG2A
PD-1
CD62L
CD69
Day 14
29.9
70.1
98.5
1.53
19.1
80.9
14.9
85.1
95.8
4.22
21.3
78.7
TOX
TCF-1
NKG2A
PD-1
CD62L
CD69
B.
% TOX+
C.
TOX MFI
D
% NKG2A+
E.
% PD-1+
F.
PD-1 MFI
G.
% TCF-1+
H.
% CD62L+
I.
% CD69+
J.
CD69 MFI
D12
D14
Time Post-injection

Figure 3.3. Phenotype of the total CD8 T cell intratumoural population in subcutaneous tumour models.

BALB/c mice (6-9 weeks) were injected with 2.5 x10^5 CT26 cells subcutaneously. Tissues were collected day 12 post-injection. All data shown are from three independent experiments. All graphs show the mean ±SD. Statistical significance was determined using an unpaired *t* test. ** = p < 0.05, ** = p < 0.01, *** = p < 0.001.*

A. Histograms demonstrating the expression of TOX, TCF-1, NKG2A, PD-1, CD62L and CD69 in the total CD8+ T cell population in a representative CT26 WT subcutaneous tumour at day 12 (top row) and day 14 (bottom row). CD8 T cells previously gated on Live CD45+ CD11b- B220- CD11c- CD3+ CD8+.
B. The percentage of intratumoural CD8+ cells that are TOX+ at day 12 and day 14.
C. The MFI of TOX expression in the intratumoural CD8+ cells at day 12 and day 14.
D. The percentage of intratumoural CD8+ cells that are NKG2A+ at day 12 and day 14.
E. The percentage of intratumoural CD8+ cells that are PD-1+ at day 12 and day 14.
F. The MFI of PD-1 expression in the intratumoural CD8+ cells at day 12 and day 14.
G. The percentage of intratumoural CD8+ cells that are TCF-1+ at day 12 and day 14.
H. The percentage of intratumoural CD8+ cells that are CD62L+ at day 12 and day 14.
I. The percentage of intratumoural CD8+ cells that are CD69+ at day 12 and day 14.
J. The MFI of CD69 expression in the intratumoural CD8+ cells at day 12 and day 14.

programme. Limited expression of either TCF-1 or CD62L was detected, consistent with a limited memory cell compartment within the tumour and a CD8 T cell population becoming exhausted. High expression of CD69 indicated that most CD8 T cells are retained within the tumour. Enumeration of these data confirmed significant increases in the percentage of CD8 T cells expressing TOX and the level of TOX expression (MFI) from day 12 to 14 (Fig. 3.3B, C). The proportion of TCF-1+ CD8 T cells was low, falling further between day 12 and 14 (Fig. 3.3D). The percentage of CD8 T cells expressing co-inhibitory receptors PD-1 and NKG2A increased over time, and the level of PD-1 also increased (Fig. 3.3E-G). A small proportion of the intratumoural CD8 population was CD62L+, falling further between day 12 and 14, conversely the proportion and level of CD69 expression increased (Fig. 3.3H-J) displaying a shift toward tissue residency. Collectively, these data indicate that the intratumoural CD8 T cell population was becoming more exhausted as the tumour persisted. Spontaneous tumour samples from the PyMT model showed a similar pattern of expression, although interestingly, these tumours also contained a putative tissue-resident T cell compartment that is absent in implanted CRC models (Appendices 3.1 & 3.2). Further controls including fluorescence minus one (FMO) controls are shown in Appendix 3.3.

The MC38-OVA CRC model enabled the examination of antigen-specific CD8 T cells. Using OVA antigen tetramer H-2Kb-SIINFEKL from the NIH Tetramer Core Facility, CD8 T cells recognising a model antigen expressed by the tumour cells could be specifically identified and compared to the total CD8 T cell population within tumours. OVA staining between intratumoural CD8 and CD4 T cell populations is shown in the appendix (Appendix 3.4).

CD8 exhaustion and activation were assessed as previously, with the addition of the marker Ly108 which has been linked to TCF-1 expression and stem-like populations.(300) There was no clear change in the expression of TOX between days 12 and 14 unlike CT26 tumours, and expression was similar between the antigen-specific and total CD8 T cell populations (Fig. 3.4A-B). TCF-1 expression was reduced over time, as in CT26 tumours, however, changes in Ly108 expression were not evident, and both markers were comparable between the total and OVA-specific CD8 populations (Fig. 3.4A,C-D). PD-1 expression was high at both day 12 and 14 and a significant increase in the proportion of PD-1+ OVA-specific CD8 T cells was evident, such that almost all these cells were positive by day 14 (Fig. 3.4A,E). Most CD8 T cells in MC38-OVA tumours, whether OVA-specific or not, lacked CD62L expression (Fig. 3.4A,F). Finally, CD69 expression remained unchanged across time points or between the two groups (Fig. 3.4A,G). Overall, these data clearly demonstrate an intratumoural CD8 T cell compartment that becomes increasingly dominated by an exhausted phenotype, across the multiple pre-clinical models used.

3.2.2. Examining changes in the intratumoural CD8 population over time

To study the effect of time within the tumour on immune populations, our lab has established an *in vivo* tumour photolabelling model, where tumours are grafted into Kaede transgenic mice and the immune compartment 'time-stamped' using violet light.(286) CRC cell lines were injected subcutaneously on the left flank as described in 2.3.1, and at day 11 photolabelling was performed. The aim of this procedure was to switch Kaede fluorescence from its native green (Kaede green) to the converted red form (Kaede red) within all host cells present in the tumour at the time of labelling. Tissues were then

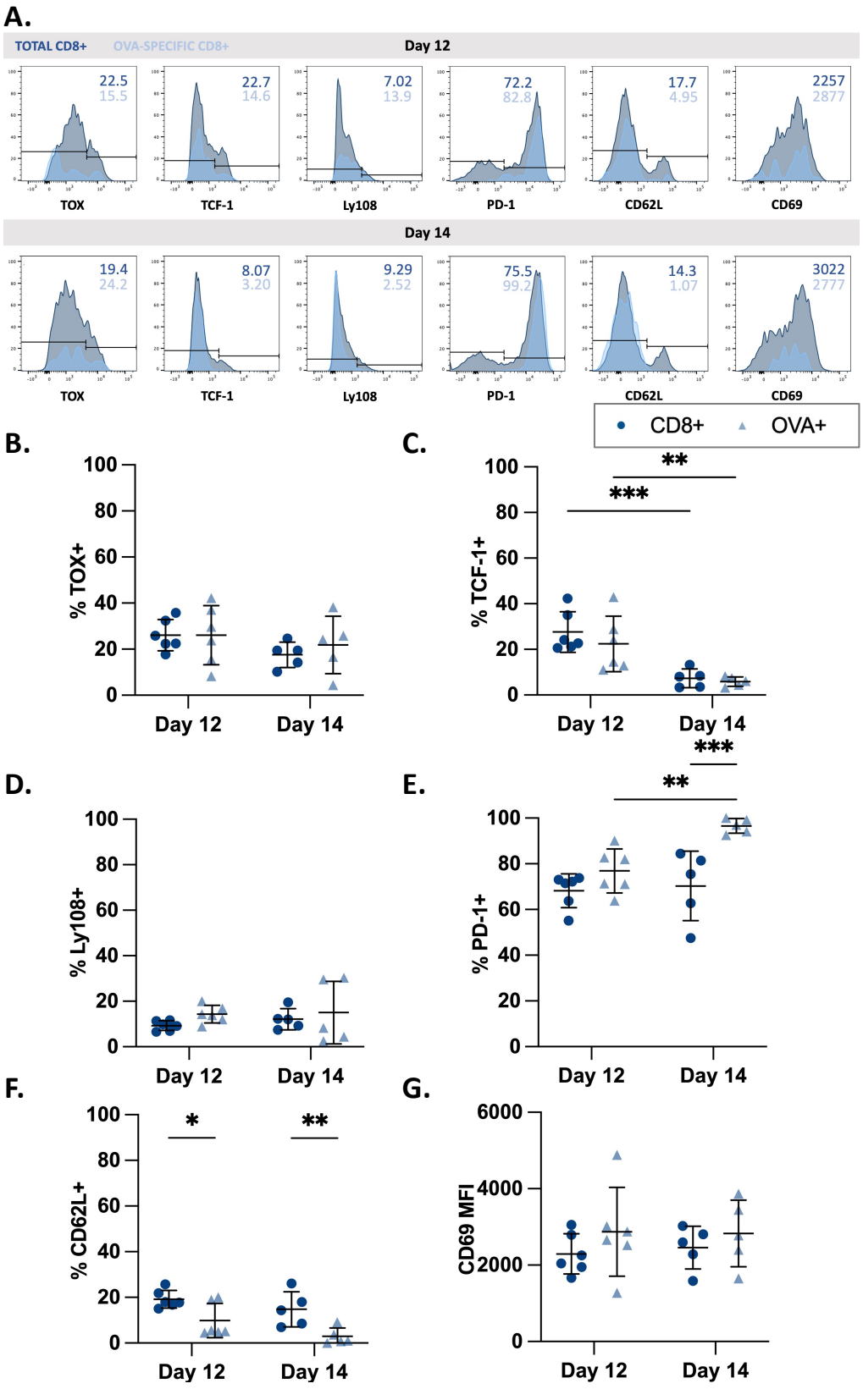

A.
TOTAL CD8+
OVA-SPECIFIC CD8+
Day 12
22.5
15.5
TOX
22.7
14.6
TCF-1
7.02
13.9
Ly108
72.2
82.8
PD-1
17.7
4.95
CD62L
2257
2877
CD69
Day 14
19.4
24.2
TOX
8.07
3.20
TCF-1
9.29
2.52
Ly108
75.5
99.2
PD-1
14.3
1.07
CD62L
3022
2777
CD69
CD8+
OVA+
B.
% TOX+
Day 12
Day 14
C.
% TCF-1+
**
***
Day 12
Day 14
D.
% Ly108+
Day 12
Day 14
E.
% PD-1+
***
**
Day 12
Day 14
F.
% CD62L+
*
**
Day 12
Day 14
G.
CD69 MFI
6000
4000
2000
0
Day 12
Day 14

Figure 3.4. Phenotype of the antigen-specific CD8 T cell intratumoural population in subcutaneous tumour models.

C57BL/6 mice (6-9 weeks) were injected with 2.5 x10^5 MC38-OVA cells subcutaneously. Tissues were collected day 12 and day 14 post-injection. All data shown are from two independent experiments. All graphs show the mean ± SD. Statistical significance was determined using a two-way ANOVA , 4 family comparison, Fisher's LSD test. ** = p < 0.05, ** = p < 0.01, *** = p< 0.001.*

A. Histograms demonstrating the expression of TOX, TCF-1, Ly108, PD-1, CD62L and CD69 in the total CD8+ T cell population in a representative MC38-OVA tumour at day 12 (top row) and day 14 (bottom row) post-injection. The MFI of markers in the OVA+ CD8+ population is shown in light blue, and in the total CD8 T cell population in grey.
B. The percentage of intratumoural CD8+ T cells versus OVA+ CD8+ T cells that are TOX+ at day 12 and day 14.
C. The percentage of intratumoural CD8+ T cells versus OVA+ CD8+ T cells that are TCF-1+ at day 12 and day 14.
D. The percentage of intratumoural CD8+ T cells versus OVA+ CD8+ T cells that are Ly108+ at day 12 and day 14.
E. The percentage of intratumoural CD8+ T cells versus OVA+ CD8+ T cells that are PD-1+ at day 12 and day 14.
F. The percentage of intratumoural CD8+ T cells versus OVA+ CD8+ T cells that are CD62L+ at day 12 and day 14.
G. The MFI of CD69 expression in intratumoural CD8+ T cells versus OVA+ CD8+ T cells at day 12 and day 14.

harvested at different times post-photolabelling (Fig. 3.5A). Photolabelling of effectively all CD3+ T cells within the tumour was achieved, evidenced by the proportion of Kaede red+ cells in the tumour immediately after photoconversion, which was effectively 100% (Fig. 3.5B). This means that any Kaede green cells found within tumours after labelling have trafficked into the tumour after photoconversion, while Kaede red cells were present in the tumour at the time of labelling. Ingress of CD8 T cells can be seen as early as 5 hours after labelling and the proportion of Kaede green+ cells increased over time, consistent with the continued influx of new cells into the tumour (Fig. 3.5C). The proportion of Kaede red CD8 T cells decreased over time in both CT26 and MC38-OVA models, but the proportion of Kaede red+ cells was notably lower in MC38-OVA tumours than CT26 (Fig. 3.5D-E). The density of Kaede red+ CD8 T cells within the tumour increased in the CT26 model over time (Fig. 3.5F), however this may reflect the significant increase in the CD8 T cell population between the two timepoints (Fig. 3.2C-D). In MC38-OVA tumours, the density of Kaede red+ CD8 T cells remained consistent across the two timepoints (Fig. 3.5G). Thus, both CT26 and MC38-OVA CRC models are amenable to photoconversion and allow the study of CD8 T cell ingress and egress.

The vascularisation of tumours is essential to their development, however immune cells will also be contained within the primitive vasculature of subcutaneous tumours and potentially provide a source of contamination in analyses of TILs. To determine the extent to which these cells trapped within the vasculature of tumours at the time of collection contribute to the overall CD8 T cell phenotype, cells in the vasculature were labelled using intravenously injected fluorescently labelled CD45 antibody and allowed to circulate for 5

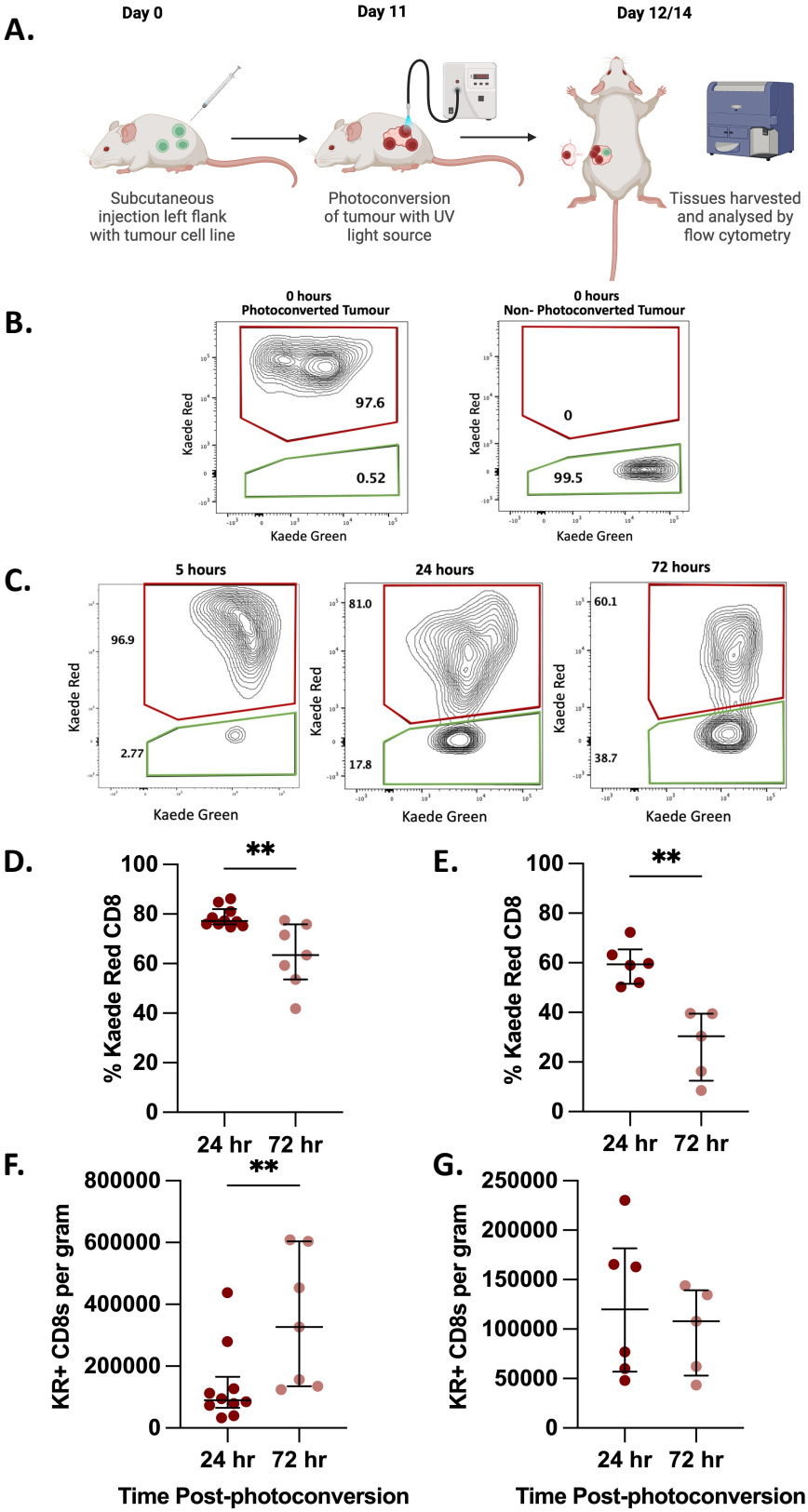

A.
Day 0
Day 11
Day 12/14
Subcutaneous injection left flank with tumour cell line
Photoconversion of tumour with UV light source
Tissues harvested and analysed by flow cytometry
B.
0 hours Photoconverted Tumour
97.6
0.52
Kaede Red
Kaede Green
0 hours Non- Photoconverted Tumour
0
99.5
Kaede Red
Kaede Green
C.
5 hours
96.9
2.77
Kaede Red
Kaede Green
24 hours
81.0
17.8
Kaede Red
Kaede Green
72 hours
60.1
38.7
Kaede Red
Kaede Green
D.
**
% Kaede Red CD8
100
80
60
40
20
0
24 hr
72 hr
E.
**
% Kaede Red CD8
100
80
60
40
20
0
24 hr
72 hr
F.
**
KR+ CD8s per gram
800000
600000
400000
200000
0
24 hr
72 hr
Time Post-photoconversion
G.
KR+ CD8s per gram
250000
200000
150000
100000
50000
0
24 hr
72 hr
Time Post-photoconversion

Figure 3.5. Using the Kaede transgenic mouse and photo-labelling of tumours to assess changes in the immune compartment over time.

BALB/c Kaede and C57BL/6 Kaede mice (6-9 weeks) were injected with 2.5 x10^5 CT26 and MC38-OVA cells subcutaneously. Subcutaneous tumours were photoconverted on day 11, and tissues collected 0, 24 and 72 hours after photoconversion. All CT26 data shown are from three independent experiments. All MC38-OVA data shown are from two independent experiments. All graphs show the median value and IQR. Statistical significance was determined using a Mann-Whitney test. ** = $p < 0.05$, ** = $p < 0.01$.*

A. Illustration outlining the set-up of subcutaneous Kaede tumour model experiments. Created using Biorender.com.
B. Flow cytometry plots demonstrating the Kaede expression in the CD3+ T cell population of un-labelled and photolabelled subcutaneous tumours. T cells were pre-gated on live CD45+ CD11b- CD11c- B220- CD3+ cells. Representative flow cytometry plots shown are from a representative CT26 tumour collected immediately following photoconversion.
C. Flow cytometry plots demonstrating the gating of Kaede red+ and Kaede green+ CD8 populations in representative CT26 tumours at 5, 24 and 72 hours (left to right) after photo-labelling.
D. The percentage of intratumoural CD8+ T cells that are Kaede red+ 24 and 72 hours after photoconversion in CT26 tumours.
E. The percentage of intratumoural CD8+ T cells that are Kaede red+ 24 and 72 hours after photoconversion in MC38-OVA tumours.
F. The number of Kaede red+ CD8 T cells per gram of tumour 24 and 72 hours following photoconversion in CT26 tumours.
G. The number of Kaede red+ CD8 T cells per gram of tumour 24 and 72 hours following photoconversion in MC38-OVA tumours.

minutes prior to collection of the tumour tissue (Fig. 3.6A). Analysis of the cells labelled by the injected anti-CD45 antibody revealed that less than 1% of the CD8 T cells isolated from the tumour were labelled, and so the likelihood of their skewing the CD8 phenotype was minimal (Fig. 3.6B-C). Phenotyping of the i.v. CD45-labelled CD8 T cells within tumours revealed that they were mostly phenotypically distinct from those cells in the tumour, with reduced expression of markers of activation or exhaustion and higher expression of CD62L (Fig. 3.6D-I). Approximately 10% of the i.v. CD45-labelled CD8 T cells were Kaede red+ (Fig. 3.6J). Overall, the contribution of immune cells within the vasculature of subcutaneously implanted tumours to overall CD8 phenotype is minimal and hence this additional further step to the *in vivo* experiments was deemed redundant in subsequent experiments.

Due to complete photolabelling of the tumour immune compartment, Kaede green cells found within the tumour at timepoints following the photolabelling procedure can be said to be newly entering. Thus, it is possible to observe how quickly these newly entered cells change with time spent in the tumour. Similar to previous results, the longer CD8 T cells spend within the tumour the more exhausted their phenotype, this can be seen through both differences between the 24- and 72-hour timepoints, but also between the Kaede red and Kaede green populations at both time points (Fig. 3.7A-D). The most marked result is how rapidly newly entering Kaede green cells become exhausted within the tumour, resembling their Kaede red counterparts (Fig. 3.7A-D & Appendices 3.5-3.7). The expression of PD-1 is a good example, Kaede green CD8 T cells at 24 hours express a low level of PD-1, clearly less than those Kaede red CD8 T cells that have been in the tumour for at least a day (Fig. 3.7C). At 72 hours post-labelling, the Kaede green CD8 T cell

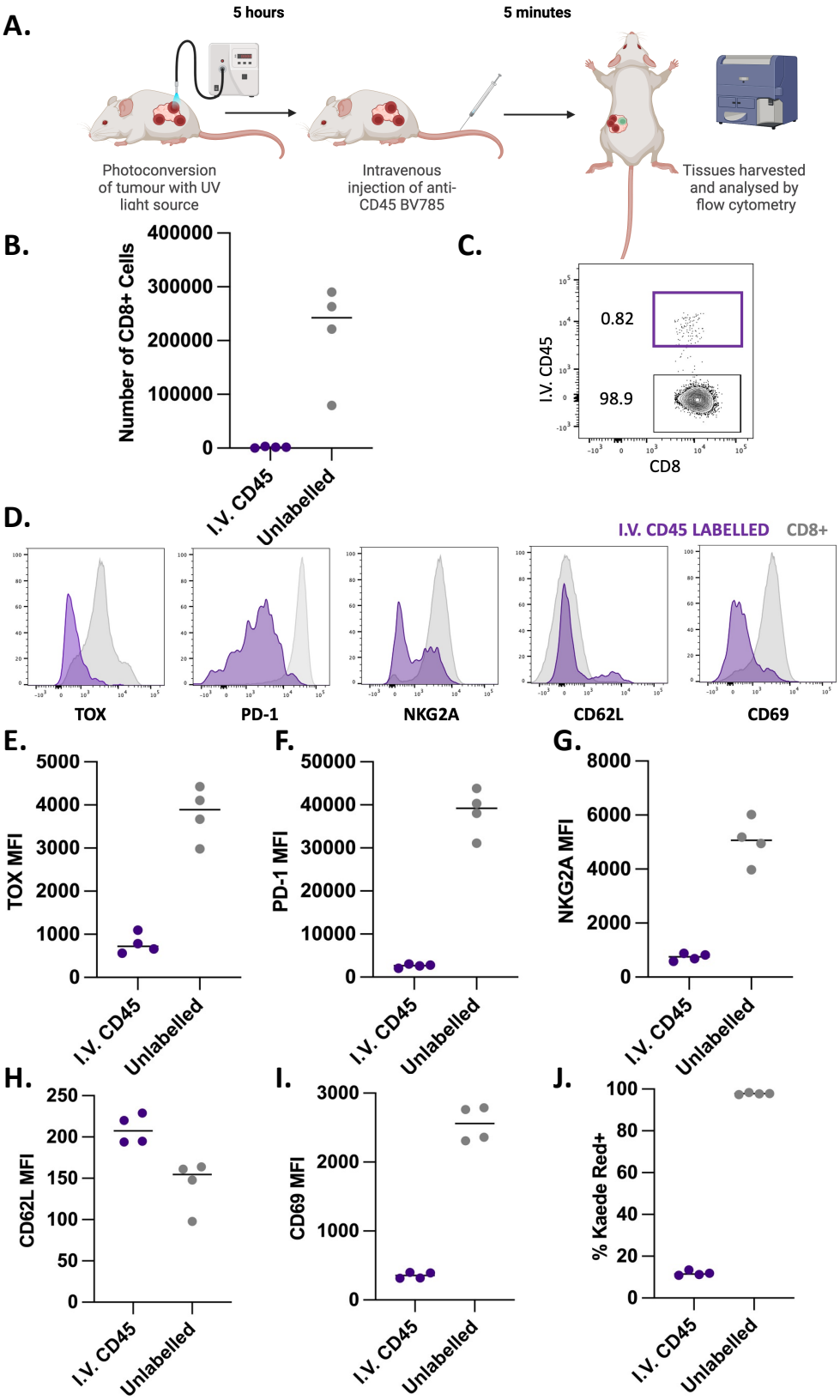
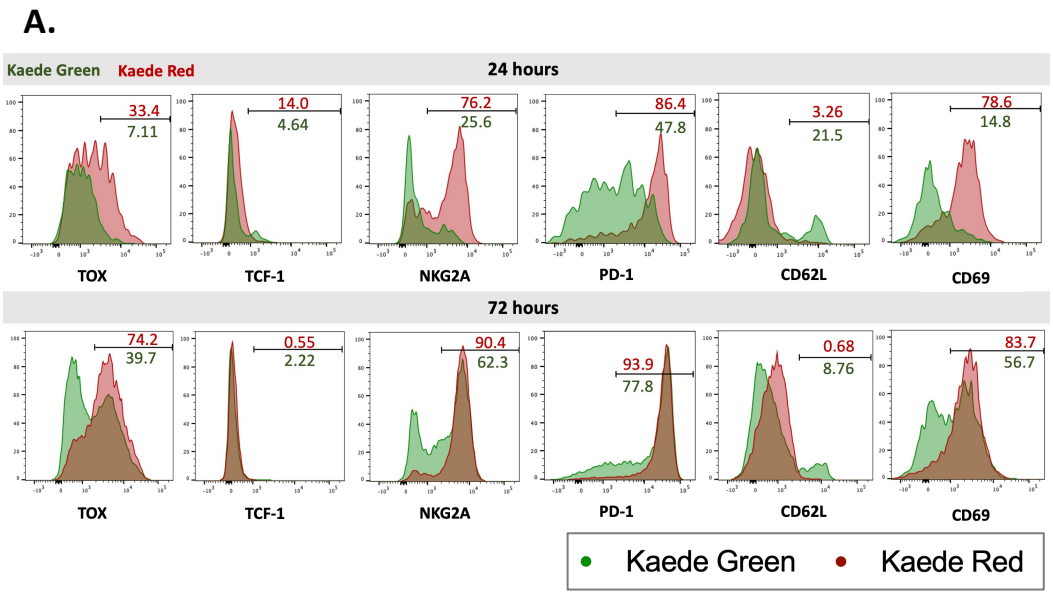
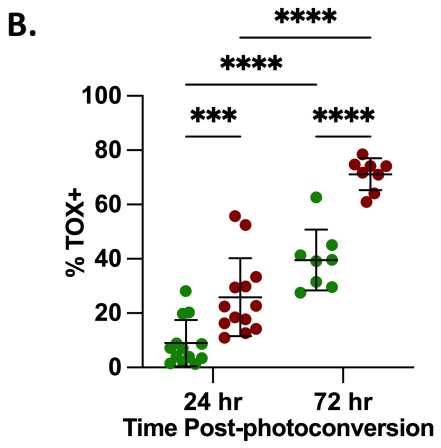

A.
5 hours
5 minutes
Photoconversion of tumour with UV light source
Intravenous injection of anti-CD45 BV785
Tissues harvested and analysed by flow cytometry
B.
Number of CD8+ Cells
400000
300000
200000
100000
0
I.V. CD45
Unlabelled
C.
I.V. CD45
0.82
98.9
CD8
D.
I.V. CD45 LABELLED
CD8+
TOX
PD-1
NKG2A
CD62L
CD69
E.
TOX MFI
5000
4000
3000
2000
1000
0
F.
PD-1 MFI
50000
40000
30000
20000
10000
0
G.
NKG2A MFI
8000
6000
4000
2000
0
H.
CD62L MFI
250
200
150
100
50
0
I.
CD69 MFI
3000
2000
1000
0
J.
% Kaede Red+
100
80
60
40
20
0

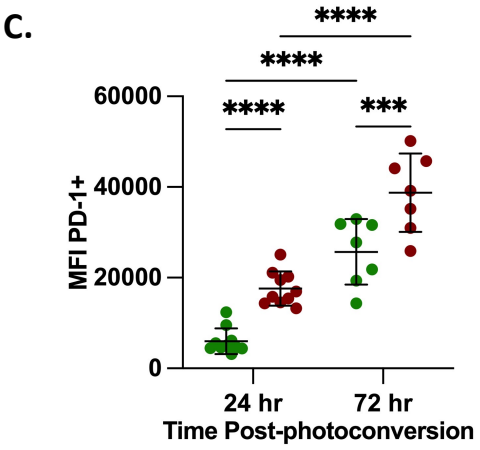
Figure 3.6. Determining the extent to which cells within the tumour vasculature contribute to the tumour infiltrating lymphocyte analysis.

BALB/c Kaede mice (6-9 weeks) were injected with 2.5 x10^5 CT26 cells subcutaneously. On day 12 following injection, 1µg BV785 CD45 antibody was injected intravenously, prior to cessation of circulation 5 minutes later and collection of tissues. All CT26 data shown are from one experiment with four animals. All graphs show the median value only.

A. Illustration outlining the set-up of i.v. labelling to ascertain the phenotype of lymphocytes residing in tumour vessels.
B. The number of CD8+ T cells in the subcutaneous tumour that are i.v. labelled versus unlabelled.
C. Flow cytometry plot demonstrating the gating of i.v. CD45 labelled CD8 T cells from representative CT26 WT tumour.
D. Histograms demonstrating the MFI of TOX, PD-1, NKG2A, CD62L, and CD69 in the total CD8 population (grey) versus the i.v. CD45 labelled CD8 population (purple) in a representative CT26 tumour sample.
E. The MFI of TOX in i.v. labelled and unlabelled CD8 cells in CT26 tumours.
F. The MFI of PD-1 in i.v. labelled and unlabelled CD8 cells in CT26 tumours.
G. The MFI of NKG2A in i.v. labelled and unlabelled CD8 cells in CT26 tumours.
H. The MFI of CD62L in i.v. labelled and unlabelled CD8 cells in CT26 tumours.
I. The MFI of CD69 in i.v. labelled and unlabelled CD8 cells in CT26 tumours.
J. The percentage of Kaede red+ i.v. labelled and unlabelled CD8 cells in CT26 tumours.


A.
Kaede Green
Kaede Red
24 hours
33.4
7.11
14.0
4.64
76.2
25.6
86.4
47.8
3.26
21.5
78.6
14.8
TOX
TCF-1
NKG2A
PD-1
CD62L
CD69
72 hours
74.2
39.7
0.55
2.22
90.4
62.3
93.9
77.8
0.68
8.76
83.7
56.7
TOX
TCF-1
NKG2A
PD-1
CD62L
CD69
Kaede Green
Kaede Red


B.
****
****
***
****
100
80
60
40
20
0
% TOX+
24 hr
72 hr
Time Post-photoconversion


C.
****
****
****
***
60000
40000
20000
0
MFI PD-1+
24 hr
72 hr
Time Post-photoconversion

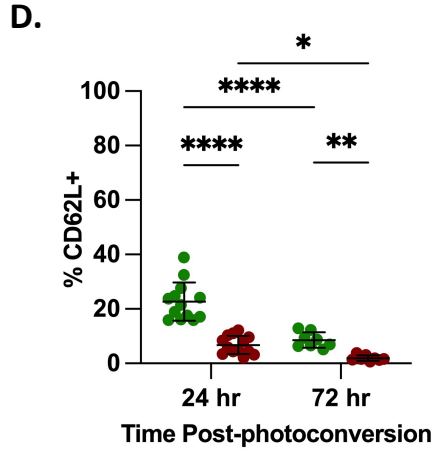

D.
*
****
****
**
100
80
60
40
20
0
% CD62L+
24 hr
72 hr
Time Post-photoconversion

Figure 3.7. Examining the effect of time in the tumour on the phenotype of the CD8 population.

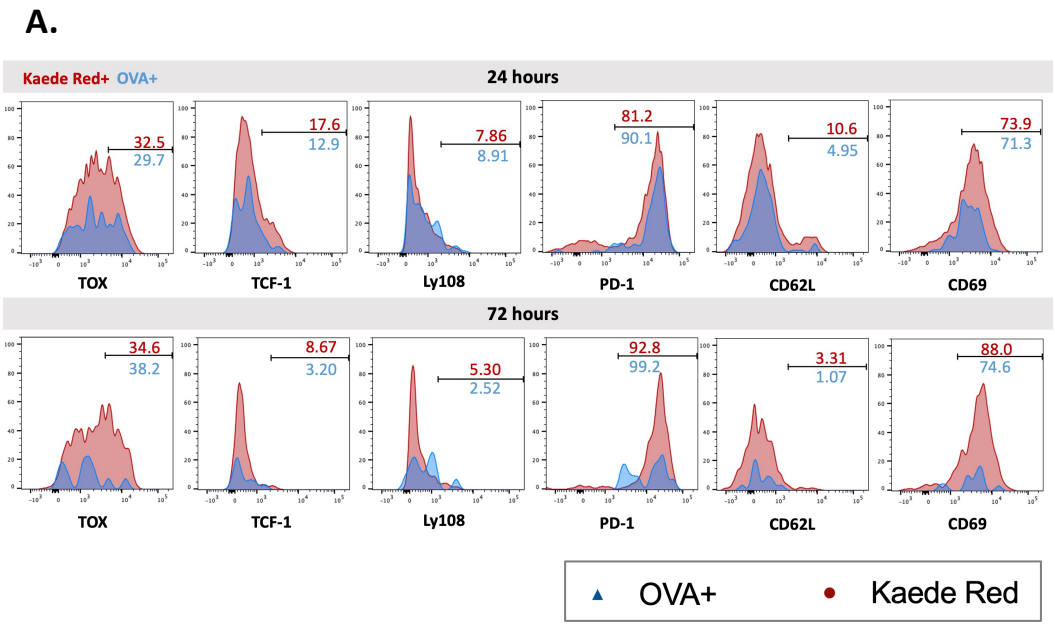
BALB/c Kaede mice (6-9 weeks) were injected with 2.5 x10^5 CT26 cells subcutaneously. Subcutaneous tumours were photoconverted on day 11, and tissues collected 24 and 72 hours after photoconversion. All CT26 data shown are from three independent experiments. All graphs show the mean ±SD. Statistical significance was determined using a two-way ANOVA , 4 family comparison, Fisher's LSD test. ** = p < 0.05, ** = p < 0.01, *** = p< 0.001, **** = p< 0.0001*

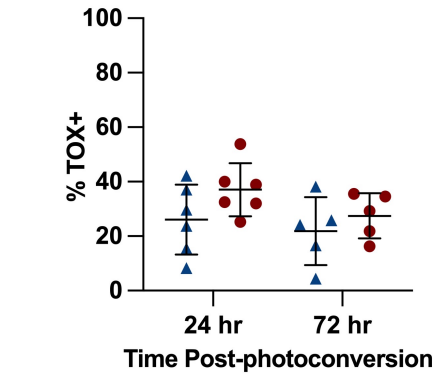
A. Histograms demonstrating the expression of TOX, TCF-1, NKG2A, PD-1, CD62L and CD69 in the Kaede green+ (green) and Kaede red+ (red) CD8 T cell populations in a representative CT26 tumour sample, 24hr (top row) and 72hr (bottom row) following photoconversion.
B. The percentage of intratumoural CD8+ Kaede red and green cells positive for TOX expression at 24 and 72 hours after photoconversion.
C. The MFI of the PD-1+ compartment in intratumoural CD8+ Kaede red and green populations at 24 and 72 hours after photoconversion.
D. The percentage of intratumoural CD8+ Kaede red and green cells positive for CD62L expression at 24 and 72 hours after photoconversion.

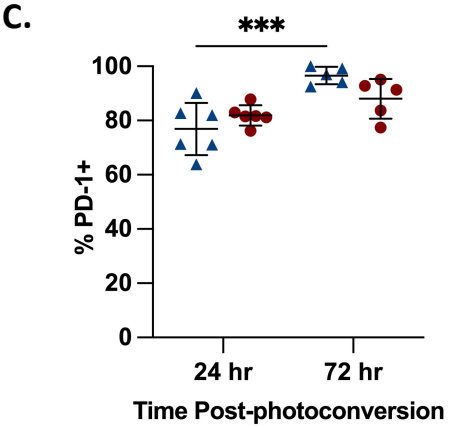
compartment now includes cells that have potentially been in the tumour for a further two days, and some cells had upregulated PD-1 expression to a level more comparable to that seen in the Kaede red population (Fig. 3.7A, C). Comparison of the tumour antigen-specific CD8 population and the tumour-resident Kaede red CD8 T cells shows that there were no significant differences between these two populations (Fig. 3.8A-D), suggesting that antigen-specific CD8 T cells become retained within the tumour.

3.2.3. Studying the changes in the intratumoural stem-like population over time

The clinical importance of the stem-like CD8 population has been strongly implicated, it is suggested that this population underpins a successful response to ICB, sustaining an intratumoural exhausted CD8 T cell population.(149, 161) Despite this, a detailed transcriptomic description of these cells in pre-clinical models of cancer is lacking, they remain rare within tumours and existing scRNA-seq data sets do not clearly define the stem-like population distinct from other TCF-1+ cells.(301) Following the establishment of subcutaneous CRC models and effective photolabelling of the tumour immune compartment, we sought to generate further transcriptomic resources defining the immune landscape of tumours. To this end we sought to optimise tumour digestion and sorting strategies and then used scRNA-seq to analyse Kaede green+ and Kaede red+ TILs and myeloid cells isolated from MC38 tumours 48-hours post-photoconversion. This experimental approach established an extensive scRNA-seq resource, rich in data characterising the immune compartment of MC38 tumours.(168, 302) Focusing on just the CD8 T cells within this data set, unbiased clustering of the CD8 compartment of these tumours revealed 12 clusters including naïve, cycling, memory, intermediate exhausted,


A.
Kaede Red+ OVA+
24 hours
32.5
29.7
17.6
12.9
7.86
8.91
81.2
90.1
10.6
4.95
73.9
71.3
TOX
TCF-1
Ly108
PD-1
CD62L
CD69
72 hours
34.6
38.2
8.67
3.20
5.30
2.52
92.8
99.2
3.31
1.07
88.0
74.6
TOX
TCF-1
Ly108
PD-1
CD62L
CD69
OVA+
Kaede Red


B.
% TOX+
100
80
60
40
20
0
24 hr
72 hr
Time Post-photoconversion


C.
***
% PD-1+
100
80
60
40
20
0
24 hr
72 hr
Time Post-photoconversion

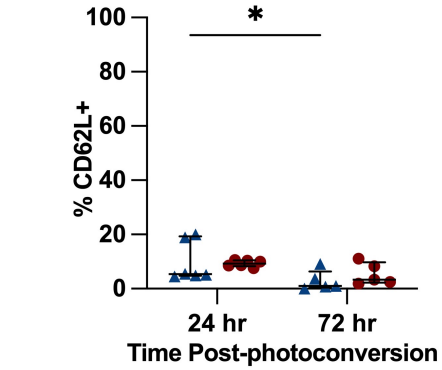

D.
*
% CD62L+
100
80
60
40
20
0
24 hr
72 hr
Time Post-photoconversion

Figure 3.8. Comparison of antigen-specific CD8 T cells versus the total CD8 compartment in tumours over time.

C57BL/6 Kaede mice (6-9 weeks) were injected with 2.5 x10^5 MC38-OVA cells subcutaneously. Subcutaneous tumours were photoconverted on day 11, and tissues collected 24 and 72 hours after photoconversion. All graphs show the mean ±SD. Statistical significance was determined using a two-way ANOVA , 4 family comparison, Fisher's LSD test. ** = p < 0.05, ** = p < 0.01, *** = p< 0.001.*

A. Histograms demonstrating the expression of TOX, TCF-1, Ly108, PD-1, CD62L and CD69 in the OVA+ CD8 (blue) and Kaede red+ CD8+ (red) populations in a representative MC38-OVA tumour sample at 24 (top row) and 72 hours (bottom row) after photoconversion.
B. The percentage of intratumoural CD8+ Kaede red+ and CD8+ OVA+ that are TOX+ 24 and 72 hours after photoconversion.
C. The percentage of intratumoural CD8+ Kaede red+ and CD8+ OVA+ that are PD-1+ 24 and 72 hours after photoconversion.
D. The percentage of intratumoural CD8+ Kaede red+ and CD8+ OVA+ that are CD62L+ 24 and 72 hours after photoconversion.

terminally exhausted, and a distinct progenitor exhausted population or stem-like compartment (Fig. 3.9A-B). This spectrum closely matched described populations in a 2023 review by Wherry *et al.*.(303) Within the 12 clusters, a cluster defined by high expression of *Tcf7, Ccr7, Pdcd1, Cxcr3,* and *Tox* was identified and termed 'CD8 T exh_prog' or stem-like cluster (Fig. 3.9B-C). Consistent with other reports, these cells lacked expression of *Havcr2* and *Entpd1*, unlike other exhausted cells (Fig. 3.9B-D).(149, 301) Comparison of this 'CD8 T exh_prog' cluster with published data sets showed an enrichment for signatures thought to be representative of stem-like cells (CXCR5+ TIM-3-, TIM-3- PD-1+) (Fig. 3.9D).(149, 301) However, according to the signatures within both published datasets, there is also a high enrichment score among memory clusters, further evidencing these do not fully resolve stem-like cells (Fig. 3.9D).(149, 301)

Flow cytometry was then used to validate the stem-like CD8 T cell transcriptome defined by scRNA-seq. Co-expression of TCF-1 and PD-1 was used to initially identify these cells. While Ly108 has been used by others to identify stem-like cells, in our hands we were concerned that co-expression of Ly108 and PD-1 falsely elevates the numbers of stem-like cells, particularly in CT26 tumours (Fig. 3.10A-D); potentially due to Ly108 protein expression being sustained after TCF-1 has been downregulated.(300) Consistent with the transcriptomic changes, TCF-1+ PD-1+ cells demonstrated higher expression of TOX and CXCR6 than TCF-1+ PD-1- cells (Fig. 3.10E-G, J). The TCF-1+ PD-1+ cells also showed very limited expression of CD39 and TIM-3 when compared to the exhausted population, again consistent with the transcriptomic data (Fig. 3.10E, H-I, K). Interestingly, these stem-like cells also demonstrated robust expression of NKG2A, though not quite as abundantly as

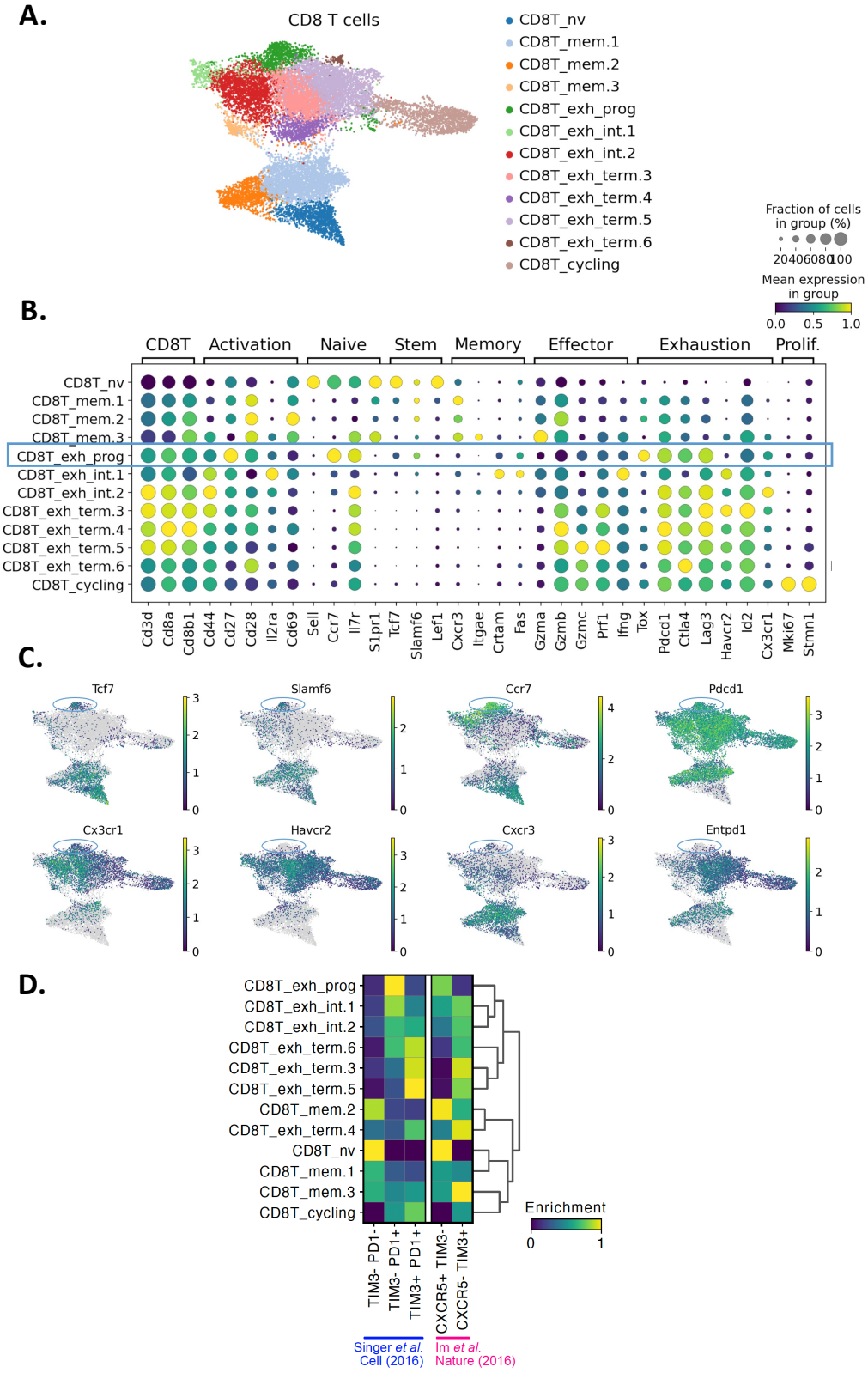

A.
CD8 T cells
CD8T_nv
CD8T_mem.1
CD8T_mem.2
CD8T_mem.3
CD8T_exh_prog
CD8T_exh_int.1
CD8T_exh_int.2
CD8T_exh_term.3
CD8T_exh_term.4
CD8T_exh_term.5
CD8T_exh_term.6
CD8T_cycling
Fraction of cells in group (%)
20406080100
Mean expression in group
0.0 0.5 1.0
B.
CD8T
Activation
Naive
Stem
Memory
Effector
Exhaustion
Prolif.
CD8T_nv
CD8T_mem.1
CD8T_mem.2
CD8T_mem.3
CD8T_exh_prog
CD8T_exh_int.1
CD8T_exh_int.2
CD8T_exh_term.3
CD8T_exh_term.4
CD8T_exh_term.5
CD8T_exh_term.6
CD8T_cycling
Cd3d Cd8a Cd8b1 Cd44 Cd27 Cd28 Il2ra Cd69 Sell Ccr7 Il7r S1pr1 Tcf7 Slamf6 Lef1 Cxcr3 Itgae Crtam Fas Gzma Gzmb Gzmc Prf1 Ifng Tox Pdcd1 Ctla4 Lag3 Havcr2 Id2 Cx3cr1 Mki67 Stmn1
C.
Tcf7
Slamf6
Ccr7
Pdcd1
Cx3cr1
Havcr2
Cxcr3
Entpd1
D.
CD8T_exh_prog
CD8T_exh_int.1
CD8T_exh_int.2
CD8T_exh_term.6
CD8T_exh_term.3
CD8T_exh_term.5
CD8T_mem.2
CD8T_exh_term.4
CD8T_nv
CD8T_mem.1
CD8T_mem.3
CD8T_cycling
Enrichment
0 1
TIM3- PD1-
TIM3- PD1+
TIM3+ PD1+
CXCR5+ TIM3-
CXCR5- TIM3+
Singer et al. Cell (2016)
Im et al. Nature (2016)

Figure 3.9. Identification of intratumoural stem-like CD8 T cells using scRNA-seq analysis of MC38-OVA subcutaneous tumours.

C57BL/6 Kaede mice (6-9 weeks) were injected with 2.5 x10^5 MC38-OVA cells subcutaneously, before photoconversion of the subcutaneous tumour on day 13. Tumours were collected 48 hours following photoconversion. Tissues were processed as per methods, before staining for CD45, CD11b, Ter119, Live/Dead. Cell suspensions were sorted using the FACS Aria II Cell Sorter (BD), sorted lymphocytes were further sorted into Kaede red+ and Kaede red-. scRNA sequencing of Kaede green+ and Kaede red+ TIL populations was carried out. For this work, scRNA-seq data from the CD8 population only is demonstrated.

A. UMAP of CD8+ T cells from scRNA-seq of MC38 tumours. Clusters (coloured) were identified using unsupervised Leiden clustering. Cluster CD8T_exh_prog represents the stem-like CD8 population.
B. Dot plot showing differentially expressed genes between CD8 clusters in MC38 tumours. Clusters (coloured) were identified using unsupervised Leiden clustering and annotated using canonical CD8 T cell subset marker gene expression. CD8T_exh_prog is highlighted.
C. UMAP demonstrating the expression of canonical gene markers between CD8 T cell clusters. CD8T_exh_prog is highlighted.
D. Clusters identified were annotated using gene signatures published by Singer et al. (2016) and Im et al. (2016).

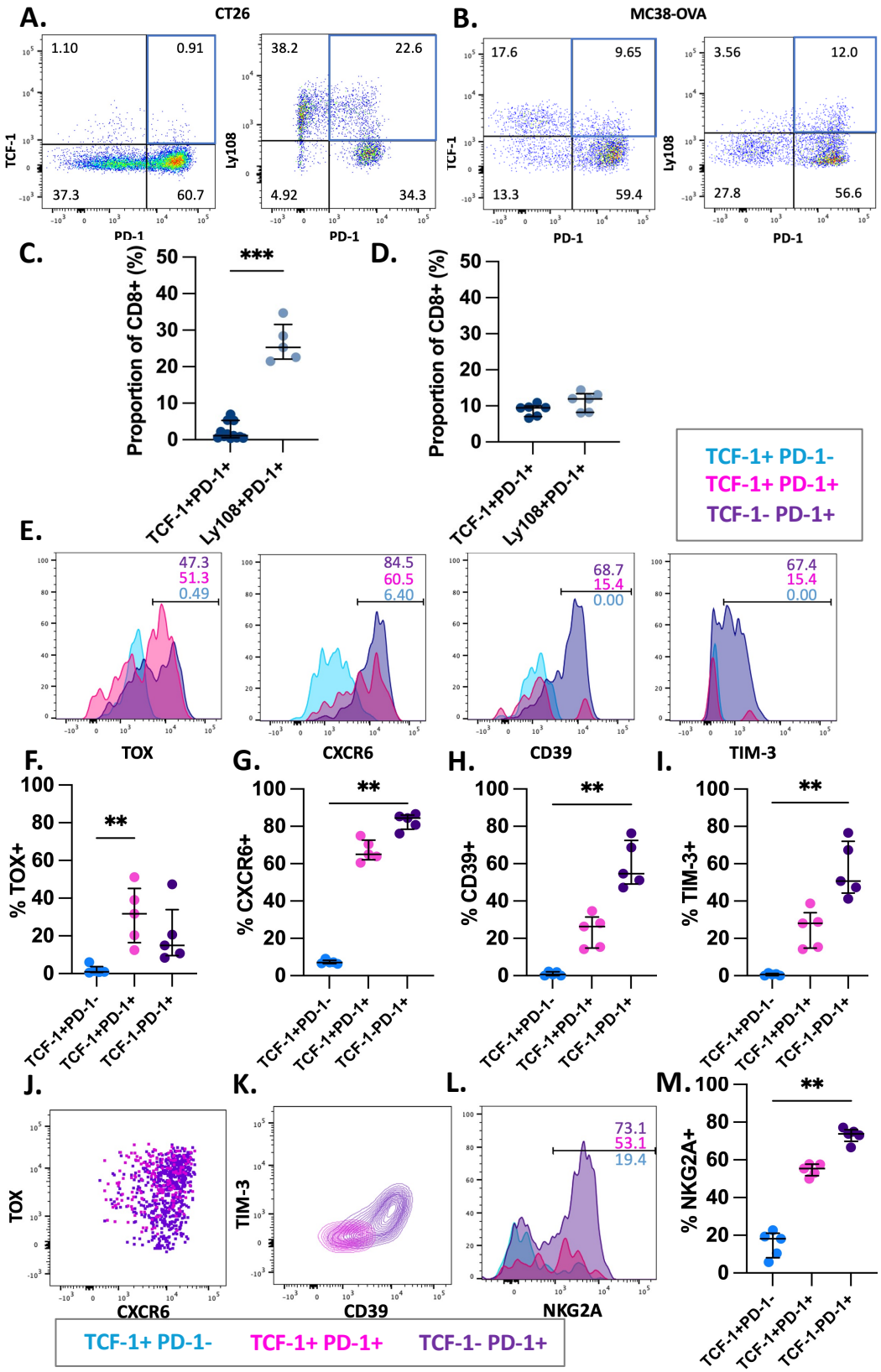

A.
CT26
1.10
0.91
37.3
60.7
TCF-1
PD-1
38.2
22.6
4.92
34.3
Ly108
PD-1
B.
MC38-OVA
17.6
9.65
13.3
59.4
TCF-1
PD-1
3.56
12.0
27.8
56.6
Ly108
PD-1
C.
Proportion of CD8+ (%)
***
TCF-1+PD-1+
Ly108+PD-1+
D.
Proportion of CD8+ (%)
TCF-1+PD-1+
Ly108+PD-1+
TCF-1+ PD-1-
TCF-1+ PD-1+
TCF-1- PD-1+
E.
47.3
51.3
0.49
TOX
84.5
60.5
6.40
CXCR6
68.7
15.4
0.00
CD39
67.4
15.4
0.00
TIM-3
F.
% TOX+
**
G.
% CXCR6+
**
H.
% CD39+
**
I.
% TIM-3+
**
TCF-1+PD-1-
TCF-1+PD-1+
TCF-1-PD-1+
J.
TOX
CXCR6
K.
TIM-3
CD39
L.
73.1
53.1
19.4
NKG2A
M.
% NKG2A+
**
TCF-1+ PD-1-
TCF-1+ PD-1+
TCF-1- PD-1+

Figure 3.10. Defining the intratumoural stem-like CD8 population by flow cytometry.

BALB/c Kaede mice (6-9 weeks) were injected with 2.5 x10^5 CT26 cells subcutaneously. Tissues were collected day 12 post-injection. All CT26 data shown are from three independent experiments. All MC38-OVA data shown are from two independent experiments. All graphs show the median value and IQR. In the case of two-column analysis statistical significance was determined using a Mann-Whitney test, in the case of multiple column analysis statistical significance was determined using a Kruskal-Wallis multiple comparison with Dunn's post-hoc correction performed. ** = $p < 0.05$, ** = $p < 0.01$, *** = $p < 0.001$.*

A. Flow cytometry plots demonstrating the co-expression of PD-1 with TCF-1 (left) and Ly108 (right) in CT26 tumours. Flow plots are pre-gated on live CD45+ CD11b- B220- CD3+ CD8+ cells in a representative tumour sample.
B. Flow cytometry plots demonstrating the co-expression of PD-1 with TCF-1 (left) and Ly108 (right) in MC38-OVA tumours. Flow plots are pre-gated on live CD45+ CD11b- B220- CD3+ CD8+ cells in a representative tumour sample.
C. The percentage of CD8 T cells that are TCF-1+ PD-1+ versus Ly108+ PD-1+ at day 12 post-injection in CT26 tumours.
D. The percentage of CD8 T cells that are TCF-1+ PD-1+ versus Ly108+ PD-1+ at day 12 post-injection in MC38 OVA tumours.
E. Histograms demonstrating the levels of TOX, CXCR6, CD39, and TIM-3 expression in the intratumoural CD8 T cell population according to TCF-1 and PD-1 expression at day 12 post-injection in a representative MC38-OVA tumour. The y axis is normalised to the mode. Histograms were generated using FlowJo software.
F. The percentage of the CD8 T cell population according to TCF-1 and PD-1 expression that are TOX+ at day 12 post-injection in MC38 OVA tumours.
G. The percentage of the CD8 T cell population according to TCF-1 and PD-1 expression that are CXCR6+ at day 12 post-injection in MC38 OVA tumours.
H. The percentage of the CD8 T cell population according to TCF-1 and PD-1 expression that are CD39+ at day 12 post-injection in MC38 OVA tumours.

I. The percentage of the CD8 T cell population according to TCF-1 and PD-1 expression that are TIM-3+ at day 12 post-injection in MC38 OVA tumours.
J. Flow cytometry plots demonstrating TOX and CXCR6 expression in the TCF-1+ PD-1+ (pink) and TCF-1- PD-1+ (purple) compartments at day 12 post-injection in a representative MC38-OVA tumour.
K. Flow cytometry plots demonstrating TIM-3 and CD39 expression in the TCF-1+ PD-1+ (pink) and TCF-1- PD-1+ (purple) compartments at day 12 post-injection in a representative MC38-OVA tumour.
L. Histogram demonstrating the level of NKG2A expression in the intratumoural CD8 T cell population according to TCF-1 and PD-1 expression at day 12 post-injection in a representative CT26 tumour. The y axis is normalised to the mode.
M. The percentage of the CD8 T cell population according to TCF-1 and PD-1 expression that are NKG2A+ at day 12 post-injection in CT26 tumours.

the TCF-1- PD-1+ cells (Fig. 3.10L-M). Thus, key transcriptomic features of the stem-like CD8 T cell compartment of tumours were validated at the protein level, providing appropriate ways to identify and track this population *in vivo.*

Photolabelling of tumours was further used to assess the migratory capabilities of the stem-like CD8 T cell population. Initially, the proportion of Kaede red+ cells within the TCF-1+ PD-1-, TCF-1+ PD-1+ and TCF-1- PD-1+ populations was compared at 24 hours post-photoconversion of MC38-OVA tumours, to provide information on the extent to which newly entering cells contribute to these compartments (Fig. 3.11A). A significantly higher proportion of the TCF-1+ PD-1+ CD8 T cells were Kaede red+ compared with the TCF-1+ PD-1- population, indicating that these cells were more retained within the tumour (Fig. 3.11B). Examining the stem-like CD8 T cell population according to their Kaede expression, and hence time in the tumour, it was clear that Kaede green+ stem-like cells that had entered the tumour within the past 24 hours had decreased expression of TOX and PD-1 compared to Kaede red counterparts (Fig. 3.11C-D); but both Kaede green and red TCF-1+ PD-1+ cells were negative for TIM-3 expression, consistent with them being true stem-like CD8 cells (Fig. 3.11E). Comparison of the TCF-1+ PD-1+ cells at 24 and 72 hours post photoconversion revealed a significant drop in the proportion of Kaede red+ cells consistent with the continued recruitment of TCF-1+ PD-1+ cells into the tumour, but at a rate less than that of other populations (such as TCF-1+ PD-1- cells) (Fig. 3.11F-G). Comparable data was also observed within CT26 tumours after labelling (Appendix 3.8). Collectively these data indicate that there is a steady influx of new stem-like T cells into the tumour.

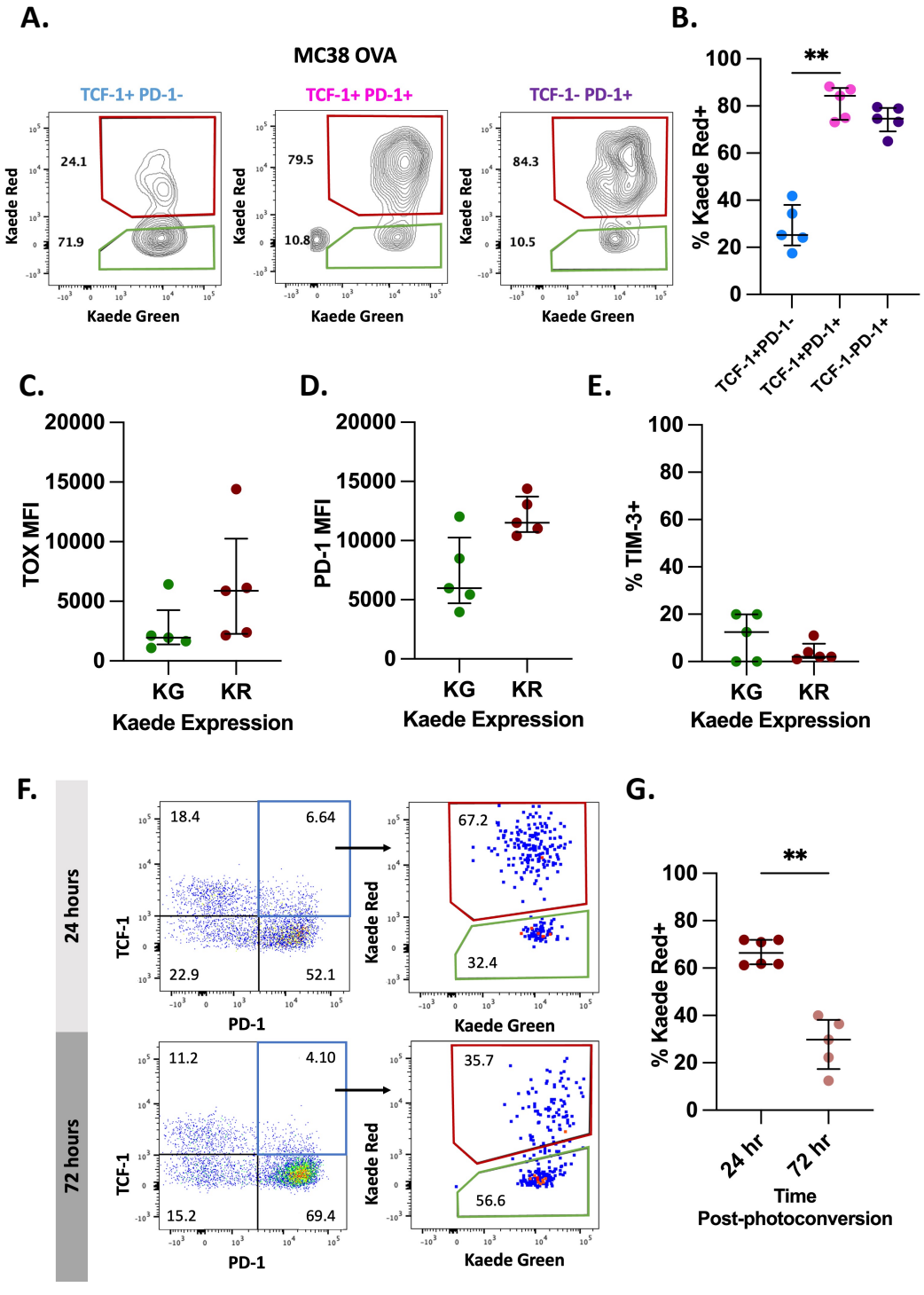

A.
MC38 OVA
TCF-1+ PD-1-
TCF-1+ PD-1+
TCF-1- PD-1+
Kaede Red
Kaede Green
24.1
71.9
79.5
10.8
84.3
10.5
B.
**
% Kaede Red+
TCF-1+PD-1-
TCF-1+PD-1+
TCF-1-PD-1+
C.
TOX MFI
KG
KR
Kaede Expression
D.
PD-1 MFI
KG
KR
Kaede Expression
E.
% TIM-3+
KG
KR
Kaede Expression
F.
24 hours
72 hours
TCF-1
PD-1
18.4
6.64
22.9
52.1
67.2
32.4
11.2
4.10
15.2
69.4
35.7
56.6
Kaede Red
Kaede Green
G.
**
% Kaede Red+
24 hr
72 hr
Time
Post-photoconversion

Figure 3.11. Phenotyping the intratumoural stem-like CD8 population over time.

C57BL/6 Kaede mice (6-9 weeks) were injected with 2.5 x10^5 MC38-OVA cells subcutaneously. Photoconversion of subcutaneous tumours occurred on day 12 post-injection, and tissues collected 24 hours later. All MC38-OVA data shown are from two independent experiments. All graphs show the median value and IQR. In the case of two-column analysis statistical significance was determined using a Mann-Whitney test, in the case of multiple column analysis statistical significance was determined using a Kruskal-Wallis multiple comparison with Dunn's post-hoc correction performed. ** = $p < 0.05$, ** = $p < 0.01$.*

A. Flow cytometry plots showing Kaede expression in the TCF-1+ PD-1- CD8+ (left), the TCF-1+ PD-1+ CD8+ (centre), and the TCF-1- PD-1+ CD8+ (right) populations. Data shown are from a representative MC38-OVA tumour 24 hours following photoconversion.
B. The percentage of Kaede red+ cells based on expression of TCF-1 and PD-1 at 24 hours following photoconversion of MC38-OVA tumours.
C. The MFI of TOX in the KR+ and KG+ TCF-1+ PD-1+ CD8 population at 24 hours following photoconversion of MC38-OVA tumours.
D. The MFI of PD-1 in the KR+ and KG+ TCF-1+ PD-1+ CD8 population at 24 hours following photoconversion of MC38-OVA tumours.
E. The percentage of TIM-3+ cells in the KR+ and KG+ TCF-1+ PD-1+ CD8 population at 24 hours following photoconversion of MC38-OVA tumours.
F. Flow cytometry plots showing the Kaede expression (right) of the TCF-1+ PD-1+ CD8+ population highlighted (blue) in the left-hand flow plot at 24 and 72 hours following photoconversion. Data shown are from representative MC38-OVA tumours at each time point.
G. The percentage of Kaede red+ in the TCF-1+ PD-1+ CD8 population at 24 and 72 hours following photoconversion of MC38-OVA tumours.

To extend these analyses of the stem-like compartment and better understand when this population becomes established within the tumour, we asked whether these cells were evident earlier in the development of tumours. Therefore, MC38-OVA tumours were established in wildtype (WT) mice and the intratumoural TCF-1+ PD-1+ CD8 T cells analysed at day 7 and day 14 post implantation. The weight of MC38-OVA tumours, as well as the proportion and density of CD8 T cells within the tumour, increased between day 7 and 14 of tumour development, as expected (Fig 3.12A-C). The number of OVA-specific CD8 T cells within the tumours also increased significantly between day 7 and 14 (Fig. 3.12D-E). Of note, there was a significant reduction in the proportion of TCF-1+ PD-1+ CD8 T cells from day 7 to 14 (Fig. 3.12F-G). The TCF-1+ PD-1+ compartment expressed low levels of TIM-3 at both day 7 and 14, whereas at day 14 the exhausted TCF-1- PD-1+ population was predominantly TIM-3+, similar to the scRNA-seq signatures (Fig. 3.12H). The level of PD-1 expression in the TCF-1+ PD-1+ population increased between day 7 and 14, though it was not statistically significant as in the TCF-1- PD-1+ population (Fig. 3.12I). The transcription factor B-cell lymphoma 6 (Bcl-6) was recently identified as a key driver of stem-like CD8 T cell persistence and provided an alternative means of identifying this population.(304) Using Bcl-6 reporter mice grafted with MC38-OVA tumours, we assessed Bcl-6 expression amongst the CD8 T cells in day 7 and 14 tumours. Due to the reporter, fixation and intracellular staining with TCF-1 was not possible, and so Ly108+ PD-1+ cells were used as a surrogate for the stem-like population. By overlaying Bcl-6+ cells onto plots of Ly108 versus PD-1, it was evident that most Ly108+ PD-1+ cells lacked Bcl-6 expression (Fig. 3.12J), consistent with Ly108 being a less than robust means to identify stem-like CD8 T cells as discussed previously. Bcl-6+ CD8 T cells were almost all Ly108+, and between day

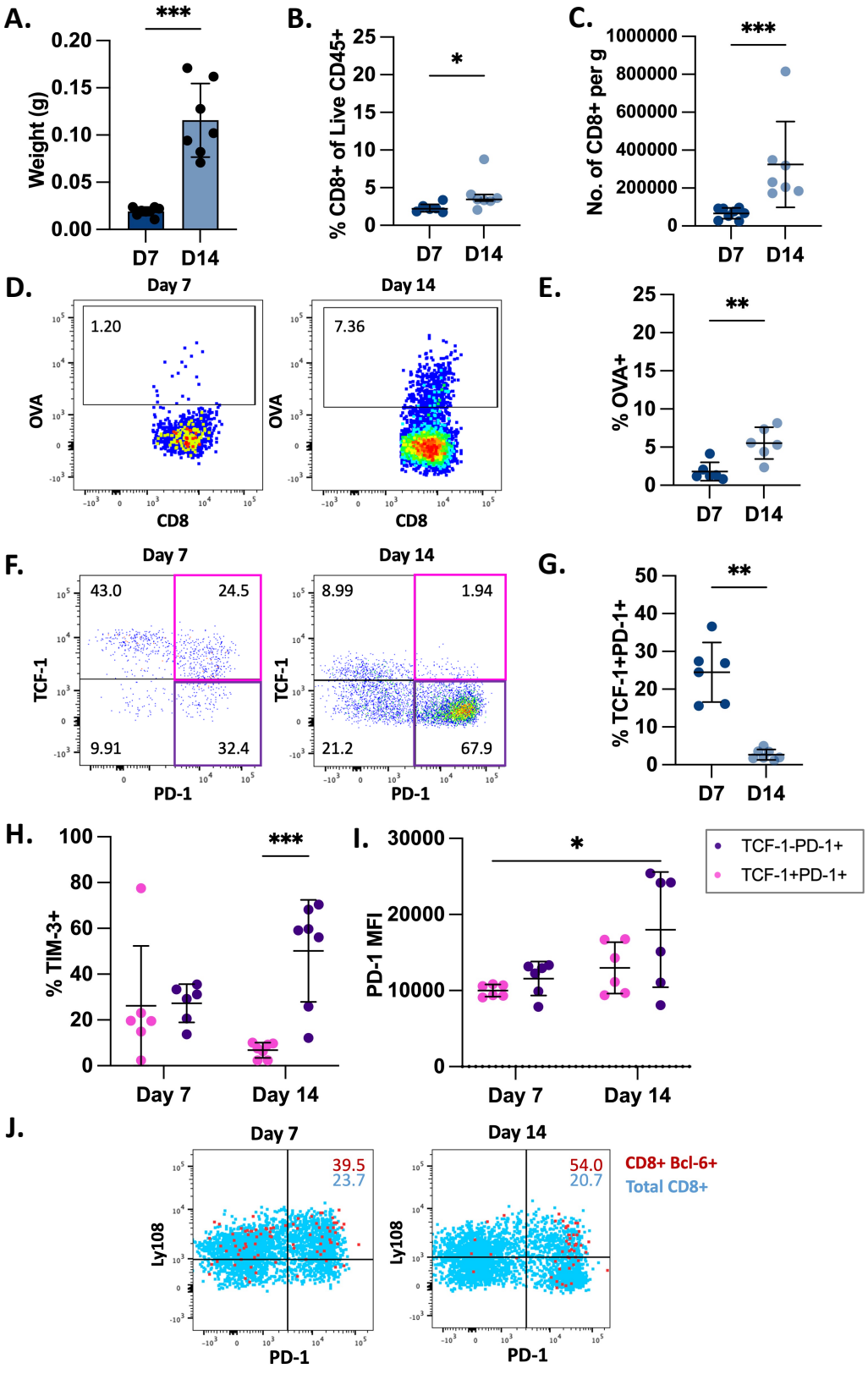

A.
***
Weight (g)
0.20
0.15
0.10
0.05
0.00
D7
D14
B.
*
% CD8+ of Live CD45+
25
20
15
10
5
0
D7
D14
C.
***
No. of CD8+ per g
1000000
800000
600000
400000
200000
0
D7
D14
D.
Day 7
1.20
OVA
CD8
Day 14
7.36
OVA
CD8
E.
**
% OVA+
25
20
15
10
5
0
D7
D14
F.
Day 7
43.0
24.5
9.91
32.4
TCF-1
PD-1
Day 14
8.99
1.94
21.2
67.9
TCF-1
PD-1
G.
**
% TCF-1+PD-1+
50
40
30
20
10
0
D7
D14
H.
***
% TIM-3+
100
80
60
40
20
0
Day 7
Day 14
I.
*
PD-1 MFI
30000
20000
10000
0
Day 7
Day 14
TCF-1-PD-1+
TCF-1+PD-1+
J.
Day 7
39.5
23.7
Ly108
PD-1
Day 14
54.0
20.7
Ly108
PD-1
CD8+ Bcl-6+
Total CD8+

Figure 3.12. Determining the expansion of the OVA+ antigen-specific CD8 population.
C57BL/6 Kaede and Bcl-6 reporter mice (6-10 weeks) were injected with 2.5 x10^5 MC38-OVA cells subcutaneously. All MC38-OVA data, in both Kaede mice and Bcl-6 mice, shown are from two independent experiments. All graphs show the mean ±SD. In the case of two-way analysis statistical significance was determined using an unpaired *t* test, in the case of grouped data a two-way ANOVA , 4 family comparison, Fisher's LSD test was used. ** = $p < 0.05$, ** = $p < 0.01$, *** = $p< 0.001$.*

A. The weight (g) of MC38-OVA tumours measured at day 7 and day 14 post-injection.
B. The percentage of live CD45+ cells that are CD8+ in MC38-OVA tumours day 7 versus day 14 post-injection.
C. The number of CD8+ cells per gram of tumour in MC38-OVA tumours day 7 versus day 14 post-injection.
D. Flow cytometry plots demonstrating OVA tetramer staining among the intratumoural CD8+ T cell population at day 7 (left) and day 14 (right) post-injection in representative MC38-OVA subcutaneous tumours.
E. The percentage of CD8+ T cells that are OVA+ at day 7 and day 14 post injection in MC38-OVA tumours.
F. Flow cytometry plots demonstrating TCF-1 and PD-1 staining in MC38-OVA tumours at day 7 (left) and day 14 (right) post injection. The TCF-1+ PD-1+ is highlighted in pink, and TCF-1- PD-1+ in purple.
G. The percentage of CD8+ cells that are TCF-1+ PD-1+ at day 7 and day 14 after injection.
H. The percentage of TIM-3+ cells in the intratumoural TCF-1+ PD-1+ and TCF-1- PD-1+ populations at day 7 and day 14 after injection.
I. The MFI of PD-1 in the intratumoural TCF-1+ PD-1+ and TCF-1- PD-1+ populations at day 7 and day 14 after injection.
J. Flow cytometry plots demonstrating Ly108 and PD-1 expression in the Bcl-6+ CD8 population (in red) and the total CD8 population (blue) at day 7 (left) and day 14 (right) after injection of 2.5x10^5 MC38-OVA cells subcutaneously into bcl-6 reporter mice.

7 and 14 there was a clear upregulation of PD-1 expression by these cells (Fig. 3.12J). In summary, a comparison of the TCF-1+ PD-1+ cells present in the tumour at day 7 and day 14 indicated phenotypic differences and suggested that this compartment changes as the tumour develops.

3.2.4. Investigating the phenotype of CD8 T cells as they enter the tumour

Photoconversion of the tumour enables newly entering CD8 T cells to be characterised and thus how cells change over time in the tumour investigated. Our comparison of Kaede green and Kaede red CD8 T cells at 24 hours post-photoconversion had highlighted significant differences in the phenotype of cells including reduced expression of PD-1 and TOX. To refine our analysis of recent tumour immigrants and specifically ask whether any cells with a stem-like phenotype were evident amongst cells that had only very recently entered the tissue, we characterised the intratumoural CD8 T cell compartment at 5 hours post-photoconversion. At this time point only a small fraction (<5%) of the CD8 T cells were Kaede green+ (Fig. 3.13A-C). Consistent with the 24-hour analysis, the majority of these cells were TCF-1-, TOX-, CD62L- and CD69-, and levels of both PD-1 and NKG2A were significantly lower on Kaede green cells than Kaede red cells (Fig. 3.13D & Appendix 3.9). Given the lower level of PD-1 expression by Kaede green cells, it was not surprising that analysing the co-expression of TCF-1 and PD-1 revealed that the TCF-1+ PD-1hi stem-like population amongst the Kaede red cells was lacking in the Kaede green compartment (Fig.3.13E-F). However, a small population of TCF-1+ PD-1-/lo cells were evident amongst the Kaede green population and comparable in frequency to the Kaede red TCF-1+ PD-1+ cells (Fig. 3.13E-); this TCF-1+ PD-1+ population on entry expresses not only lower levels of

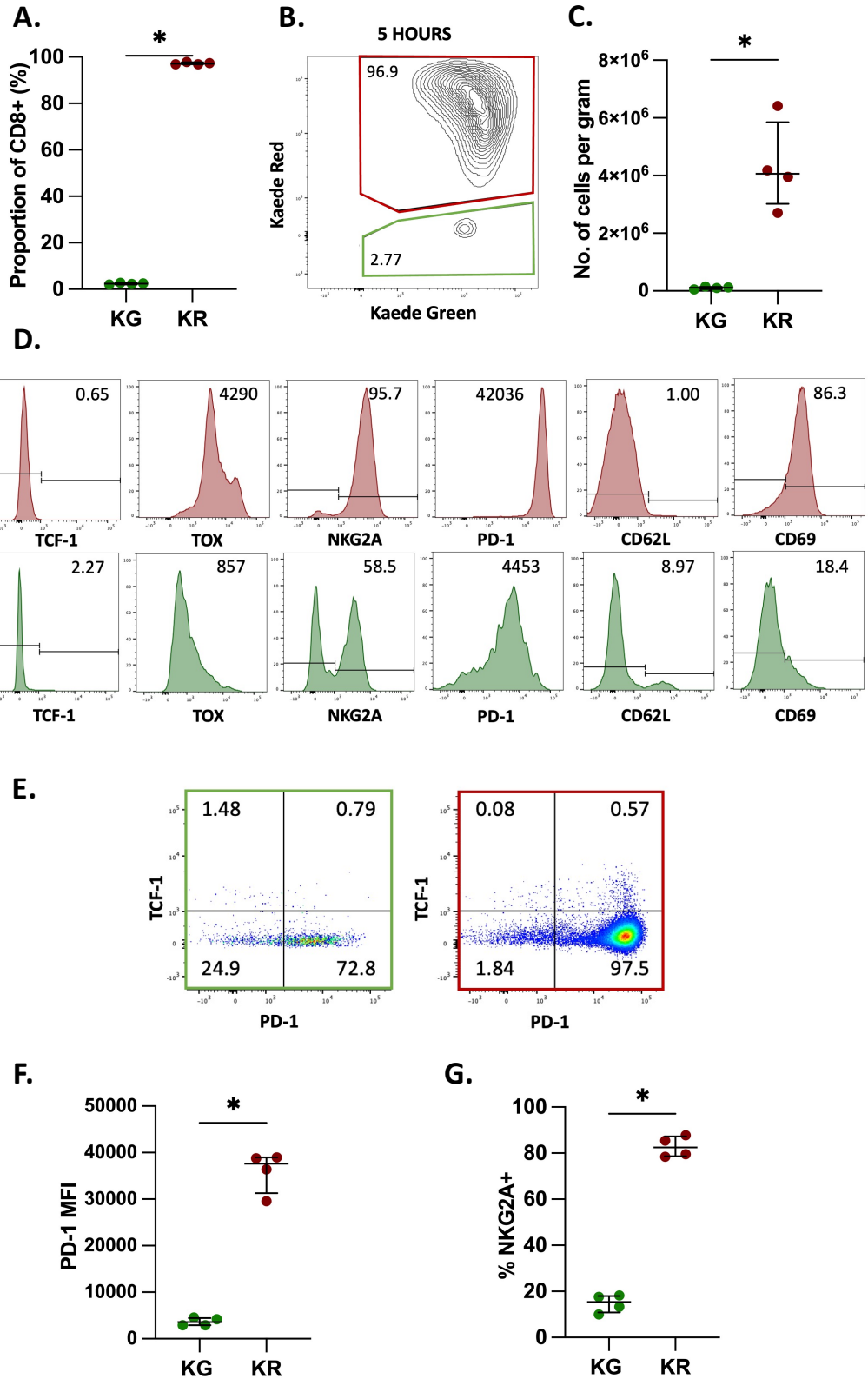

A.
Proportion of CD8+ (%)
100
80
60
40
20
0
*
KG
KR
B.
5 HOURS
96.9
2.77
Kaede Red
Kaede Green
C.
No. of cells per gram
8×10^6
6×10^6
4×10^6
2×10^6
0
*
KG
KR
D.
0.65
4290
95.7
42036
1.00
86.3
TCF-1
TOX
NKG2A
PD-1
CD62L
CD69
2.27
857
58.5
4453
8.97
18.4
TCF-1
TOX
NKG2A
PD-1
CD62L
CD69
E.
1.48
0.79
24.9
72.8
TCF-1
PD-1
0.08
0.57
1.84
97.5
TCF-1
PD-1
F.
PD-1 MFI
50000
40000
30000
20000
10000
0
*
KG
KR
G.
% NKG2A+
100
80
60
40
20
0
*
KG
KR

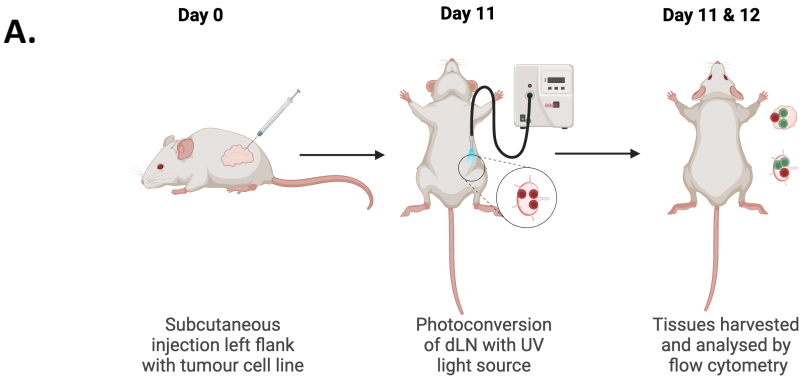
Figure 3.13. Phenotype of CD8 T cells entering the tumour within 5 hours of photoconversion.

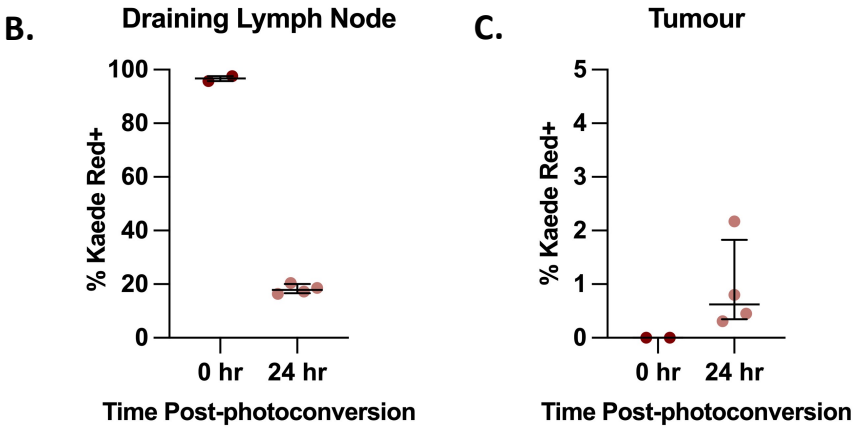
BALB/c Kaede mice (6-9 weeks) were injected with 2.5 x10^5 CT26 cells subcutaneously. Photoconversion of the subcutaneous tumour occurred on day 11, and tissue collection 5 hours following the procedure. All CT26 data shown are from two independent experiments. All graphs show the median value and IQR. Statistical significance was determined using a Mann-Whitney test. ** = $p < 0.05$.*

A. The proportion of CD8+ cells that are Kaede green+ and Kaede red+ in CT26 tumours 5 hours following photoconversion.
B. Flow cytometry plot demonstrating Kaede expression in the CD8 T cell compartment of a representative CT26 s.c. tumour harvested 5 hours following photoconversion.
C. The number of Kaede red and Kaede green CD8+ cells per gram in CT26 s.c. tumours 5 hours following photoconversion.
D. Histograms demonstrating the expression of TCF-1, TOX, NKG2A, PD-1, CD62L and CD69 in Kaede red+ CD8+ cells (top row) and Kaede green+ CD8+ cells (bottom row) 5 hours after photoconversion.
E. Flow cytometry plots demonstrating TCF-1 and PD-1 expression in the Kaede green (left plot) and Kaede red (right plot) CD8 populations 5 hours following photoconversion.
F. The MFI of PD-1 in KG+ and KR+ TCF-1+ PD-1+ CD8 T cells 5 hours after photoconversion.
G. The percentage of NKG2A+ cells in the KG+ and KR+ TCF-1+PD-1+ CD8 populations 5 hours after photoconversion.

PD-1 but also most were NKG2A- (Fig. 3.13F-G). Collectively, our data indicate that the stem-like TCF-1+ PD-1+ population of tumours is continuously seeded by new cells entering the tumour, and these cells have phenotypic differences including a lower level of inhibitory receptor expression.

Photoconversion of the tumour enables identification of cells entering after labelling, but does not identify the source of these cells, for example whether they come from the blood, the dLN (via the blood) or from reservoirs of responding T cells in peripheral lymphoid tissues. To specifically ask whether the cells entering the tumour were recently present within the dLN, we used photoconversion of this tissue, adapting approaches previously used to label LNs.(298) The tumour draining inguinal LN was transcutaneously photoconverted at day 11 post-injection of CT26 cell line into the left flank, both the tumour and photoconverted LN were then either collected at 0- or 24 hours following labelling (Fig. 3.14A). Lymph nodes were successfully photoconverted without labelling of the subcutaneous tumour, at 0 hours all CD8 T cells in labelled LNs were Kaede red+ and no intratumoural CD8 T cells were Kaede red+ (Fig. 3.14B-D). Due to anatomical variation between animals, and distortion of normal anatomy due to the presence of a tumour, labelling of the inguinal LN was technically difficult and only about 20-30% of attempts were successful in terms of fully labelling the LN. When samples were taken at 24 hours post-labelling of the dLN, only mice in which the dLN contained a distinct Kaede red+ compartment (typically 15-20% of the total CD8 T cells) were considered as fully labelled. In these mice, the tumour consistently contained a very small, but distinct population of Kaede red+ CD8 T cells (Fig. 3.14D). Given that only partial dLN labelling was achieved in


A.
Day 0
Day 11
Day 11 & 12
Subcutaneous injection left flank with tumour cell line
Photoconversion of dLN with UV light source
Tissues harvested and analysed by flow cytometry


B.
Draining Lymph Node
% Kaede Red+
100
80
60
40
20
0
0 hr
24 hr
Time Post-photoconversion
C.
Tumour
% Kaede Red+
5
4
3
2
1
0
0 hr
24 hr
Time Post-photoconversion

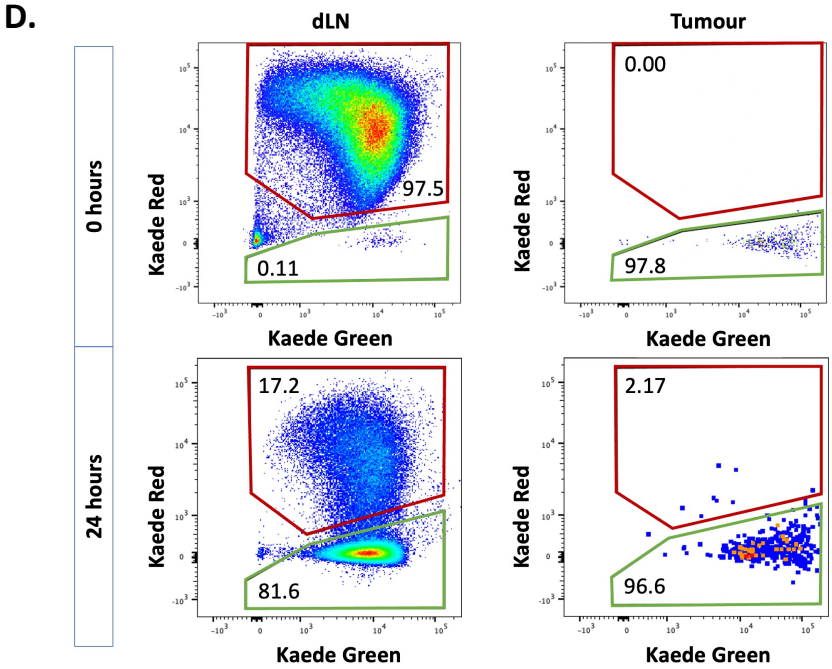

D.
dLN
Tumour
0 hours
24 hours
Kaede Red
Kaede Green
97.5
0.11
0.00
97.8
17.2
81.6
2.17
96.6

Figure 3.14. Photoconversion of the tumour draining lymph node allows tracking of CD8 T cells migrating into the tumour.

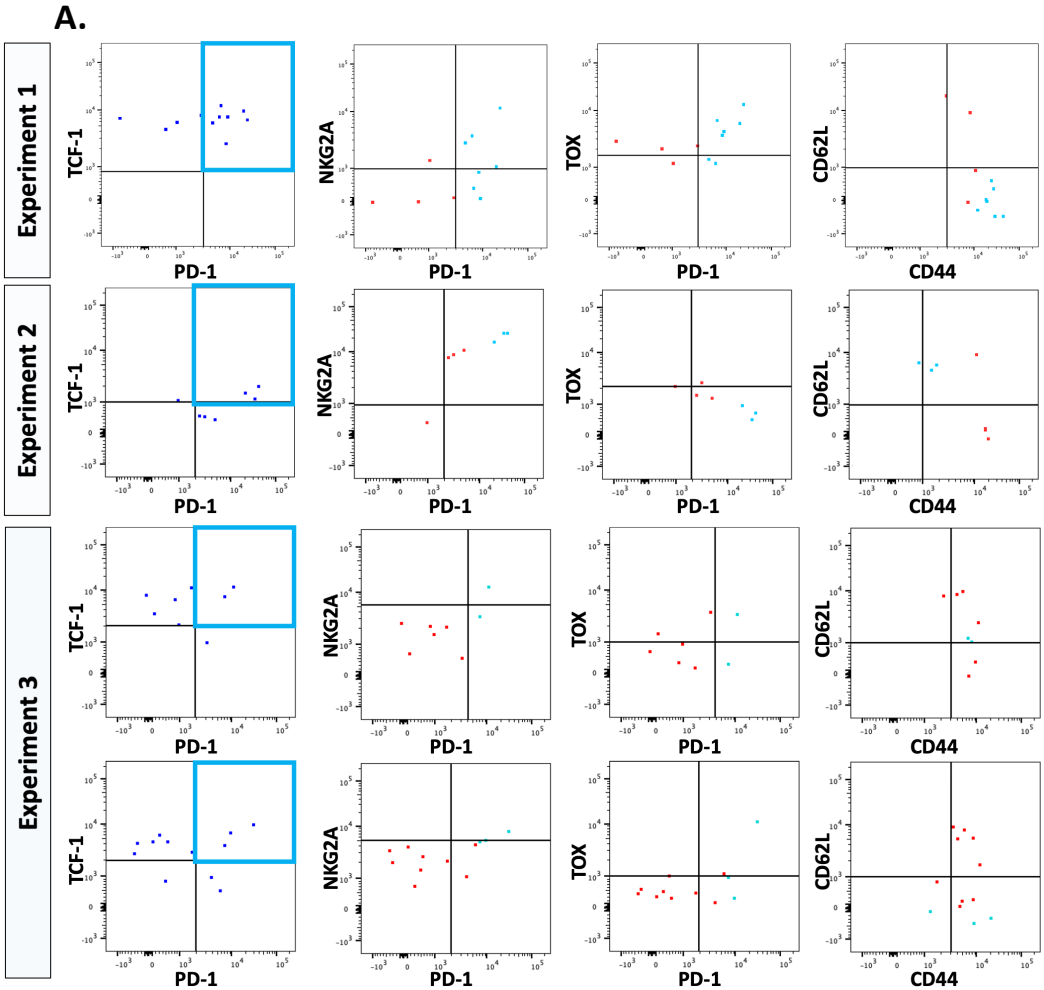
BALB/c Kaede mice (6-9 weeks) were injected with 2.5 x10^5 CT26 cells subcutaneously. Photoconversion of the tumour dLN (inguinal) occurred on day 11, and tissue collection 24 hours following the procedure. All CT26 data shown are from three independent experiments. All graphs show the median value and IQR.

A. Illustration showing the set-up of tumour dLN photoconversion experiments. Created using Biorender.com.
B. The percentage of CD8 T cells in the dLN that are Kaede red+ 0 hrs and 24 hrs following photoconversion of the dLN.
C. The percentage of CD8 T cells in the subcutaneous tumour that are Kaede red+ at 0 hrs and 24 hrs following photoconversion of the dLN.
D. Flow cytometry plots demonstrating Kaede labelling in the dLN (left), and tumour (right), 0hrs (top row) and 24hrs (bottom row) after UV labelling of the tumour dLN.

most mice and this potentially undermined detection of cells trafficking to the tumour, we performed three separate experiments where dLN labelling was attempted. Fig. 3.15A shows analysis of the Kaede red+ CD8 T cells in the tumour of different mice where we were confident that the dLN was robustly labelled. Strikingly, while the number of Kaede red+ CD8 T cells detected in the tumour was consistently very low, TCF-1+ PD-1+ CD8 T cells were always detected (Fig. 3.15A-B). These data suggest that amongst the few CD8 T cells that traffic from the dLN to the tumour within a 24-hour time frame, cells resembling stem-like CD8 T cells are consistently present. Furthermore, these data highlight that most of the newly entering CD8 T cells within the tumour have not left the dLN within 24 hours. Rather, these data suggest that T cells emigrating the dLN spend a period of time, that likely comprises several days, within the periphery before successfully trafficking to the tumour. Why this occurs and what this means for the anti-tumour T cell response requires further investigation.

3.2.5. Examining the composition of CD8 T cells that egress the tumour

So far, our data has highlighted that TCF-1+ PD-1+ stem-like CD8 T cells are present within the tumour and likely retained here, although there appears to be continuous seeding of this population with new cells that show modest phenotypic differences such as reduced PD-1 expression. These data are consistent with a reservoir of cells in the dLN that replenishes the CD8 T cell compartment of the tumour.(106) To understand whether the entry of new stem-like CD8 T cells into the tumour was balanced by the egress of this population, we sought to investigate what CD8 T cells, if any, leave the tumour. Therefore, subcutaneous tumours were labelled 48 hours prior to collection of dLNs. Single cell RNA-


A.
Experiment 1
Experiment 2
Experiment 3
TCF-1
NKG2A
TOX
CD62L
PD-1
CD44

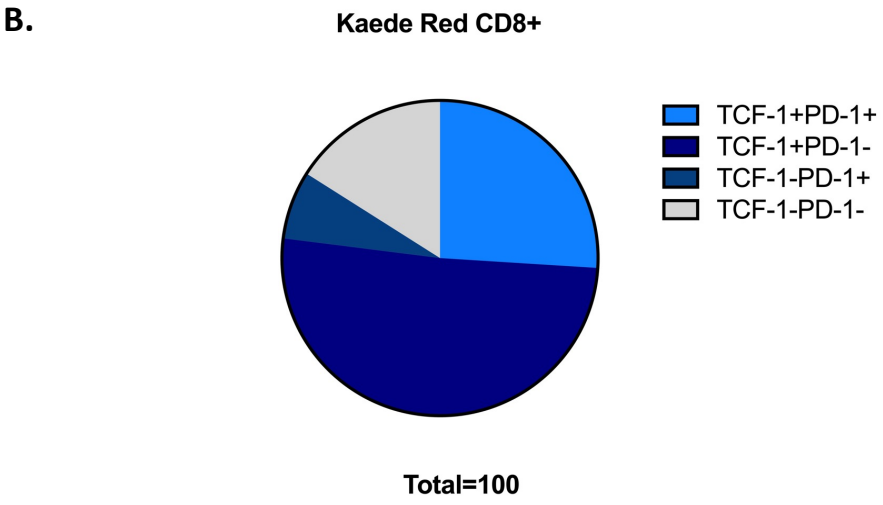

B.
Kaede Red CD8+
TCF-1+PD-1+
TCF-1+PD-1-
TCF-1-PD-1+
TCF-1-PD-1-
Total=100

Figure 3.15. Characterisation of Kaede red+ CD8 T cells trafficking to the tumour within 24 hours of photoconversion of the draining lymph node.

BALB/c Kaede mice (6-9 weeks) were injected with 2.5 x10^5 CT26 cells subcutaneously. Photoconversion of the tumour dLN (inguinal) occurred on day 11, and tissue collection 24 hours following the procedure. All CT26 data shown are from three independent experiments.

A. Flow cytometry plots showing expression of TCF-1, PD-1, NKG2A, TOX, CD62L and CD44 in the Kaede red+ CD8 population found within the subcutaneous tumour following LN photoconversion. The left-hand column shows TCF-1+ PD-1+ CD8 T cells highlighted in blue. In subsequent flow plots (three left hand plots) TCF-1+ PD-1+ CD8 T cells are represented by blue dots in the plots.
B. Pie chart showing the proportion of Kaede red+ CD8 T cells that are TCF-1+ PD-1+ (light blue).

sequencing of Kaede red+ TILs isolated from the tumour dLN of MC38 tumours was used to unbiasedly characterise the labelled cells that had trafficked from the tumour. Five CD8 T cell clusters were identified within the Kaede red+ CD8 T cell compartment in tumour dLNs labelled CD8T_a to CD8T_e (Fig. 3.16A). Clusters a-c comprised the majority of the cells and expressed high levels of *Tcf7* and *Ccr7* (Fig. 3.16A-C). CD8T_d appeared to describe a more effector population, expressing *Gzma, Gzmb, Prf1* and *Ifng.*(Fig. 3.16A-C). CD8T_e was a small cluster of proliferating cells (Fig. 3.16A-C). Of note, CD8T_a was distinct from clusters CD8T_b and c by nature of high *Pdcd1*, *Tox* and *Cxcr6* expression in the absence of *Havcr2* and *Entpd1*, consistent with a stem-like CD8 T cell phenotype (Fig. 3.16A-C). Which CD8 T cell cluster in the tumour most resembled CD8T_a was modelled, and it was found that CD8T_a most resembled the CD8 T exh_prog/ stem-like cluster from the tumour (Fig. 3.16D-E). Thus, an unbiased analysis of the CD8 T cells egressing the tumour identified a clear population of stem-like CD8 T cells at the transcriptional level.

Having investigated the transcriptome of CD8 T cells egressing the tumour, we sought to validate these expression data at the protein level and identify stem-like CD8 T cells. Immune cells were isolated from the tumour dLN and stained, CD8 T cells were gated as Live/Dead^{TM}- CD45+ CD11b- CD3+ CD8+ cells (Fig. 3.17A). After identifying the CD8 T cell population in the dLN, Kaede red+ cells that had migrated from the tumour were selected (Fig. 3.17A), and the proportion and number quantified (Fig. 3.17B-C). In both MC38-OVA and CT26 tumour models Kaede red+ CD8 T cells could be identified in the tumour dLN, and both the number and proportion of Kaede red+ CD8 T cells increased between 24 and 72 hours (Fig. 3.17B-C). To confirm that the Kaede red labelling was not an artefact or by-

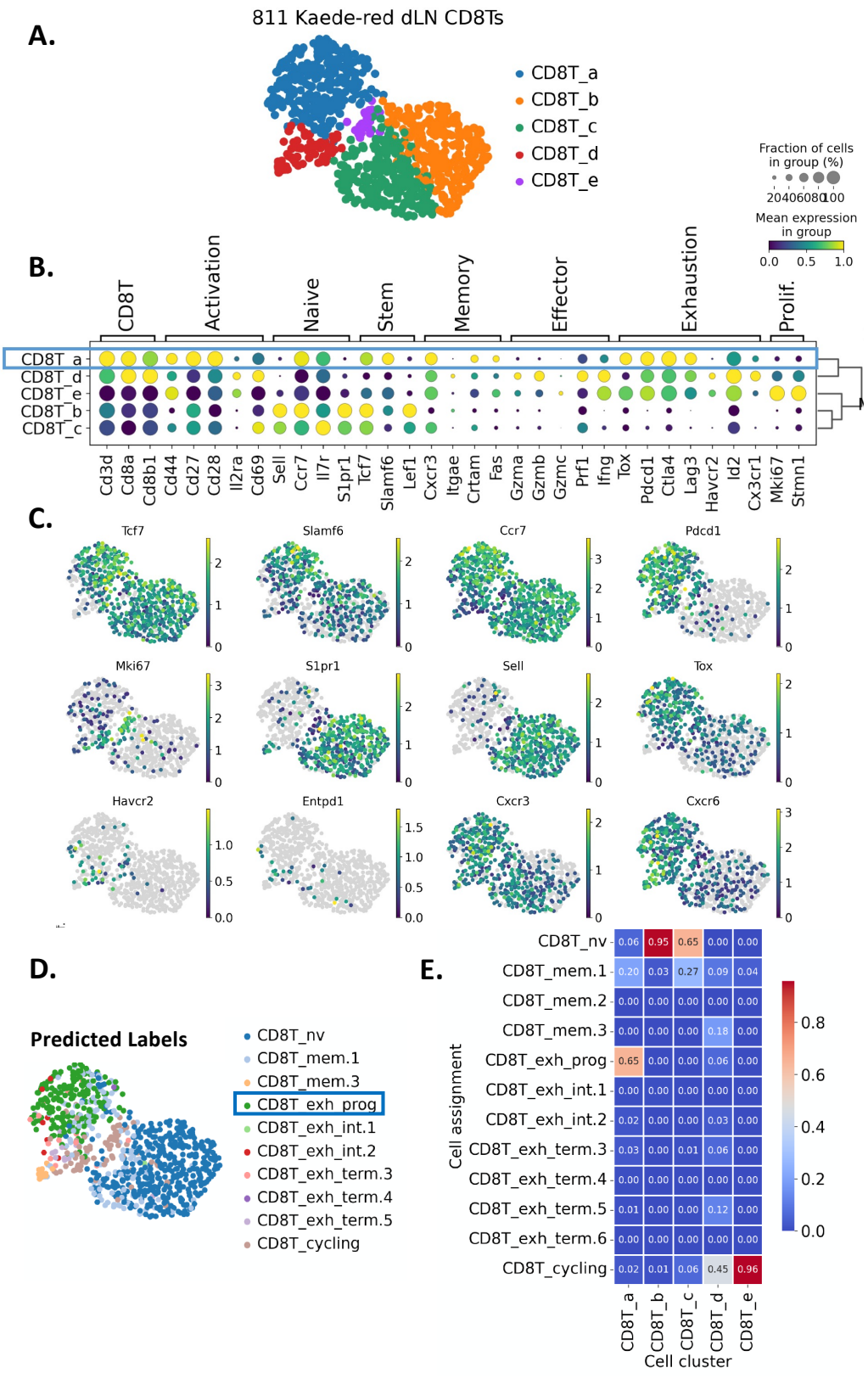
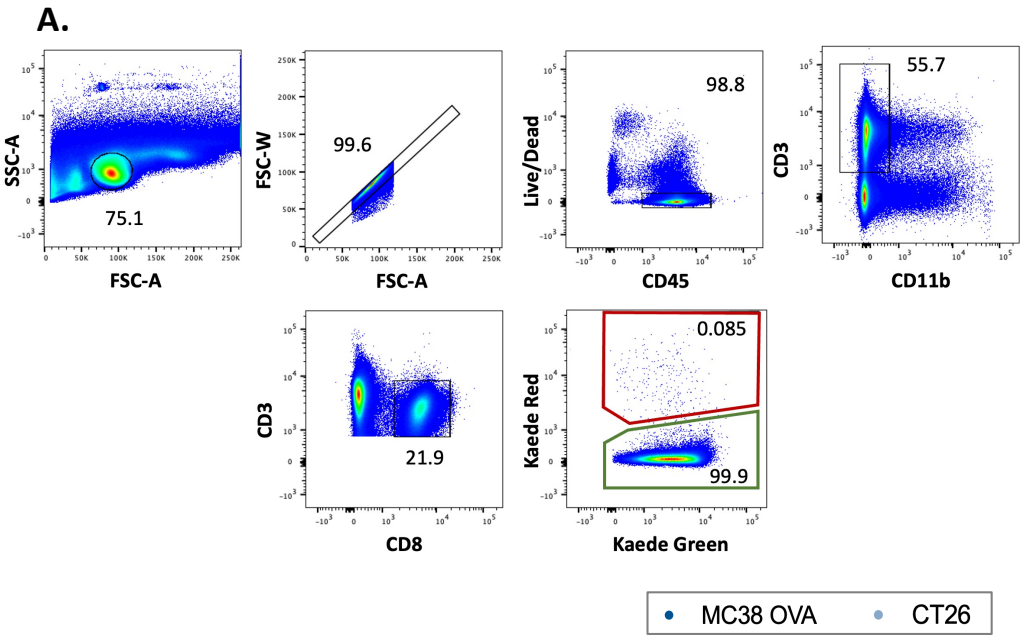

A.
811 Kaede-red dLN CD8Ts
CD8T_a
CD8T_b
CD8T_c
CD8T_d
CD8T_e
Fraction of cells in group (%)
Mean expression in group
B.
CD8T
Activation
Naive
Stem
Memory
Effector
Exhaustion
Prolif.
CD8T_a
CD8T_d
CD8T_e
CD8T_b
CD8T_c
Cd3d Cd8a Cd8b1 Cd44 Cd27 Cd28 Il2ra Cd69 Sell Ccr7 Il7r S1pr1 Tcf7 Slamf6 Lef1 Cxcr3 Itgae Crtam Fas Gzma Gzmb Gzmc Prf1 Ifng Tox Pdcd1 Ctla4 Lag3 Havcr2 Id2 Cx3cr1 Mki67 Stmn1
C.
Tcf7
Slamf6
Ccr7
Pdcd1
Mki67
S1pr1
Sell
Tox
Havcr2
Entpd1
Cxcr3
Cxcr6
D.
Predicted Labels
CD8T_nv
CD8T_mem.1
CD8T_mem.3
CD8T_exh_prog
CD8T_exh_int.1
CD8T_exh_int.2
CD8T_exh_term.3
CD8T_exh_term.4
CD8T_exh_term.5
CD8T_cycling
E.
CD8T_nv 0.06 0.95 0.65 0.00 0.00
CD8T_mem.1 0.20 0.03 0.27 0.09 0.04
CD8T_mem.2 0.00 0.00 0.00 0.00 0.00
CD8T_mem.3 0.00 0.00 0.00 0.18 0.00
CD8T_exh_prog 0.65 0.00 0.00 0.06 0.00
CD8T_exh_int.1 0.00 0.00 0.00 0.00 0.00
CD8T_exh_int.2 0.02 0.00 0.00 0.03 0.00
CD8T_exh_term.3 0.03 0.00 0.01 0.06 0.00
CD8T_exh_term.4 0.00 0.00 0.00 0.00 0.00
CD8T_exh_term.5 0.01 0.00 0.00 0.12 0.00
CD8T_exh_term.6 0.00 0.00 0.00 0.00 0.00
CD8T_cycling 0.02 0.01 0.06 0.45 0.96
Cell assignment
CD8T_a CD8T_b CD8T_c CD8T_d CD8T_e
Cell cluster

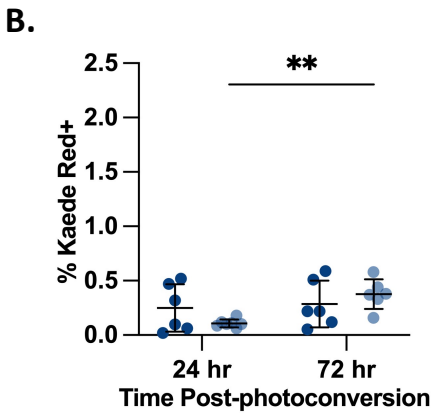
Figure 3.16. Identification of a stem-like population in Kaede Red+ CD8 T cells trafficking to the tumour draining lymph node on scRNA-seq.

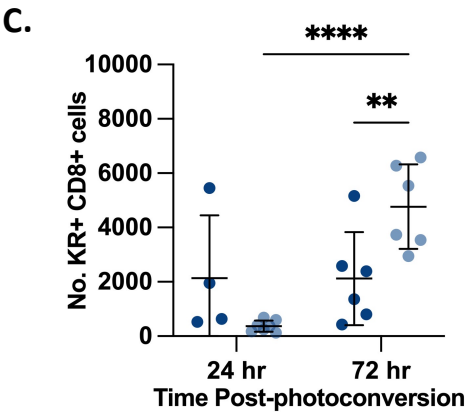
C57BL/6 Kaede mice (6-9 weeks) were injected with 2.5 x10^5 MC38-OVA cells subcutaneously, before photoconversion of the subcutaneous tumour on day 13. dLNs were collected 48 hours following photoconversion. Tissues were processed as per methods, before staining for CD45, CD11b, Ter119, Live/Dead. Cell suspensions were sorted using the FACS Aria II Cell Sorter (BD), sorted lymphocytes were further sorted into Kaede red+ and Kaede red-. scRNA sequencing of Kaede green+ and Kaede red+ lymphocyte population was carried out. For this work, scRNA-seq data from the CD8 population only is demonstrated.

A. UMAP of scRNA sequencing of Kaede red+ CD8 T cells isolated from the tumour-dLNs (from tumours in Fig 3.9). Clusters (coloured) were identified using unsupervised Leiden clustering.
B. Dot plot showing differentially expressed genes between clusters in the CD8 Kaede red+ population identified in MC38 tumour dLNs. Clusters (coloured) were identified using unsupervised Leiden clustering and annotated using canonical CD8 T cell subset marker gene expression. CD8T_a is highlighted.
C. UMAP demonstrating the expression of canonical gene markers between CD8 T cell clusters.
D. Predicted cell identities of dLN KR+ CD8 T cells corresponding to tumour CD8 T cells. A lasso and elastic-net regularised generalised linear model (glmnet) was fit to the tumour CD8 T cell single-cell gene expression matrices from Fig 3.9 using a multinomial regression, and the optimal regularisation parameter (lambda) was selected using a cross-validation approach (n = 100). The resulting model was applied to the gene expression matrices from Kaede-red dLN CD8 T cells (A) to obtain predicted cellular identities (coloured). CD8T_exh_prog are highlighted on the key.
E. Heatmap of multinomial classification results of Kaede-red dLN CD8 T cells. Colours and values correspond to the proportion of the dLN CD8 T cell cluster that was assigned a particular identity from the tumour CD8 T cell labels.


A.
SSC-A
FSC-A
75.1
FSC-W
FSC-A
99.6
Live/Dead
CD45
98.8
CD3
CD11b
55.7
CD3
CD8
21.9
Kaede Red
Kaede Green
0.085
99.9

MC38 OVA
CT26


B.
% Kaede Red+
2.5
2.0
1.5
1.0
0.5
0.0
**
24 hr
72 hr
Time Post-photoconversion


C.
No. KR+ CD8+ cells
10000
8000
6000
4000
2000
0
****
**
24 hr
72 hr
Time Post-photoconversion

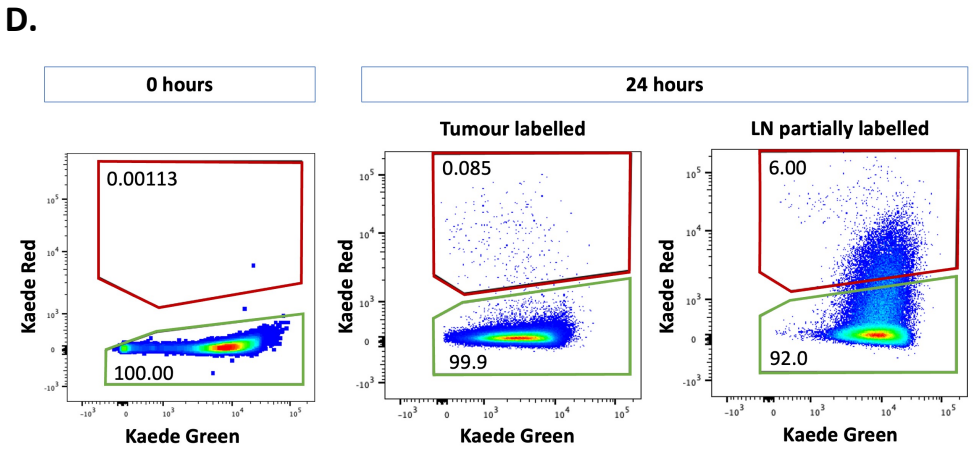

D.
0 hours
24 hours
Tumour labelled
LN partially labelled
Kaede Red
Kaede Green
0.00113
100.00
0.085
99.9
6.00
92.0

Figure 3.17. A population of Kaede Red+ CD8 T cells can be found in the draining lymph node following photoconversion of the subcutaneous tumour.

BALB/c Kaede and C57BL/6 mice (6-9 weeks) were injected with 2.5 x10^5 CT26 and MC38-OVA cells subcutaneously. Photoconversion of the subcutaneous tumour occurred on day 11, and tissue collection 24 and 72 hours following the procedure. All data shown are from two independent experiments. All graphs show the mean ±SD. Statistical significance was determined using a two-way ANOVA , 4 family comparison, Fisher's LSD test was used. ** = p < 0.05, ** = p < 0.01, *** = p< 0.001, **** = p< 0.0001.*

A. Flow cytometry plots showing the initial gating used to identify Kaede red+ CD8 T cells that have migrated to the dLN in a representative mouse.
B. The percentage of Kaede red+ cells in the CD8 population of the tumour dLN in MC38-OVA and CT26 tumours at 24 and 72 hours after photoconversion.
C. The number of Kaede red+ CD8 cells in the tumour dLN in MC38-OVA and CT26 tumours at 24 and 72 hours after photoconversion.
D. Flow cytometry plots demonstrating Kaede red labelling of CD8 T cells in the dLN, 0 hours (left hand side), and 24 hours (right two plots) after labelling. The 24-hour flow plots show examples of a LN in which Kaede red labelling is from CD8 T cells trafficking from a labelled tumour (middle panel), and artefactually labelled due to partial UV labelling of the LN at the time of photoconversion (right plot).

stander labelling, firstly LNs were taken immediately after photoconversion revealing no Kaede red+ CD8 T cells (Fig. 3.17D); in addition, LNs from tumours not covered with the plastic guard were taken to demonstrate how partially photoconverted LNs appear in comparison (Fig. 3.17D).

Analysis of the Kaede red+ CD8 T cells in the dLN indicated that approximately 15% of these were stem-like TCF-1+ PD-1+ cells at 24 hours post-photolabelling and this rose to nearly 30% by 72 hours (Fig. 3.18A-B). The Kaede red+ TCF-1+ PD-1+ CD8 T cells had higher expression of TOX, NKG2A, and CD69 than the total Kaede red CD8 population, consistent with a mix of cells egressing the tumour including TCF-1+ PD-1+ cells as indicated by the scRNA-seq (Fig. 3.18C-G). Comparison of Kaede red+ CD8 T cells in the dLN at 24- and 72-hours post-labelling revealed the upregulated expression of TOX, NKG2A and CD69, with reciprocal further loss of CD62L (Fig. 3.18C-G). This data might suggest that a proportion of migratory CD8 T cells, already committed to an exhausted trajectory, migrate as far as the dLN before becoming fully exhausted and resident within the dLN. In experiments using MC38-OVA tumours, we confirmed that antigen-specific CD8 T cells were present within the Kaede red+ CD8 population migrating to the dLN (Fig. 3.19A). The migratory antigen-specific population appeared different from the total Kaede red+ CD8 population found in the tumour dLN, as they showed lower expression of TCF-1 and CD62L, but higher TOX and PD-1 (Fig. 3.19A-F). Interestingly, over time the migratory antigen-specific CD8 population showed decreases in expression of TCF-1, TOX and CD62L, but increased CD69 and PD-1 (Fig. 3.19A-F). This antigen-specific CD8 T cell population was enriched for stem-like TCF-1+ PD-1+ cells (Fig. 3.19G-H). The total number of Kaede red+ stem-like CD8 T cells found

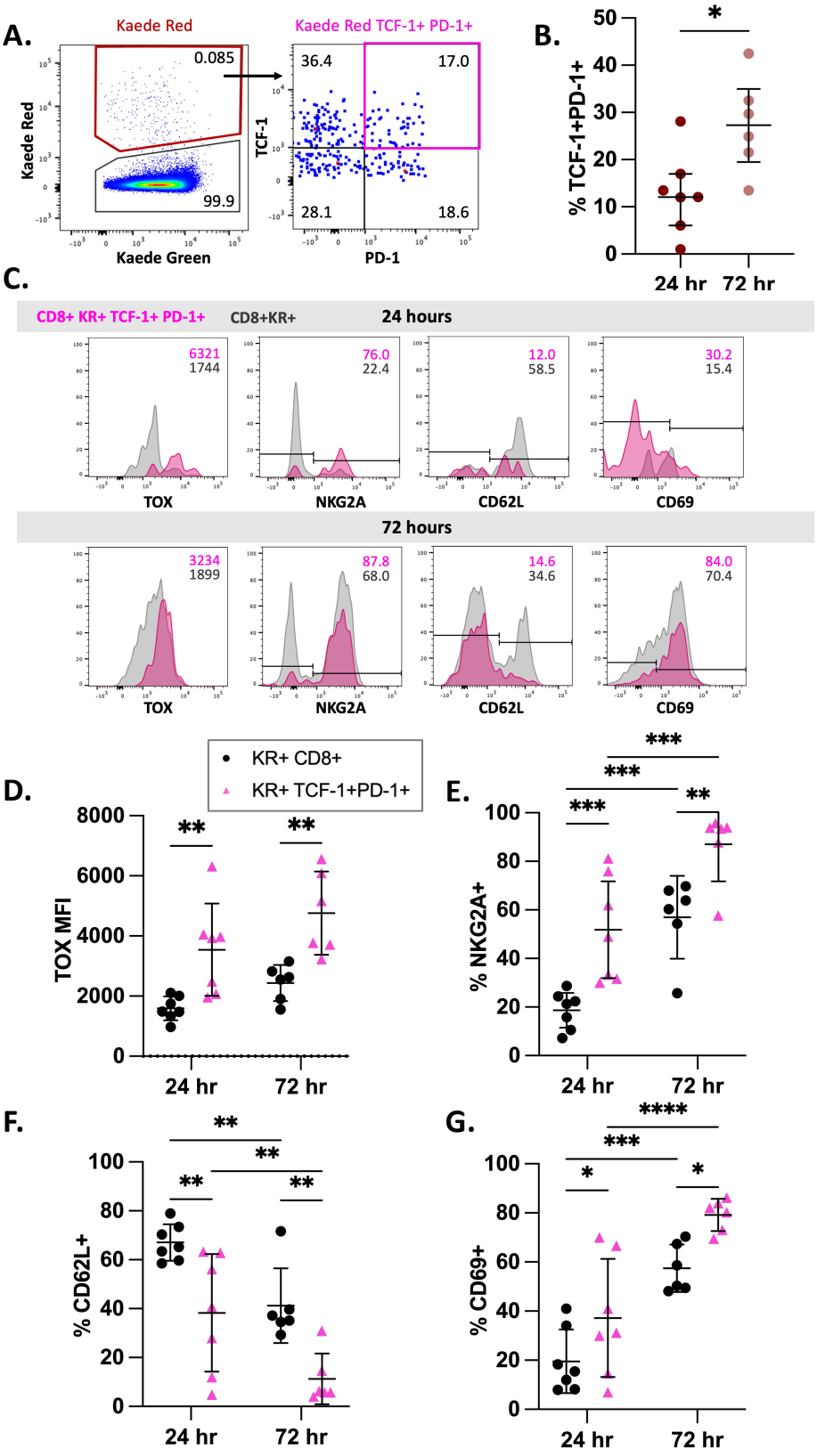

A.
Kaede Red
Kaede Red TCF-1+ PD-1+
0.085
99.9
36.4
17.0
28.1
18.6
Kaede Red
Kaede Green
TCF-1
PD-1
B.
% TCF-1+PD-1+
24 hr
72 hr
C.
CD8+ KR+ TCF-1+ PD-1+
CD8+KR+
24 hours
6321
1744
76.0
22.4
12.0
58.5
30.2
15.4
TOX
NKG2A
CD62L
CD69
72 hours
3234
1899
87.8
68.0
14.6
34.6
84.0
70.4
D.
KR+ CD8+
KR+ TCF-1+PD-1+
TOX MFI
E.
% NKG2A+
F.
% CD62L+
G.
% CD69+

Figure 3.18. Phenotyping the Kaede Red+ CD8 population trafficking to the draining lymph node in CT26 tumours.

BALB/c Kaede mice (6-9 weeks) were injected with 2.5 x10^5 CT26 cells subcutaneously. Photoconversion of the subcutaneous tumour occurred on day 11, and tissue collection 24 and 72 hours following the procedure. All CT26 data shown are from two independent experiments. All graphs show the mean ±SD. In the case of two column analysis statistical significance was determined using an unpaired *t* test, in the case of grouped data a two-way ANOVA , 4 family comparison, Fisher's LSD test was used. ** = p < 0.05, ** = p < 0.01, *** = p< 0.001, **** = p< 0.0001*

A. Flow cytometry plots demonstrating the gating of Kaede red (left) CD8 T cells, and the TCF-1+ PD-1+ (right) pre-gated on CD8+ KR+.
B. The percentage of TCF-1+ PD-1+ cells in the Kaede red+ CD8 population in the tumour dLN 24 and 72 hours following photoconversion of the tumour.
C. Histograms demonstrating the expression of TOX, NKG2A, CD62L and CD69 in the Kaede red+ CD8+ population (grey) and Kaede red+ TCF-1+ PD-1+ population (pink), 24 hrs (top row) and 72 hrs (bottom row) after photoconversion. A representative dLN at each time point was chosen. The y axis is normalised to the mode. Histograms were generated using FlowJo software.
D. The MFI of TOX in the KR+ CD8+ and TCF-1+ PD-1+ KR+ CD8+ populations in the dLN at 24 and 72 hours after photoconversion.
E. The percentage of NKG2A+ cells in the KR+ CD8+ and TCF-1+ PD-1+ KR+ CD8+ populations in the dLN at 24 and 72 hours after photoconversion.
F. The percentage of CD62L+ cells in the KR+ CD8+ and TCF-1+ PD-1+ KR+ CD8+ populations in the dLN at 24 and 72 hours after photoconversion.
G. The percentage of CD69+ cells in the KR+ CD8+ and TCF-1+ PD-1+ KR+ CD8+ populations in the dLN at 24 and 72 hours after photoconversion.

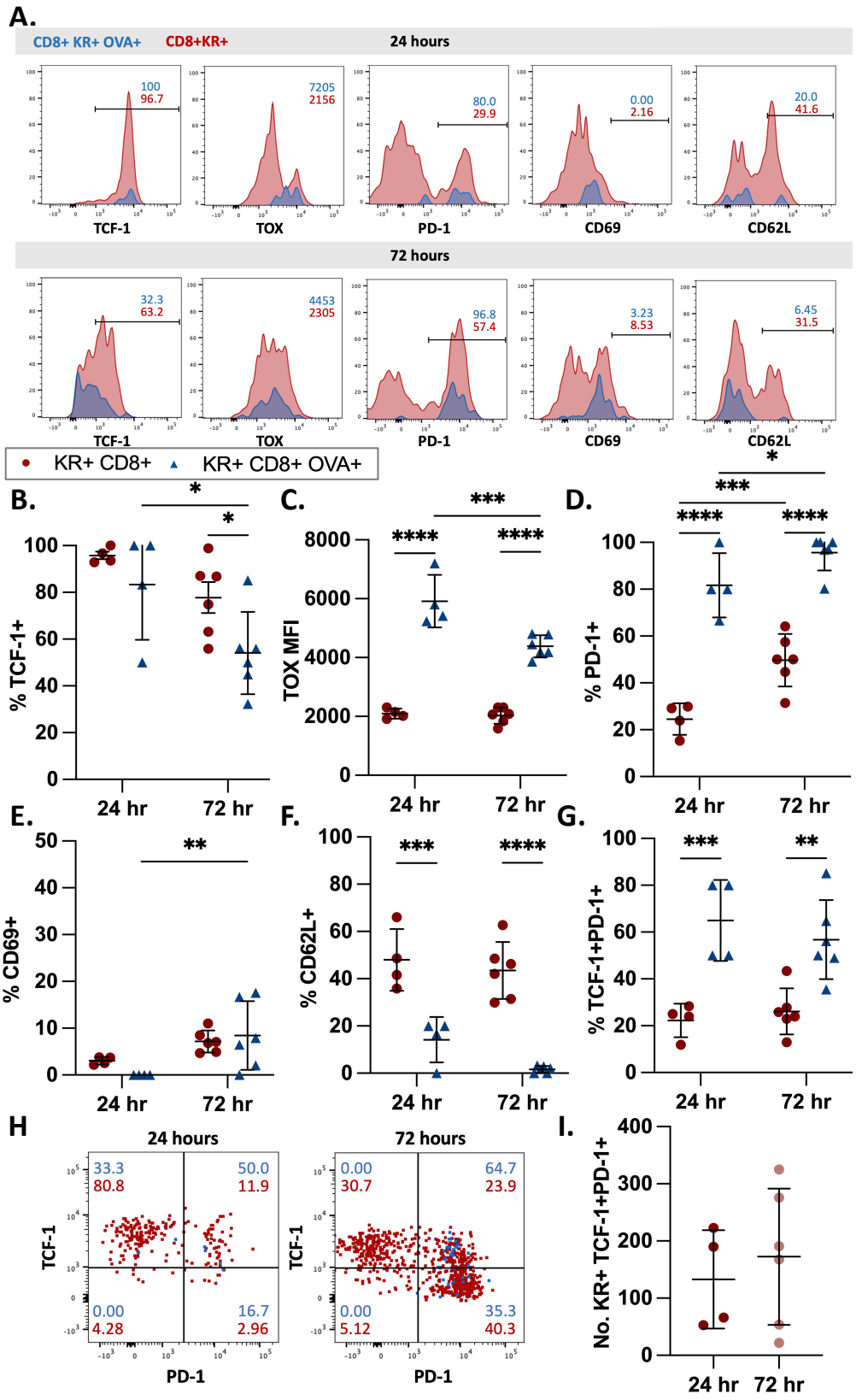

A.
CD8+ KR+ OVA+
CD8+KR+
24 hours
100
96.7
7205
2156
80.0
29.9
0.00
2.16
20.0
41.6
TCF-1
TOX
PD-1
CD69
CD62L
72 hours
32.3
63.2
4453
2305
96.8
57.4
3.23
8.53
6.45
31.5
KR+ CD8+
KR+ CD8+ OVA+
B.
% TCF-1+
C.
TOX MFI
D.
% PD-1+
E.
% CD69+
F.
% CD62L+
G.
% TCF-1+PD-1+
24 hr
72 hr
H
24 hours
72 hours
33.3
80.8
50.0
11.9
0.00
4.28
16.7
2.96
0.00
30.7
64.7
23.9
0.00
5.12
35.3
40.3
I.
No. KR+ TCF-1+PD-1+

Figure 3.19. Understanding antigen-specific CD8 T cell trafficking to the tumour draining lymph node in MC38 OVA tumours.

C57BL/6 Kaede mice (6-9 weeks) were injected with 2.5 x10^5 MC38-OVA cells subcutaneously. Photoconversion of the subcutaneous tumour occurred on day 11, and tissue collection 24 and 72 hours following the procedure. All MC38-OVA data shown are from two independent experiments. All graphs show the mean ±SD. In the case of two column analysis statistical significance was determined using an unpaired *t* test, in the case of grouped data a two-way ANOVA , 4 family comparison, Fisher's LSD test was used. ** = p < 0.05, ** = p < 0.01, *** = p< 0.001, **** = p< 0.0001*

A. Histograms demonstrating TCF-1, TOX, PD-1, CD69 and CD62L expression in the Kaede red+ CD8+ population (red) and Kaede red+ OVA+ population (blue), 24 hrs (top row) and 72 hrs (bottom row) after photoconversion. A representative MC38-OVA dLN at each time point is shown. The y axis is normalised to the mode.
B. The percentage of TCF-1+ cells in the KR+ CD8+ (red) and OVA+ KR+ CD8+ population (blue) in the dLN, 24 and 72 hours after photoconversion.
C. The MFI of TOX in the KR+ CD8+ (red) and OVA+ KR+ CD8+ population (blue) in the dLN, 24 and 72 hours after photoconversion.
D. The percentage of PD-1+ cells in the KR+ CD8+ (red) and OVA+ KR+ CD8+ population (blue) in the dLN, 24 and 72 hours after photoconversion.
E. The percentage of CD69+ cells in the KR+ CD8+ (red) and OVA+ KR+ CD8+ population (blue) in the dLN, 24 and 72 hours after photoconversion.
F. The percentage of CD62L+ cells in the KR+ CD8+ (red) and OVA+ KR+ CD8+ population (blue) in the dLN, 24 and 72 hours after photoconversion.
G. The percentage of TCF-1+ PD-1+ cells in the KR+ CD8+ population (red) and OVA+ KR+ CD8+ population (blue) in the dLN, 24 and 72 hours after photoconversion.
H. Flow cytometry plots demonstrating TCF-1 and PD-1 expression in the Kaede red+ CD8+ population (red) and OVA+ KR+ CD8+ population (overlayed in blue) in the dLN, 24 (left) and 72 (right) hours after photoconversion.
I. The number of Kaede red+ TCF-1+ PD-1+ cells within the tumour dLN 24 and 72 hours following photoconversion.

within the dLN did not significantly increase between the two timepoints; perhaps indicating their dissemination beyond, rather than accumulation in, the lymph node (Fig. 3.19I).

3.2.6. Examining the dissemination of stem-like CD8 T cells

The cellular basis to systemic protection from tumours and their metastatic spread remains incompletely understood. Exhausted T cells are impaired in their ability to generate long-lived memory populations.(135) Therefore, understanding the dissemination of tumour experienced T cells may provide new insight into how systemic memory compartments are established and ultimately inform of how protection from metastatic disease is coordinated. As a crude initial model of metastatic disease and to allow the extent of immune cell trafficking between tumours to be assessed, a dual flank tumour model using CRC cell lines was established. Animals were injected with the 2.5 $x10^5$ CT26 cells on each flank, at day 11 one tumour was then photoconverted but the other left unlabelled, and tissues collected 24 hours after (Fig. 3.20A). As before, near complete labelling of the T cell compartment of the photoconverted tumour was achieved (Fig. 3.20B, E). Analysis of peripheral tissues showed that there was no Kaede red+ contamination immediately following the photoconversion procedure (Fig. 3.20B). There was no difference in the weight or proportion of CD8 T cells of photoconverted tumours versus those that were not photolabelled (Fig. 3.20C-D). Analysis of peripheral tissues 24 hours after photoconversion of the subcutaneous tumour showed that it was possible to identify Kaede red+ CD8 T cells that had migrated from the tumour beyond the tumour dLN (Fig. 3.20F-G). Again, Kaede red+ TCF-1+ PD-1+ CD8 T cells were identified in the dLN, but also in the contralateral LNs

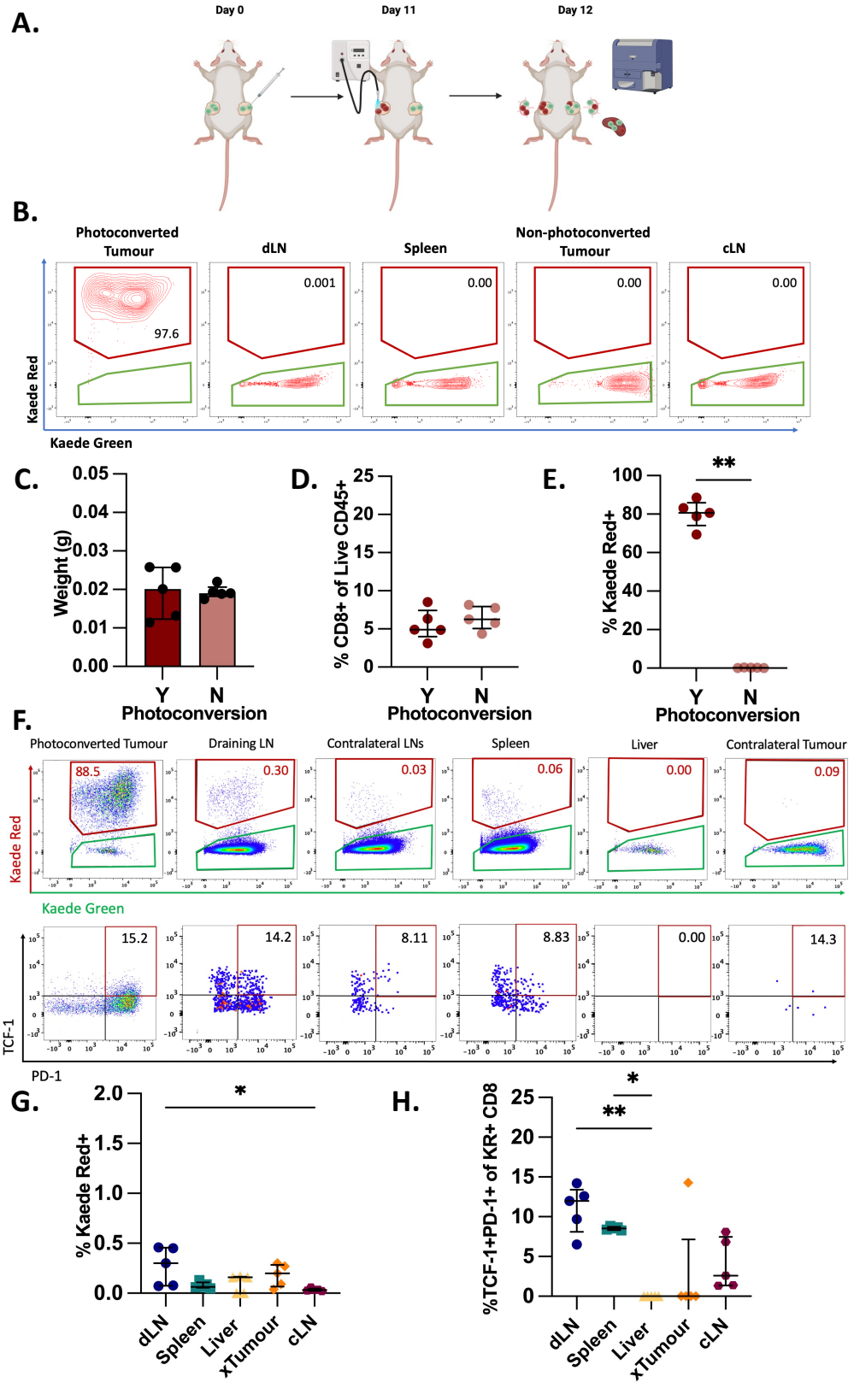

A.
Day 0
Day 11
Day 12
B.
Photoconverted Tumour
dLN
Spleen
Non-photoconverted Tumour
cLN
97.6
0.001
0.00
0.00
0.00
Kaede Red
Kaede Green
C.
Weight (g)
0.05
0.04
0.03
0.02
0.01
0.00
Y
N
Photoconversion
D.
% CD8+ of Live CD45+
25
20
15
10
5
0
Y
N
Photoconversion
E.
**
% Kaede Red+
100
80
60
40
20
0
Y
N
Photoconversion
F.
Photoconverted Tumour
Draining LN
Contralateral LNs
Spleen
Liver
Contralateral Tumour
88.5
0.30
0.03
0.06
0.00
0.09
Kaede Red
Kaede Green
15.2
14.2
8.11
8.83
0.00
14.3
TCF-1
PD-1
G.
*
% Kaede Red+
2.0
1.5
1.0
0.5
0.0
dLN
Spleen
Liver
xTumour
cLN
H.
*
**
%TCF-1+PD-1+ of KR+ CD8
25
20
15
10
5
0
dLN
Spleen
Liver
xTumour
cLN

Figure 3.20. Establishing a dual flank subcutaneous tumour model to understand the migration of CD8 T cells between tumours and peripheral lymphoid tissues –CT26.

BALB/c Kaede mice (6-9 weeks) were injected with 2.5 x10^5 CT26 cells subcutaneously into both left and right flanks. Photoconversion of one subcutaneous tumour occurred on day 11, and tissue collection 24 and 72 hours following the procedure. Spleen and liver samples in this experiment were CD8 enriched. All CT26 data shown are from two independent experiments. All graphs show the median value and IQR. In the case of two column analysis statistical significance was determined using a Mann-Whitney test, in the case of multiple comparisons statistical significance was determined with a Kruskal-Wallis multiple comparison test with post-hoc Dunn's correction. ** = $p < 0.05$, ** = $p < 0.01$.*

A. Illustration demonstrating the set-up of dual flank s.c. tumour photoconversion experiments. Created with Biorender.com.
B. Flow cytometry plots demonstrating Kaede red expression in the CD8 population in different tissues 0 hours following photoconversion. Plots are from one representative mouse implanted with L and R flank tumours, with the L flank tumour photoconverted.
C. The weight (g) of right and left flank tumours (unphotoconverted and photoconverted tumours) at the time of collection.
D. The percentage of live CD45+ cells that are CD8+, between right and left flank tumours (unphotoconverted and photoconverted tumours) at the time of collection.
E. The percentage of CD8 T cells that are Kaede red+, between right and left flank tumours (unphotoconverted and photoconverted tumours) at the time of collection.
F. Flow cytometry plots pre-gated on live CD45+ CD8+ population from different tissues. Top row demonstrates Kaede labelling in different tissues. Bottom row is pre-gated on KR+ CD8+ T cells and shows the TCF-1 PD-1 expression in different tissues, with the TCF-1+ PD-1+ population highlighted. The plots are from a representative animal 24 hours post-photoconversion.

G. The percentage of CD8 T cells in different tissues that are Kaede red+ 24 hours following photoconversion.
H. The percentage of KR+ CD8+ T cells in different tissues that are TCF-1+ PD-1+ 24 hours following photoconversion.

and spleen, consistent with their further dissemination beyond the dLN to become a circulatory population (Fig. 3.20F,H). Only a tiny fraction of the Kaede red+ CD8 cells were found to have disseminated to the contralateral tumour and no Kaede red+ T cells were observed in the liver (Fig. 3.20F-G).

We then repeated this dual flank model using MC38-OVA, rather than CT26, to support tracking of antigen-specific CD8 T cells. Photoconversion of MC38-OVA tumours did not influence the weight of tumours nor the proportion of total CD8 T cells, stem-like or OVA-specific CD8 T cells when compared to those tumours not photoconverted (Fig. 3.21A-D). Kaede red+ CD8 T cells were found in the dLN, spleen, contralateral tumour and contralateral LN including OVA-specific CD8 T cells (Fig. 3.21E-G). As in the CT26 dual flank model, a stem-like CD8 population represented a proportion of the Kaede red+ CD8 T cells found in the periphery (Fig. 3.21E,H). However, beyond the dLN OVA-specific stem-like CD8 T cells became undetectable, potentially due to their relatively low frequency and dissemination throughout the mouse (Fig. 3.21E,H).

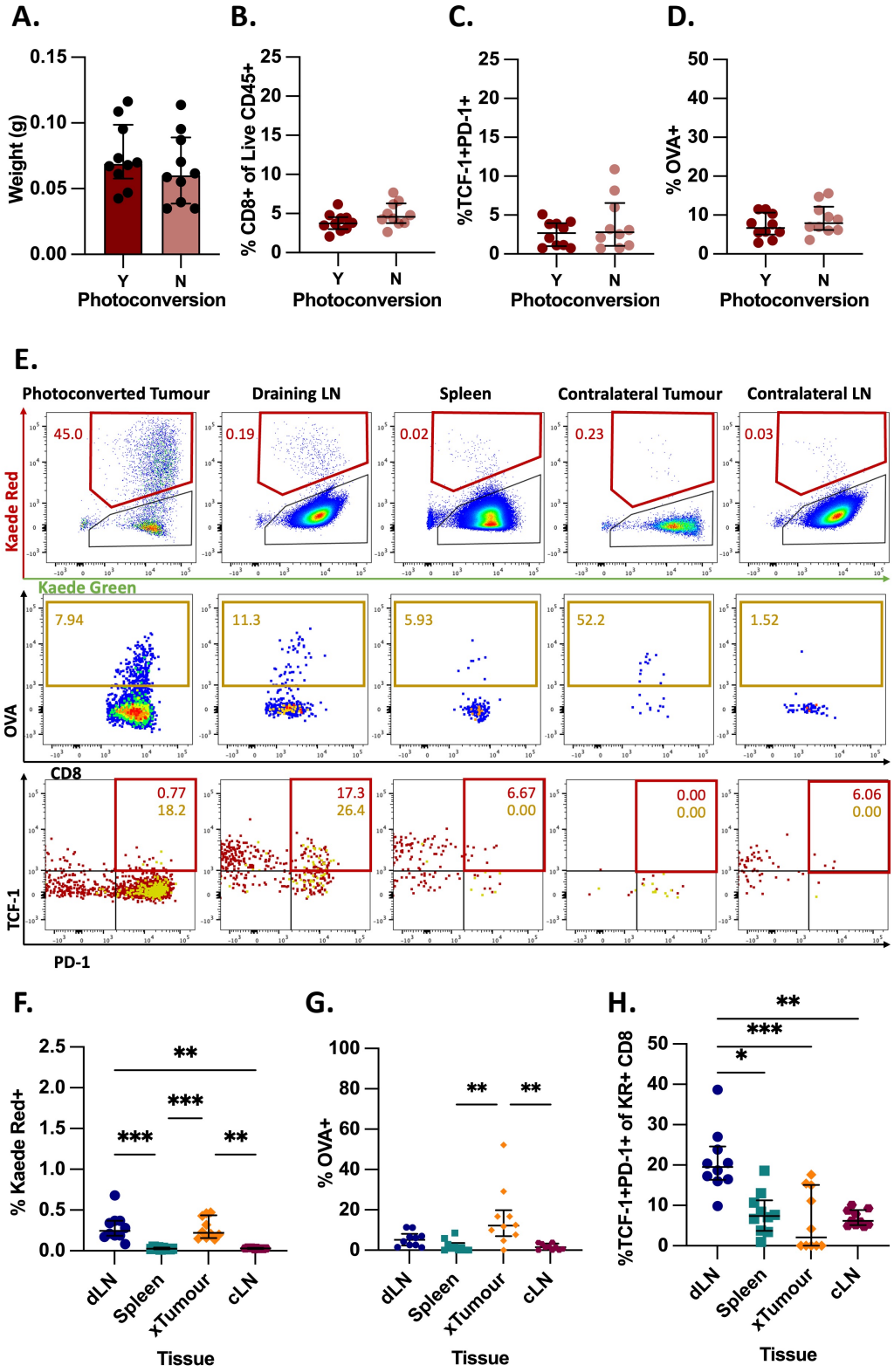

A.
B.
C.
D.
Weight (g)
% CD8+ of Live CD45+
%TCF-1+PD-1+
% OVA+
Y
N
Photoconversion
E.
Photoconverted Tumour
Draining LN
Spleen
Contralateral Tumour
Contralateral LN
Kaede Red
Kaede Green
OVA
CD8
TCF-1
PD-1
45.0
0.19
0.02
0.23
0.03
7.94
11.3
5.93
52.2
1.52
0.77
18.2
17.3
26.4
6.67
0.00
0.00
0.00
6.06
0.00
F.
G.
H.
% Kaede Red+
% OVA+
%TCF-1+PD-1+ of KR+ CD8
dLN
Spleen
xTumour
cLN
Tissue

Figure 3.21. Using the dual flank subcutaneous tumour model to understand the migration of antigen-specific CD8 T cells beyond the draining lymph node –MC38-OVA.
C57BL/6 Kaede mice (6-9 weeks) were injected with 2.5 x10^5 MC38-OVA cells subcutaneously into both left and right flanks. Photoconversion of one subcutaneous tumour occurred on day 11, and tissue collection 24 and 72 hours following the procedure. Tissues were processed according to methods, splenic samples in this experiments were CD8 enriched. All MC38-OVA data shown are from two independent experiments. All graphs show the median value and IQR. In the case of two column analysis statistical significance was determined using a Mann-Whitney test, in the case of multiple comparisons statistical significance was determined with a Kruskal-Wallis multiple comparison test with post-hoc Dunn's correction. ** = p < 0.05, ** = p < 0.01.*

A. The weight (g) of right and left flank tumours (unphotoconverted and photoconverted tumours) at the time of collection.
B. The percentage of live CD45+ cells that are CD8+, between right and left flank tumours (unphotoconverted and photoconverted tumours) at the time of collection.
C. The percentage of CD8+ cells that are TCF-1+ PD-1+, between right and left flank tumours (unphotoconverted and photoconverted tumours) at the time of collection.
D. The percentage of CD8+ cells that are OVA+, between right and left flank tumours (unphotoconverted and photoconverted tumours) at the time of collection.
E. Flow cytometry plots of the CD8 population from different tissues. Top row demonstrates Kaede labelling, with the Kaede red+ population highlighted. The middle row is pre-gated on KR+ CD8+ T cells and shows the OVA+ expression highlighted. The bottom row is pre-gated on KR+ CD8+ T cells and shows the TCF-1+ PD-1+ expression highlighted in, the OVA+ cells are shown overlayed as yellow dots. The plots are from a representative mouse 24 hours after photoconversion.
F. The percentage of CD8 T cells in different tissues that are Kaede red+ 24 hours following photoconversion.

G. The percentage of KR+ CD8 T cells in different tissues that are OVA+ 24 hours following photoconversion.
H. The percentage of KR+ CD8 T cells in different tissues that are TCF-1+ PD-1+ 24 hours following photoconversion.

3.3. Summary

Given the current lack of knowledge regarding precisely where stem-like CD8 T cells reside, whether these are truly tumour-resident populations and what T cells egress the tumour to seed the periphery, this chapter aimed to utilise the Kaede tumour labelling approach to track this immune subset *in vivo.* First, using two pre-clinical models of CRC (CT26 and MC38-OVA) we ensured that Kaede tumour labelling approaches were optimised, and established a way of identifying tumour-specific CD8 T cells. Once established, using both scRNA-seq and flow cytometry, we were able to define the intratumoural stem-like CD8 compartment in subcutaneous pre-clinical tumour models with the addition of temporal labelling. Following this, using flow cytometry to analyse the dissemination of Kaede red+ CD8 T cells from the tumour to the periphery, we were able to identify a TCF-1+ PD-1+ stem-like CD8 population among migratory cells. Finally, using a dual flank subcutaneous tumour model, the movement of CD8 T cells between tumours at anatomically distinct sites was examined.

3.3.1. Identifying changes in the intratumoural stem-like CD8 population over time

There is no single marker that defines the stem-like CD8 population, and there is variation within the current literature as to what combination of markers to use. Chronic viral infection models using LCMV in mice have been fundamental to informing the phenotyping of stem-like CD8 T cells, this stem-like population has been defined as being positive for TCF-1, Ly108, CD73, PD-1 alongside low levels of CD127, CD62L, and TIM-3.(149, 158, 300) scRNA sequencing of MC38 tumours performed in the lab revealed a clear stem-like

population among intratumoural CD8 T cells with a resolution beyond that of published studies.(286) This provided a key resource to then define the phenotype of this T cell compartment further. The most faithful marker of the stem-like CD8 population across both CRC models used in this work was co-expression of both TCF-1 and PD-1, with this population matching the expression profile of stem-like cells identified in our scRNA-seq. Robust expression of TOX, combined with a lack of CD39 and TIM-3 expression, are key parameters to define these cells. Using the Kaede model, differences in the phenotype of TCF-1+ PD-1+ cells newly entering the tumour could be discerned, with Kaede green cells expressing less TOX and PD-1, suggesting these are upregulated within the TME.

As a means of examining when this stem-like population truly becomes established within the tumour, the compartment was compared at day 7 and day 14. The TCF-1+ PD-1+ CD8 T cells at day 7 looked different to the mature phenotype seen at day 14, that more closely matched the description of stem-like cells in the literature. This could reflect the two-step activation process proposed by Prokhnevska *et al.*, in which antigen-specific stem-like CD8 T cells in the tumour dLN were activated, but only upon further co-stimulation and APC help within the tumour did this population mature into an anti-tumour effector CD8 phenotype.(106) Both phenotype and TCR overlap were used to link the stem-like population in the dLN with the intratumoural stem-like CD8 population that arose.(106) To investigate this seeding of the tumour with stem-like cells, we used a short photoconversion timepoint of just 5 hours to allow characterisation of populations first entering the tumour. In this population entering the tumour, there was a lack of a TCF-1+ PD-1hi population but instead a TCF-1+ PD-1lo population was observed, this population

was not negative for PD-1 and further hints at the two-step activation process described above. The upregulation of inhibitory receptors observed could reflect further signalling through the TCR which is likely to occur within tumour.

3.3.2. Investigating the migratory potential of stem-like CD8 T cells

Utilising our Kaede tumour photolabelling approach, the stem-like compartment within the tumour was shown to be predominantly resident, with the percentage of Kaede red+ stem-like CD8 T cells comparable to the exhausted compartment at 24 hours post-labelling. The low proportion of Kaede green+ cells suggests that there is not a large influx of new stem-like CD8 T cells into the tumour, most cells entering are likely effector cells (TCF-1-, PD-1 and CD62L low) that then become exhausted within the tumour. However, over time the proportion of Kaede green+ stem-like CD8 T cells increases, suggesting that there is new input from outside of the tumour. These data may support existing work in the field, suggesting that there is seeding of the tumour with stem-like cells from the dLN.(106, 292, 293)

To examine the hypothesis that stem-like CD8 T cells from the dLN seed the tumour, we used photolabelling of the dLN to probe whether this compartment was present in the Kaede red CD8 T cells trafficking back to the tumour within a 24-hour period. The most striking observation from these experiments was that only a few Kaede red+ T cells were detected within the tumour, despite the influx of Kaede green cells observed 24 hours after tumour photoconversion. These data clearly indicate that the majority of cells entering the tumour have not left the dLN in the last 24 hours. Rather, these cells have almost certainly

been present within the periphery for an as yet undetermined period of time. Despite the small fraction of Kaede red+ CD8 T cells that were found to have trafficked to the tumour in the 24-hour period, there was a consistent fraction of these cells that were TCF-1+ PD-1+. Hence, we were able to provide a more direct means of tracking the movement of the stem-like CD8 population from the dLN into the tumour, but there remain unanswered questions around the kinetics of this and where cells that egress the dLN reside before entering the tumour and for how long.

Finally, to answer the question of whether stem-like cells once within the tumour are capable of egress or stuck within the tumour to be retained as per exhausted populations, we traced the migration of Kaede red+ TCF-1+ PD-1+ cells from photoconverted tumours to the periphery. Single-cell RNA sequencing of Kaede red+ CD8 T cells in the dLN of photoconverted tumours provided an unbiased analysis of migratory T cells, and within this a cluster of CD8 T cells expressing all the hallmarks of TCF-1+ PD-1+ stem-like cells was identified. Transcriptomically, these resembled the stem-like population within the tumour. By flow cytometry, we were able to track Kaede red+ CD8 T cells in the periphery that had migrated from the tumour. Using multiple experimental approaches, the dissemination of stem-like CD8 T cells from the tumour to distal tissues is evident within our data, suggesting that perhaps a fraction of these cells retain their migratory capacity to form a population potentially capable of providing systemic protection (Fig. 3.22).

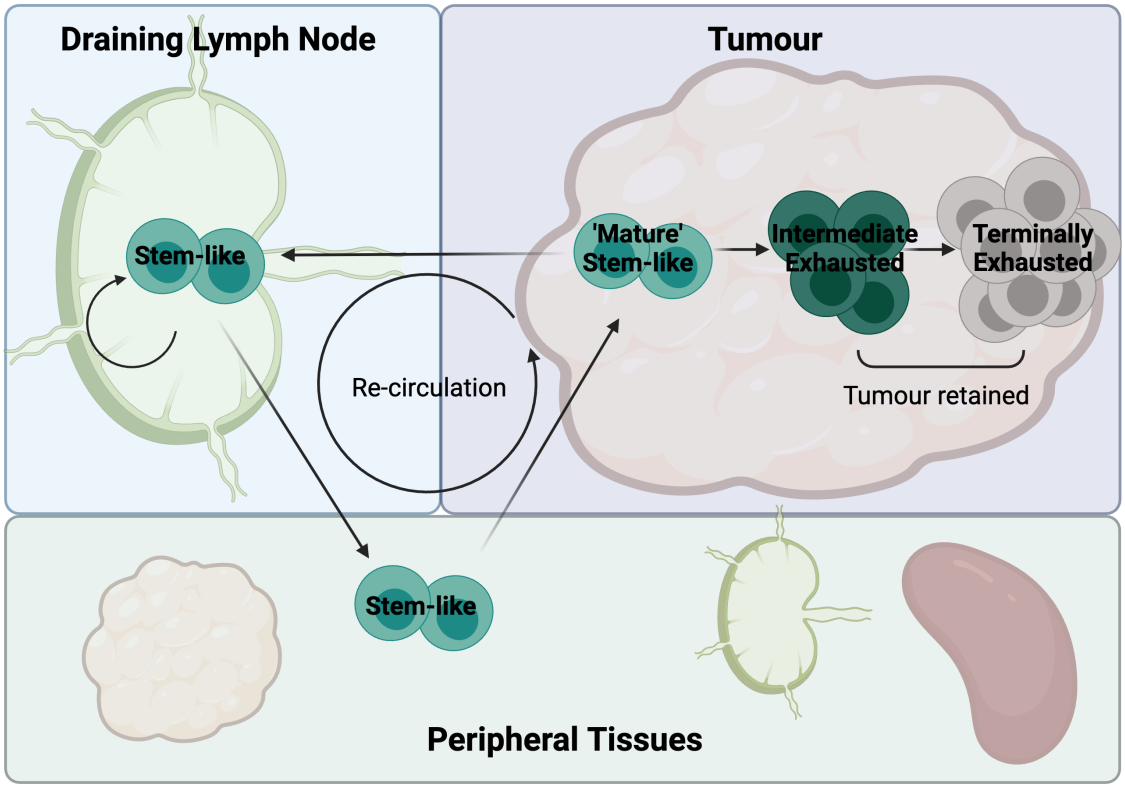


Figure 3.22. Illustration demonstrating the proposed establishment and migration of the stem-like CD8 compartment.

The findings of this thesis alongside previous work by Prokhnevska *et al.* support a model whereby tumour specific stem-like CD8 T cells are maintained within the dLN. This stem-like CD8 population is then able to migrate to the tumour and sustain the exhausted intratumoural CD8 compartment. According to work in this Chapter utilising the Kaede model, a population of these stem-like cells are capable of systemic dissemination from the tumour. Created using Biorender.com.

Chapter 4

Establishing Liver and Colon Orthotopic Tumour Models

4.1. Introduction

4.1.1. Limitations of pre-clinical tumour models

An essential step in the progression of new therapies in oncology is the use of pre-clinical models to demonstrate impact *in vivo*. Progress in the field of cancer immunology is dependent upon having the appropriate *in vivo* systems to robustly test research hypotheses. The study of tumour immunology using *in vivo* tumour models began with the injection of tumour cell lines subcutaneously in studies by Gross in 1943.(12) Subcutaneous tumour models still form the basis of most *in vivo* tumour work to the current day. This is largely because these models are technically easy to establish, highly reproducible and can be implanted into different host mice to assess mechanisms *in vivo*. Furthermore, tumour growth typically reaches clinical end points within weeks. This supports relatively quick *in vivo* experiments that can be appropriately powered and permit side-by-side testing of therapy combinations and controls. These models have underpinned many of the advances in cancer immunology made in the last 30 years including the development of the immunotherapies that have revolutionised how cancers are now treated. However, there are very clear limitations with these models, and it is increasingly apparent that their predictive role in the development of treatment combinations for particular cancer types is very limited. A major concern with these models is that the TME is 'underdeveloped' and essentially lacks key cellular components prevalent in human cancers, for example cancer associated fibroblasts (CAFs), a cell type that appears to strongly influence treatment efficacy.(50) Focusing on CAFs, it is apparent that this population plays an important role in regulating the anti-tumour response, and increasing CAFs has been shown to limit

sensitivity to ICB in the MC38 model.(50, 53) This strongly suggests that modelling anti-cancer immune responses in the absence of an appropriate TME and key suppressive mechanisms, will incorrectly identify appropriate treatments and represents a major limitation of conventional subcutaneous tumour cell line models.

Given that a wealth of cell lines are injected subcutaneously, regardless of their tissue of origin, the inadequate modelling of the TME raises the question of whether the site of cell line implantation matters. The intratumoural immune composition was found to be altered depending on whether syngeneic tumour cell lines 4T1 and CMT167 were implanted subcutaneously or orthotopically, suggesting that immune populations associated with certain tumours may be lacking when the equivalent cell line is injected subcutaneously.(305) Different tissues naturally possess different frequencies or types of certain immune cells, for example comparing the colon versus the lung, but this detail is clearly lost in subcutaneous implantation of colonic or lung tumour cell lines.(306) This can then result in models that lack key aspects of the response that are relevant in the clinic.(307) Finally, there are key differences in innate immune populations, mutational load and resultant lymphocyte infiltration within human tumours versus murine syngeneic subcutaneous tumour models.(308-311). It is clear after many years of clinical trials using different immunotherapies to build on the success of ICB, that the subcutaneous tumour models that have been the workhorse of pre-clinical studies, are not predictive of responses in patients. As we seek to build upon the success of ICB with therapy combinations tailored to specific cancer types, appropriate pre-clinical models are essential.

Subcutaneous tumour models fail to fully recapitulate the anatomy of most cancers, growing rapidly in a restricted tissue space and bypassing many of the initial stages of tumour development. For example, the vasculature in pre-clinical subcutaneous tumour models is often referred to as 'immature', owing to the bolus injection of rapidly dividing tumour cells in which the angiogenic switch has already occurred leading to rapid development of a disorganised and fragile network of vessels.(312-314) Angiogenesis is a key therapeutic target, a study found that blocking VEGF led to the normalisation of tumour vasculature, and importantly improved lymphocyte infiltration and an enhanced anti-tumour response.(315) Clearly the tumour vasculature, and also lymphatics, are essential for lymphocyte migration as well as impacting metastatic progression, and so there is a need to develop anatomically faithful *in vivo* tumour models. Orthotopic colorectal cancer models have been developed, through implantation of cell lines directly into the caecum or colon, and the limited immunophenotyping carried out suggests that the site of injection does impact intratumoural immune composition.(316, 317) However, these approaches are technically complex and there remains limited data on the composition of the T cell compartment in these models and how this is shaped by the migration or retention of specific populations. Subcutaneous tumour models do not readily metastasise, however there are models of CT26 that metastasise when injected into the colon wall, providing a means of studying the fundamental issue of metastatic disease.(318)

4.1.2. The importance of modelling metastatic disease

Colorectal cancer is primarily a surgical disease, with around half of patients surviving 10 years.(246, 247) Unfortunately, one in five of those with CRC have metastatic disease at the time of presentation, with many developing metastatic disease later in the disease course.(258, 259) Liver metastasis accounts for over half of CRC metastases, and importantly is an indicator of poor clinical outcome, hence it is essential to better model the burden of this disease to facilitate the development of treatments specific for liver metastases.(258, 260) There are existing models of CRC liver metastasis involving the injection of cancer cells into the hepatic portal vein or into the spleen, as well as orthotopically implanted CRC cell lines that naturally metastasise.(318-320) These approaches model aspects of the establishment of the metastatic niche, however, they present challenges in controlling the timing and site of liver metastases, with multiple foci scattered within the liver. A key aim of this study was to establish approaches enabling the photolabelling of liver tumours *in situ*, to aid understanding of immune cell dynamics at this site, but to do this we anticipated that a single tumour growing near the outer border of a liver lobe was required. A 2021 paper used direct injection of CRC cell lines into the liver to model ICB efficacy in pMMR CRC liver metastasis, finding key differences in the dynamics of the T cell and DC response in these tumours versus the same cell line implanted subcutaneously.(321) This approach was decided as the most appropriate due to the predictable growth and peripheral location of tumours to support efficient photoconversion.

4.1.3. Chapter aims

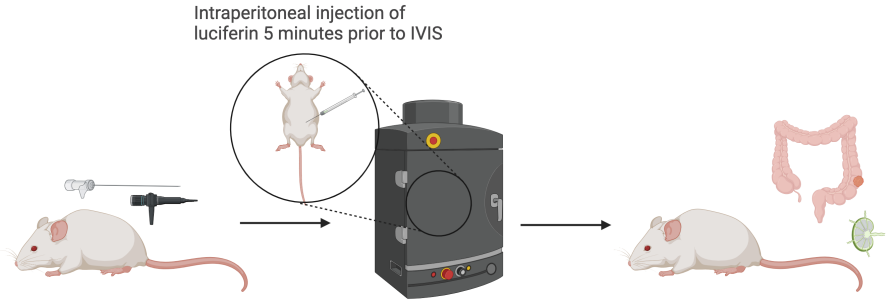
The primary aim of this chapter was to establish orthotopic tumours using CRC cell lines in the hope that this better models primary and metastatic disease in patients. This required the development of two new experimental approaches in the lab – firstly, the endoscopic injection of cells into the colon wall, and secondly the direct injection of cells into the liver to model the main site of CRC metastasis. We hypothesise that the CD8 T cell response in these orthotopic tumours will differ from that of subcutaneous tumours established with the same cell lines. To test this, I will interrogate the composition and phenotype of the CD8 T cell compartment using flow cytometry, then characterise their spatial organisation using microscopy. To better understand how the T cell compartment is formed and sustained, it is also important to develop photolabeling approaches to assess immune cell migration in these models. Therefore, the secondary aim of this chapter was to develop methods enabling the photo-labelling of orthotopic tumours to support detailed study of immune cell dynamics, as established for subcutaneous tumours.

4.2. Results

4.2.1. Establishing an orthotopic model of colorectal cancer

Subcutaneous tumour models are a useful tool in the study of cancer immunology, but as highlighted previously, lack the relevant anatomical context that likely impacts aspects of the response including immune cell migration and retention. The intracolonic injection of both cell lines and organoids is an established technique in a few research labs.(322-324) Initial experiments aimed to establish that in our hands tumour cell lines could be injected into the correct anatomical space, and growth monitored successfully. To this end, it was envisaged that the IVIS® imaging platform would enable detailed monitoring of tumour growth, IVIS® is an *in vivo* imaging system providing information regarding the concentration and anatomical location of fluorescence/ bioluminescence of reporters.(325) Using the methods outlined in Chapter 2, 2.5 x10^5 CT26 GFP Luciferase cells (GenTarget Inc; SC061-LG) were injected into the colon wall. Using IVIS, the site of the injected cells was assessed at day 2 following injection. Subsequent IVIS imaging performed on days 5 and 10, aimed to correlate the magnitude of bioluminescence with the size of the colon tumour *in situ,* prior to tissue collection two weeks post-injection (Fig. 4.1A). Due to the high resolution of images taken with the light endoscope, success of the initial injection could be roughly determined according to the development of a protrusion in the colon lumen during injection (Fig. 4.1B). However, to allay concerns that the needle had perforated the colon wall and cells consequently injected intraperitoneally, IVIS imaging was used; a diffuse non-localised signal across the abdomen of the animal indicated a failed injection, whereas a localised bioluminescent signal demonstrated successful intracolonic

A.



Day 0

Injection of CT26 GFP luciferase cell line into the colon wall via colonoscopy-guided injection

Day 2, 5, 10

Monitoring of tumour growth in anaesthetised mice using IVIS imaging

Day 14

Tissues collected

B.

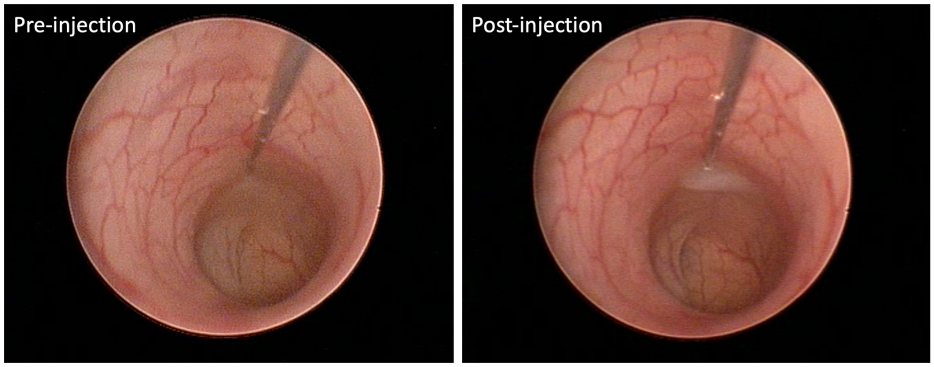


Figure 4.1. Implantation of CT26 GFP Luciferase colorectal cancer cell line into the colon wall of BALB/c mice.

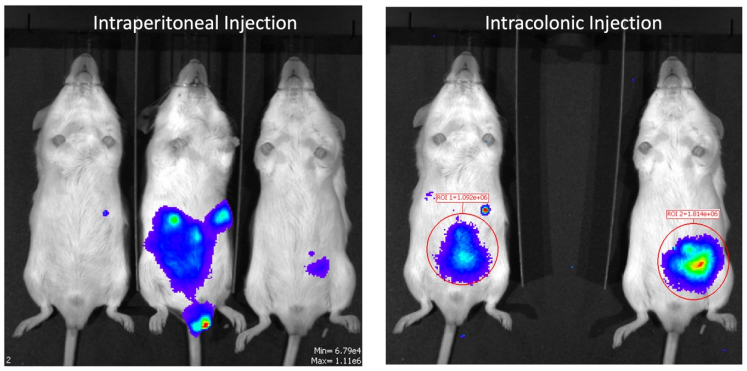
In an initial pilot experiment, 2.5 x10^5 CT26 GFP Luc tumour cells were injected into the colon wall of 10-week-old BALB/C Kaede mice.

A. Illustration outlining the timeline of initial orthotopic colon tumour experiments. Created with Biorender.com.
B. Images demonstrating the injection of tumour cell lines into the wall of the colon. The left-hand panel shows the colon lumen prior to injection and right-hand panel after injection. Images were taken using a Karl Storz Endoskope with a multi-purpose rigid telescope.

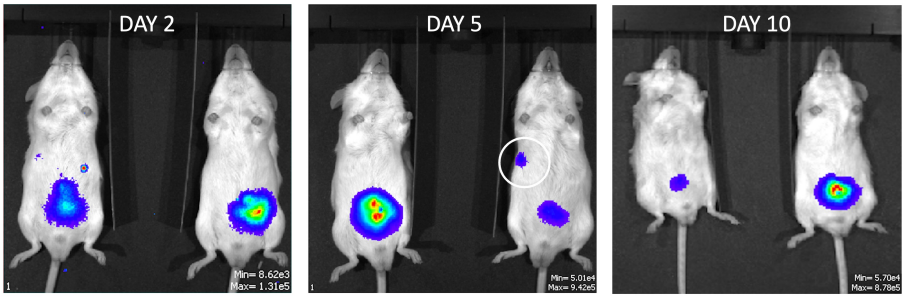
injection (Fig. 4.2A). IVIS imaging on days 5 and 10 was used to record bioluminescence of the primary colon tumour, but also revealed hepatic bioluminescent signal in 33% of animals (Fig. 4.2B). The hepatic bioluminescence suggested circulation of the tumour cells during initial tumour development, though in both mice this signal was no longer present on imaging at day 10 (Fig. 4.2B). The bioluminescence of the colon tumour that developed, recorded as total flux p/s, fluctuated during the course of the experiment with peak signal reported early on in tumour growth, an observation that was consistent across three independent experiments (Fig. 4.2C). Importantly, final readings for total flux did not correlate with the size of the tumour excised (Fig. 4.2D). Despite tumours developing during each of the initial experiments, the overall yield was low with only 20% of animals injected having developed colon tumours at tissue harvest. This raised concerns as to the success of the injection, but also uncertainties over the immunogenicity of the cell line and potential rejection of the tumours over time (Fig. 4.2E).

To specifically test whether the CT26 GFP Luc cell line was more immunogenic, and thus leading to spontaneous rejection, we decided to track the growth of this cell line alongside the WT CT26 line in the same host utilising a dual flank tumour model. Therefore, mice received 2.5 $x10^5$ of CT26 WT cells into one flank and 2.5 $x10^5$ CT26 GFP Luc cells into the opposite flank. To further explore the immunogenicity, the sensitivity of this cell line to ICB was assessed, the mice were further split into two groups and treated with either anti-PD-L1 or isotype control (administered on days 7 and 11), before collection and analysis of both tumours on day 14 post-injection (Fig. 4.3A). The growth of CT26 GFP Luc tumours clearly plateaued at day 7 when compared with the growth of CT26 WT tumours in the

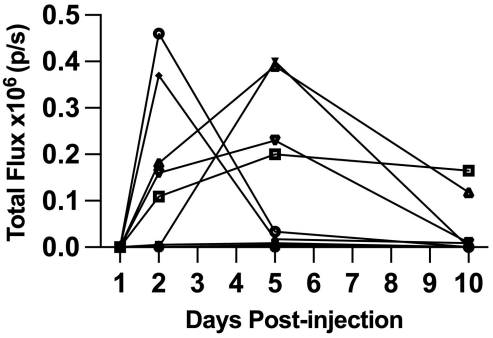
A.



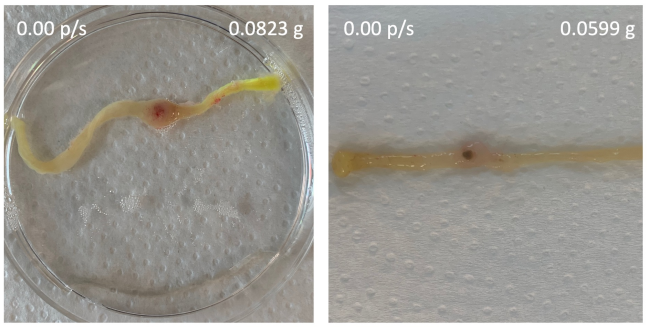
B.



C.



D.



E.

Experiment No.	Animals Injected	Tumour Status	
		Tumour Present	None
1	5	1	4
2	15	3	12
3	10	2	8

Figure 4.2. Monitoring the growth of CT26 GFP Luc colon tumours using IVIS.

BALB/c Kaede mice (aged 9-12 weeks) were injected with 2.5 x10^5 CT26 GFP Luc cells into the colon wall. CT26 GFP Luc data are from three independent experiments. IVIS images were collected and exported using LivingImage software.

A. IVIS images demonstrating intraperitoneal injection (left panel) and two successful colon wall injections (right panel). Images acquired day 2 post-injection of CT26 GFP Luc into the colon wall.
B. IVIS images of the same mice at different timepoints (days 2, 5, and 10) after injection. The middle image has a white circle added to highlight IVIS signal in the liver as well as the colon.
C. Total flux (p/s) in the colon tumour ROI at day 2, day 5 and day 10 post-injection for each animal that developed a tumour within the colon. The maximum total flux reading reached on each day is recorded per mouse on the graph, paired data is demonstrated with a line between points over time.
D. Images of tumours and surrounding colon *ex vivo*, recorded on each image is the maximum flux recorded at day 10 IVIS (top left) and the weight of the excised tumour (top right).
E. Table demonstrating the number of colon tumours that developed, or did not, following injection of CT26 GFP Luc into the colon wall of BALB/c mice per experiment.

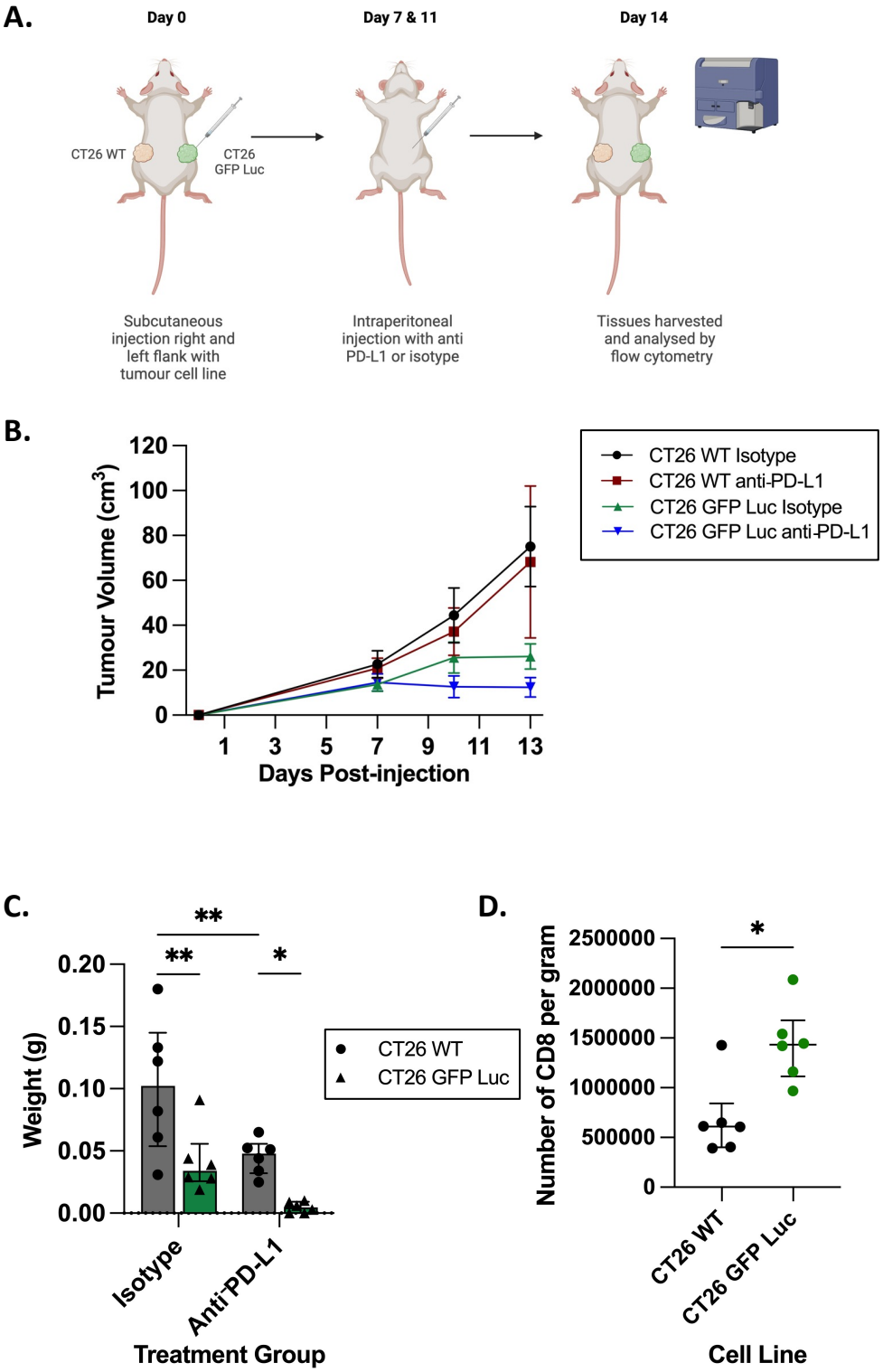

A.
Day 0
Day 7 & 11
Day 14
CT26 WT
CT26 GFP Luc
Subcutaneous injection right and left flank with tumour cell line
Intraperitoneal injection with anti PD-L1 or isotype
Tissues harvested and analysed by flow cytometry
B.
Tumour Volume (cm3)
Days Post-injection
CT26 WT Isotype
CT26 WT anti-PD-L1
CT26 GFP Luc Isotype
CT26 GFP Luc anti-PD-L1
C.
Weight (g)
Isotype
Anti-PD-L1
Treatment Group
CT26 WT
CT26 GFP Luc
D.
Number of CD8 per gram
CT26 WT
CT26 GFP Luc
Cell Line

Figure 4.3. Expression of GFP and luciferase renders CT26 more immunogenic.

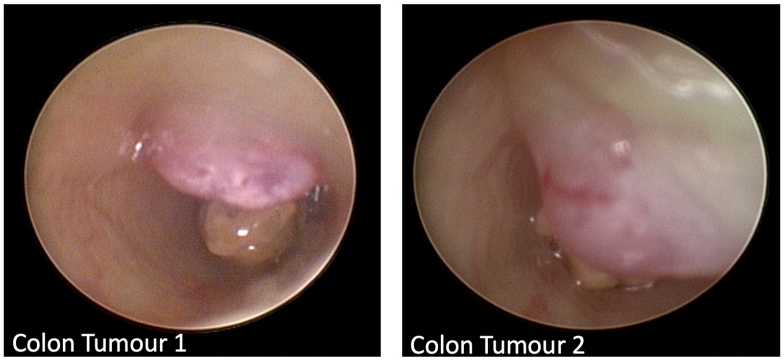
BALB/c Kaede mice (8-10 weeks) were injected with 2.5 x10^5 CT26 GFP Luc or CT26 WT cells subcutaneously. Anti–PD-L1 mouse IgG1 (Clone 80, SP16-260; AstraZeneca) or NIP228 isotype control mouse IgG1 (SP16-017; AstraZeneca) were administered by intraperitoneal injection using one dose of 200 µg diluted in 200 µl PBS (10 mg/kg body weight) on day 7 and day 11. Tissues were harvested on day 14 post-injection. Cells were isolated from subcutaneous tumours as per methods. Data shown are from two independent experiments. All graphs show the median value and IQR. Statistical significance was determined using a Mann-Whitney test. ** = $p < 0.05$, ** = $p < 0.01$.*

A. Illustration demonstrating the set-up of experiments to test the immunogenicity of the CT26 GFP Luc cell line. Created with Biorender.com.
B. Growth curves demonstrating the difference in tumour volume upon anti-PD-L1 treatment between CT26 GFP Luc and CT26 WT.
C. Tumour weight in grams day 14 post-injection, showing difference between CT26 WT and CT26 GFP Luc tumours treated with isotype or anti-PD-L1.
D. Number of CD8 T cells per gram of tumour at day 14, showing difference between CT26 WT and CT26 GFP Luc tumours treated with isotype antibodies. Note, data from the anti-PD-L1 treated group is not shown as the samples were too small to perform flow cytometry analysis on.

same animal (Fig. 4.3B). Furthermore, a more marked effect on tumour growth was evident with anti-PD-L1 treatment (Fig. 4.3B). The final weights of CT26 GFP Luc tumours were significantly decreased when compared with CT26 WT tumours in the same animal (Fig. 4.3C). Notably, complete clearance of some CT26 GFP Luc tumours was achieved following treatment with anti-PD-L1; this was not seen with CT26 WT tumours in the treated arm, though there was an expected significant decrease in tumour weight caused by administration of anti-PD-L1 Abs (Fig. 4.3C). Finally, examination of CD8 infiltration in the isotype tumour group showed a significant increase in the number of CD8 T cells per gram of tumour weight in CT26 GFP Luc tumours, consistent with an enhanced T cell response (Fig. 4.3D). This analysis was not possible in the anti-PD-L1 treated animals due to complete clearance and small size of the tumours.

Having established that the CT26 GFP Luc tumours were significantly more immunogenic than WT CT26, we reasoned that the failure of orthotopic CT26 GFP Luc tumours to grow in the majority of injected mice likely reflected spontaneous clearance of these tumours. Therefore, we decided to use intracolonic injection of CT26 WT, with repeat colonoscopy to monitor tumour growth. Repeat colonoscopy using a light endoscope was performed weekly to ensure occlusion of the colon lumen had not occurred (Fig. 4.4A). Colon tumours developed in 66% of animals injected (Fig. 4.4B-C), a clear improvement on the success of CT26 GFP Luc injections. We further compared CT26 tumours growing within the colon to CT26 tumours grown subcutaneously on the flank of mice for the same period of time. Colon tumours were first excised from the surrounding colon tissue prior to analysis and were of a consistent size (Fig. 4.4D). The weight of CT26 WT tumours grown in the colon

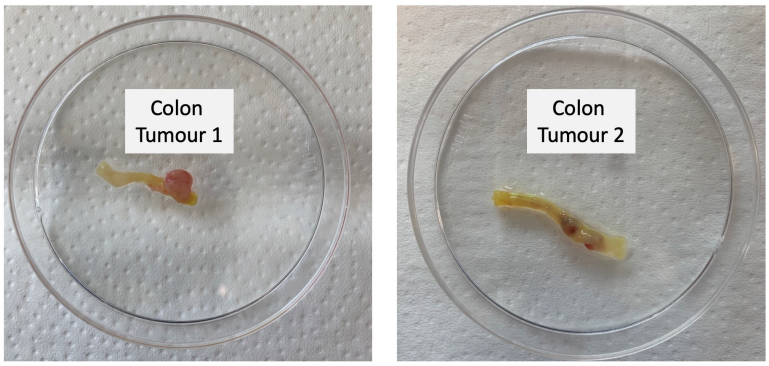
A.



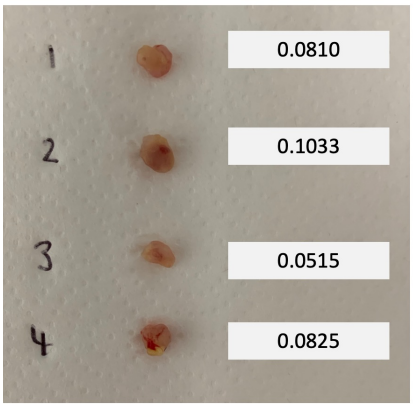
B.

Experiment No.	Animals Injected	Tumour Status	
		Tumour Present	None
1	6	4	2
2	6	4	2

C.



D.



E.

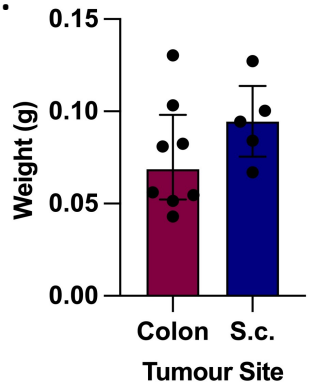


Figure 4.4. Monitoring the growth of CT26 WT tumours using repeat colonoscopy.

BALB/c mice (8-10 weeks) were injected with CT26 WT cells into either the colon wall or subcutaneously. Data shown are from two independent experiments. The graph shows the median value and IQR. Statistical significance was determined using a Mann-Whitney test.

A. Images of the colon lumen, colon tumours are present on the top right of both images. The images were captured during repeat colonoscopy, used as an alternative method of monitoring tumour growth, using a Karl Storz Endoskope with a multi-purpose rigid telescope. Images from two different experiments at day 7.
B. Table demonstrating the number of colon tumours that developed following injection of CT26 WT cells into the colon wall of BALB/c mice per experiment.
C. Images of the tumours and surrounding colon tissues *ex vivo*. The tumours shown correspond to the images taken in figure A.
D. Images of the tumours excised from the colon wall, all from the first experiment, and weights (g) recorded on the right.
E. Tumour weight (g) at day 14 post-injection, showing the difference between CT26 WT colon and CT26 WT subcutaneous tumours.

was not significantly different to those grown subcutaneously (Fig. 4.4E). Collectively, these data demonstrate the successful establishment of an orthotopic model of CRC using direct injection into the colon wall via endoscopy.

4.2.2. Characterisation of the intratumoural CD8 T cell population in orthotopic colon tumours compared to subcutaneous tumours

Having established CT26 tumours in the colon, we then sought to compare the composition of intratumoural CD8 T cells in colorectal cancer cell lines implanted orthotopically versus subcutaneously. Therefore, mice were implanted with CT26 tumours either orthotopically or subcutaneously and these were assessed 14 days later by flow cytometry with their CD8 T cell compartments compared. Flow cytometry was used to identify CD8 T cells, according to the gating strategy shown in Appendix 4.1, and phenotype them. Alongside the tumours, CD8 T cells in the colon proximal to the tumour were also assessed to help establish the background composition of cells in this tissue. The proportion of live CD45+ cells that were CD8+ T cells and their density within the tumour was slightly increased in those grown subcutaneously versus in the colon (Fig. 4.5A-B). However, the phenotype of CD8 T cells found within CT26 WT tumours at both sites was not significantly altered according to markers of activation, exhaustion, and migratory potential (Fig. 4.5C-I). Briefly, the proportion of cells expressing either PD-1 or TOX, was not significantly different between tumours. In comparison, the CD8 population in the background healthy colon tissue, used as an additional control, expressed significantly lower levels of inhibitory receptors and significantly higher levels of TCF-1 (Fig. 4.5D, E, G). To further investigate the exhausted CD8 T cell compartment, expression of PD-1 versus TOX was assessed. As expected, a

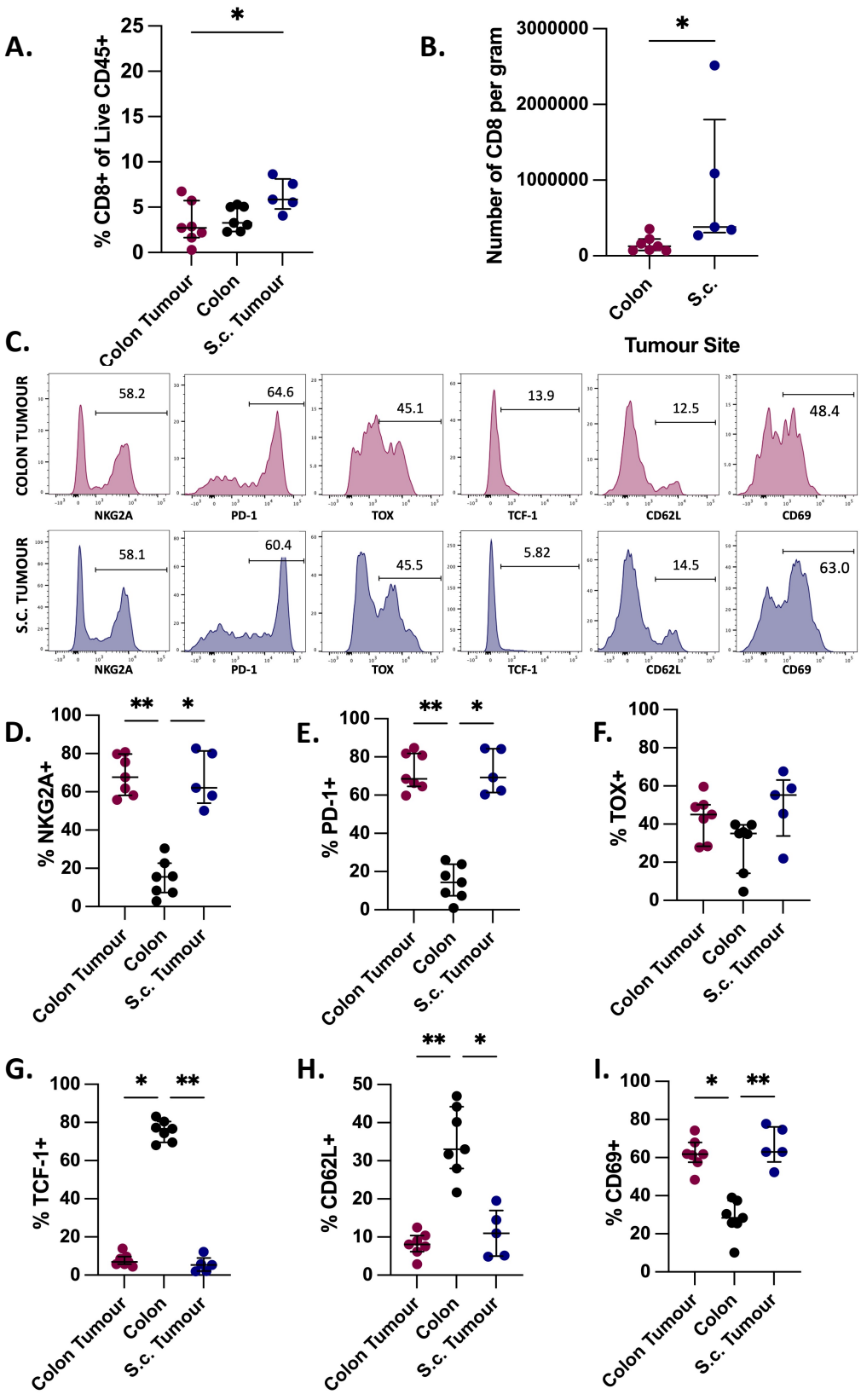

A.
% CD8+ of Live CD45+
25
20
15
10
5
0
*
Colon Tumour
Colon
S.c. Tumour
B.
Number of CD8 per gram
3000000
2000000
1000000
0
*
Colon
S.c.
C.
Tumour Site
COLON TUMOUR
58.2
64.6
45.1
13.9
12.5
48.4
NKG2A
PD-1
TOX
TCF-1
CD62L
CD69
S.C. TUMOUR
58.1
60.4
45.5
5.82
14.5
63.0
NKG2A
PD-1
TOX
TCF-1
CD62L
CD69
D.
% NKG2A+
100
80
60
40
20
0
**
*
Colon Tumour
Colon
S.c. Tumour
E.
% PD-1+
100
80
60
40
20
0
**
*
Colon Tumour
Colon
S.c. Tumour
F.
% TOX+
100
80
60
40
20
0
Colon Tumour
Colon
S.c. Tumour
G.
% TCF-1+
100
80
60
40
20
0
*
**
Colon Tumour
Colon
S.c. Tumour
H.
% CD62L+
50
40
30
20
10
0
**
*
Colon Tumour
Colon
S.c. Tumour
I.
% CD69+
100
80
60
40
20
0
*
**
Colon Tumour
Colon
S.c. Tumour

Figure 4.5. Characterising the difference in the CD8 population of CT26 tumours implanted in the colon versus subcutaneously.

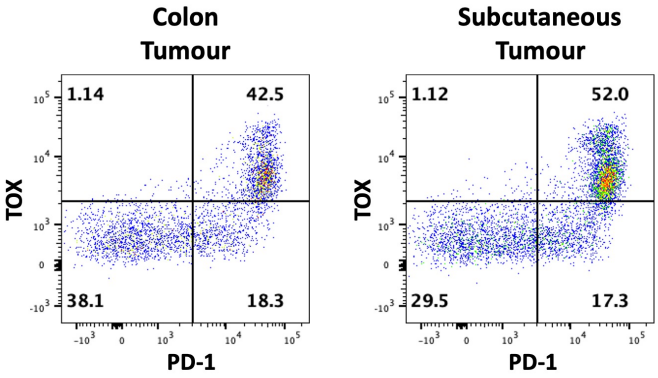
BALB/c mice (8-10 weeks) were injected with CT26 WT cells into the colon wall or subcutaneously. Subcutaneous tumours were collected at the same time as colon tumours at day 14 post-injection and served as controls, as an additional control 2cm of healthy proximal colon was taken from animals with colon tumours. Data shown are from two independent experiments. All graphs show the median value and IQR. In the case of two column analysis statistical significance was determined using a Mann-Whitney test. In the case of multiple comparisons statistical significance was determined with a Kruskal-Wallis multiple comparison test. ** = $p < 0.05$, ** = $p < 0.01$.*

A. The percentage of live CD45+ cells that are CD8+ in colon tumour, colon tissue and s.c. tumour.
B. The number of CD8+ cells per gram of tumour, comparing colon and s.c. tumour.
C. Histograms demonstrating the expression of NKG2A, PD-1, TOX, TCF-1, CD62L, and CD69 in the total CD8+ population in a representative CT26 WT colon tumour (top row) and s.c. tumour (bottom row). The percentage of the population that is positive for the stated marker is shown. CD8 T cells previously gated on live CD45+ CD11b- B220- CD11c- CD3+ CD8+.
D. The percentage of CD8+ T cells that are NKG2A+ in the colon tumour, colon tissue and s.c. tumour.
E. The percentage of CD8+ T cells that are PD-1+ in the colon tumour, colon tissue and s.c. tumour.
F. The percentage of CD8+ T cells that are TOX+ in the colon tumour, colon tissue and s.c. tumour.
G. The percentage of CD8+ T cells that are TCF-1+ in the colon tumour, colon tissue and s.c. tumour.
H. The percentage of CD8+ T cells that are CD62L+ in the colon tumour, colon tissue and s.c. tumour.
I. The percentage of CD8+ T cells that are CD69+ in the colon tumour, colon tissue and s.c. tumour.

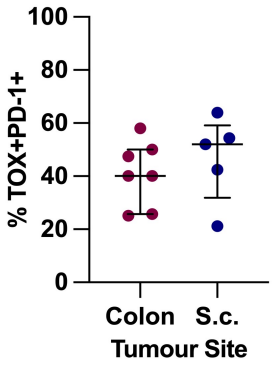
comparable PD-1hi TOX+ population was observed (Fig. 6A, B). Finally, the stem-like TCF-1+ PD-1+ population was assessed and again no significant difference in the portion of CD8 T cells with this phenotype was observed when the two tumour sites were assessed (Fig. 4.6C-E). Collectively, these data indicate that the CD8 T cell compartment in CT26 tumours implanted at these two anatomically distinct sites appeared broadly comparable in their phenotype and composition.

Alongside phenotyping the intratumoural CD8 population at both sites by flow cytometry, spatial characterisation of CD8 T cells was performed using immunofluorescence confocal microscopy. The aim of this approach was to check whether any gross differences existed in the distribution of T cells in the tumour and to check that T cells were able to fully penetrate these tumours. There appeared to be an enrichment in the number of CD8 T cells at the border of subcutaneously implanted tumour cell lines (Fig. 4.7A-B). Although the number of CD8 T cells found in the centre of the tumour appeared to be fewer in number, CD8 T cells were still evident (Fig. 4.7A, C). To identify the location of CD8 T cells in tumours embedded within the colon wall, pancytokeratin was used to differentiate the colon wall from the substance of the tumour (Fig. 4.8A). As with subcutaneously implanted tumours, the highest number of CD8 T cells were found at the tumour-colon border (Fig. 4.8B); whilst CD8 T cells were found but at decreased density in the centre of the colon tumour (Fig. 4.8C). Positive controls for both CD8 and pancytokeratin antibodies used in the microscopy analysis can be found in Appendix 4.2. These initial analyses indicate that the distribution of CD8 T cells in CT26 tumours appears similar regardless of whether the

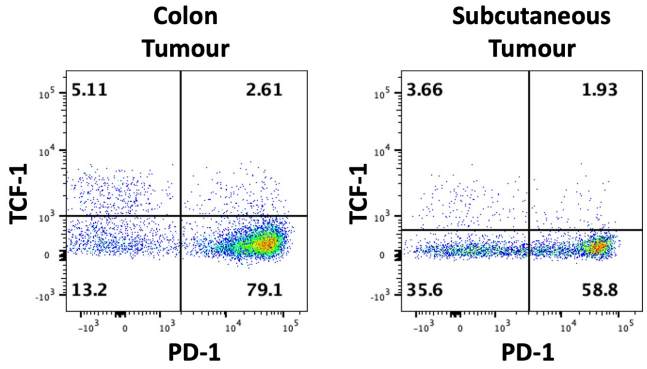
A.


Colon Tumour
Subcutaneous Tumour
1.14
42.5
38.1
18.3
1.12
52.0
29.5
17.3
TOX
PD-1

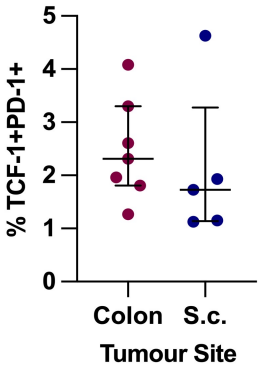
B.


% TOX+PD-1+
100
80
60
40
20
0
Colon
S.c.
Tumour Site

C.


Colon Tumour
Subcutaneous Tumour
5.11
2.61
13.2
79.1
3.66
1.93
35.6
58.8
TCF-1
PD-1

D.


% TCF-1+PD-1+
5
4
3
2
1
0
Colon
S.c.
Tumour Site

E.

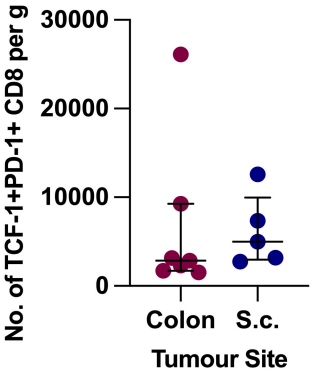

No. of TCF-1+PD-1+ CD8 per g
30000
20000
10000
0
Colon
S.c.
Tumour Site

Figure 4.6. Identifying the stem-like CD8 population in CT26 tumours implanted in the colon versus subcutaneously.

BALB/c mice (8-10 weeks) were injected with CT26 WT cells into the colon wall or subcutaneously. Subcutaneous tumours were collected at the same time as colon tumours at day 14 post-injection and served as controls. Data shown are from two independent experiments. All graphs show the median value and IQR. Statistical significance was determined using a Mann-Whitney test. ** = $p < 0.05$, ** = $p < 0.01$.*

A. Representative flow cytometry plots demonstrating TOX and PD-1 co-expression at day 12 post-injection in CT26 colon (left) and s.c. tumours (right).
B. The percentage of total CD8 T cells that are TOX+ PD-1+ at day 12 post-injection, in the colon and s.c. tumour.
C. Representative flow cytometry plots demonstrating TCF-1 and PD-1 co-expression at day 12 post-injection in CT26 colon (left) and s.c. tumours (right).
D. The percentage of total CD8 T cells that are TCF-1+ PD-1+ at day 12 post-injection, in the colon and s.c. tumour.
E. The number of TCF-1+ PD-1+ CD8+ T cells per gram of tumour at day 12 post-injection, in the colon and s.c. tumour.

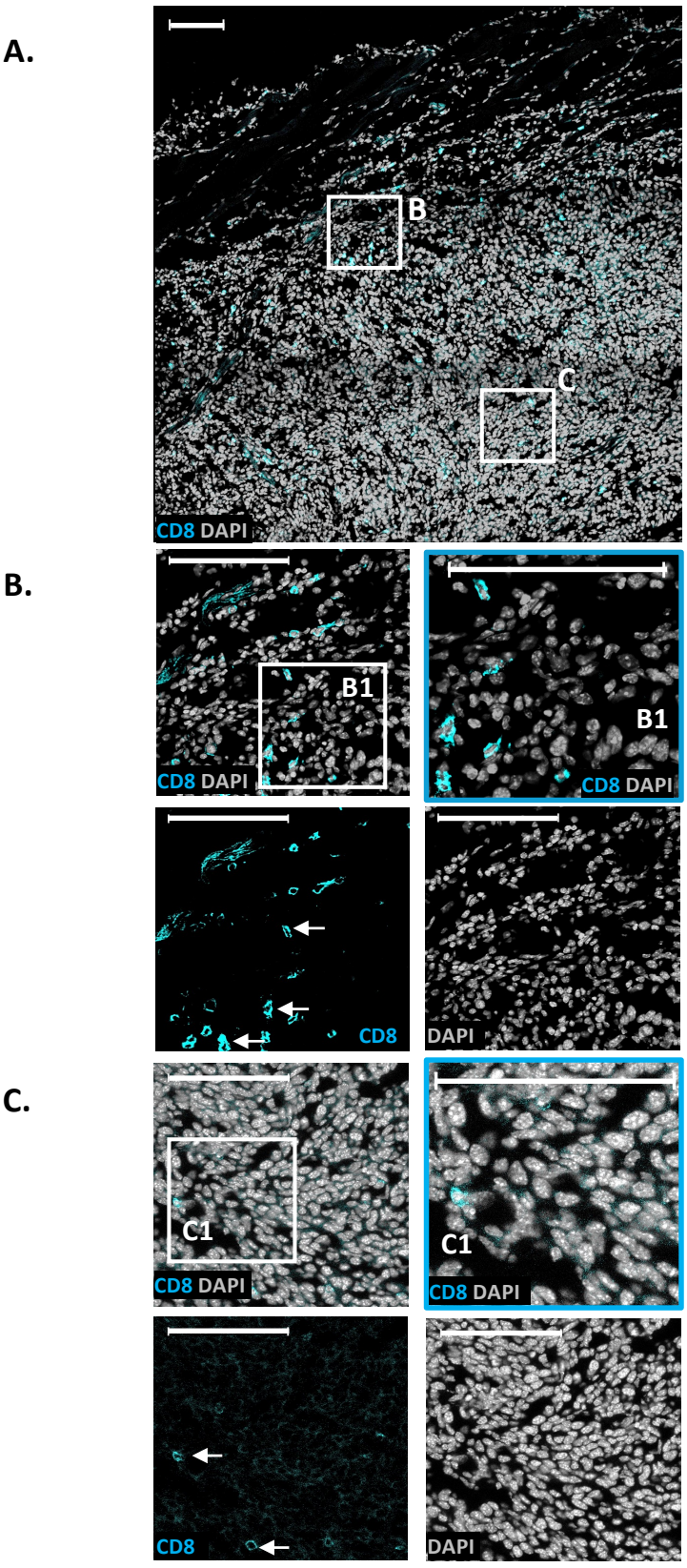

A.
B
C
CD8 DAPI
B.
B1
CD8 DAPI
B1
CD8 DAPI
CD8
DAPI
C.
C1
CD8 DAPI
C1
CD8 DAPI
CD8
DAPI

Figure 4.7. Examining the spatial distribution of T cells in subcutaneous tumour models. Immunofluorescent microscopy of a CT26 WT tumour embedded subcutaneously in a BALB/c WT mouse (n=3). Sections were stained for CD8 and counterstained with DAPI to allow CD8 T cells within the tissue to be identified. Representative images shown. All scale bars represent 100μm. DAPI is shown in grey and CD8 show in cyan.

A. x25 tile scan of a CT26 WT tumour. White boxes B and C represent the ROIs shown in figures B and C at higher magnification.
B. x40 image of the edge of a subcutaneous tumour (labelled in figure A). The ROI highlighted in the top left image B1, is shown zoomed in highlighted in blue on the right. Arrows mark CD8 T cells.
C. x40 image of the middle of a subcutaneous tumour (labelled in figure A). The ROI highlighted in the top left image C1, is shown zoomed in highlighted in blue on the right. Arrows mark CD8 T cells.

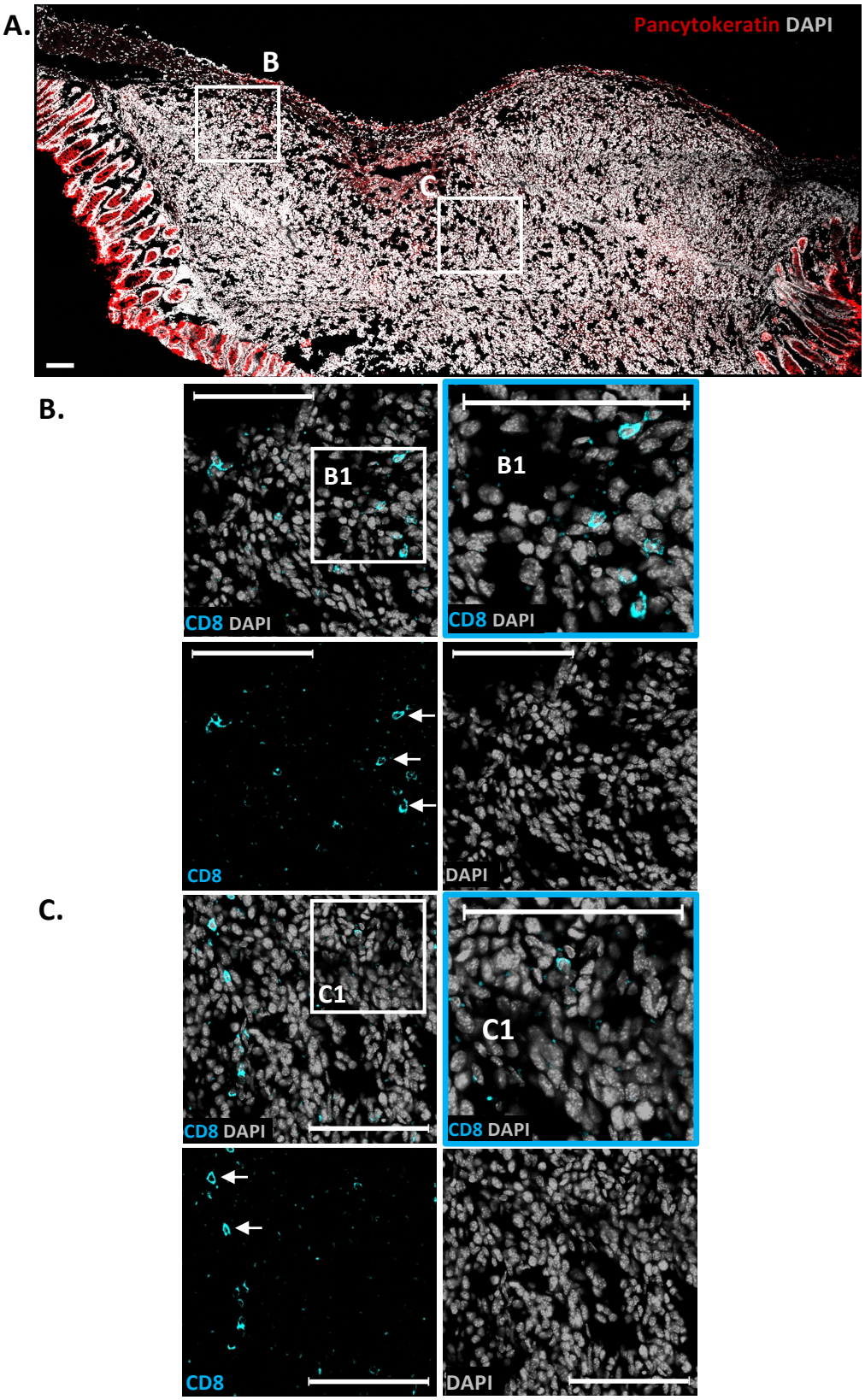

A.
Pancytokeratin DAPI
B
C
B.
B1
CD8 DAPI
B1
CD8 DAPI
CD8
DAPI
C.
C1
CD8 DAPI
C1
CD8 DAPI
CD8
DAPI

Figure 4.8. Examining the spatial distribution of T cells in orthotopic colon tumour models.

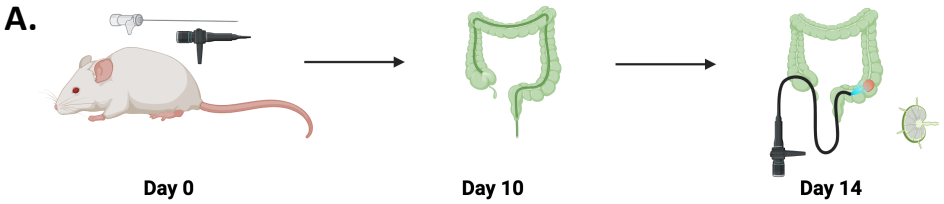
Immunofluorescent microscopy images of a CT26 WT tumour embedded in the colon wall of a BALB/c WT mouse (n=3). Sections were stained for pancytokeratin, CD8 and counterstained with DAPI to allow CD8 T cells within the tissue to be identified. Representative images shown. All scale bars represent 100µm. DAPI is shown in grey, pancytokeratin in red, and CD8 in cyan.

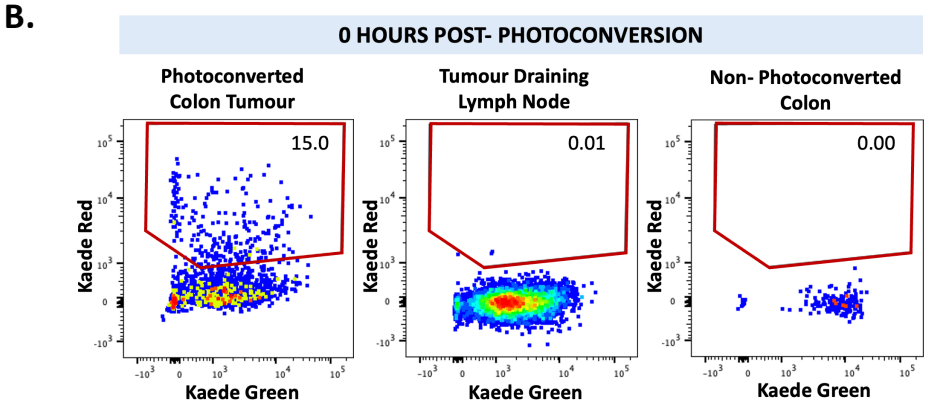
A. x25 tile scan of a CT26 WT colon tumour. White boxes B and C represent the ROIs shown in figures B and C at higher magnification.
B. x40 image of the edge of a colon tumour (labelled in figure A). The ROI highlighted in the top left image B1, is shown zoomed in highlighted in blue on the right. Arrows mark CD8 T cells.
C. x40 image of the middle of a colon tumour (labelled in figure A). The ROI highlighted in the top left image C1, is shown zoomed in highlighted in blue on the right. Arrows mark CD8 T cells.

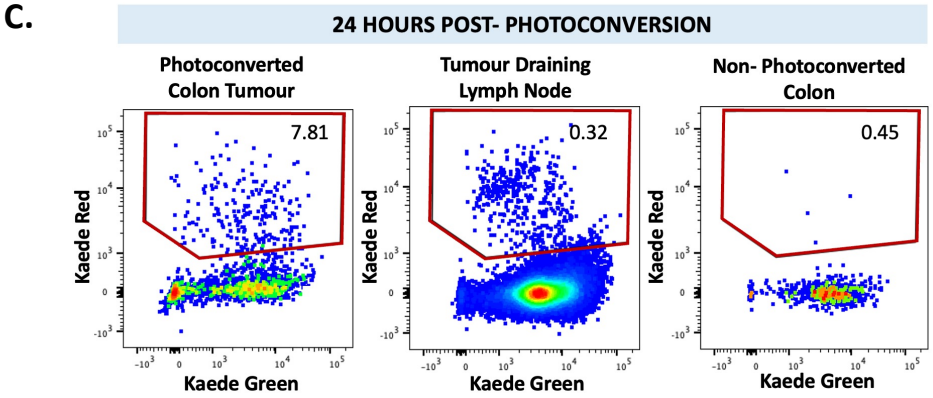
tumour is grown subcutaneously or orthotopically in the colon, with dense and rapidly growing tumours forming at both sites.

4.2.3. Establishing a model to track the migration of immune cells in orthotopic colon tumours

The broad phenotype and location of intratumoural CD8 T cells were similar between CRC cell lines implanted subcutaneously versus orthotopically, however the migration of immune populations may be influenced by the different anatomical locations of the tumour. Building from the dynamic labelling models established in the lab, I aimed to develop a tumour labelling approach for tumours within the colon wall.(286) In the initial pilot experiment, CT26 WT CRC cells were injected into the wall of the colon and growth monitored using the light colonoscope. At day 12 the colon tumour was then exposed to UV light *in vivo* using a modified endoscope that emits violet light (Fig. 4.9A). Tissues were collected either immediately or 24 hours after photolabeling with the UV colonoscope. In tumours collected immediately following the photoconversion procedure there were Kaede red+ CD3+ T cells found within the tumour (Fig. 4.9B). However, photolabelling of the intratumoural T cell compartment was by no means complete within this pilot experiment. There appeared to be no bystander labelling of the tumour dLN nor adjacent colon proximal to the tumour (Fig. 4.9B). In tumours collected 24 hours after photolabelling, Kaede red+ CD3+ T cells could still be identified in the tumour, and a clear Kaede red+ T cell population was found to have migrated to the tumour dLN (Fig. 4.9C). All the colon tumours collected 24 hours after photoconversion, and their weights after excision from the surrounding colon are shown in Fig. 4.9D. Kaede red labelling in T cell


A.
Day 0
Day 10
Day 14
Injection of CT26 GFP luciferase cell line into the colon wall via colonoscopy-guided injection
Monitoring of tumour growth in anaesthetised mice using colonoscopy
Tumour photoconversion using UV light colonoscope. Tissues taken after procedure (0 hours)


B.
0 HOURS POST- PHOTOCONVERSION
Photoconverted Colon Tumour
Tumour Draining Lymph Node
Non- Photoconverted Colon
15.0
0.01
0.00
Kaede Red
Kaede Green


C.
24 HOURS POST- PHOTOCONVERSION
Photoconverted Colon Tumour
Tumour Draining Lymph Node
Non- Photoconverted Colon
7.81
0.32
0.45
Kaede Red
Kaede Green

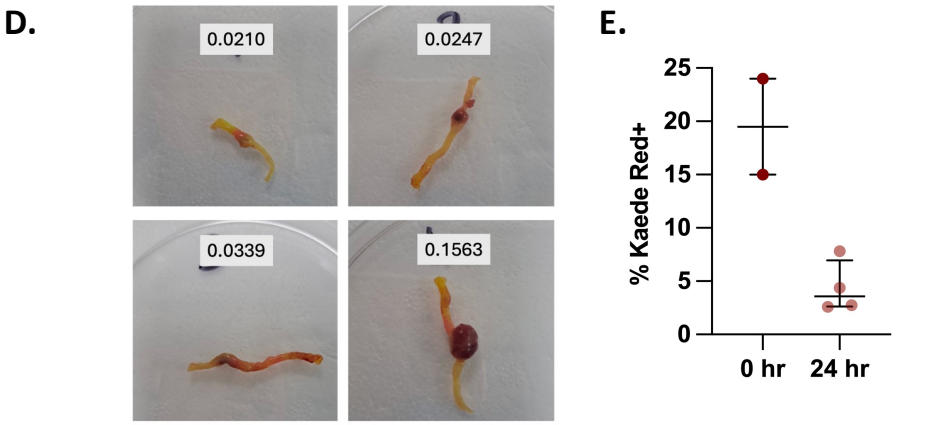

D.
0.0210
0.0247
0.0339
0.1563
E.
% Kaede Red+
25
20
15
10
5
0
0 hr
24 hr

Figure 4.9. Photolabelling of colon tumours *in situ* using a UV colonoscope.

In the pilot experiment for colon tumour photoconversion, 5 x10^5 CT26 WT cells were injected into the colon wall, followed by photoconversion using a custom UV endoscope (Zibra Corp.) at day 12 post-injection. Tissues were collected either immediately after or 24 hours after photoconversion. Graphs display the median and IQR.

A. Illustration of the timeline of initial colon tumour photoconversion experiments. Created using Biorender.com.
B. Representative flow cytometry plots demonstrating the efficiency of photoconversion through Kaede red and green expression in the CD3+ T cell population at 0 hours post-photoconversion; shown, left to right, are a photoconverted colon tumour, the dLN of a photoconverted colon tumour, and unphotoconverted colon proximal to the colon tumours. All tissues shown were taken from the same mouse.
C. Representative flow cytometry plots demonstrating the efficiency of photoconversion through Kaede red and green expression in the CD3+ T cell population at 24 hours post-photoconversion; shown, left to right, are a photoconverted colon tumour, the dLN of a photoconverted colon tumour, and unphotoconverted colon proximal to the colon tumour. All tissues shown are taken from the same mouse.
D. Images of the tumours and surrounding colon 24 hours following photoconversion. The weight (g) of tumours once excised is stated on each image.
E. The proportion of Kaede red+ cells in the CD3+ T cell population within colon tumours 0 and 24 hrs following photoconversion.

compartment of tumours immediately after photoconversion was around 20%, which after 24 hours fell to under 5% (Fig. 4.9E). Examining the egress of immune cells from the colon tumour to the dLN, Kaede red+ CD4 and CD8 T cells, alongside Kaede red+ DCs could be identified within the dLN (Fig. 4.10A-D). Dendritic cells were the most common among the CD45+ Kaede red+ migratory population found in the dLN (Fig. 4.10E). Finally, a population of Kaede red+ TCF-1+ PD-1+ stem-like CD8 T cells was evident in the dLN, consistent with data produced in the CT26 WT subcutaneous model in Chapter 3 (Fig. 4.10F-G). The acquisition of this new endoscope in early 2024 prevented further experiments, but the results of the pilot study indicate the potential of this labelling approach.

4.2.4. Establishing a liver tumour model through direct injection following limited surgical exposure

Given that the liver is a common site for colorectal cancer metastasis, we sought to establish a model of hepatic colorectal cancer metastasis. Murine injection models of liver metastasis have been established using hemi-splenic injection of cells, which results in multiple foci of disease within the liver.(320) Anticipating that we wanted to limit tumour growth to a single site in the liver in order to facilitate photolabelling, we identified direct injection into a surgically exposed liver lobe as the most appropriate model to use. Training in this was kindly provided by Jack Leslie's group at the University of Newcastle. Pilot experiments aimed to ensure injections were accurate and cells remained within the correct anatomical space, again seeking to use the IVIS platform in conjunction with CT26 GFP Luc cells. Via a small abdominal incision, the larger left lobe of the liver was exposed and CT26 GFP Luciferase gradually injected in 30 µL 30% Matrigel before wound closure.

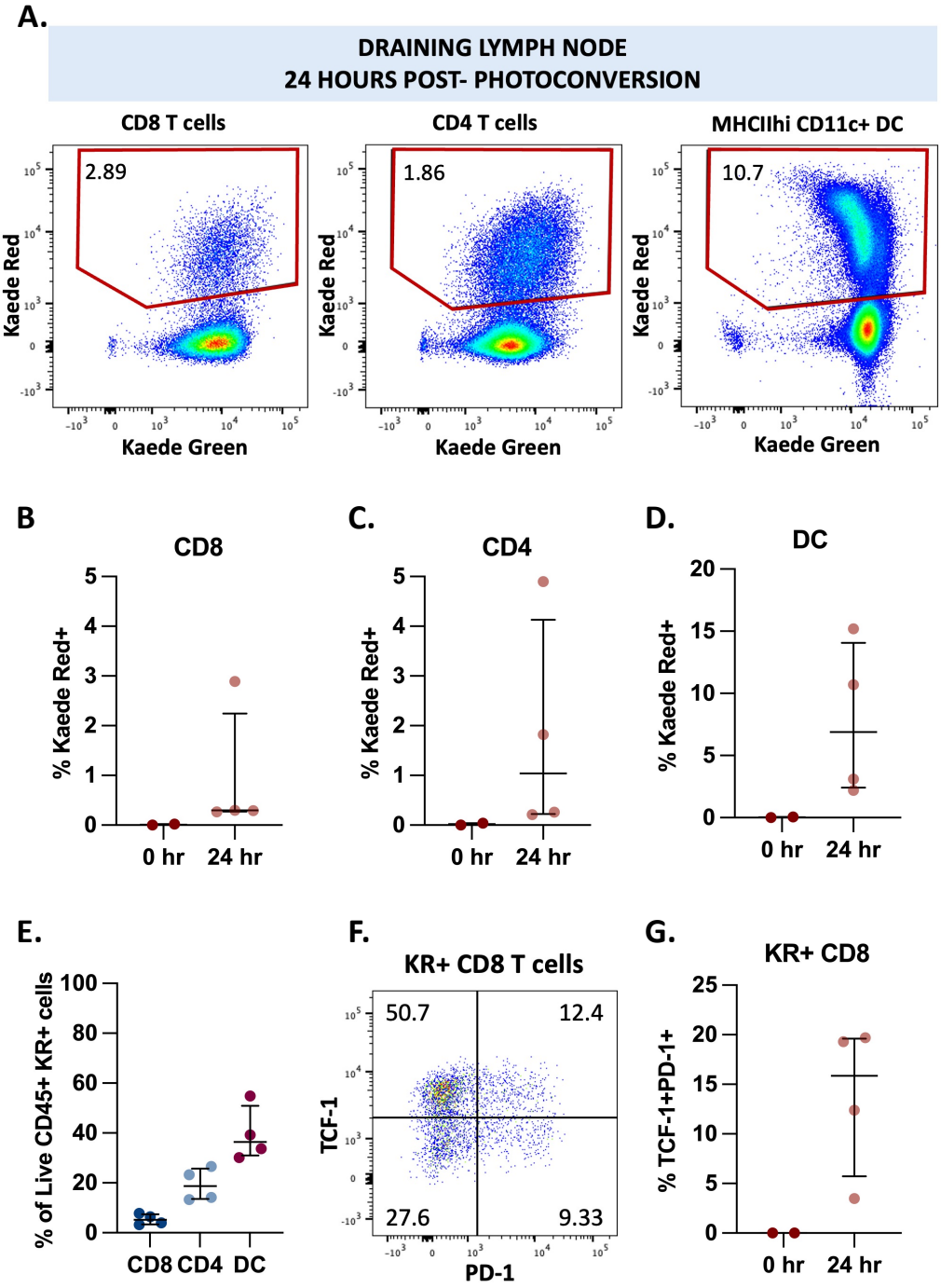

A.
DRAINING LYMPH NODE
24 HOURS POST- PHOTOCONVERSION
CD8 T cells
CD4 T cells
MHCIIhi CD11c+ DC
2.89
1.86
10.7
Kaede Red
Kaede Green
B
CD8
C.
CD4
D.
DC
% Kaede Red+
0 hr
24 hr
E.
% of Live CD45+ KR+ cells
CD8 CD4 DC
F.
KR+ CD8 T cells
50.7
12.4
27.6
9.33
TCF-1
PD-1
G.
KR+ CD8
% TCF-1+PD-1+

Figure 4.10. Studying egress of immune cells to the draining lymph node following photolabelling of colon tumours *in situ.*

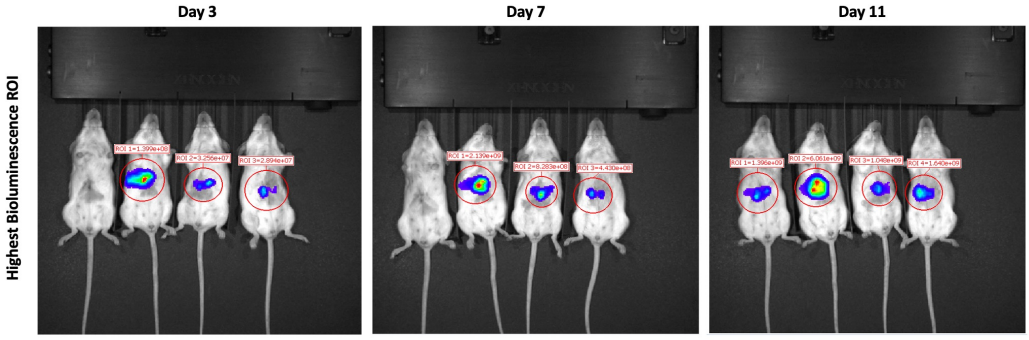
In the pilot experiment for colon tumour photoconversion, 5 x10^5 CT26 WT cells were injected into the colon wall, followed by photoconversion using a custom UV endoscope (Zibra Corp.) at day 12 post-injection. Tissues were collected either immediately after or 24 hours after photoconversion. Graphs display the median and IQR.

A. Representative flow cytometry plots demonstrating the efficiency of photoconversion through Kaede red and green expression in the CD8, CD4 and DC populations (left to right), in the dLN of a photoconverted colon tumour 24 hours following photoconversion. All flow plots are from the same mouse.
B. The proportion of Kaede red+ cells in the CD8+ T cell population within the dLN 0 and 24 hrs following photoconversion.
C. The proportion of Kaede red+ cells in the CD4+ T cell population within the dLN 0 and 24 hrs following photoconversion.
D. The proportion of Kaede red+ cells in the DC population within the dLN 0 and 24 hrs following photoconversion.
E. The proportion of Kaede red+ CD45+ cells within the dLN that are CD8+, CD4+ or MHCIIhi CD11c+ DC, 24 hours following photoconversion.
F. Flow cytometry plot demonstrating TCF-1 and PD-1 expression in the KR+ CD8+ T cell population in the dLN 24 hours after photoconversion.
G. The proportion of TCF-1+ PD-1+ cells in the KR+ CD8+ T cell population within the dLN 0 and 24 hrs following photoconversion.

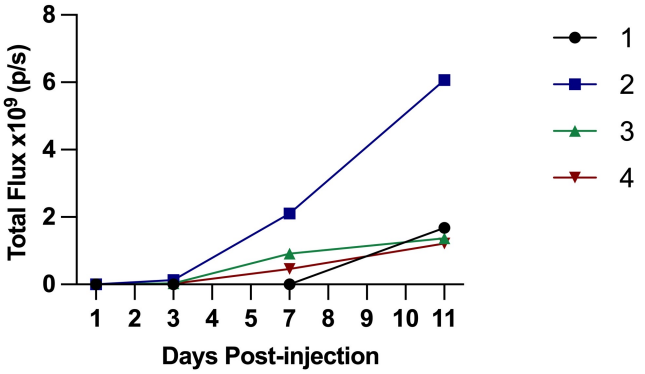
IVIS imaging of the animals on days 3, 7 and 11, showed localised hepatic bioluminescent signal, providing important evidence that cells had not 'leaked' into the abdominal cavity post-injection (Fig. 4.11A). By day 11, all four animals in the pilot experiment demonstrated bioluminescence in the liver, with a gradual increase in signal per ROI with time (Fig. 4.11B). Tissues were collected two weeks after injection and in each animal injected there was a discrete tumour mass growing within the largest lobe of the liver, with consistent tumour weights within 0.073g variation (Fig. 4.11C-D).

Colorectal cancer cell lines were initially injected using a 30% Matrigel carrier to minimise the risk of cells leaking back into the abdominal cavity, as advised by researchers at University of Newcastle. However, Matrigel may influence cell trafficking into and out of the tumour mass, which is the key focus of this work. Therefore, it was of interest to investigate whether tumour cells could be injected without the use of Matrigel, instead using the normal PBS carrier used throughout this thesis. IVIS demonstrated that there was no leakage of cells into the abdominal cavity with PBS carrier, and there was a similar gradual increase in bioluminescent signal in the liver with PBS and 30% Matrigel (Fig. 4.12A-C); in addition, the final weight of the excised tumours was not significantly different between the two groups (Fig. 4.12D). Flow cytometry was used to identify and phenotype CD8 T cells within the liver tumours (Appendix 3.3). The proportion and density of CD8 T cells within liver tumours was consistent regardless of the cell carrier used (Fig. 4.13A-B). Finally, CD8 T cell phenotype was unchanged by the cell carrier, with high levels of co-inhibitory receptor, TOX and CD69 expression, and reduced expression of TCF-1 and CD62L (Fig. 4.13C-I). Collectively, these data demonstrate the successful growth of tumours in the

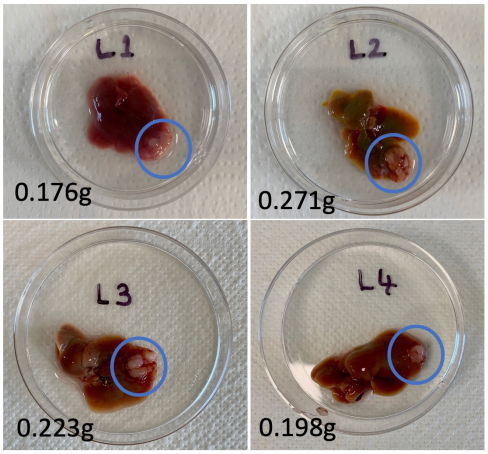
A.


Day 3
Day 7
Day 11
Highest Bioluminescence ROI

B.


Total Flux x10⁹ (p/s)
8
6
4
2
0
1 2 3 4 5 7 8 9 10 11
Days Post-injection
1
2
3
4

C.


L1
0.176g
L2
0.271g
L3
0.223g
L4
0.198g

D.

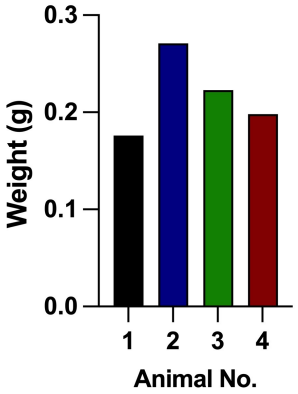
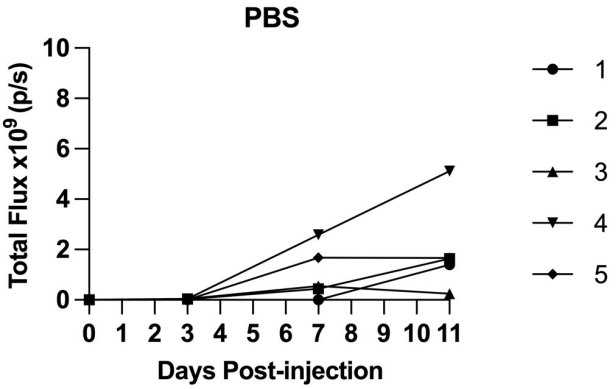

Weight (g)
0.3
0.2
0.1
0.0
1 2 3 4
Animal No.

Figure 4.11. Monitoring the growth of CT26 GFP Luc liver tumours using IVIS.

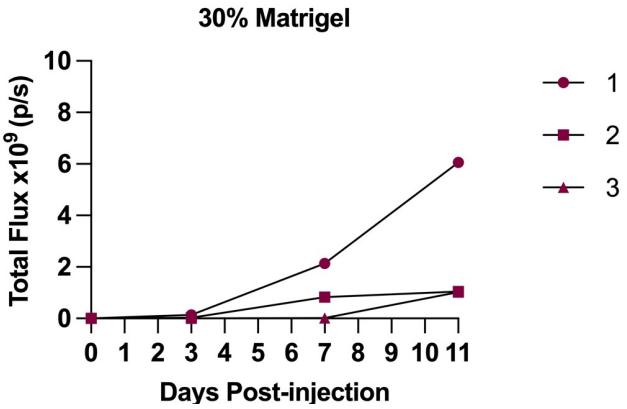
In this pilot experiment, BALB/c Kaede mice (12 weeks) were injected with 2.5 x10^5 CT26 GFP Luc cells in 30% Matrigel into the liver lobe. IVIS imaging was conducted on day 3, 7, and 11 post-injection. Tissues were collected on day 14 post-injection of tumour cell lines. Data shown is from one pilot experiment. Individual data points for each mouse are shown. IVIS images are collected and exported using LivingImage software.

A. IVIS images of the same mice at different timepoints (days 3, 7, and 11) after injection.
B. The maximum reading for total flux (p/s) in the liver tumour ROI plotted against the days post-injection. The maximum total flux reading reached on each day is recorded for each mouse, paired data is demonstrated with a line between points over time.
C. Images of the liver tumours (circled in blue) within the liver *ex vivo*. Recorded on each image is the weight (g) of the liver tumour once excised from the surrounding tissue.
D. The weight (g) of the CT26 GFP Luc liver tumour plotted for each mouse in the pilot experiment.

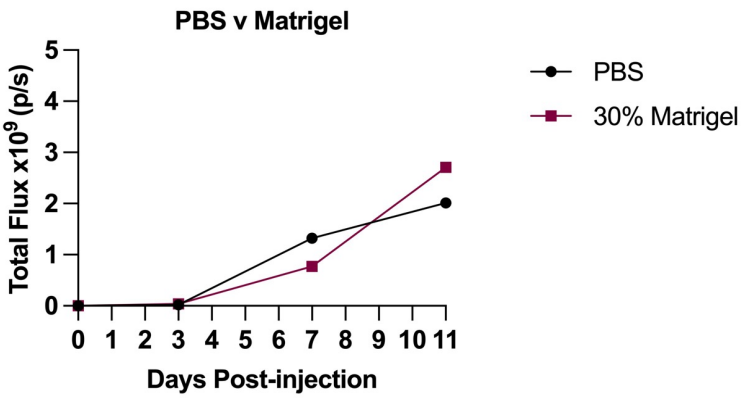
A.


PBS
Total Flux x10^9 (p/s)
0
2
4
6
8
10
0 1 2 3 4 5 6 7 8 9 10 11
Days Post-injection
1
2
3
4
5

B.


30% Matrigel
Total Flux x10^9 (p/s)
0
2
4
6
8
10
0 1 2 3 4 5 6 7 8 9 10 11
Days Post-injection
1
2
3

C.


PBS v Matrigel
Total Flux x10^9 (p/s)
0
1
2
3
4
5
0 1 2 3 4 5 6 7 8 9 10 11
Days Post-injection
PBS
30% Matrigel

D.

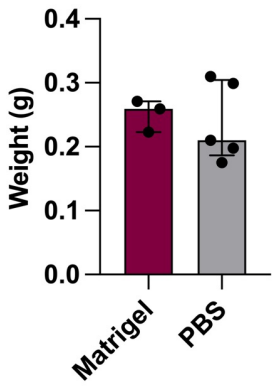

Weight (g)
0.0
0.1
0.2
0.3
0.4
Matrigel
PBS

Figure 4.12. Monitoring the growth of CT26 GFP Luc liver tumours with different cell carriers.

BALB/c Kaede mice (12 weeks) were injected with 2.5 x10^5 CT26 GFP Luc cells in 30% Matrigel or PBS carrier into the liver lobe. IVIS imaging was conducted on day 3, 7, and 11. Tissues were collected on day 14 post-injection of tumour cell lines. All CT26 GFP Luc data shown are from two independent experiments. In the case of two column analysis statistical significance was determined using a Mann-Whitney test.

A. The maximum reading for total flux (p/s) in the liver tumour ROI plotted against the days post-injection of CT26 GFP Luc in PBS carrier. Each individual mouse from the two experiments is shown.
B. The maximum reading for total flux (p/s) in the liver tumour ROI plotted against the days post-injection of CT26 GFP Luc in 30% Matrigel carrier. Each individual mouse from the two experiments is shown.
C. The median value for total flux (p/s) in the liver tumour ROI from each group (30% Matrigel carrier v PBS carrier) is plotted against the days post-injection.
D. The weight (g) of liver tumours implanted in 30% Matrigel or PBS. The weight of each individual tumour is shown, the bar represents the median value with IQR demonstrated. All tumours were collected day 14 post-injection.

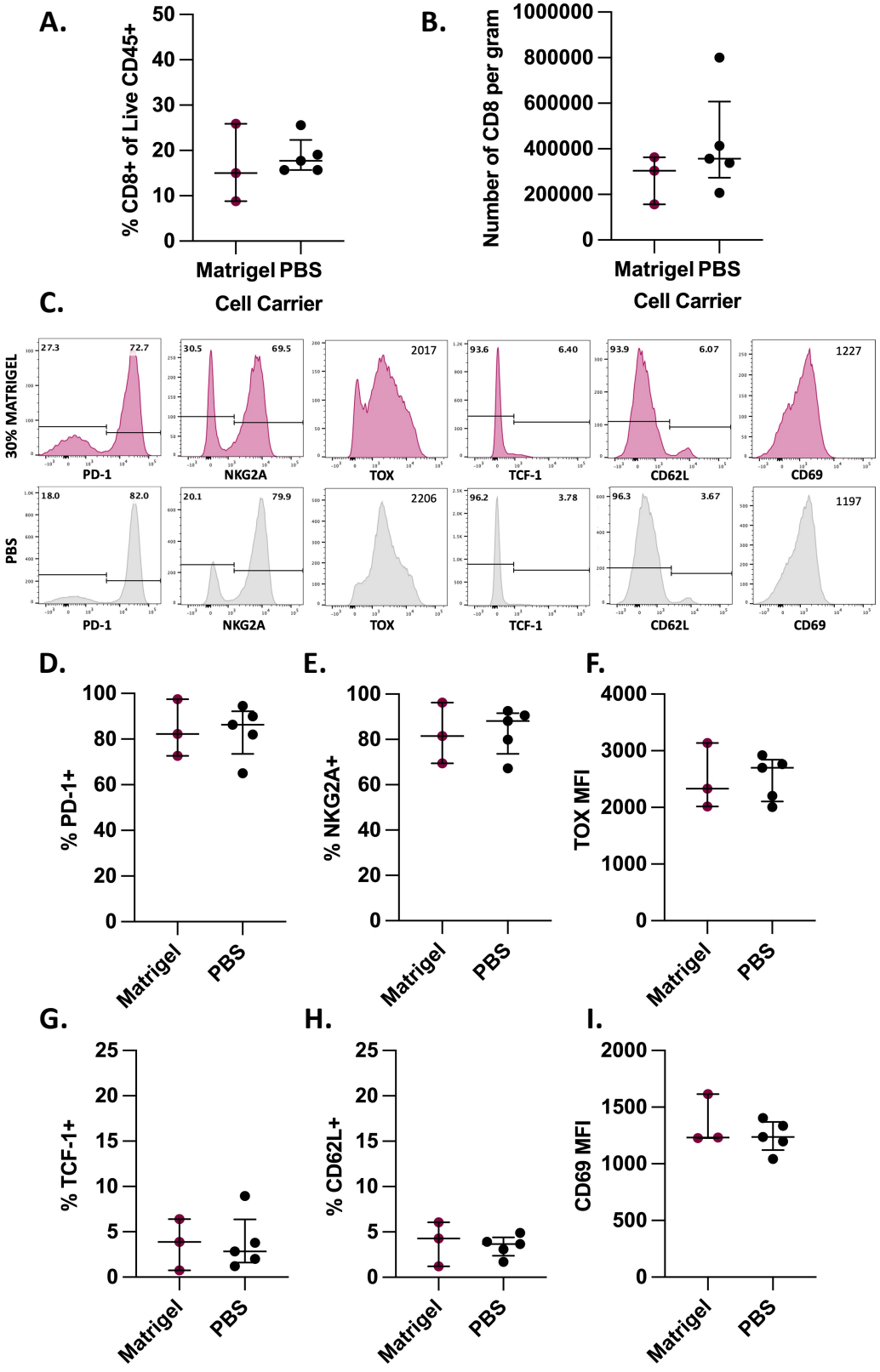

A.
% CD8+ of Live CD45+
50
40
30
20
10
0
Matrigel PBS
Cell Carrier
B.
Number of CD8 per gram
1000000
800000
600000
400000
200000
0
Matrigel PBS
Cell Carrier
C.
30% MATRIGEL
PBS
27.3
72.7
30.5
69.5
2017
93.6
6.40
93.9
6.07
1227
18.0
82.0
20.1
79.9
2206
96.2
3.78
96.3
3.67
1197
PD-1
NKG2A
TOX
TCF-1
CD62L
CD69
D.
% PD-1+
E.
% NKG2A+
F.
TOX MFI
G.
% TCF-1+
H.
% CD62L+
I.
CD69 MFI
Matrigel
PBS

Figure 4.13. Characterising the difference in the CD8 population of CT26 GFP Luc tumours implanted in the liver in Matrigel versus PBS.

BALB/c Kaede mice (12 weeks) were injected with 2.5 x10^5 CT26 GFP Luc cells in 30% Matrigel or PBS carrier into the liver lobe. IVIS imaging was conducted on day 3, 7, and 11. Tissues were collected on day 14 post-injection of tumour cell lines. All CT26 GFP Luc data shown are from two independent experiments. All graphs show the median value and IQR. In the case of two column analysis statistical significance was determined using a Mann-Whitney test. ** = $p < 0.05$.*

A. The percentage of live CD45+ cells that are CD8+ in liver tumours implanted using 30% Matrigel carrier versus PBS carrier.
B. The number of CD8+ T cells per gram of tumour, comparing liver tumours implanted using 30% Matrigel carrier versus PBS carrier.
C. Histograms demonstrating the expression of PD-1, NKG2A, TOX, TCF-1, CD62L, and CD69 in the total CD8+ T cell population in a representative CT26 WT liver tumour implanted using 30% Matrigel carrier (top row) and PBS carrier (bottom row). CD8 T cells previously gated on live CD45+ CD11b- B220- CD11c- CD3+ CD8+.
D. The percentage of CD8+ T cells that are PD-1+ in liver tumours implanted using 30% Matrigel carrier versus PBS carrier.
E. The percentage of CD8+ T cells that are NKG2A+ in liver tumours implanted using 30% Matrigel carrier versus PBS carrier.
F. The MFI of TOX in CD8+ cells in liver tumours implanted using 30% Matrigel carrier versus PBS carrier.
G. The percentage of CD8+ T cells that are TCF-1+ in liver tumours implanted using 30% Matrigel carrier versus PBS carrier.
H. The percentage of CD8+ T cells that are CD62L+ in liver tumours implanted using 30% Matrigel carrier versus PBS carrier.
I. The MFI of CD69 in CD8+ T cells in liver tumours implanted using 30% Matrigel carrier versus PBS carrier.

liver without additional peritoneal disease burden. Matrigel appeared redundant in the injection process and so was excluded to minimise potential artefacts of injecting this medium, in particular the possible effects on immune cell migration.

The spatial organisation of CD8 T cells was characterised, using the same fixation and staining methods as previous. Pancytokeratin was used to highlight the surrounding liver tissue, with the tumour clearly demonstrated through bright DAPI staining and complete absence of cytokeratin (Fig. 4.14A). As per CRC cell lines grown both subcutaneously and within the colon, the greatest number of CD8 T cells appeared to congregate at the tumour-liver parenchyma border (Fig. 4.14B); with fewer CD8 T cells also found throughout the tumour mass (Fig. 4.14C). Thus, no gross differences in the recruitment of CD8 T cells into the liver tumour were evident.

4.2.5. Establishing a model to track the migration of immune cells in liver tumour models

To better understand the effect that liver tumours have on the systemic anti-tumour immune response, it would be advantageous to be able to trace lymphocyte egress and ingress from liver tumours. Therefore, we sought to adapt the Kaede tumour photolabeling model previously deployed by the group, to enable the same tracking of lymphocytes into and out of liver tumours. Initial experiments to establish this model involved implanting colorectal tumour cells within the liver as before (4.2.4.), then at day 12 of tumour growth another small abdominal incision was made to allow the tumour bearing lobe of the liver to be re-exposed (Fig. 4.15A). Upon re-exposure a black guard was placed over the surrounding liver tissue so that only the liver tumour was exposed, tumour tissue was then

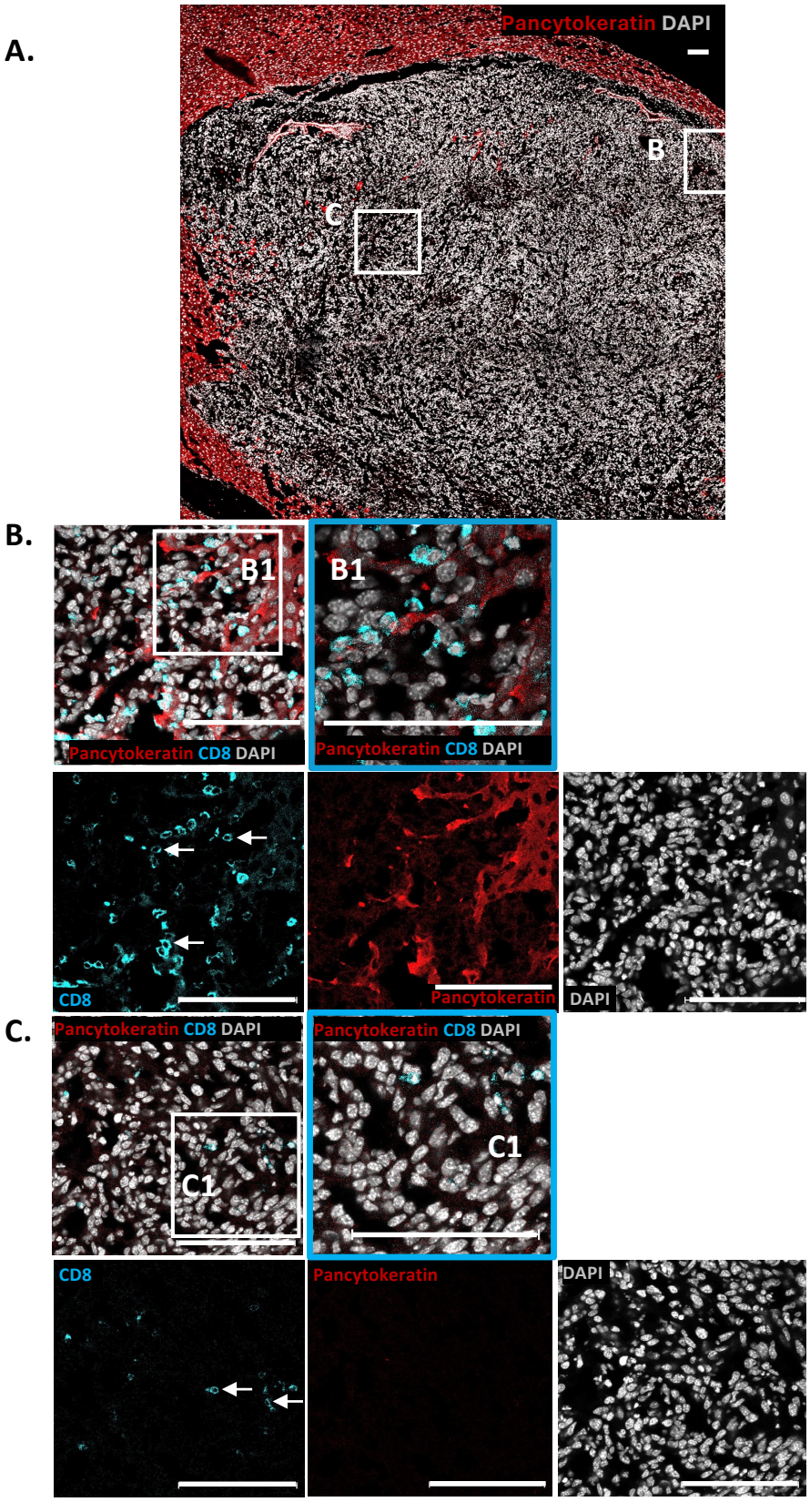
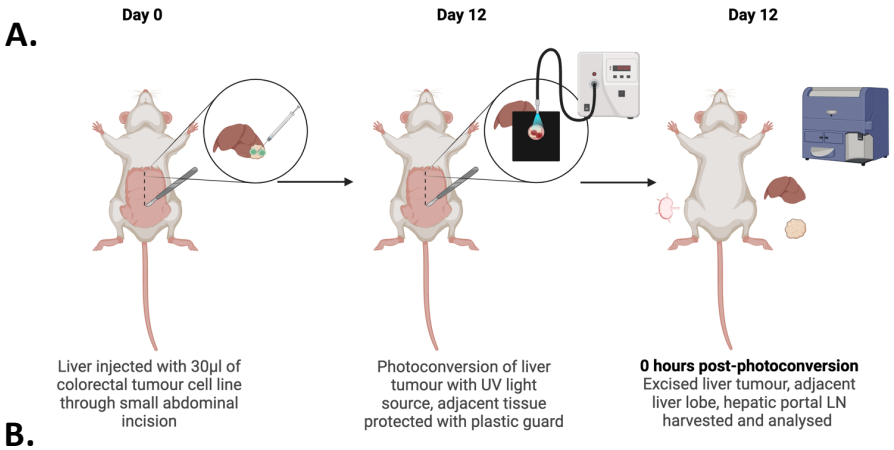
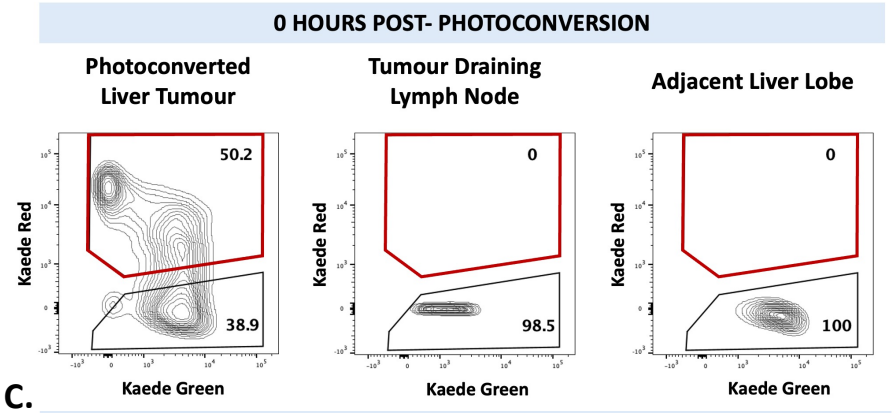

A.
Pancytokeratin DAPI
B
C
B.
B1
B1
Pancytokeratin CD8 DAPI
Pancytokeratin CD8 DAPI
CD8
Pancytokeratin
DAPI
C.
Pancytokeratin CD8 DAPI
Pancytokeratin CD8 DAPI
C1
C1
CD8
Pancytokeratin
DAPI

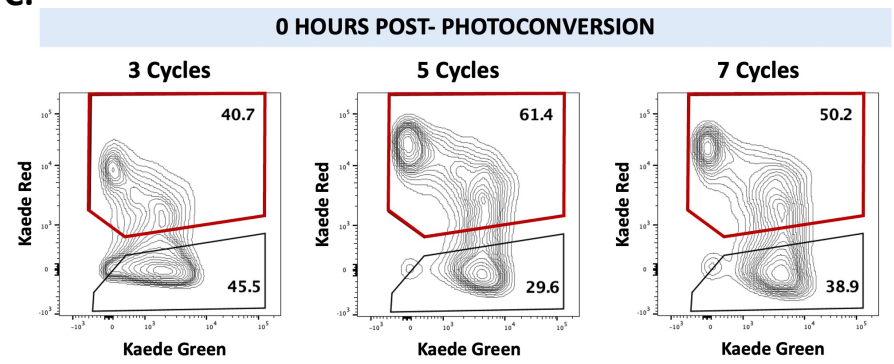
Figure 4.14. Examining the spatial distribution of T cells in liver tumour models.

Immunofluorescent microscopy of a CT26 WT tumour embedded in the liver lobe of a BALB/c WT mouse (n=3). Sections were stained for pancytokeratin, CD8 and counterstained with DAPI to allow CD8 T cells within the tissue to be identified. Representative images shown. All scale bars represent 100μm. DAPI is shown in grey, pancytokeratin is shown in red, and CD8 show in cyan.

A. x25 tile scan of a CT26 WT liver tumour. White boxes B and C represent the ROIs shown in figures B and C at higher magnification.
B. x40 image of the edge of a liver tumour (labelled in figure A). The ROI highlighted in the top left image B1, is shown zoomed in highlighted in blue on the right. Arrows mark CD8 T cells.
C. x40 image of the middle of a liver tumour (labelled in figure A). The ROI highlighted in the top left image C1, is shown zoomed in highlighted in blue on the right. Arrows mark CD8 T cells.


A.
Day 0
Day 12
Day 12
Liver injected with 30µl of colorectal tumour cell line through small abdominal incision
Photoconversion of liver tumour with UV light source, adjacent tissue protected with plastic guard
0 hours post-photoconversion
Excised liver tumour, adjacent liver lobe, hepatic portal LN harvested and analysed


B.
0 HOURS POST- PHOTOCONVERSION
Photoconverted Liver Tumour
Tumour Draining Lymph Node
Adjacent Liver Lobe
Kaede Red
Kaede Green
50.2
38.9
0
98.5
0
100


C.
0 HOURS POST- PHOTOCONVERSION
3 Cycles
5 Cycles
7 Cycles
Kaede Red
Kaede Green
40.7
45.5
61.4
29.6
50.2
38.9

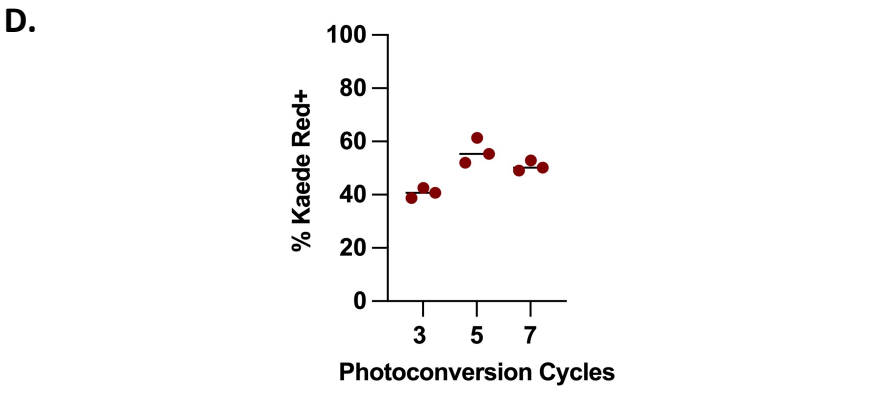

D.
% Kaede Red+
100
80
60
40
20
0
3
5
7
Photoconversion Cycles

Figure 4.15. Photolabelling of liver tumours *in situ.*

In the pilot experiment for liver tumour photoconversion, 2.5 x10^5 CT26 WT cells were injected into the liver, followed by photoconversion using the Dymax BlueWave QX4 system at day 12 post-injection. Tissues were collected immediately after photoconversion. Anatomically distinct adjacent liver lobes and dLNs acted as a control for the contamination of surrounding tissue during the photoconversion procedure. Graphs display the median.

A. Illustration of the timeline of initial liver tumour photoconversion experiments. Created using Biorender.com.
B. Representative flow cytometry plots demonstrating the efficiency of photoconversion through Kaede red and green expression in the CD8 T cell population 0 hours following photoconversion; shown, left to right, are a photoconverted liver tumour, the dLN of a photoconverted liver tumour, and an unphotoconverted adjacent liver lobe.
C. Representative flow cytometry plots demonstrating the efficiency of photoconversion with varying exposure times to UV light source, Kaede red and green expression by CD8 T cells are shown in a photoconverted liver tumour exposed for 3, 5 and 7 cycles respectively.
D. The percentage of CD8+ T cells that are Kaede red+ in liver tumours exposed to UV light for different lengths of time. This data reflects Kaede red labelling immediately following photoconversion.

exposed to UV light for different lengths of time; tissues were collected immediately following the photolabeling procedure to allow labelling efficiency to be assessed (Fig. 4.15A). Immediately following photolabeling of the liver tumour it was clear that over half of the intratumoural CD8 T cells were labelled, in addition there was no bystander labelling of the adjacent liver nor tumour dLN (Fig. 4.15B). The most appropriate number of UV light cycles was found to be 5, as the labelling efficiency improved up until that point before plateauing at 7 cycles (Fig. 4.15C-D). It was a concern that direct exposure of internal tissues to the UV light source would cause damage, but the proportion of live CD45+ cells was comparable between photoconverted and non-photoconverted liver tumours, and health of the animals was maintained following the procedure.

Immunofluorescence confocal microscopy was used to assess the spatial organisation of photolabelled T cells within liver tumours and enable us to explore whether this approach could label T cells centrally in liver tumours. In all the following experiments described tumours were photoconverted and tissues collected 24 hours after. Tissues were fixed using the methods shared with us by the Anderson group in Birmingham ensuring fluorescent reporters were conserved;(326) samples then had to be stained and imaged within 72 hours of photoconversion. In subcutaneously injected CT26 WT tumours, Kaede expression by host tissues allowed a simple means of differentiating tumour cells from host cells (Fig. 4.16A). Effective photolabeling of T cells was apparent upon imaging, with most of the T cells at the border of the tumour labelling Kaede red, and many of the T cells at the centre of the tumour also Kaede red+ (Fig. 4.16B-C). Microscopy controls, both positive and negative, for Kaede are shown in Appendix 3.4. The same experiment was also

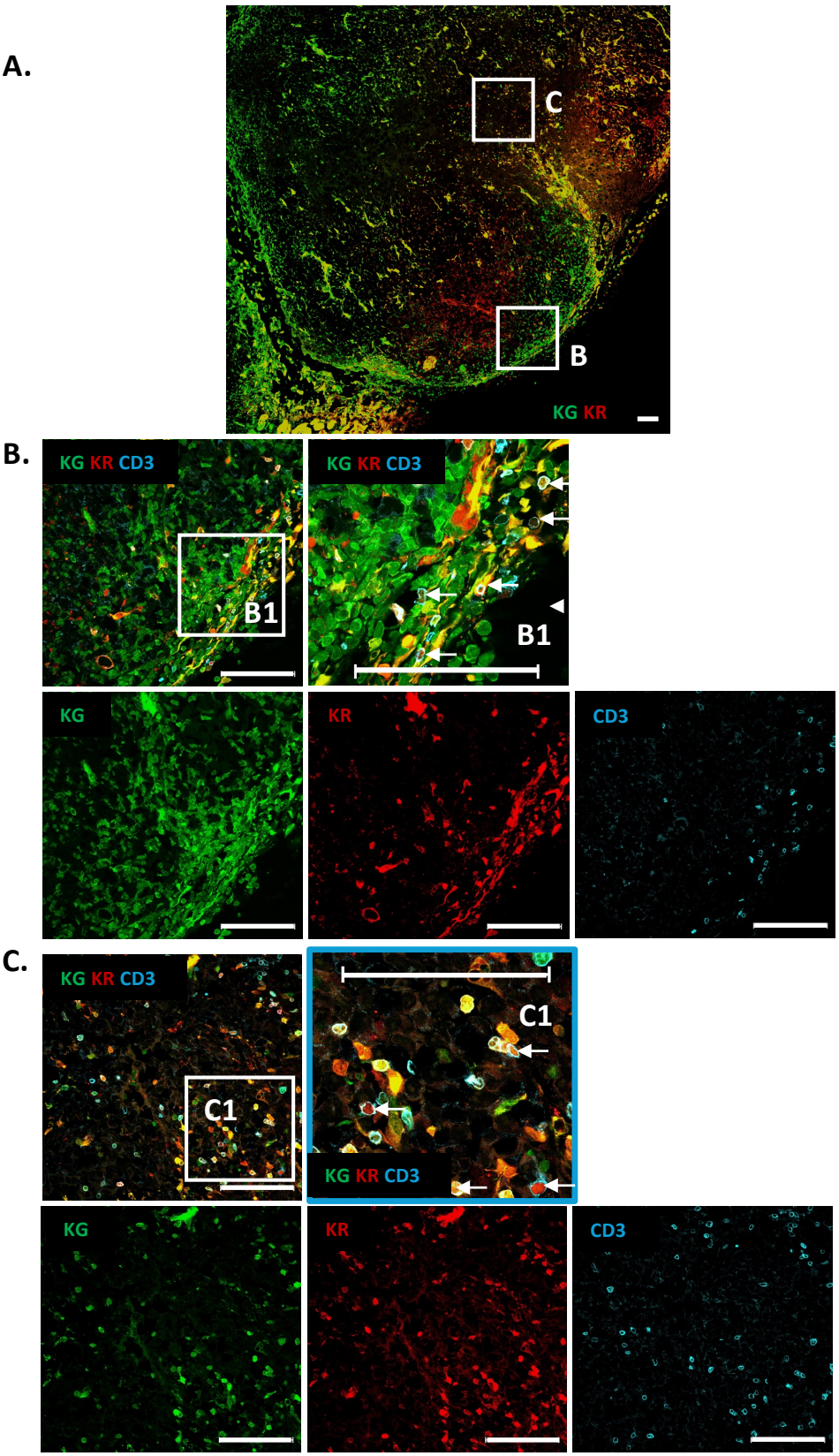

A.
C
B
KG KR
B.
KG KR CD3
B1
KG KR CD3
B1
KG
KR
CD3
C.
KG KR CD3
C1
C1
KG KR CD3
KG
KR
CD3

Figure 4.16. Spatial characterisation of photolabelled T cells in transcutaneously labelled subcutaneous tumours.

Immunofluorescent microscopy of a photoconverted CT26 WT tumour implanted subcutaneously in a BALB/c Kaede mouse, 24 hours after photoconversion (n=3). Sections were stained for CD3 and counterstained with DAPI. Kaede green and Kaede Red reflect the natural fluorescence of the tissue. Representative images are shown. All scale bars represent 100µm. Kaede green is shown in green, Kaede red in red, and CD3 in cyan.

A. x25 tile scan of a CT26 WT photoconverted s.c. tumour. White boxes B and C represent the ROIs shown in figures B and C at higher magnification.
B. x40 image of the edge of a photoconverted s.c. tumour (labelled in figure A). The ROI highlighted in the top left image B1, is shown zoomed in highlighted in blue on the right. Arrows mark photoconverted Kaede red+ CD3 T cells.
C. x40 image of the middle of a photoconverted s.c. tumour (labelled in figure A). The ROI highlighted in the top left image C1, is shown zoomed in highlighted in blue on the right. Arrows mark photoconverted Kaede red+ CD3 T cells.

conducted with photoconverted liver tumour tissues, Kaede expression again provided an easy means of defining tumour tissue versus liver parenchyma (Fig. 4.17A). Although the vasculature sometimes obscured clear visualisation of all T cells within the image, examples of Kaede red expression by T cells within the tumour, both peripherally and centrally, were found repeatedly (Fig. 4.17B-C). The effectiveness of liver photoconversion is therefore not only quantifiable by flow cytometry but can also be visually confirmed by confocal imaging.

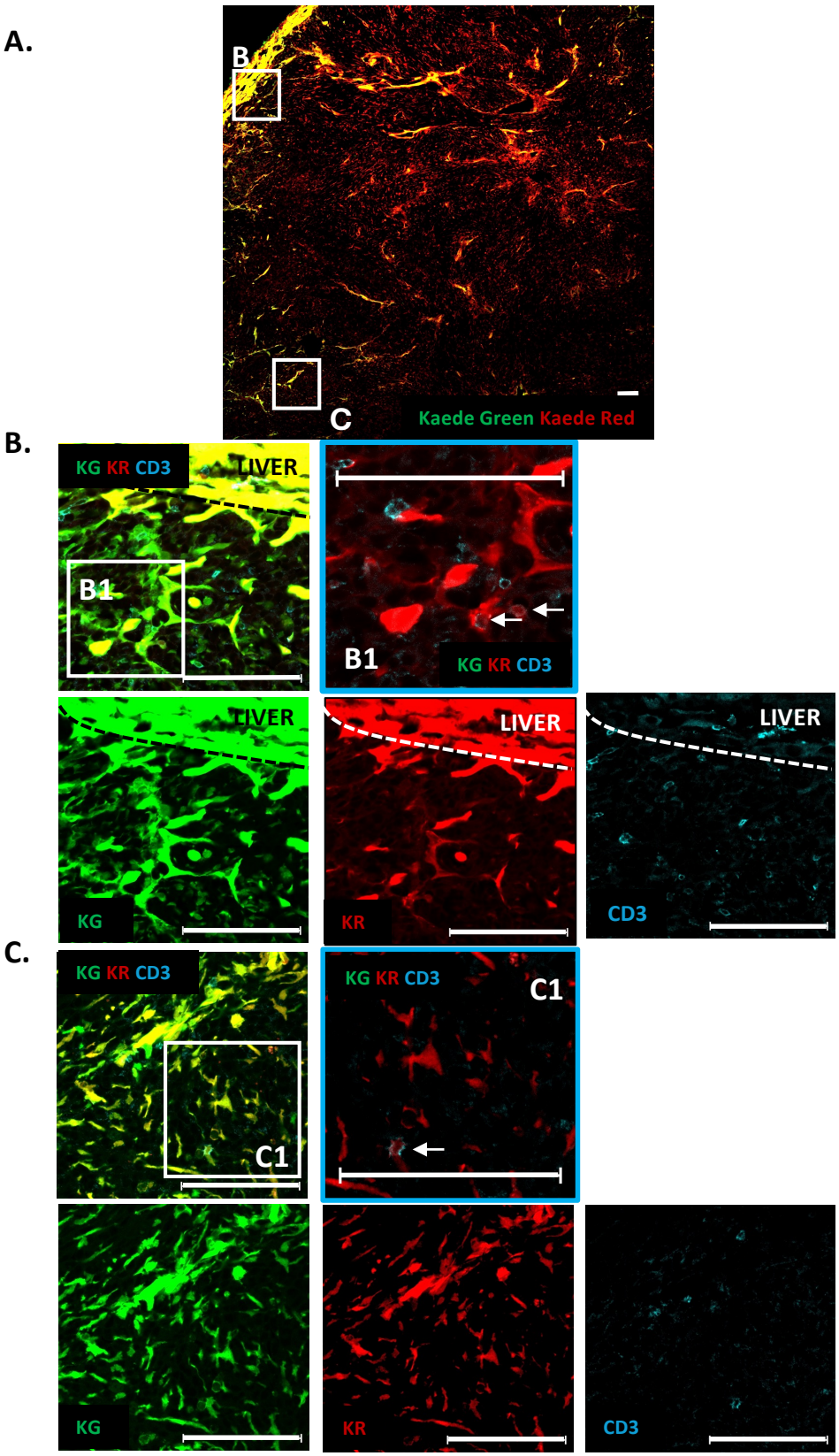

A.
B
C
Kaede Green Kaede Red
B.
KG KR CD3
LIVER
B1
B1
KG KR CD3
LIVER
KG
LIVER
KR
LIVER
CD3
C.
KG KR CD3
C1
KG KR CD3
C1
KG
KR
CD3

Figure 4.17. Spatial characterisation of photolabelled T cells in liver tumours.

Immunofluorescent microscopy of a photoconverted CT26 WT tumour embedded in the liver lobe of a BALB/c Kaede mouse, 24 hours after photoconversion (n=3). Sections were stained for CD3 and counterstained with DAPI. Kaede green and Kaede Red reflect the natural fluorescence of the tissue. Representative images are shown. All scale bars represent 100µm. Kaede green is shown in green, Kaede red in red, and CD3 in cyan.

A. x25 tile scan of a CT26 WT photoconverted liver tumour embedded within the liver parenchyma. White boxes B and C represent the ROIs shown in figures B and C at higher magnification.
B. x40 image of the edge of a photoconverted liver tumour (labelled in figure A). The ROI highlighted in the top left image B1, is shown zoomed in highlighted in blue on the right. Arrows mark photoconverted Kaede red+ CD3 T cells.
C. x40 image of the middle of a photoconverted liver tumour (labelled in figure A). The ROI highlighted in the top left image C1, is shown zoomed in highlighted in blue on the right. Arrows mark photoconverted Kaede red+ CD3 T cells.

4.3. Summary

Given the limitations of pre-clinical models of CRC using the injection of tumour cell lines subcutaneously, this chapter sought to establish approaches to implant CRC cell lines into the colon or liver with the aim of establishing more physiologically relevant models of both primary and metastatic colorectal cancer.(50, 305, 307, 308, 310, 311) Using colonoscopy-guided injection of tumour cell lines, tumours were successfully grown within the wall of the colon. Initial steps in developing the photolabelling of these colorectal tumours were also made. The establishment of tumours in the liver required surgical exposure and the development of a distinct skill set, compared to the colonoscopy required to model primary disease. Direct injection of tumour cells into the liver proved to be an efficient means of establishing liver tumours and crucially allowed precise control over where these tumours formed. Furthermore, no issues with spread of cells from the injection site into the peritoneum were observed, an initial concern given the readiness with which injected tumour cells will grow within the body cavity. While liver tumours grew rapidly, it was still possible to establish robust photolabelling of this site, providing an approach to explore immune cell egress from these tumours.

4.3.1. Immunogenicity of modified cell lines

To facilitate tracking of tumour growth in the colon and liver, we anticipated exploiting the IVIS platform, utilising a modified CT26 cell line expressing both GFP and Luciferase. Expression of Luciferase would support bioluminescence studies to track tumour growth, while the GFP expression would support the tracking of antigen-specific T cells.(327)

However, across the studies described here, the challenges with the growth of the CT26 GFP Luc cell line highlighted the importance of considering immunogenicity when modifying cell lines to aid experimental approaches. Initial efforts with CT26 GFP Luc had a high failure rate of tumour formation, which may have reflected poor injection technique. However, use of the IVIS platform to track tumour growth suggested some tumours had failed to grow after initial seeding, raising concerns over potential spontaneous rejection. To test this, we designed an experiment using subcutaneous injection of both WT CT26 and CT26 GFP Luc within the same host and assessed the subsequent response of tumours to treatment with anti-PD-L1 therapy. Even subcutaneously, the dynamics of the anti-tumour immune response was changed in CT26 GFP Luc tumours, with two doses of ICB unexpectedly clearing these tumours but not WT CT26 tumours. Consistent with the hypothesis that the modified CT26 GFP Luc cell line was driving tumour rejection, once WT CT26 cells were injected in the colon the success rate of implantation, in terms of the number of mice injected that successfully grew colonic tumours, increased from 20% to 66%. Interestingly, the CT26 GFP Luc cell line was not spontaneously rejected when injected intrahepatically, consistent with the liver environment being naturally immunosuppressive.(328) Initial pilot experiments establishing tumours within the liver used Matrigel as a cell carrier, but due to concerns over the impact of Matrigel on immune cell migration, it was of interest to establish whether a PBS carrier could instead be used. The choice of cell carrier did not alter the growth of tumours nor the phenotype of intratumoural CD8 populations, therefore the use of a carrier medium was deemed redundant.

The growth kinetics of tumours implanted within alternative sites in this work perfectly demonstrates the altered immune environment in different tissues.(317) The same number of tumour cells implanted intrahepatically produced much larger tumours than when grown subcutaneously. Whereas to produce tumours of the same size in the colon wall, the number of tumour cells injected had to be doubled versus subcutaneously. Tumour growth within the liver seemed more rapid than within the colon or subcutaneously, this may have been due to a combination of increased vascularisation and the natural immunosuppressive liver environment. Collectively, this work has highlighted the importance of using unmodified cell lines where possible to reduce impacts on tumour immunogenicity, and reducing the use of modified media where there is limited clear benefit to reduce potential artefacts. Furthermore, titration of cell numbers for each tissue site is needed to control for differing tissue-specific growth kinetics.

4.3.2. Orthotopic and subcutaneous tumours have comparable CD8 T cell compartments

Having established tumours within the colon and liver, we were then able to ask whether the CD8 T cell compartment was grossly altered when the WT CT26 cell line grew in specific tissues. Surprisingly, and despite evidence that location influences tumour growth, there was little proof that the phenotype or location of intratumoural CD8 T cells was altered, at least by the parameters considered here. Across tumour sites, flow cytometric analysis revealed a comparable level of expression of key markers PD-1, TOX, TCF-1 and CD69, including TOX+ PD-1hi cells characteristic of exhaustion. The proportions of exhausted T cells and the specific stem-like compartment appeared similar, indicating that the CD8 compartment of colon and liver tumours was not significantly different to tumours

implanted subcutaneously. Important to note, this analysis lacks markers of T cell function, such as IFNγ or granzyme production, which may be altered by the site of tumour implantation. Ultimately, it appears as though the CD8 population within colon and liver tumours is committed to the same fate as in subcutaneous tumours, with exhausted CD8 T cells comprising most of the infiltrate.(132, 286, 329) Of course, whether other immune populations differ, thinking in particular of innate cells, remains to be assessed.

While flow cytometry provides detailed phenotypic characterisation of T cells within the tumour, it does not provide information on their location. To assess whether there were differences in T cell penetration into the tumour core dependent on site, immunofluorescence microscopy was used to examine the distribution of T cells within tumours. Within subcutaneous, colon and liver tumour models studied there was a peripheral enrichment of CD8 T cells at the tumour-tissue border. However, T cells were also found throughout the tumour in the cell line models developed here. In this way the model is not reflective of the majority of colorectal cancers or their subsequent metastasis in humans, as pMMR CRC accounts for most disease and is defined by a reduced immune infiltrate and limited responsiveness to ICB.(250, 251, 330) The use of cell lines appears to result in fast growing tumours regardless of site, and this likely contributes to a failure in modelling human disease and establishment of the mechanisms that impede the T cell response. The key to more accurately modelling anti-tumour immune responses may still be in using orthotopic models, but instead choosing slower models of disease such as mouse derived organoids from spontaneous tumours.(331) Aside from slowed growth kinetics, orthotopic organoid models have been shown to contain a more developed

stromal compartment, as well as naturally metastasising, both important considerations in pre-clinical cancer models.(324, 331, 332) Further consideration of the stromal compartment of the orthotopic tumours is a key area of future work and remains understudied in this chapter.

4.3.3. Photolabelling of orthotopic tumours

A secondary aim within this chapter was to establish a method of effectively photolabelling tumours. The dynamic labelling of the immune compartment of subcutaneous tumours revealed just how quickly T cell populations change. The data discussed in Chapter 3 highlighted the extent to which certain T cell subsets, such as the stem-like CD8 compartment, are able to disseminate. Currently, it is unclear whether the recirculation of CD8 T cell populations is a feature of subcutaneous models or tumours in general. Therefore, to explore cell dynamics in more physiological tumours, we wanted to develop the same photolabelling approaches in orthotopic models which has never been done before. Unlike the photolabelling of subcutaneous tumours in Chapter 3, in which complete photoconversion of the intratumoural immune compartment is regularly achieved, so far this was not possible for colon or liver tumour models.(286) Part of the challenge here was the rapid growth of tumours within the colon and liver, alongside the limited tumour measurements possible prior to labelling. Due to the incomplete labelling, studying the retention or entry of immune cells into the primary tumour mass is limited. However, clear Kaede red labelling was still achieved in the intratumoural immune population such that the egress of cells could be studied, and traffic of both T cells and DCs from the colon tumour to the dLN was evident. Building on our recent studies of DC

retention and egress from subcutaneous MC38 tumours, it would be interesting to explore whether DC behaviour in orthotopic tumour models was similar.(83) Interestingly, there was clear evidence of stem-like CD8 migration to the dLN of CT26 WT colon tumours, supporting the data produced in Chapter 3.

Within this chapter, both colon and liver orthotopic models were successfully established alongside photolabelling approaches, enabling the study of the intratumoural CD8 population at different sites and its migration. Ultimately, the application of photolabelling to orthotopic tumour models will allow for the characterisation of immune cell migration in more anatomically relevant settings. Using this model, I aim to further investigate the CD8 response in the setting of CRC liver metastasis.

Chapter 5

Investigating the Systemic Suppression of Anti-Tumour Immunity Mediated by Liver Metastases

5.1. Introduction

Immunotherapy has had a negligible impact in the treatment of pMMR CRC.(250) Therefore, understanding the mechanisms underlying this arrested anti-cancer immune response in pMMR CRC is essential to improving patient outcomes.(250) Metastatic disease poses one of the greatest challenges in the treatment of colorectal cancer. Hepatic metastases account for over half of CRC metastases, and in this patient group the prognosis is poor, with 9-month median survival post-diagnosis.(258, 259) Liver metastases, even in more immunogenic cancers with a high TMB such as melanoma, result in poorer responses to treatment.(262-264) Furthermore, it is clear that the site of metastatic burden in CRC is key, and reduced efficacy of ICB in the presence of liver metastasis versus lung has been demonstrated clearly in the clinic.(260, 261) Treatment failure was associated with not only local progression of liver disease, but systemic disease progression. Ultimately, understanding how liver metastases mediate suppressive local and systemic changes to the anti-tumour immune response is key to facilitating therapeutic advancement for patients most in need, likely through the development of tailored immunotherapy approaches.

5.1.1. The liver is an immune suppressive environment

The immunological environment of the liver is skewed toward tolerance to prevent constant pathological inflammation in response to food antigen carried in the hepatic portal vein. The tolerogenic hepatic environment is best evidenced by successful liver transplantation with less stringent immune suppressive regimens than seen in other

transplant settings.(333) However, in the context of cancer within the liver, this tendency toward immune tolerance has negative implications. Multiple mechanisms underlie hepatic immune tolerance which are briefly outlined here.

There are fundamental differences in the immune populations within the liver. Liver resident immune cells produce anti-inflammatory cytokines (IL-10 and prostaglandins) alongside reduced levels of co-stimulatory molecules (CD80 & CD86).(334-338) Furthermore, hepatocytes themselves can be induced to express PD-L1 in response to locally produced IL-10, contributing to T cell anergy.(334, 339) Dendritic cells within the liver express lower MHC as well as co-stimulatory molecules (CD80 & CD86), and are associated with type 2 T helper (Th2) responses and regulatory T cell generation.(340-342) Tregs are thought to play an essential role in maintaining liver tolerance, and the enrichment of Tregs within the liver environment has been suggested as a reason for the poor prognosis in liver cancer.(343, 344)

In addition to underlying differences in immune populations, the stromal compartment of the liver also impacts its immunology. Hepatic stellate cells are important in the production of extracellular matrix, and also produce retinoid, which can skew CD4 T cells towards a regulatory phenotype.(345) Liver sinusoidal endothelial cells (LSECSs), forming the boundary between the hepatic circulation and hepatocytes, can act as APCs, but similar to many resident cells of the liver induce tolerance. Antigen presentation by LSECs results in tolerance, in CD8 T cells through upregulation of immune checkpoints, and a Treg phenotype is induced in CD4 T cells due to low levels of co-stimulatory molecules.(346,

347) It is clear that the liver is set up at baseline to dampen immune responses. However, precisely which mechanisms are key to driving local and systemic suppression of the anti-tumour response remains less well defined. Further insight here has the potential to support tailored immunotherapy approaches specifically for liver metastases.

5.1.2. Proposed mechanisms underlying the systemic suppressive effects of liver metastasis

In recent years, several mechanisms have been suggested to explain the apparent systemic anti-tumour immune suppressive effect of liver metastasis. In a paper published in 2021, Yu *et al.* used a pre-clinical dual liver and subcutaneous tumour model, with CRC cell lines, to highlight a potential role for macrophage populations within the liver in this phenomenon.(265) First, looking at clinical data, they highlighted that patients with liver metastases responded poorly to ICB and had diminished overall survival. The authors then demonstrated that a murine dual liver and subcutaneous tumour model could recapitulate liver tumour related systemic suppression, with the presence of liver tumours in mice preventing a response to anti-PD-L1 in a distal subcutaneous tumour. Mice bearing liver tumours were reported to have a diminished peripheral antigen-specific CD8 T cell pool, this effect was mirrored in clinical data. This diminished CD8 T cell pool was proposed to be due to monocyte-derived macrophage populations within liver tumours selectively

removing these cells from circulation through the induction of apoptosis, thus depleting systemic T cell protection.(265)

Lee *et al.* proposed a role for liver tumour Treg populations in suppression of the anti-tumour immune response.(266) The authors similarly utilised a murine dual liver and subcutaneous tumour model to demonstrate ICB failure, though melanoma rather than CRC cell lines were used. However, the loss of a peripheral anti-tumour T cell pool was not identified by the authors here. Instead, the suppression of a successful response to ICB when tumour antigen was present in the liver, was found to be linked to Treg activation. Disruption of regulatory T cell function facilitated an effect of anti-PD-L1 therapy in the setting of liver metastasis.(266) Both of these papers utilise a dual tumour model to explore the mechanisms driving systemic suppression of the anti-tumour response in the context of ICB, summarised in Figure 5.1. Given the limited studies in this important field, alongside conflicting data as to precisely why the response is suppressed, further *in vivo* experimentation is needed.

Fundamentally, substantial gaps remain in our understanding of how intratumoural T cells interface with the peripheral T cell pool and the nature of the systemic immune compartment in general. From data within our own lab, it appears that the majority of exhausted T cells remain within the tumour, but specific CD8 subsets retain migratory capacity (see Chapter 3).(286) Further experimental data is needed to confirm whether this is altered by the presence of tumour within the liver, and the additional mechanisms

involved in its suppression of the anti-tumour response. Through interrogating this, better approaches to specifically overcome this suppression can be developed.

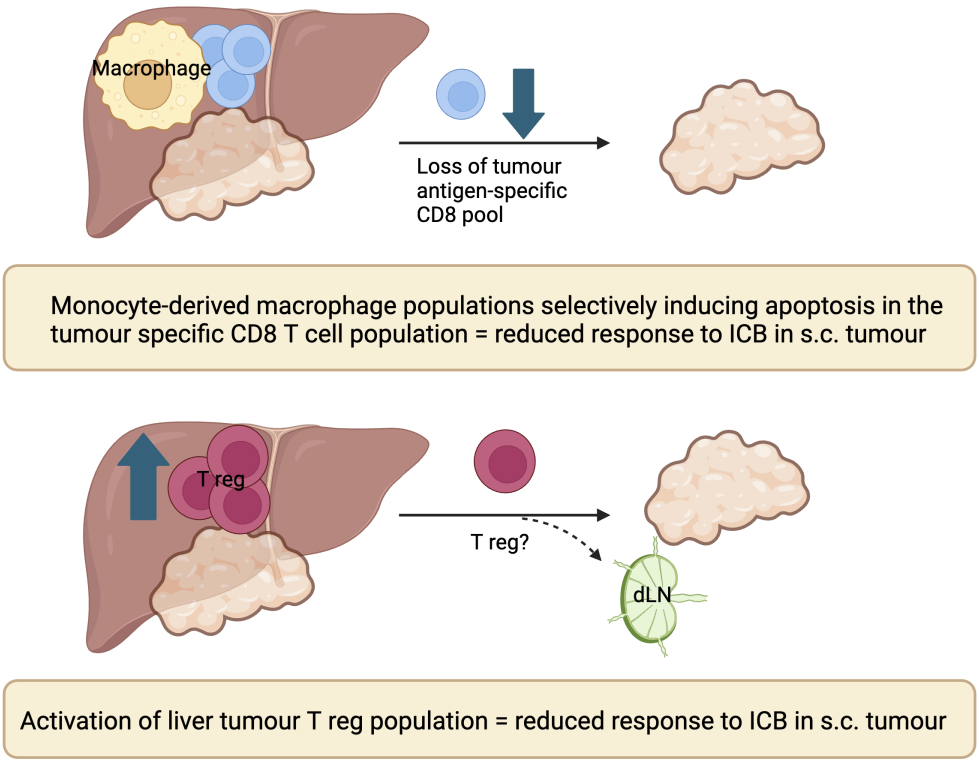


Figure 5.1. Illustration of proposed mechanisms behind the liver tumour-mediated diminished response to ICB.

Yu *et al.*'s (top model) proposed mechanism entails the depletion of tumour specific CD8 T cells by liver-resident macrophages. Lee *et al.* (bottom model) link the activation state of regulatory T cells within the liver to the decreased response to ICB at the subcutaneous site. Created using Biorender.com.

5.1.3. Aims

The experiments described in Chapters 3 and 4 were focused on establishing *in vivo* models of colorectal cancer, and utilising these to investigate the dynamics of the T cell response within primary tumours and how this linked to the systemic immune response. Different models of primary cancer, including colon and liver orthotopic models, were developed to assess potential tissue-specific effects on the nature of the T cell response. The overarching aim of this chapter was to bring together some of these experimental models to investigate the relationship between primary tumours and liver metastases and build upon recent published studies by other groups. Different mechanisms have been proposed to mediate the systemic suppression observed within simplified dual (liver and subcutaneous) tumour models. Given the huge clinical challenge of treating patients with liver metastases, here we sought to establish an *in vivo* model of liver tumour-mediated systemic immune suppression and explore cellular traffic between these tumour sites to further investigate the mechanisms that restrict the anti-tumour response.

Chapter aims:

1. Establish an *in vivo* model in which subcutaneous and liver tumours are both present, demonstrating systemic suppression of the anti-tumour response.
2. Assess whether the presence of liver tumours alters the dynamics of the T cell response in the subcutaneous tumour.
3. Investigate the direct trafficking of immune cells between the two tumour sites.
4. Test the cellular basis of systemic suppression of the anti-tumour immune response.

5.2. Results

5.2.1. Investigating the composition of intratumoural CD8 T cells in orthotopic liver models

To understand the systemic suppressive effect of liver tumours on the anti-cancer response at different sites, a dual liver and subcutaneous tumour model had to be established. The initial set up of the liver tumour model is described in further detail within Chapter 4. Having established CRC cell lines within the liver, we first sought to understand whether the intratumoural CD8 population within liver tumours versus subcutaneously implanted tumours was different. Mice were injected with 2.0 x10^5 WT CT26 cells intrahepatically or subcutaneously and tumours harvested and phenotyped using flow cytometry 12 days later. CT26 WT cells implanted within the liver grew more rapidly than when implanted subcutaneously, with liver tumours weighing significantly more at day 12 than subcutaneous tumours (Fig. 5.2A). The proportion of CD8+ T cells and their density within the tumour was slightly increased in those tumours grown within the liver versus subcutaneously (Fig. 5.2B-C). Phenotypically, looking at markers of exhaustion, activation, and migratory capacity, the CD8 T cells within CT26 tumours at both sites were comparable (Fig. 5.2D-J); with no significant difference seen between the percentage of CD8 T cells expressing PD-1, NKG2A, TCF-1, and CD62L, or the MFI of CD69 (Fig. 5.2D-H, J). FMOs are shown in Appendix 5.1. However, a difference was seen in the MFI of TOX, with the intratumoural CD8 T cells within liver tumours displaying a higher MFI than their subcutaneous counterparts (Fig. 5.2G). To further investigate this difference and what it meant for the CD8 T cell compartment, the co-expression of TOX alongside PD-1 was

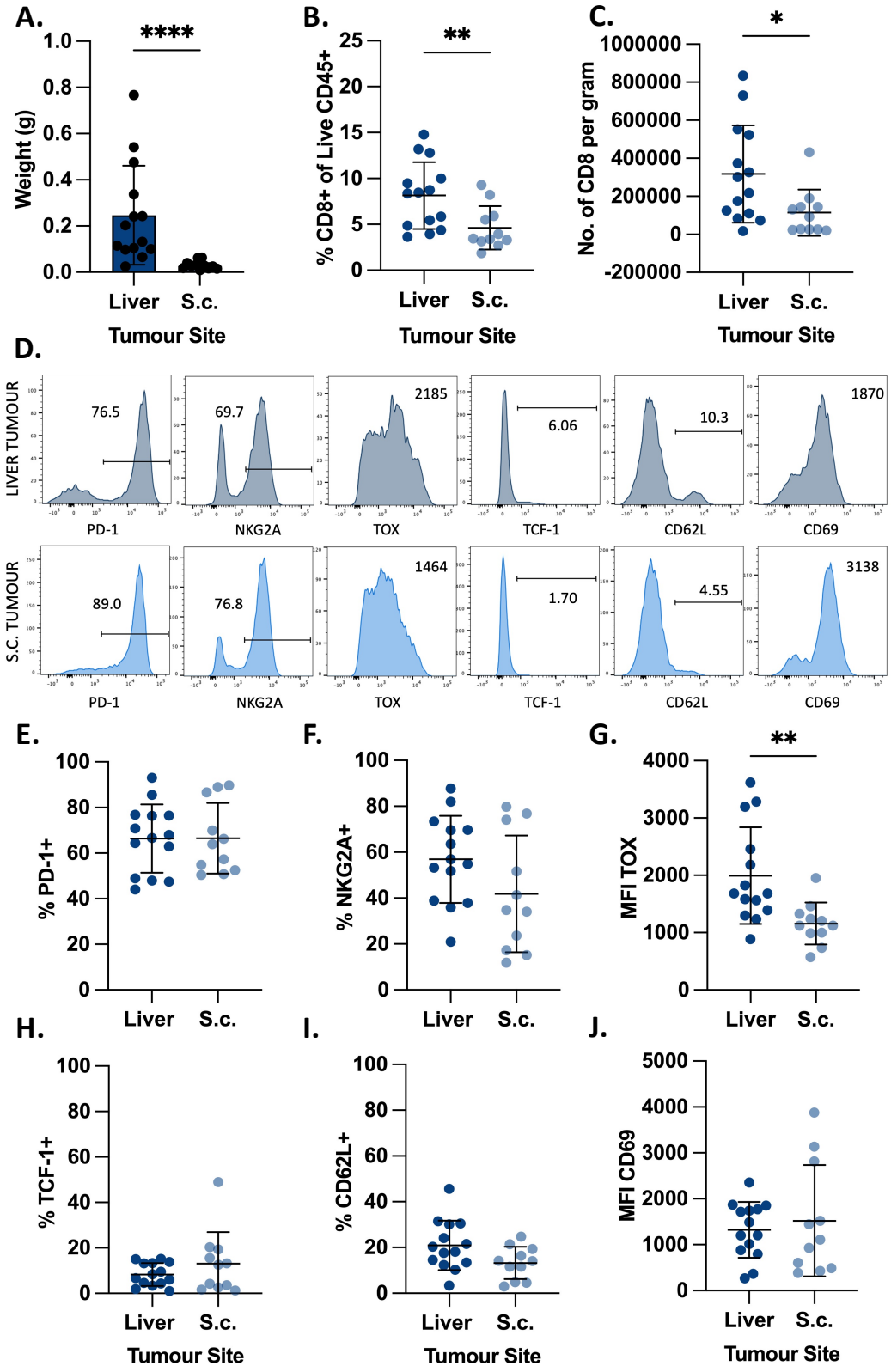

A.
****
Weight (g)
1.0
0.8
0.6
0.4
0.2
0.0
Liver
S.c.
Tumour Site
B.
**
% CD8+ of Live CD45+
25
20
15
10
5
0
Liver
S.c.
Tumour Site
C.
*
No. of CD8 per gram
1000000
800000
600000
400000
200000
0
-200000
Liver
S.c.
Tumour Site
D.
LIVER TUMOUR
76.5
69.7
2185
6.06
10.3
1870
PD-1
NKG2A
TOX
TCF-1
CD62L
CD69
S.C. TUMOUR
89.0
76.8
1464
1.70
4.55
3138
PD-1
NKG2A
TOX
TCF-1
CD62L
CD69
E.
% PD-1+
100
80
60
40
20
0
Liver
S.c.
F.
% NKG2A+
100
80
60
40
20
0
Liver
S.c.
G.
**
MFI TOX
4000
3000
2000
1000
0
Liver
S.c.
H.
% TCF-1+
100
80
60
40
20
0
Liver
S.c.
Tumour Site
I.
% CD62L+
100
80
60
40
20
0
Liver
S.c.
Tumour Site
J.
MFI CD69
5000
4000
3000
2000
1000
0
Liver
S.c.
Tumour Site

Figure 5.2. Phenotypic comparison of CD8 T cells in CT26 tumours implanted intrahepatically versus subcutaneously.

BALB/c mice (9-12 weeks) were injected with 2.0 x10^5 CT26 WT cells subcutaneously or intrahepatically. Tissues were harvested on day 12 post-injection. All data shown are from three independent experiments. All graphs show the mean ± SD. Statistical significance was determined using an unpaired *t* test. ** = p < 0.05, ** = p < 0.01, *** = p < 0.001, **** = p < 0.0001*

A. The weight (g) of CT26 tumours implanted in the liver versus subcutaneously.
B. The percentage of live CD45+ cells that are CD8+ in CT26 tumours implanted subcutaneously or intrahepatically.
C. The number of CD8+ T cells per gram of tumour in CT26 tumours implanted subcutaneously or intrahepatically.
D. Histograms demonstrating the expression of PD-1, NKG2A, TOX, TCF-1, CD62L and CD69 in the total CD8+ population in a representative CT26 WT liver tumour (top row) and subcutaneous tumour (bottom row). CD8 T cells previously gated on Live CD45+ CD11b- B220- CD11c- CD3+ CD8+.
E. The percentage of intratumoural CD8+ T cells that are PD-1+ in liver tumours versus subcutaneous tumours.
F. The percentage of intratumoural CD8+ T cells that are NKG2A+ in liver tumours versus subcutaneous tumours.
G. The MFI of TOX expression in the intratumoural CD8+ T cells in liver tumours versus subcutaneous tumours.
H. The percentage of intratumoural CD8+ T cells that are TCF-1+ in liver tumours versus subcutaneous tumours.
I. The percentage of intratumoural CD8+ T cells that are CD62L+ in liver tumours versus subcutaneous tumours.
J. The MFI of CD69 expression in the intratumoural CD8+ T cells in liver tumours versus subcutaneous tumours.

quantified. A small but significant increase in the proportion of tumour infiltrating CD8 T cells that were TOX+ PD-1+ was detected in liver versus subcutaneous tumours (Fig. 5.3A-C). In addition, the stem-like TCF-1+ PD-1+ population was examined, and there was found to be a higher infiltration of stem-like CD8 T cells within subcutaneous tumours (Fig. 5.3D-F). Whether this effect is due to the smaller tumour size, and subsequently enhanced infiltration, is uncertain.

In Chapter 3, the establishment of the stem-like CD8 T cell compartment was characterised within subcutaneous tumours by comparing this population at day 7 and 14, and a similar approach was used here within liver tumours. Comparison of tumour weights showed that both subcutaneous and liver tumours were larger at day 14 than day 7 as expected, and as previously observed liver tumours at day 14 were larger than subcutaneous tumours, though at day 7 this difference was not yet apparent (Fig. 5.4A). The proportion of CD8 T cells among live CD45+ cells in the tumour was highest in the day 14 liver tumours at around 12%, compared to the 2.5-5% observed within subcutaneous tumours and at day 7 within the liver (Fig. 5.4B). The TCF-1+ PD-1+ population within liver tumours was lower at both day 7 and 14, though the TCF-1+ PD-1+ population in subcutaneous tumours present at day 7 is PD-1 intermediate rather than high, as discussed in Chapter 3 (Fig. 5.4C & Appendix 5.2). The fact that within day 7 liver tumours this TCF-1+ PD-1+ stem-like population is PD-1 high, suggests the more rapid development of a mature phenotype in this tissue (Fig. 5.4C). The proportion of intratumoural CD8 T cells that are TIM-3+ and PD-1+ at both sites are similar, both at day 7 and day 14, but the level of PD-1 expression is higher in liver tumours at day 7 than subcutaneous tumours (Fig. 5.4D & Appendix 5.2).

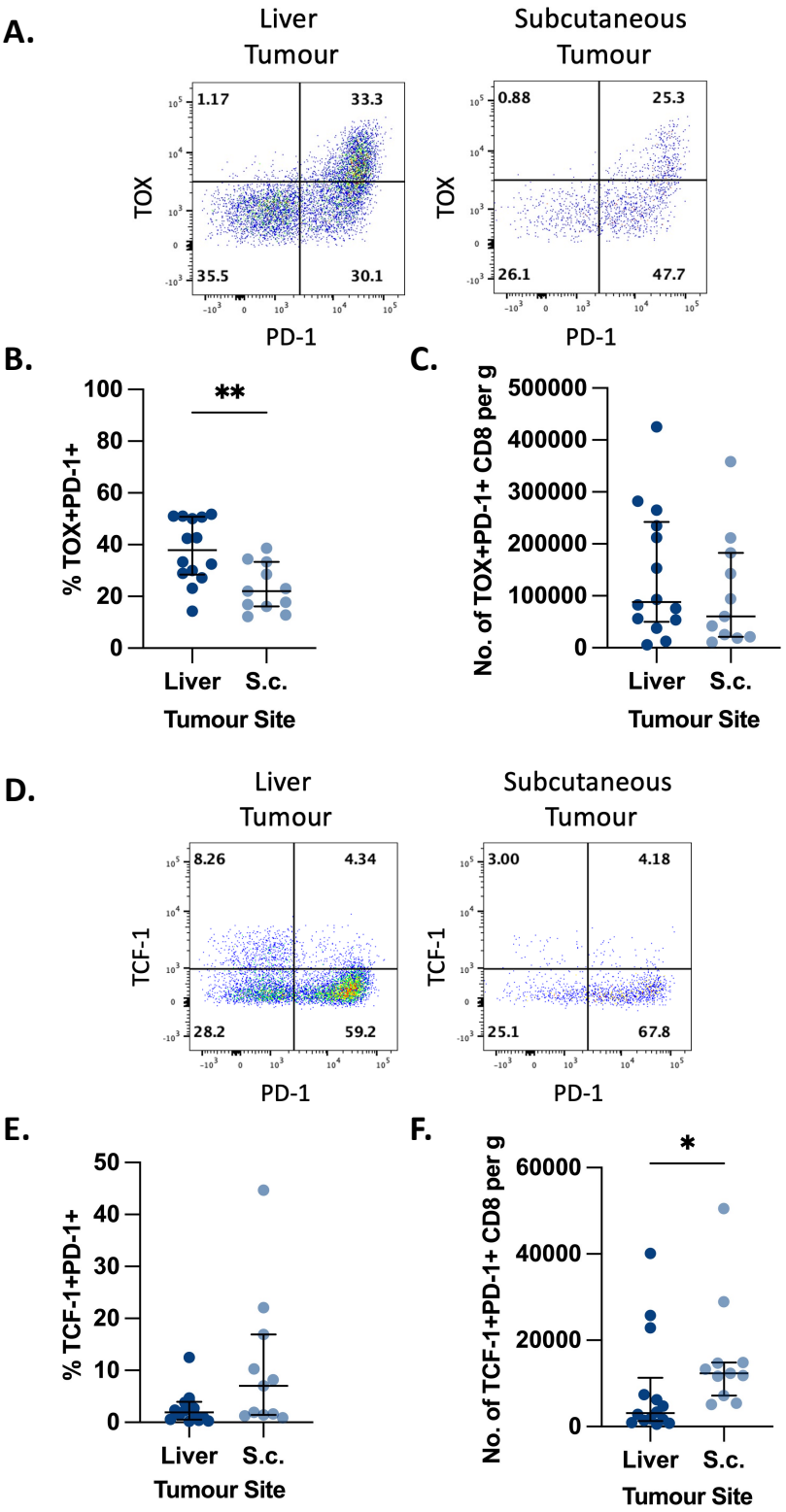

A.
Liver Tumour
Subcutaneous Tumour
1.17
33.3
35.5
30.1
0.88
25.3
26.1
47.7
TOX
PD-1
B.
% TOX+PD-1+
**
Liver
S.c.
Tumour Site
C.
No. of TOX+PD-1+ CD8 per g
D.
Liver Tumour
Subcutaneous Tumour
8.26
4.34
28.2
59.2
3.00
4.18
25.1
67.8
TCF-1
PD-1
E.
% TCF-1+PD-1+
F.
No. of TCF-1+PD-1+ CD8 per g
*

Figure 5.3. Comparison of exhausted CD8 T cell populations within tumours implanted intrahepatically versus subcutaneously.

BALB/c mice (9-12 weeks) were injected with 2.0 x10^5 CT26 WT cells subcutaneously or intrahepatically. Tissues were harvested on day 12 post-injection. All data shown are from three independent experiments. All graphs show the median and IQR. Statistical significance was determined using a Mann-Whitney. ** = p < 0.05, ** = p < 0.01*

A. Flow cytometry plots demonstrating staining and co-expression of PD-1 and TOX in CT26 liver (left) and subcutaneous (right) tumours. Flow plots are pre-gated on Live CD45+ CD11b- B220- CD11c- CD3+ CD8+ cells in a representative tumour sample.
B. The percentage of CD8+ T cells that are TOX+ PD-1+ at day 12 post-injection in liver tumours and s.c. tumours.
C. The number of TOX+ PD-1+ CD8+ T cells per gram of tumour at day 12 post-injection in liver tumours and s.c. tumours.
D. Flow cytometry plots demonstrating staining and co-expression of PD-1 and TCF-1 in CT26 liver (left) and subcutaneous (right) tumours. Flow plots are pre-gated on Live CD45+ CD11b- B220- CD11c- CD3+ CD8+ cells in a representative tumour sample.
E. The percentage of CD8+ T cells that are TCF-1+ PD-1+ at day 12 post-injection in liver tumours and s.c. tumours.
F. The number of TCF-1+ PD-1+ CD8+ T cells per gram of tumour at day 12 post-injection in liver tumours and s.c. tumours.

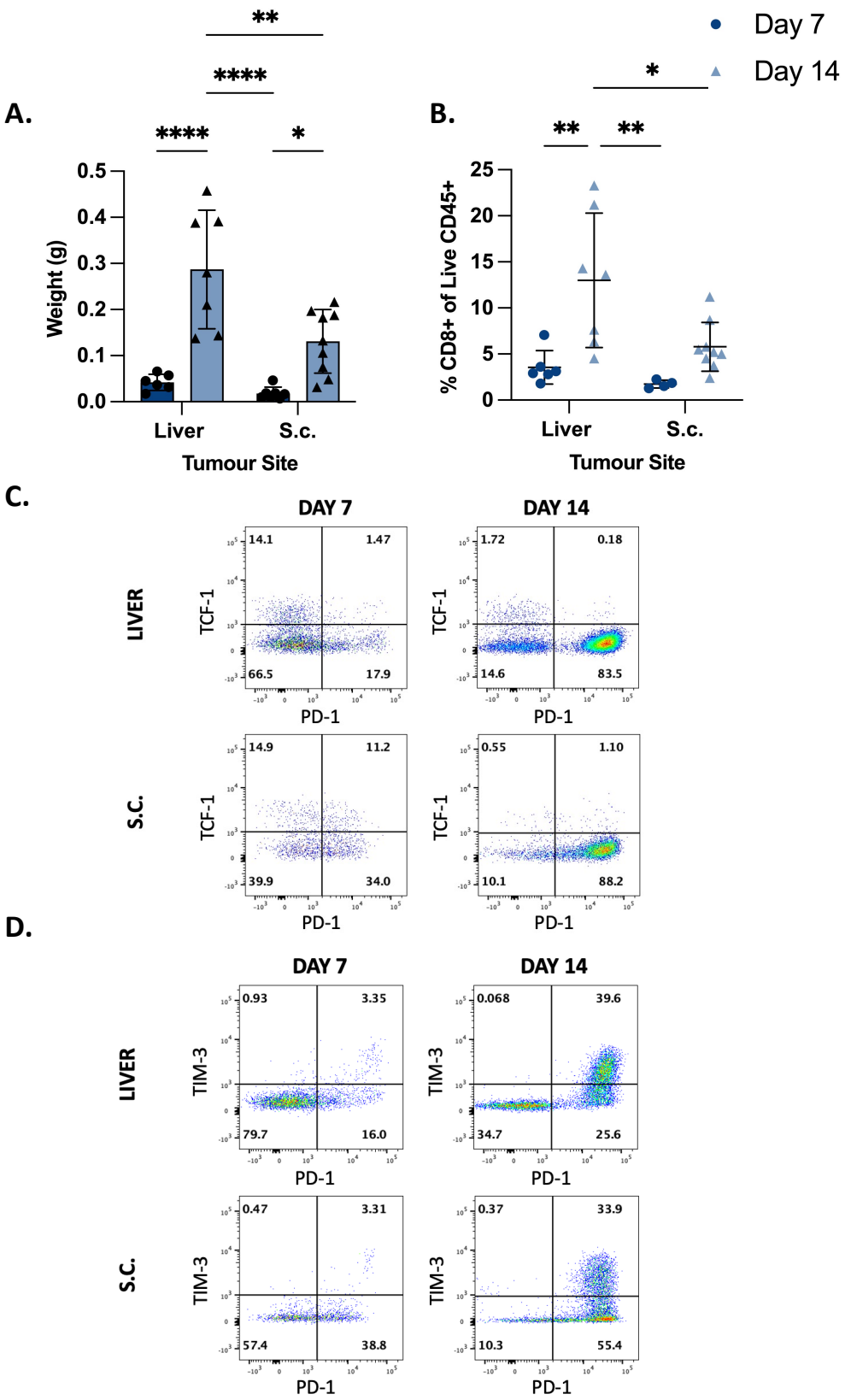

A.
B.
C.
D.
Day 7
Day 14
**
****
****
*
*
**
**
Weight (g)
0.5
0.4
0.3
0.2
0.1
0.0
Liver
S.c.
Tumour Site
% CD8+ of Live CD45+
25
20
15
10
5
0
Liver
S.c.
Tumour Site
DAY 7
DAY 14
LIVER
S.C.
TCF-1
PD-1
14.1
1.47
66.5
17.9
1.72
0.18
14.6
83.5
14.9
11.2
39.9
34.0
0.55
1.10
10.1
88.2
TIM-3
PD-1
0.93
3.35
79.7
16.0
0.068
39.6
34.7
25.6
0.47
3.31
57.4
38.8
0.37
33.9
10.3
55.4

Figure 5.4. Comparison of exhausted CD8 T cell populations in liver tumours at day 7 and 14.

BALB/c mice (9-12 weeks) were injected with 2.0 x10^5 CT26 WT cells subcutaneously or intrahepatically. Tissues were harvested on day 7 or day 14 post-injection. All data shown are from two independent experiments. All graphs show the mean ± SD. Statistical significance was determined using a 2-way ANOVA with Tukey's correction for multiple comparison. ** = p < 0.05, ** = p < 0.01, *** = p < 0.001, **** = p < 0.0001*

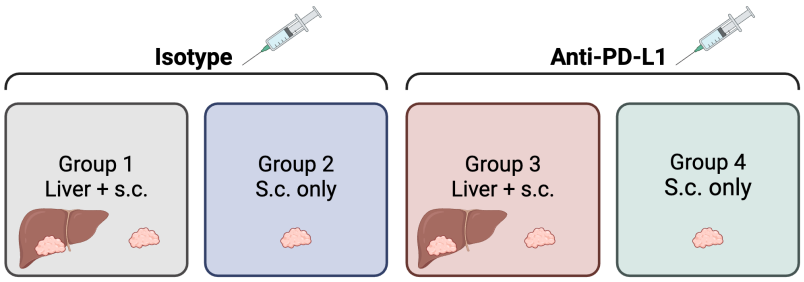
A. Comparison of the weight (g) of CT26 tumours implanted in the liver versus subcutaneously at day 7 and day 14 post-injection.
B. Comparison of the percentage of live CD45+ cells that are CD8+ in CT26 tumours implanted in the liver versus subcutaneously at day 7 and day 14 post-injection.
C. Flow cytometry plots demonstrating TCF-1 and PD-1 expression in the CD8+ populations in liver tumours (top) versus subcutaneous tumours (below), at day 7 (left) and day 14 (right). Representative tumours have been chosen at each time point.
D. Flow cytometry plots demonstrating TIM-3 and PD-1 expression in the CD8+ populations in liver tumours (top) versus subcutaneous tumours (below), at day 7 (left) and day 14 (right). Representative tumours have been chosen at each time point.

5.2.2. The presence of liver tumours impedes the effects of anti-PD-L1 treatment

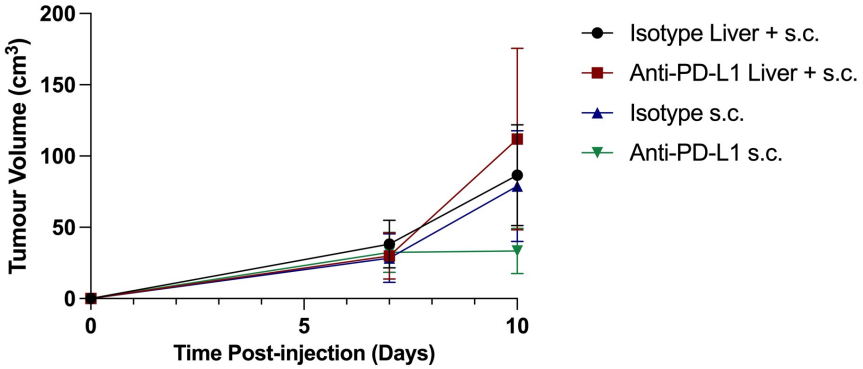
Previous studies using dual implantation of tumours into the liver and subcutaneously established that the presence of liver tumours impedes a productive anti-tumour response within subcutaneous tumours that were previously responsive to treatment with ICB.(265, 266) Prior to further investigation of the immune suppressive effect of liver tumours, we first wanted to ensure that in our tumour models with CRC cell lines, this effect was still observable. To do this, four experimental groups were used, with half the animals receiving a single dose of anti-PD-L1 at day 7 and the other half receiving isotype (10 mg/kg body weight), within each of these treatment groups half were injected with CT26 WT intrahepatically and subcutaneously, whilst the other half received CT26 WT subcutaneously only (Fig. 5.5A). Measurements of subcutaneous tumours were taken at day 7 and day 10 post-injection and revealed that prior to administration of treatment tumour growth between groups was the same (Fig 5.5B). Following treatment, the subcutaneous tumours of mice with liver tumours, in both isotype and anti-PD-L1 treated groups, grew larger than their subcutaneous tumour only counterparts (Fig. 5.5B); this was true on measuring but also visually and on weighing the tumours, with the smallest subcutaneous tumours seen in the subcutaneous only group receiving anti-PD-L1 treatment (Fig. 5.5B-D).

Flow cytometry was then used to further phenotype the CD8 T cells within the subcutaneous tumours among the different groups. The proportion of live CD45+ cells that were CD8 T cells within subcutaneous tumours did not significantly differ between any of the groups (Fig. 5.6A). However, CD8 T cell infiltration according to the number of cells per

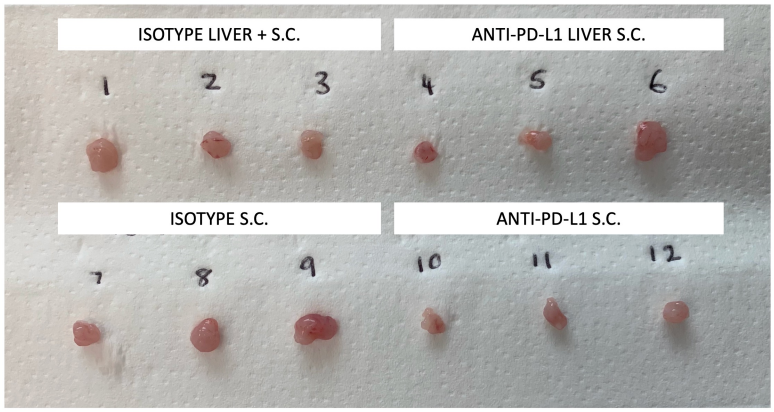
A.


Isotype
Anti-PD-L1
Group 1
Liver + s.c.
Group 2
S.c. only
Group 3
Liver + s.c.
Group 4
S.c. only

B.


Tumour Volume (cm³)
200
150
100
50
0
0
5
10
Time Post-injection (Days)
Isotype Liver + s.c.
Anti-PD-L1 Liver + s.c.
Isotype s.c.
Anti-PD-L1 s.c.

C.


ISOTYPE LIVER + S.C.
ANTI-PD-L1 LIVER S.C.
1
2
3
4
5
6
ISOTYPE S.C.
ANTI-PD-L1 S.C.
7
8
9
10
11
12

D.

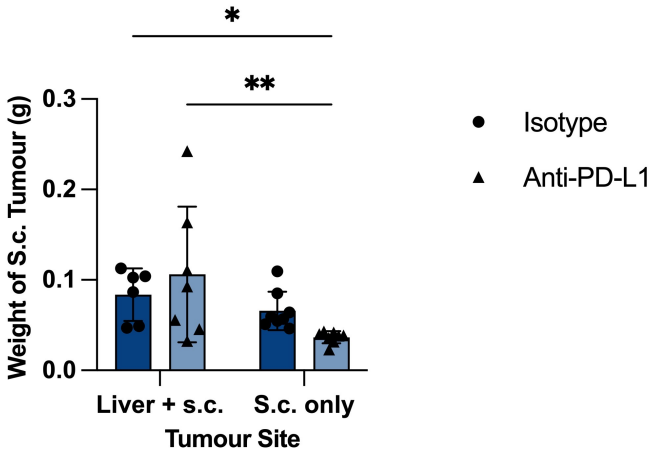

*
**
Weight of S.c. Tumour (g)
0.3
0.2
0.1
0.0
Liver + s.c.
S.c. only
Tumour Site
Isotype
Anti-PD-L1

Figure 5.5. Intrahepatic tumour burden blunts anti-PD-L1 enhancement of the anti-tumour response.

BALB/c mice (9-12 weeks) were injected with 2.0 x10^5 CT26 WT subcutaneously and intrahepatically, or subcutaneously only. Anti–PD-L1 mouse IgG1 (Clone 80, SP16-260; AstraZeneca) or NIP228 isotype control mouse IgG1 (SP16-017; AstraZeneca) was administered by intraperitoneal injection using one dose of 200 µg diluted in 200 µl PBS (10 mg/kg body weight) on day 7. Tissues were harvested on day 12 post-injection. All data shown are from two independent experiments. All graphs show the mean ± SD. Statistical significance was determined using a 2-way ANOVA with Tukey's correction for multiple comparison. ** = $p < 0.05$, ** = $p < 0.01$*

A. Representation of the groups used within the experiment, comparing the subcutaneous tumour response to anti-PD-L1 in mice bearing liver tumours versus not. Created with BioRender.com.
B. Growth curves showing the estimated tumour volume, from measurements taken on day 7 and 10.
C. Images showing the subcutaneous tumours only from each of the four experimental groups. One representative experiment of two is shown here.
D. The weight (g) of CT26 s.c. tumours in each of the four groups.

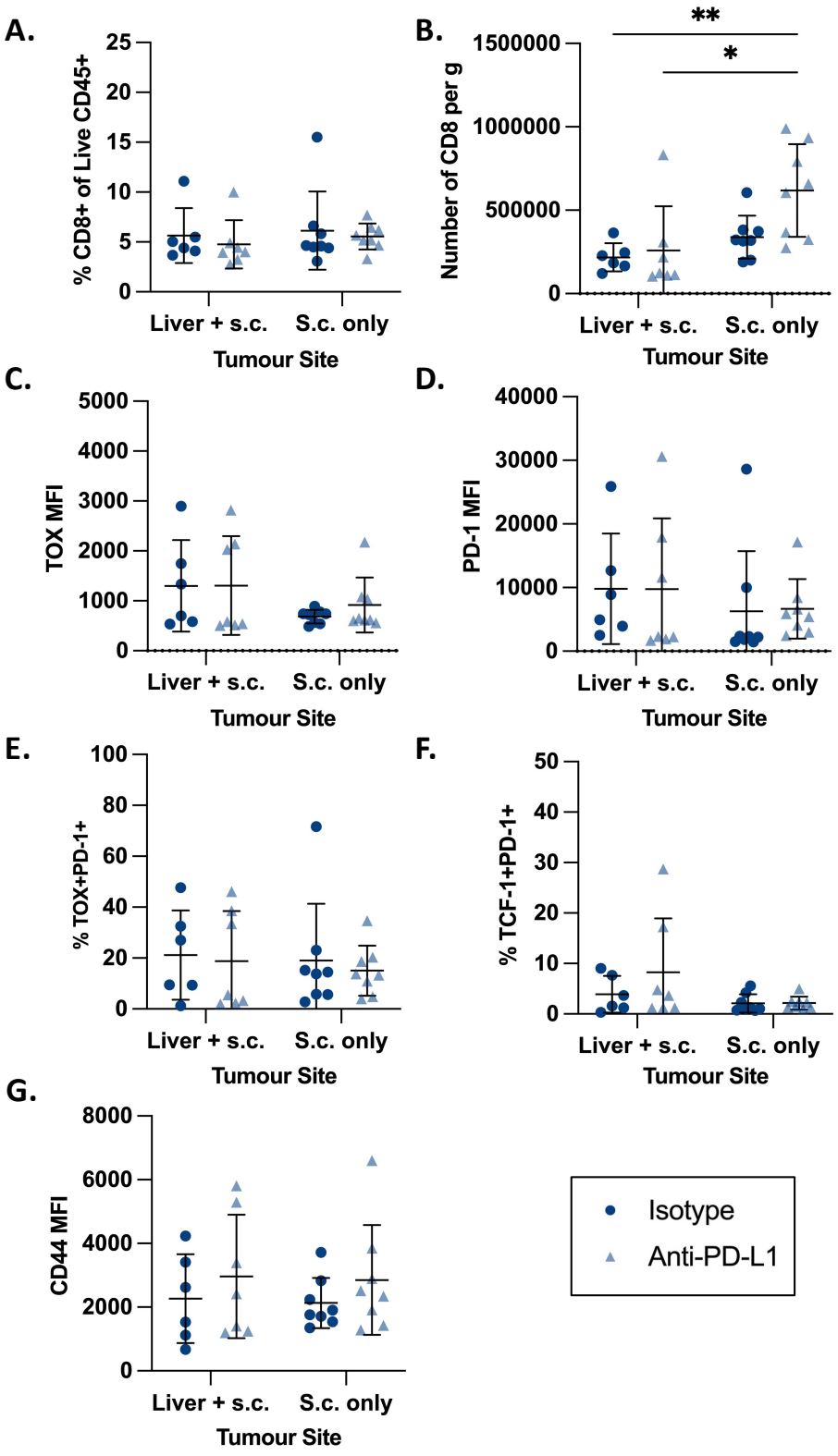

A.
% CD8+ of Live CD45+
25
20
15
10
5
0
Liver + s.c.
S.c. only
Tumour Site
B.
**
*
Number of CD8 per g
1500000
1000000
500000
0
Liver + s.c.
S.c. only
Tumour Site
C.
TOX MFI
5000
4000
3000
2000
1000
0
Liver + s.c.
S.c. only
Tumour Site
D.
PD-1 MFI
40000
30000
20000
10000
0
Liver + s.c.
S.c. only
Tumour Site
E.
% TOX+PD-1+
100
80
60
40
20
0
Liver + s.c.
S.c. only
Tumour Site
F.
% TCF-1+PD-1+
50
40
30
20
10
0
Liver + s.c.
S.c. only
Tumour Site
G.
CD44 MFI
8000
6000
4000
2000
0
Liver + s.c.
S.c. only
Tumour Site
Isotype
Anti-PD-L1

Figure 5.6. Liver tumours do not drive overt changes in CD8 T cell phenotype but do result in altered density within the tumour.

BALB/c mice (9-12 weeks) were injected with 2.0 x10^5 CT26 WT subcutaneously and intrahepatically, or subcutaneously only. Anti–PD-L1 mouse IgG1 (Clone 80, SP16-260; AstraZeneca) or NIP228 isotype control mouse IgG1 (SP16-017; AstraZeneca) was administered by intraperitoneal injection using one dose of 200 µg diluted in 200 µl PBS (10 mg/kg body weight) on day 7. Tissues were harvested on day 12 post-injection. All data shown are from two independent experiments. All graphs show the mean ± SD. Statistical significance was determined using a 2-way ANOVA with Tukey's correction for multiple comparison. ** = p < 0.05, ** = p < 0.01*

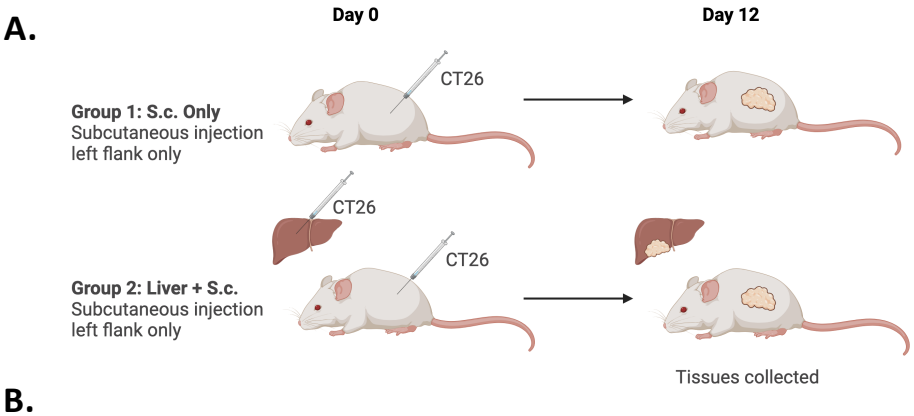
A. The percentage of live CD45+ cells that are CD8+ in CT26 subcutaneous tumours, in isotype or anti-PD-L1 treated mice, with liver and subcutaneous tumours or subcutaneous tumours only.
B. The number of CD8+ cells per gram of tumour in CT26 subcutaneous tumours, in isotype or anti-PD-L1 treated mice, with liver and subcutaneous tumours or subcutaneous tumours only.
C. The MFI of TOX in the CD8 T cell population of CT26 subcutaneous tumours, in isotype or anti-PD-L1 treated mice, with liver and subcutaneous tumours or subcutaneous tumours only.
D. The MFI of PD-1 in the CD8 T cell population of CT26 subcutaneous tumours, in isotype or anti-PD-L1 treated mice, with liver and subcutaneous tumours or subcutaneous tumours only.
E. The percentage of CD8+ T cells that are TOX+ PD-1+ in CT26 subcutaneous tumours, in isotype or anti-PD-L1 treated mice, with liver and subcutaneous tumours or subcutaneous tumours only.
F. The percentage of CD8+ T cells that are TCF-1+ PD-1+ in CT26 subcutaneous tumours, in isotype or anti-PD-L1 treated mice, with liver and subcutaneous tumours or subcutaneous tumours only.

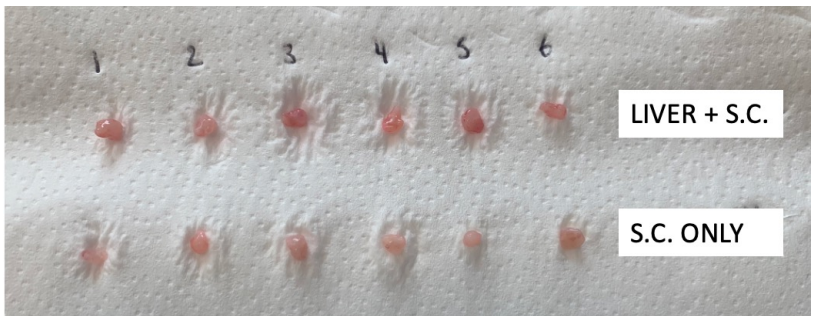
G. The MFI of CD44 in the CD8 T cell population of CT26 subcutaneous tumours, in isotype or anti-PD-L1 treated mice, with liver and subcutaneous tumours or subcutaneous tumours only.

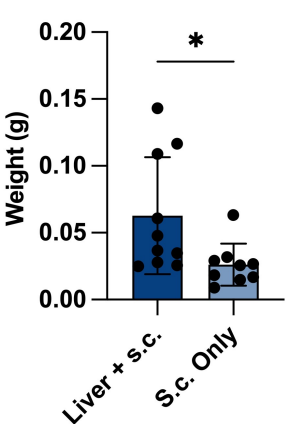
gram of subcutaneous tumour, was significantly higher in the subcutaneous tumour only group receiving a dose of anti-PD-L1 (Fig. 5.6B). Phenotypically, the intratumoural CD8 population was similar among all groups, in particular focusing on markers of exhaustion (TOX MFI, PD-1 MFI and percentage TOX+ PD-1+), stem-like (TCF-1+ PD-1+), and activation (CD44 MFI) (Fig. 5.6C-G). Collectively, these data indicate that we have reproduced the dual liver/subcutaneous tumour model described by others and in our hands observe an impaired response to anti-PD-L1 treatment when liver tumours are present.(265, 266)

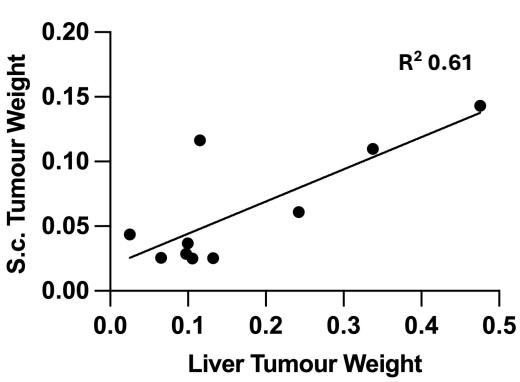
5.2.3. Liver tumours alter the anti-tumour response in peripheral tumours

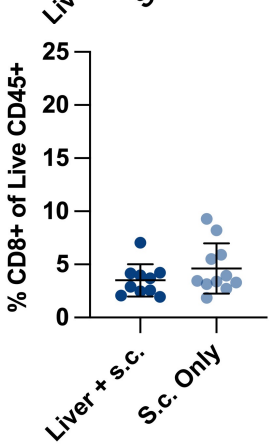
So far, our data have shown that the anti-tumour effect of anti-PD-L1 on subcutaneous tumours is abolished in the presence of liver tumours. To understand whether this immune suppressive effect of liver tumours is only present or observable in the response to ICB, the growth of subcutaneous tumours in mice bearing liver tumours or without, was compared in the absence of therapeutic interventions. Mice were injected with 2 x10^5 CT26 WT cells subcutaneously and intrahepatically, or subcutaneously only, and subcutaneous tumours (as well as the accessory lobe of the liver, and liver tumour where applicable) collected and analysed on day 12 after injection (Fig. 5.7A). The size and weight of subcutaneous tumours in mice without liver tumours was significantly lower than those with liver tumours (Fig. 5.7B-C). The weight of liver tumours was plotted against subcutaneous tumour weight in mice bearing both liver and subcutaneous tumours, and there appeared to be a moderate positive correlation between liver tumour burden and the weight of the subcutaneous tumour (Fig. 5.7D). Similar to previous results, the percentage of CD8 T cells among the live CD45+ population did not significantly differ between the two groups, whereas the number


A.
Day 0
Day 12
Group 1: S.c. Only
Subcutaneous injection
left flank only
CT26
Group 2: Liver + S.c.
Subcutaneous injection
left flank only
CT26
CT26
Tissues collected


B.
1
2
3
4
5
6
LIVER + S.C.
S.C. ONLY


C.
Weight (g)
0.20
0.15
0.10
0.05
0.00
*
Liver + s.c.
S.c. Only


D.
S.c. Tumour Weight
0.20
0.15
0.10
0.05
0.00
R² 0.61
0.0
0.1
0.2
0.3
0.4
0.5
Liver Tumour Weight


E.
% CD8+ of Live CD45+
25
20
15
10
5
0
Liver + s.c.
S.c. Only

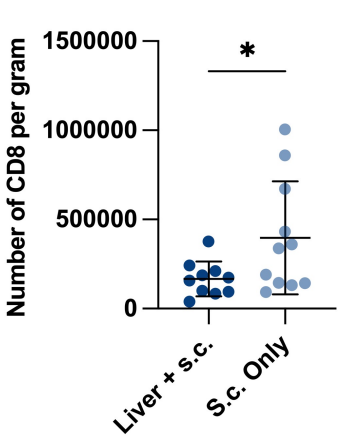

F.
Number of CD8 per gram
1500000
1000000
500000
0
*
Liver + s.c.
S.c. Only

Figure 5.7. Intrahepatic tumour burden influences the growth of s.c. tumours at distal sites.

BALB/c mice (9-12 weeks) were injected with 2.0 x10^5 CT26 WT subcutaneously and intrahepatically, or subcutaneously only. Tissues were harvested on day 12 post-injection. All data shown are from two independent experiments. All graphs show the mean ± SD. Statistical significance was determined using an unpaired *t* test. ** = $p < 0.05$*

A. Illustration outlining the experimental set-up of subcutaneous CRC tumour models and liver CRC metastasis models. Created with Biorender.com.
B. Image of the subcutaneous tumours from mice bearing liver tumours (top row) and mice with no liver tumour burden (bottom row).
C. The weight (g) of CT26 subcutaneous tumours from mice bearing liver tumours and mice with no liver tumour.
D. Correlation between the weight of liver tumours and the weight of s.c. tumours within the same animal. Simple linear regression analysis demonstrated, R-sq value 61% shown on graph.
E. The percentage of live CD45+ cells that are CD8+ in subcutaneous tumours from mice bearing liver tumours or with no liver tumour.
F. The number of CD8 T cells per gram of tumour in subcutaneous tumours from mice bearing liver tumours or with no liver tumour.

of CD8 T cells per gram of subcutaneous tumour was significantly higher in the subcutaneous tumour only mice (Fig. 5.7E-F). There was a small, but statistically significant reduction in stem-like CD8 T cell infiltration into subcutaneous tumours in animals with liver tumours, though the proportion of these cells among all CD8 T cells in the tumour was comparable (Fig. 5.8A-C). Equally, there was a significant increase in the number of exhausted TOX+ PD-1+ CD8 T cells per gram of subcutaneous tumours in animals with liver tumours, but percentage of TOX+ PD-1+ cells was similar (Fig. 5.8D-F). Further phenotyping of the subcutaneous CD8 population between groups is shown in Appendix 5.3.

Having investigated the effect of liver tumour burden on a peripheral tumour, in the same experiment the smaller left lobe of the liver from all mice was collected, to assess whether the presence of tumour altered the immune composition within other areas of the liver. The anatomically distinct non-tumour bearing accessory lobe of the liver, will be referred to as the 'background liver'. Immune cells were isolated from the liver lobe according to the methods outlined in Chapter 2, then stained with viability dye to allow immunophenotyping of live CD45+ cells by flow cytometry, phenotyping then focussed on the intrahepatic CD11b- CD11c- B220- CD3+ CD8+ population. The proportion of CD8 T cells among live CD45+ cells remained the same in the background liver of mice with and without liver tumours, however, the CD8 T cell population within the background liver of mice bearing liver tumours showed signs of exhaustion (Fig. 5.9); a higher proportion of CD8 T cells were positive for PD-1, NKG2A, as well as having higher expression of TOX and CD69 (Fig. 5.9A,C-F). In addition, there was a distinct TOX+ PD-1+ exhausted CD8 T cell population clearly present in the background liver of mice bearing liver tumours, which

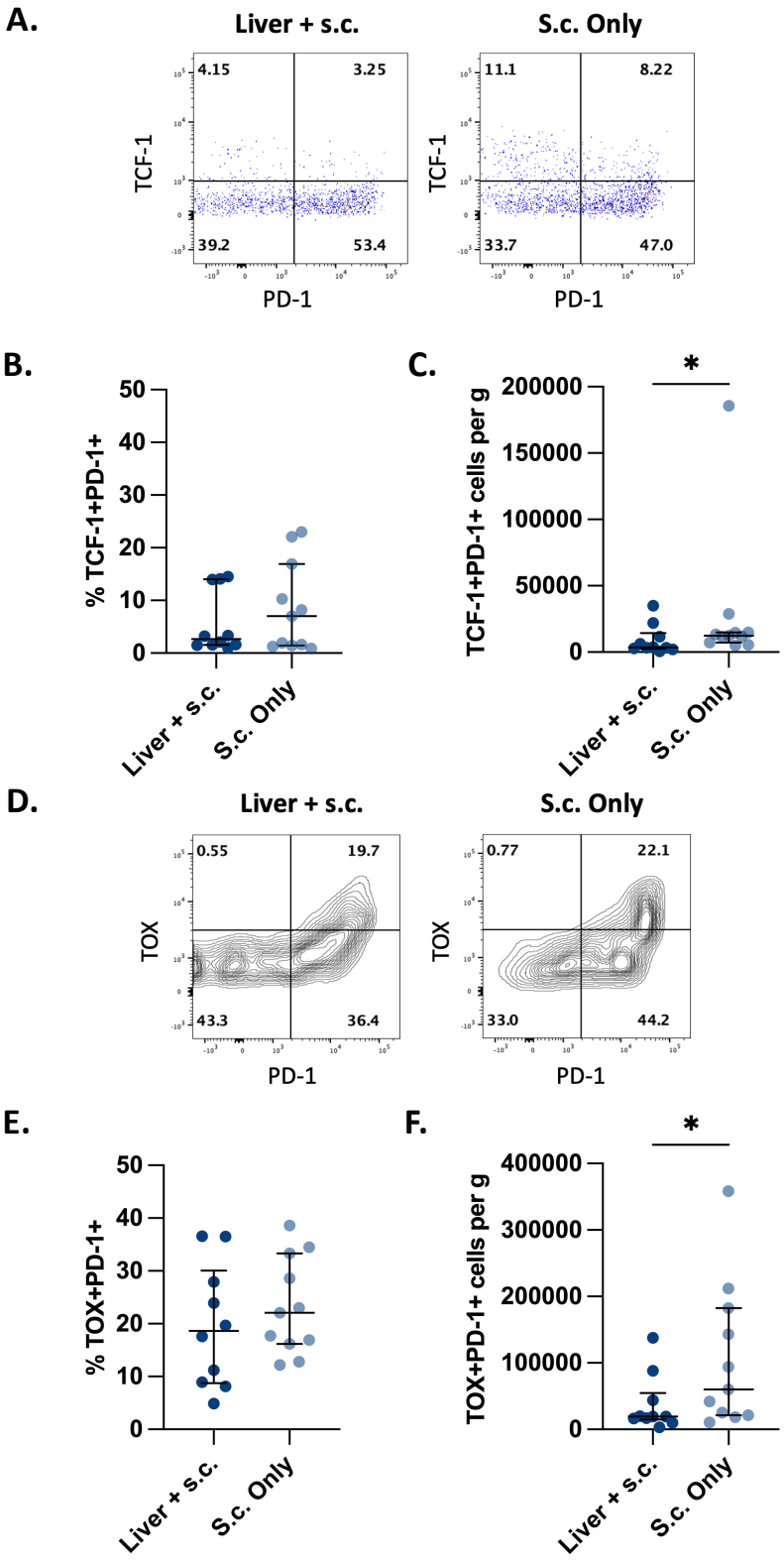

A.
Liver + s.c.
S.c. Only
4.15
3.25
39.2
53.4
11.1
8.22
33.7
47.0
TCF-1
PD-1
B.
% TCF-1+PD-1+
Liver + s.c.
S.c. Only
C.
*
TCF-1+PD-1+ cells per g
D.
Liver + s.c.
S.c. Only
0.55
19.7
43.3
36.4
0.77
22.1
33.0
44.2
TOX
PD-1
E.
% TOX+PD-1+
F.
*
TOX+PD-1+ cells per g

Figure 5.8. Intrahepatic tumour burden does not influence the phenotype of intratumoural CD8 populations at distal sites.

BALB/c mice (9-12 weeks) were injected with 2.0 x10^5 CT26 WT subcutaneously and intrahepatically, or subcutaneously only. Tissues were harvested on day 12 post-injection. All data shown are from two independent experiments. All graphs show the median and IQR. Statistical significance was determined using a Mann-Whitney. ** = $p < 0.05$*

A. Flow cytometry plots demonstrating TCF-1 and PD-1 expression in the CD8+ populations in the subcutaneous tumours of mice with liver tumours (left) versus without liver tumours (right). Representative tumours have been chosen from the same experiment.
B. The percentage of CD8+ T cells that are TCF-1+ PD-1+ in CT26 subcutaneous tumours, in mice with liver tumours (liver + s.c. label) and without (s.c. only label).
C. The number of TCF-1+PD-1+ CD8 T cells per gram of CT26 subcutaneous tumours, in mice with liver tumours (liver + s.c. label) and without (s.c. only label).
D. Flow cytometry plots demonstrating TOX and PD-1 expression in the CD8+ populations in the subcutaneous tumours of mice with liver tumours (left) versus without liver tumours (right). Representative tumours have been chosen from the same experiment.
E. The percentage of CD8+ T cells that are TOX+ PD-1+ in CT26 subcutaneous tumours, in mice with liver tumours (liver + s.c. label) and without (s.c. only label).
F. The number of TOX+PD-1+ CD8 T cells per gram of CT26 subcutaneous tumours, in mice with liver tumours (liver + s.c. label) and without (s.c. only label).

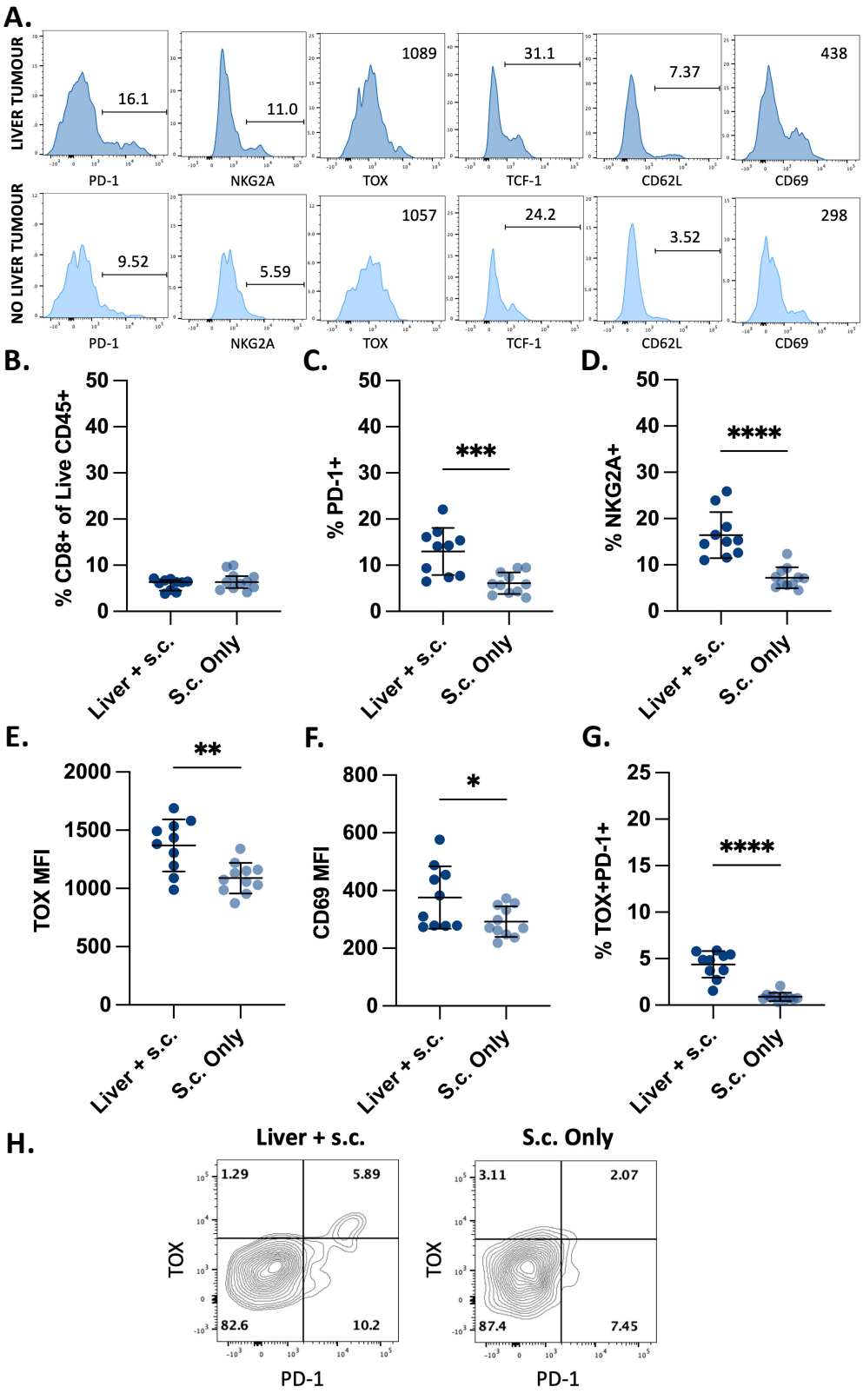

A.
LIVER TUMOUR
NO LIVER TUMOUR
16.1
11.0
1089
31.1
7.37
438
9.52
5.59
1057
24.2
3.52
298
PD-1
NKG2A
TOX
TCF-1
CD62L
CD69
B.
% CD8+ of Live CD45+
C.
% PD-1+
***
D.
% NKG2A+
****
Liver + s.c.
S.c. Only
E.
TOX MFI
**
F.
CD69 MFI
*
G.
% TOX+PD-1+
****
H.
Liver + s.c.
S.c. Only
1.29
5.89
82.6
10.2
3.11
2.07
87.4
7.45
TOX
PD-1

Figure 5.9. The presence of tumour intrahepatically changes the phenotype of CD8 T cells within anatomically distinct lobes of the liver.

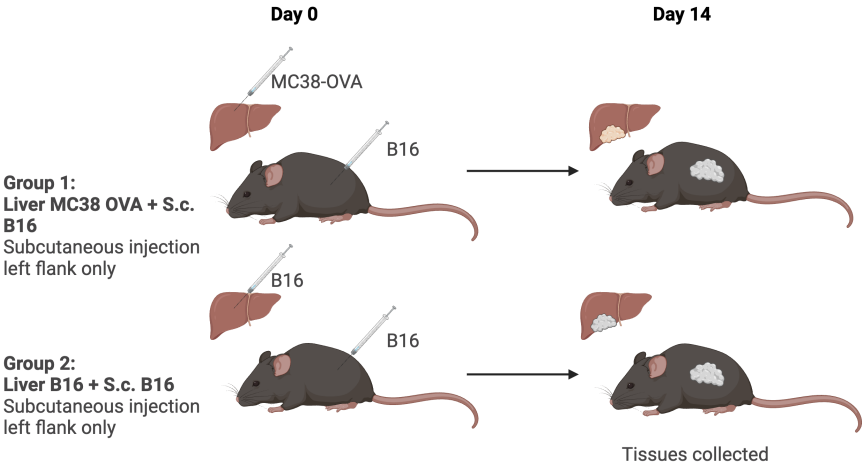
BALB/c mice (9-12 weeks) were injected with 2.0 x10^5 CT26 WT subcutaneously and intrahepatically, or subcutaneously only. Tissues were harvested on day 12 post-injection. All data shown are from two independent experiments. All graphs show the median and IQR. Statistical significance was determined using a Mann-Whitney. ** = $p < 0.05$*

A. Histograms demonstrating the levels of PD-1, NKG2A, TOX, TCF-1, CD62L, CD69 expression in the CD8+ populations in the accessory lobe of the liver at day 12 post-injection, in mice with a liver tumours (top row) and no liver tumours (bottom row). The y axis is normalised to the mode. Histograms were generated using FlowJo software.
B. The percentage of live CD45+ cells that are CD8+ in the accessory lobe of the liver, in mice with liver tumours versus those with no liver tumour.
C. The percentage of PD-1+ CD8 T cells in the accessory lobe of the liver, in mice with liver tumours versus those with no liver tumour.
D. The percentage of NKG2A+ CD8 T cells in the accessory lobe of the liver, in mice with liver tumours versus those with no liver tumour.
E. The MFI of TOX in CD8 T cells in the accessory lobe of the liver, in mice with liver tumours versus those with no liver tumour.
F. The MFI of CD69 in CD8 T cells in the accessory lobe of the liver, in mice with liver tumours versus those with no liver tumour.
G. The percentage of TOX+ PD-1+ CD8 T cells in the accessory lobe of the liver, in mice with liver tumours versus those with no liver tumour.
H. Flow plots demonstrating TOX and PD-1 expression in the CD8+ populations in the accessory lobe of the liver of mice with liver tumours (left) versus without liver tumours (right). Representative liver samples have been chosen from the same experiment.

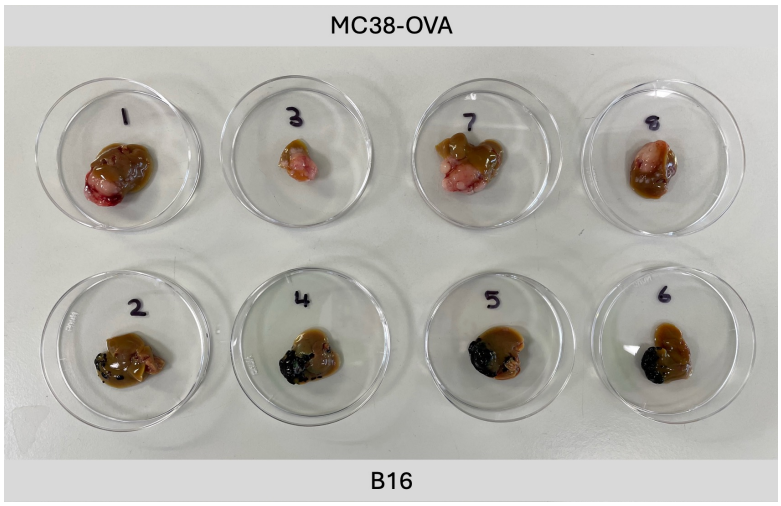
was not present in mice without liver tumour burden (Fig. 5.9.G-H). These data suggest that the presence of tumour in one liver lobe alters the immune composition of in the background liver.

It is clear that the presence of tumour burden within the liver licenses the subcutaneous tumour to grow at an accelerated rate, and it is reasonable to assume that this reflects suppression of the anti-tumour immune response. Other studies using a similar approach have indicated that suppression requires the same cell line to be implanted within the liver and subcutaneous site.(265, 266) If true, this implies that the systemic suppression mediated by the liver tumour influences antigen-specific immune compartments and thus brings mechanisms involving lymphocytes to the fore, including regulatory T cells.(266) To explore this, a pilot experiment was conducted, in which mice were injected subcutaneously with 2.0 $x10^5$ B16 melanoma cells, then injected intrahepatically with 2.0 $x10^5$ B16 melanoma cells or 2.0 $x10^5$ MC38-OVA CRC cells; then liver and subcutaneous tumours harvested and analysed by flow cytometry day 14 after injection (Fig. 5.10A). Hence, half of the mice had liver and subcutaneous tumours with shared antigen and half had tumours in which there was no common antigen. Due to this being a pilot experiment, the number of mice per group was low and there were differences observed in the growth kinetics of the B16 and MC38-OVA liver tumours, and MC38-OVA liver tumours were much larger than B16 on collection (Fig. 5.10B-C). Dissecting the response at the peripheral B16 subcutaneous tumour showed that the MC38-OVA liver tumour group had larger peripheral subcutaneous tumours (Fig. 5.11A-B). A positive correlation between size of the liver tumour burden and weight of the subcutaneous tumour was again observed (Fig.

A.


Day 0
Day 14
MC38-OVA
B16
Group 1:
Liver MC38 OVA + S.c. B16
Subcutaneous injection left flank only
B16
B16
Group 2:
Liver B16 + S.c. B16
Subcutaneous injection left flank only
Tissues collected

B.


MC38-OVA
1
3
7
8
2
4
5
6
B16

C.

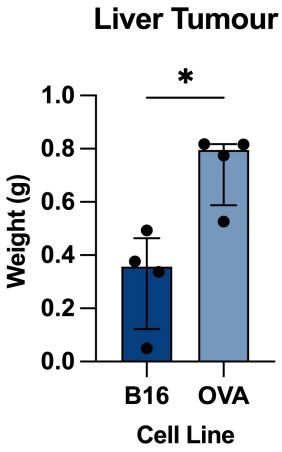

Liver Tumour
*
1.0
0.8
0.6
0.4
0.2
0.0
Weight (g)
B16
OVA
Cell Line

Figure 5.10. Setting up a model to investigate whether the systemic immune suppressive effect of liver tumours is antigen dependent.

C57BL/6 mice (9-12 weeks) were injected with 2.0 $x10^5$ B16 subcutaneously and intrahepatically, or with 2.0 $x10^5$ B16 subcutaneously and 2.0 $x10^5$ MC38-OVA intrahepatically. Tissues were harvested on day 14 post-injection. All data shown is from one experiment. All graphs show the median value with IQR. Statistical significance was determined using a Mann-Whitney test. *$* = p < 0.05$.*

A. Illustration outlining the experimental set-up of subcutaneous CRC tumour models and liver CRC metastasis tumour model, testing the importance of shared antigen between tumour sites. Created with Biorender.com.
B. Image of the liver tumours and surrounding liver tissue from mice bearing MC38-OVA liver tumours (top row) and mice with B16 liver tumours (bottom row).
C. The weight (g) of B16 and MC38-OVA liver tumours.

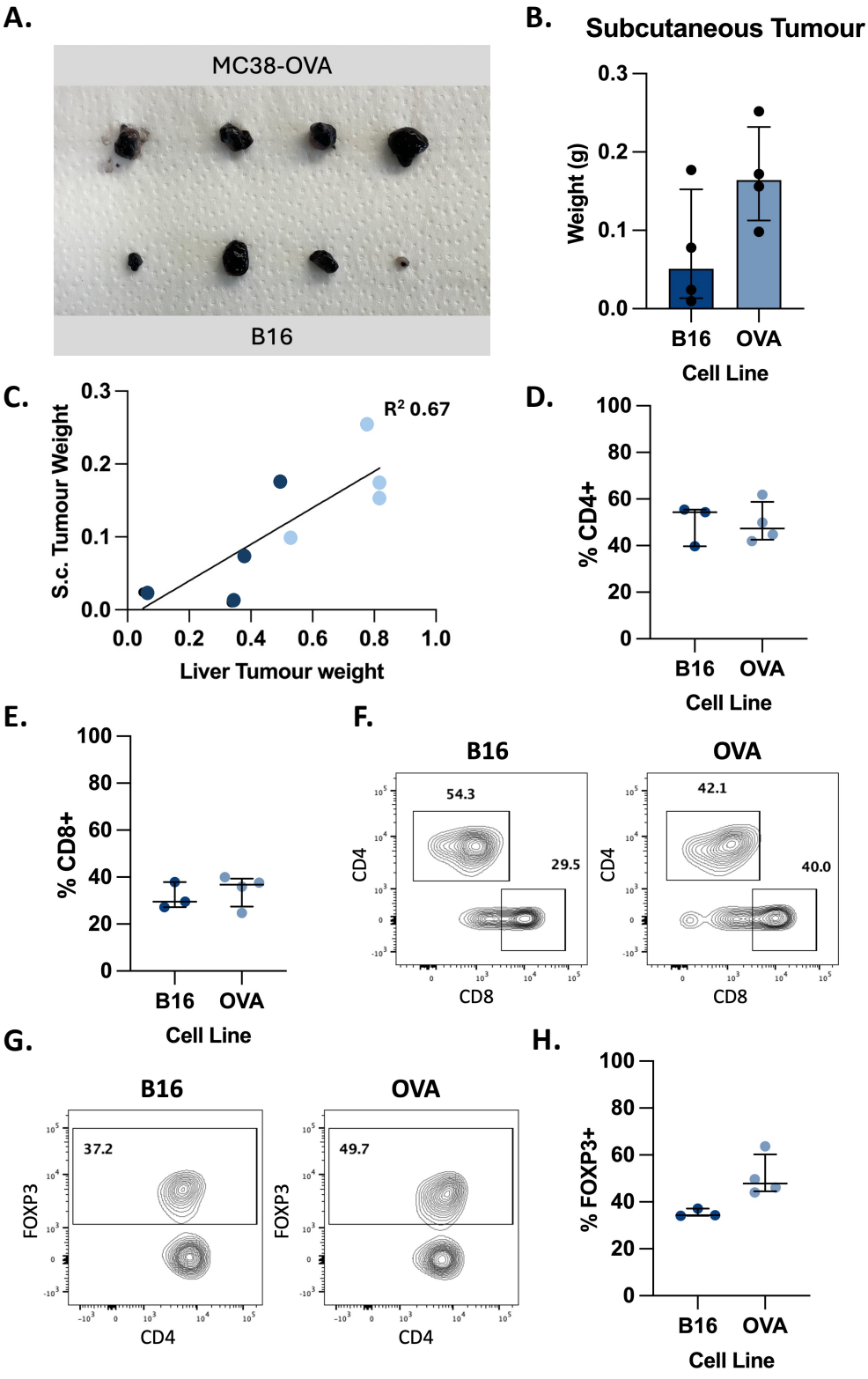

A.
MC38-OVA
B16
B.
Subcutaneous Tumour
Weight (g)
0.3
0.2
0.1
0.0
B16
OVA
Cell Line
C.
S.c. Tumour Weight
R² 0.67
0.0
0.2
0.4
0.6
0.8
1.0
Liver Tumour weight
D.
% CD4+
100
80
60
40
20
0
B16
OVA
Cell Line
E.
% CD8+
B16
OVA
Cell Line
F.
B16
OVA
54.3
29.5
42.1
40.0
CD4
CD8
G.
B16
OVA
37.2
49.7
FOXP3
CD4
H.
% FOXP3+
B16
OVA
Cell Line

Figure 5.11. The systemic immune suppressive effect of liver tumours appears volume dependent rather than antigen-specific.

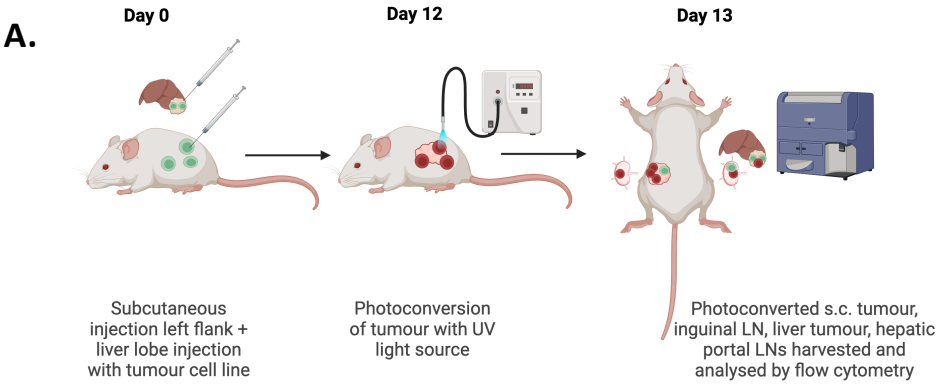
C57BL/6 mice (9-12 weeks) were injected with 2.0 x10^5 B16 subcutaneously and intrahepatically, or with 2.0 x10^5 B16 subcutaneously and 2.0 x10^5 MC38-OVA intrahepatically. Tissues were harvested on day 14 post-injection. All data shown is from one experiment. All graphs show the median value with IQR. Statistical significance was determined using a Mann-Whitney test.

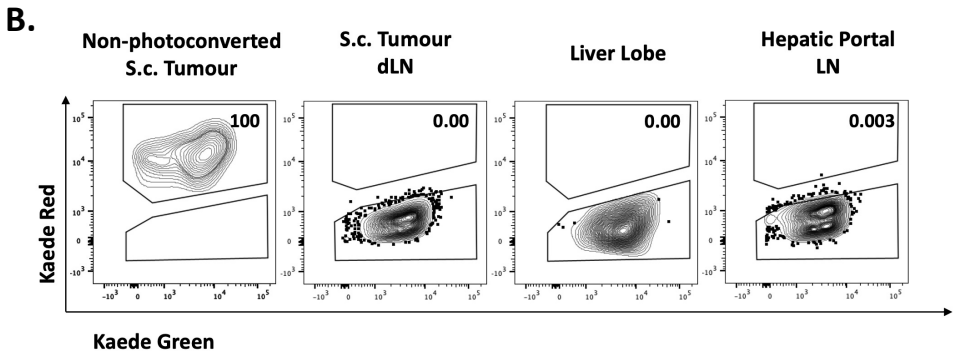
A. Image of the subcutaneous B16 tumours from mice bearing MC38-OVA liver tumours (top row) and mice with B16 liver tumours (bottom row).
B. The weight (g) of B16 subcutaneous tumours from mice bearing B16 liver tumours versus MC38-OVA liver tumours.
C. Correlation between the weight of liver tumours and the weight of s.c. tumours within the same animal. Simple linear regression analysis performed, with R-sq value of 67%.
D. The percentage of T cells that were CD4+ in B16 subcutaneous tumours, from mice bearing B16 liver tumours versus MC38-OVA liver tumours.
E. The percentage of T cells that were CD8+ in B16 subcutaneous tumours, from mice bearing B16 liver tumours versus MC38-OVA liver tumours.
F. Flow cytometry plots demonstrating CD4 and CD8 distribution in the T cell population in B16 subcutaneous tumours from mice bearing B16 liver tumours (left) versus MC38-OVA liver tumours (right). Representative tumours have been chosen.
G. Flow cytometry plots demonstrating FOXP3+ staining in the CD4+ CD3+ population in B16 subcutaneous tumours from mice bearing B16 liver tumours (left) versus MC38-OVA liver tumours (right). Representative tumours have been chosen.
H. The percentage of FOXP3+ CD4+ T cells in B16 subcutaneous tumours from mice bearing B16 liver tumours versus MC38-OVA liver tumours.

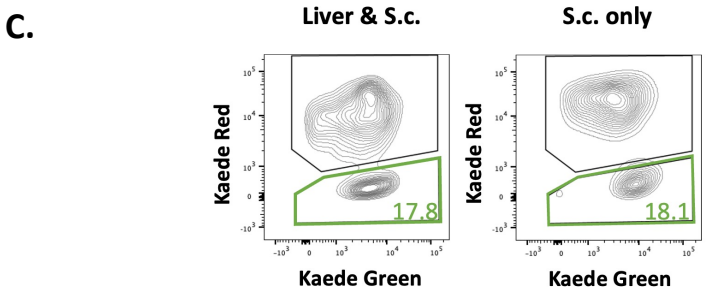
5.11C). There were no significant differences between the CD4: CD8 ratio in subcutaneous tumours between the two groups, and the proportion of FOXP3+ Tregs was not significantly different (Fig. 5.11 D-H). Though no statistically significant differences were observed, this could simply reflect underpowering of the data, and there appear to be slight alterations in the immune response within the subcutaneous tumours between the two groups. Due to this being a pilot experiment no firm conclusions can be drawn, but the results hint at the extent of the liver tumour burden being more important than shared antigen.

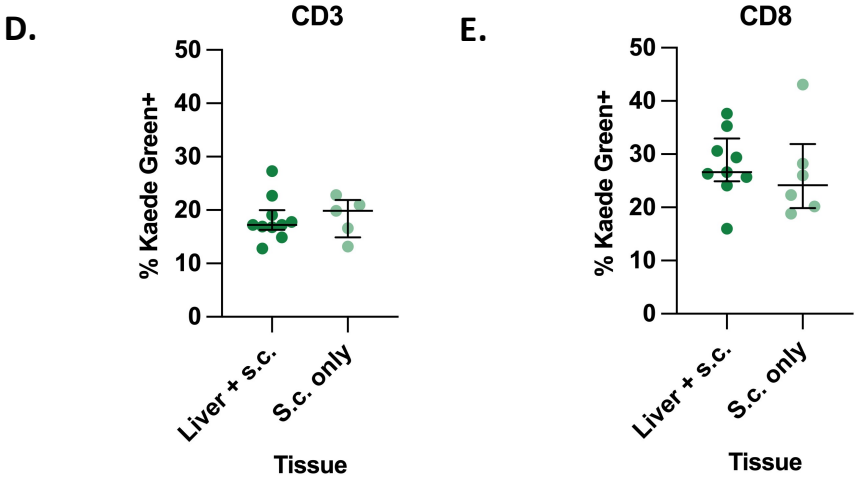
5.2.4. Investigating immune cell traffic between liver tumours and subcutaneous tumours

In this work, the dual liver and subcutaneous tumour model has been established to investigate mechanisms of immune suppression that systemically impact the anti-tumour response. Utilising the site-specific labelling afforded by Kaede mice, the direct trafficking of immune cells between the two tumour sites can be investigated to further explore how suppression is mediated. To ask whether liver tumours alter the influx of T cells into the subcutaneous tumour, and to investigate the trafficking of cells from the peripheral tumour to the liver tumour, photolabelling of the subcutaneous tumour was performed. BALB/c Kaede mice were injected with 2.0 $x10^5$ WT CT26 cells both intrahepatically and subcutaneously, followed by photolabelling of the subcutaneous tumour on day 12 post-injection, prior to tissue collection 24 hours following the labelling procedure (Fig. 5.12A). Figure 5.12B confirmed that complete Kaede red labelling of the intratumoural CD8


A.
Day 0
Day 12
Day 13
Subcutaneous injection left flank + liver lobe injection with tumour cell line
Photoconversion of tumour with UV light source
Photoconverted s.c. tumour, inguinal LN, liver tumour, hepatic portal LNs harvested and analysed by flow cytometry


B.
Non-photoconverted S.c. Tumour
S.c. Tumour dLN
Liver Lobe
Hepatic Portal LN
100
0.00
0.00
0.003
Kaede Red
Kaede Green


C.
Liver & S.c.
S.c. only
Kaede Red
17.8
18.1
Kaede Green


D.
CD3
% Kaede Green+
50
40
30
20
10
0
Liver + s.c.
S.c. only
Tissue

E.
CD8
% Kaede Green+
50
40
30
20
10
0
Liver + s.c.
S.c. only
Tissue

Figure 5.12. Establishing a dual liver + flank subcutaneous tumour model to understand immune cell migration out of and into subcutaneous tumours.

BALB/c Kaede mice (9-12 weeks) were injected with 2.0 x10^5 CT26 WT subcutaneously and intrahepatically, or subcutaneously only. Subcutaneous tumours were photoconverted on day 12 post-injection, and tissues collected 24 hours after. All data shown are from two independent experiments. All graphs show the median value with IQR. Statistical significance was determined using a Mann-Whitney test.

A. Illustration demonstrating the set-up of dual liver + s.c. tumour photoconversion experiments, subcutaneous tumours were photoconverted on day 12 post-injection and collected 24 hours later. Created with Biorender.com.
B. Flow cytometry plots demonstrating Kaede red expression in live CD45+ CD11b- CD11c- B220- CD3+ CD8+ cells in different tissues at 0 hours following photoconversion, demonstrating no Kaede red contamination in the periphery at baseline. Plots are from one representative mouse.
C. Flow cytometry plots demonstrating Kade expression in CD3+ population, pre-gated on live CD45+ CD11b- CD11c- B220- cells, in subcutaneous CT26 tumours. The right-hand plot shows the s.c. tumour in animals with CT26 liver tumours, and the left-hand plot shows the subcutaneous tumour in animals with no liver tumours burden.
D. Proportion of Kaede green+ CD3 cells in subcutaneous tumours in animals with liver tumours versus without liver tumours.
E. Percentage of Kaede green+ CD8 T cells in subcutaneous tumours in animals with liver tumours versus without liver tumours.

compartment of the subcutaneous tumour can be achieved, and immediately after labelling there is no Kaede red contamination of peripheral tissues, including the liver.

To understand whether the presence of tumour intrahepatically, influences T cell infiltration into subcutaneous tumours, the proportion of Kaede green T cells 24 hours following labelling was investigated. There was no clear difference in the proportion of either CD3 nor CD8 T cells that recently entered subcutaneous tumours in mice with or without liver tumours (Fig. 5.12C-E). Migration from the subcutaneous tumour to the periphery was then examined through tracking Kaede red cells in peripheral tissues. Analysis of peripheral tissues 24 hours after photoconversion detected a distinct Kaede red+ T cell population, however, few Kaede red T cells were evident beyond the dLN of the subcutaneous tumour (Fig. 5.13A-D). CD8 T cells accounted for less than 50% of the Kaede red T cells detected. Within the Kaede red labelled CD8 population in peripheral tissues, the majority lacked PD-1 expression although a small TCF-1+ PD-1+ stem-like population was evident in lymphoid tissues (Fig. 5.13E-F). These data are consistent with previous observations showing there is clear systemic dissemination of cells, and evidence of stem-like CD8 trafficking. The nature of the different T cells trafficking from the subcutaneous tumour requires further investigation.

Using the novel liver tumour photolabelling approach outlined in Chapter 4, I then sought to directly assess immune cell trafficking from liver tumours to the subcutaneous tumour. BALB/c Kaede mice were injected with 2.0 $x10^5$ CT26 both subcutaneously and intrahepatically, followed by photolabelling of the liver tumour through an abdominal

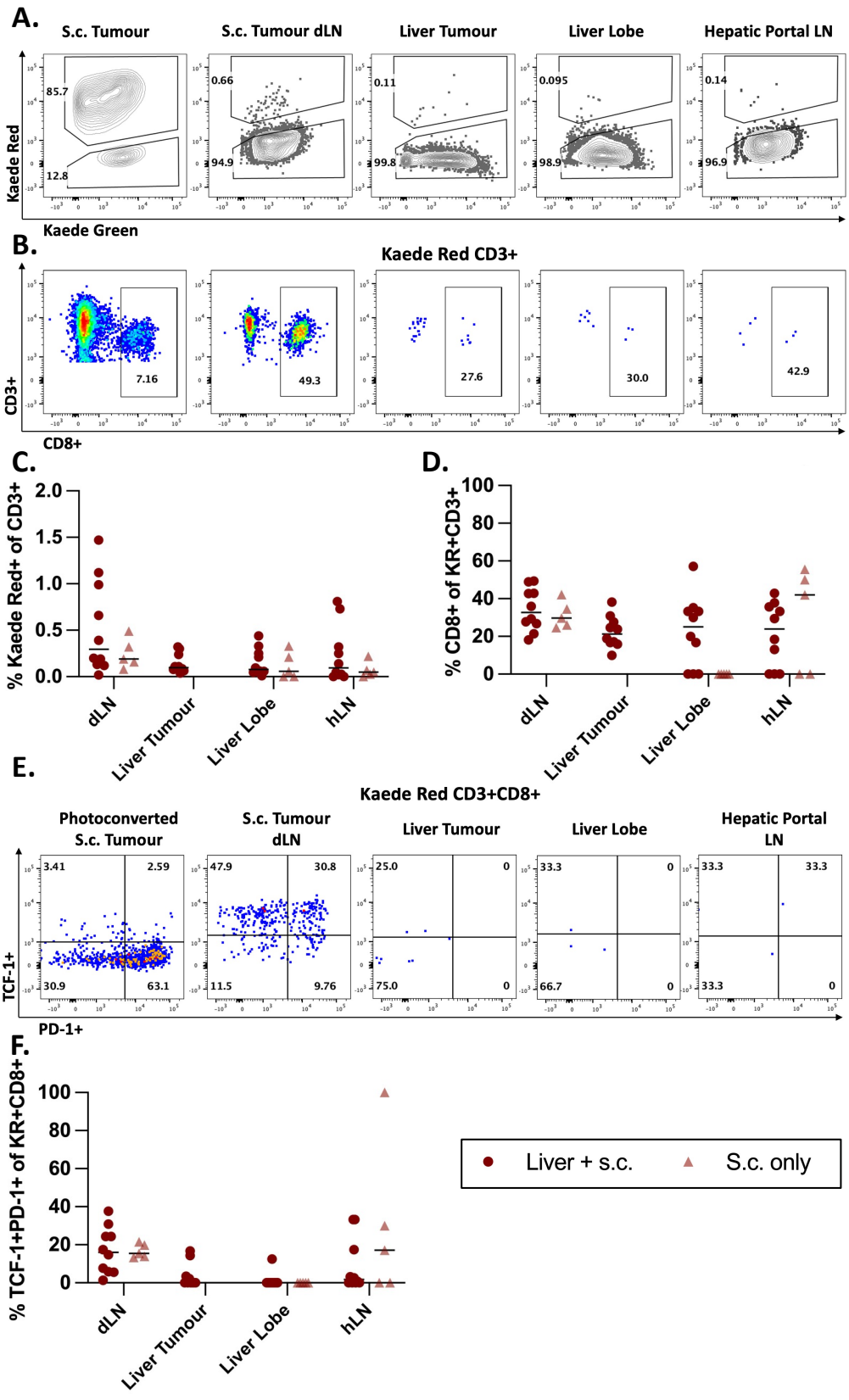

A.
S.c. Tumour
S.c. Tumour dLN
Liver Tumour
Liver Lobe
Hepatic Portal LN
Kaede Red
Kaede Green
85.7
12.8
0.66
94.9
0.11
99.8
0.095
98.9
0.14
96.9
B.
Kaede Red CD3+
CD3+
CD8+
7.16
49.3
27.6
30.0
42.9
C.
% Kaede Red+ of CD3+
dLN
Liver Tumour
Liver Lobe
hLN
D.
% CD8+ of KR+CD3+
E.
Kaede Red CD3+CD8+
Photoconverted S.c. Tumour
S.c. Tumour dLN
Liver Tumour
Liver Lobe
Hepatic Portal LN
TCF-1+
PD-1+
3.41
2.59
30.9
63.1
47.9
30.8
11.5
9.76
25.0
0
75.0
0
33.3
0
66.7
0
33.3
33.3
33.3
0
F.
% TCF-1+PD-1+ of KR+CD8+
Liver + s.c.
S.c. only

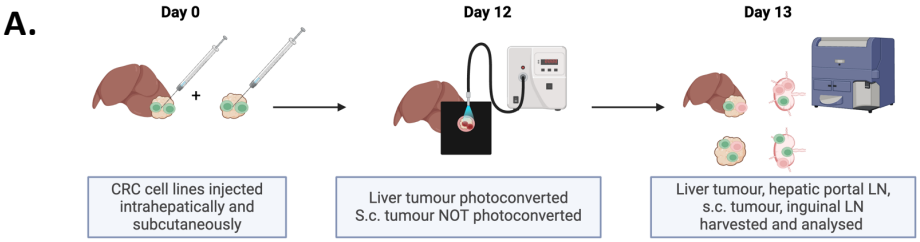
Figure 5.13. Establishing a dual liver + flank subcutaneous tumour model to understand the migration of CD8 T cells from the subcutaneous tumour to liver tumour.

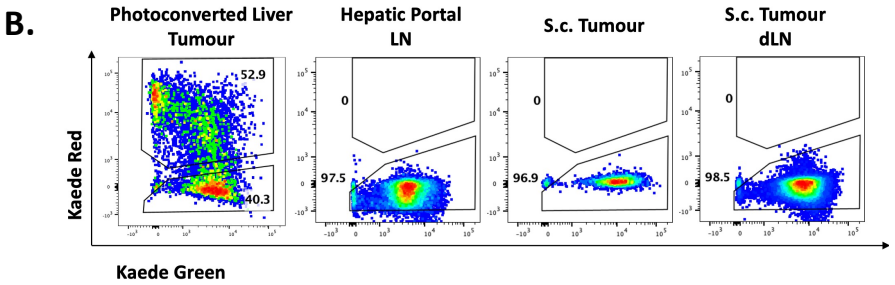
BALB/c Kaede mice (9-12 weeks) were injected with 2.0 x10^5 CT26 WT subcutaneously and intrahepatically, or subcutaneously only. Subcutaneous tumours were photoconverted on day 12 post-injection, and tissues collected 24 hours after. All data shown are from two independent experiments. All graphs show the median value. Statistical significance was determined using a Mann-Whitney test.

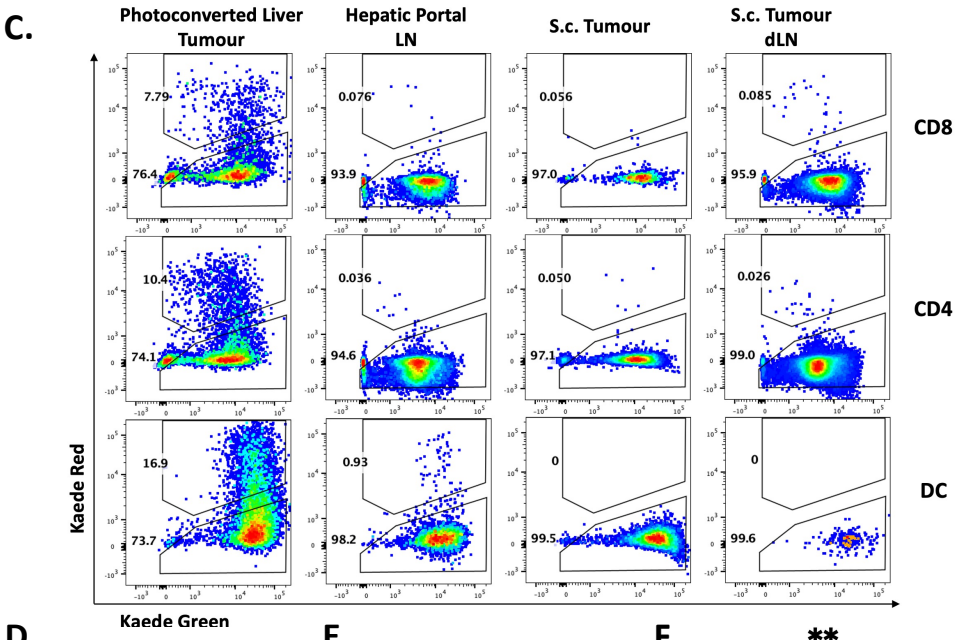
A. Flow cytometry plots of the CD3 population demonstrating Kaede red expression in different tissues. The plots are from the same mouse (with liver tumours) 24 hours post-photoconversion.
B. Flow cytometry plots of CD8+ expression in the migratory KR+ CD3+ T cells in different tissues. The plots are from the same mouse (with liver tumours) 24 hours post-photoconversion. Order of tissues same as A.
C. The percentage of Kaede red+ CD3 T cells in different tissues 24 hours following photoconversion, between mice with liver tumours and without liver tumours.
D. The percentage of CD8+ cells in the Kaede red+ CD3+ population in different tissues 24 hours following photoconversion, between mice with liver tumours and without liver tumours.
E. Flow cytometry plots of TCF-1 and PD-1 expression among migratory KR+ CD8+ T cells in different tissues. The plots are from the same mouse (with liver tumours) 24 hours post-photoconversion.
F. The percentage of TCF-1+ PD-1+ cells in the Kaede red+ CD8+ population in different tissues 24 hours following photoconversion, between mice with liver tumours and without liver tumours.

incision on day 12 post-injection, prior to tissue collection 24 hours following the labelling (Fig. 5.14A). Figure 5.14B shows the extent of photolabelling possible with this approach. Rapid growth of the liver tumours resulted in only partial labelling, but importantly, there was no unintended labelling of peripheral tissues (Fig. 5.14B). Complete photolabelling of the liver tumour is not currently achievable and hence phenotyping of newly entering Kaede green cells was not meaningful, however the egress of Kaede red cells can still be assessed. In these initial pilot experiments, the aim was to find evidence that immune cells trafficked from the liver tumour and to begin to investigate where they migrated to. Figure 5.14C-F shows that it is possible to identify Kaede red+ CD4, CD8, and DC populations in the hepatic portal dLN. Gating of MHCIIhi CD11c+ dendritic cells can be found in Appendix 5.4. Analysis of DC migration was an important control given that labelled DC should be evident within the hepatic portal LN, but not in peripheral tissues (Fig. 5.14C,F). In contrast, Kaede red CD4 and CD8 T cells were detected in the dLN of the liver tumour, but also within the peripheral subcutaneous tumour and its dLN (Fig. 4.14C-E), consistent with the dissemination of these cells systemically. Thus, these initial liver photoconversion pilot studies provided proof of principle that immune cell movement from liver tumours to peripheral tissues could be assessed in our model to better understand how systemic suppression is mediated.

To enable a more focused analysis of the CD8 T cell response, including the tracking of antigen-specific CD8 T cells, photoconversion of liver tumours in a dual liver and subcutaneous MC38-OVA tumour model was performed. Analysis at 24 hours after liver tumour photoconversion again identified Kaede red T cells within the dLN and beyond,


A.
Day 0
Day 12
Day 13
CRC cell lines injected intrahepatically and subcutaneously
Liver tumour photoconverted
S.c. tumour NOT photoconverted
Liver tumour, hepatic portal LN, s.c. tumour, inguinal LN harvested and analysed


B.
Photoconverted Liver Tumour
Hepatic Portal LN
S.c. Tumour
S.c. Tumour dLN
Kaede Red
Kaede Green
52.9
40.3
0
97.5
0
96.9
0
98.5


C.
Photoconverted Liver Tumour
Hepatic Portal LN
S.c. Tumour
S.c. Tumour dLN
CD8
CD4
DC
Kaede Red
Kaede Green
7.79
76.4
0.076
93.9
0.056
97.0
0.085
95.9
10.4
74.1
0.036
94.6
0.050
97.1
0.026
99.0
16.9
73.7
0.93
98.2
0
99.5
0
99.6

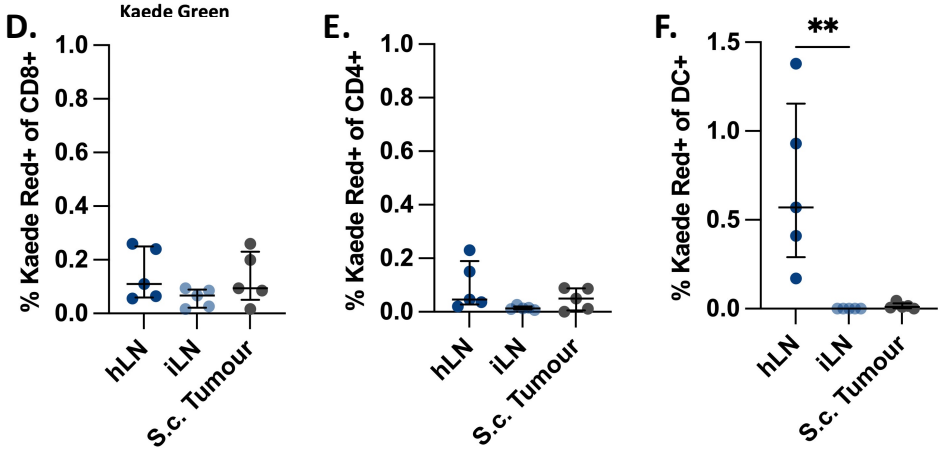

D.
% Kaede Red+ of CD8+
1.0
0.8
0.6
0.4
0.2
0.0
hLN
iLN
S.c. Tumour
E.
% Kaede Red+ of CD4+
1.0
0.8
0.6
0.4
0.2
0.0
hLN
iLN
S.c. Tumour
F.
**
% Kaede Red+ of DC+
1.5
1.0
0.5
0.0
hLN
iLN
S.c. Tumour

Figure 5.14. Establishing a dual liver + flank subcutaneous tumour model to understand the migration of CD8 T cells from liver tumour to subcutaneous tumour.

BALB/c Kaede mice (9-12 weeks) were injected with 2.0 x10^5 CT26 WT subcutaneously and intrahepatically, or subcutaneously only. Liver tumours were photoconverted day 12 post-injection through a limited abdominal incision, and tissues collected 24 hours after. All data shown are from two independent experiments. All graphs show the median value with IQR. Statistical significance was determined using a Kruskal-Wallis multiple comparison with post-hoc Dunn's correction. ** = p < 0.05, ** = p < 0.01.*

A. Illustration demonstrating the set-up of dual liver + s.c. flank tumour photoconversion experiments, 24hr photoconversion of the liver tumour only via small abdominal incision. Created with Biorender.com.
B. Flow cytometry plots demonstrating Kaede red expression in the CD8 T cell population of the photoconverted liver tumours and peripheral tissues immediately following photoconversion, showing no background labelling of tissues. The plots are from the same mouse 0 hours post-photoconversion.
C. Flow cytometry plots demonstrating Kaede red expression in the photoconverted liver tumours and peripheral tissues 24 hours following photoconversion. The top row demonstrates Kaede labelling in the CD8 population, middle row CD4 population, and bottom row dendritic cell population (MHCIIhi 11c+).The plots are from the same mouse 0 hours post-photoconversion.
D. Proportion of Kaede red+ CD8 cells in peripheral tissues 24 hours following photoconversion of the liver tumour.
E. Proportion of Kaede red+ CD4 cells in peripheral tissues 24 hours following photoconversion of the liver tumour.
F. Proportion of Kaede red+ DC cells in peripheral tissues 24 hours following photoconversion of the liver tumour.

with CD8 T cells typically accounting for less than 50% of this population within the different tissues (Fig. 5.15A-D). Focusing further on the phenotype of Kaede red+ CD8 T cells migrating from the liver tumours, a stem-like TCF-1+ PD-1+ population was detected within the LNs (Fig. 5.15E-F). Antigen-specific CD8 T cells were largely undetectable within the Kaede red population, but given the frequency of Kaede red cells, this may simply reflect the size of this endogenous response. Collectively, these data reveal that TCF-1+ PD-1+ CD8 T cells egress liver tumours and can be detected in draining and peripheral lymphoid tissues, as identified in the subcutaneous tumour models (Chapter 3). These data further highlight the potential of the photolabelling approach to explore the different immune cells that egress liver tumours, including CD4 T cells that may include regulatory populations.

5.2.5. Assessing which lymphocyte populations are required for anti-tumour control in the dual liver and subcutaneous model

The data from tumour photolabelling in this chapter demonstrates that there is migration of both CD8 and CD4 populations between tumours implanted in the liver and subcutaneously. To better understand which of these lymphocyte populations is required for anti-tumour control within the dual liver and subcutaneous model, antibodies were administered to deplete CD4 and CD8 T cell responses *in vivo*. The antibodies used recognised non-polymorphic epitopes on CD4 and CD8 and efficiently deplete the respective T cell populations following one systemic dose (Dr N. Jones personal communication). To first assess whether the antibodies effectively depleted CD4 and CD8 T cells *in vivo* in our hands, including within tumours, a pilot study using subcutaneous

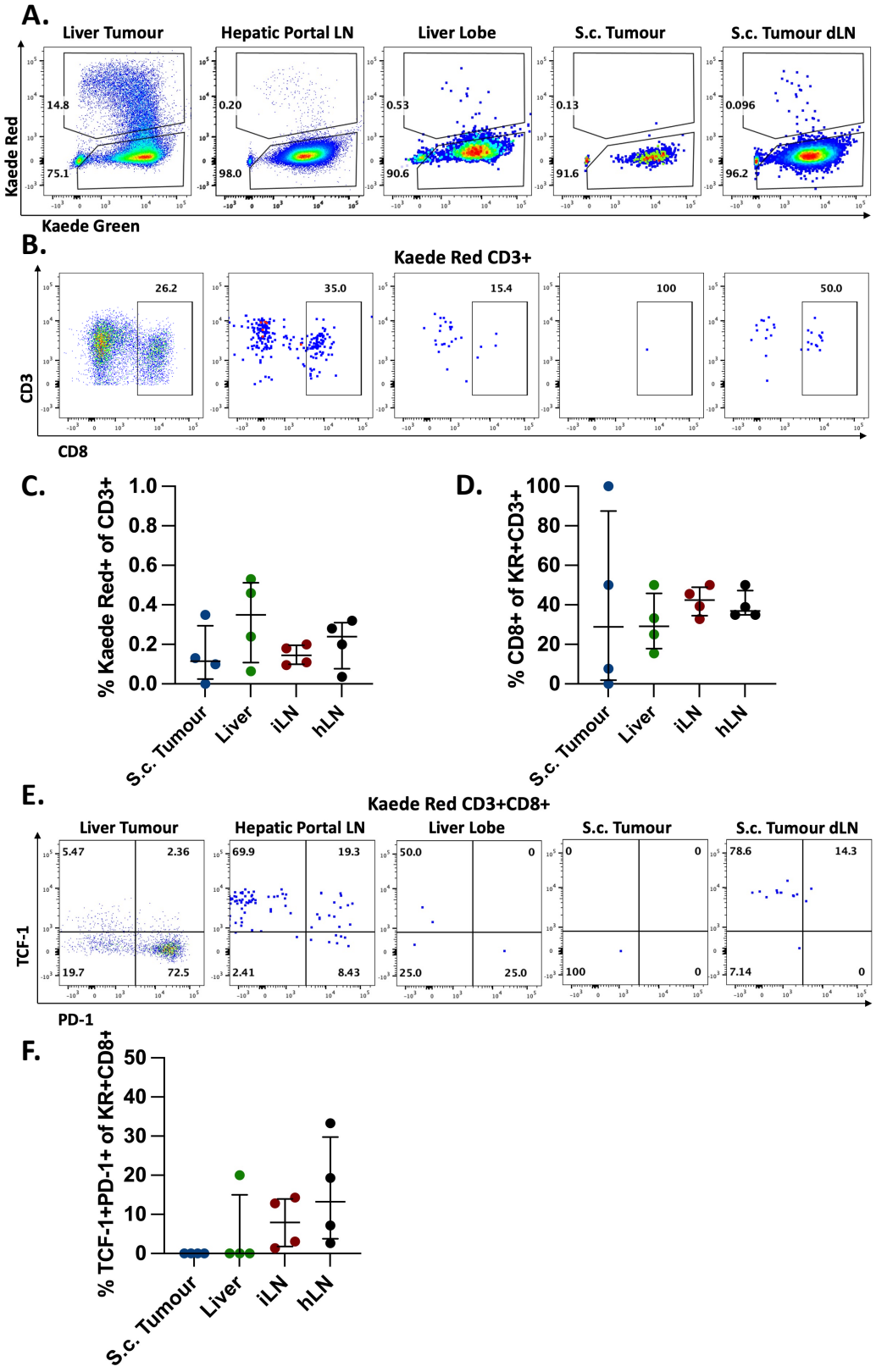

A.
Liver Tumour
Hepatic Portal LN
Liver Lobe
S.c. Tumour
S.c. Tumour dLN
Kaede Red
Kaede Green
14.8
75.1
0.20
98.0
0.53
90.6
0.13
91.6
0.096
96.2
B.
Kaede Red CD3+
CD3
CD8
26.2
35.0
15.4
100
50.0
C.
% Kaede Red+ of CD3+
1.0
0.8
0.6
0.4
0.2
0.0
S.c. Tumour
Liver
iLN
hLN
D.
% CD8+ of KR+CD3+
100
80
60
40
20
0
S.c. Tumour
Liver
iLN
hLN
E.
Kaede Red CD3+CD8+
Liver Tumour
Hepatic Portal LN
Liver Lobe
S.c. Tumour
S.c. Tumour dLN
TCF-1
PD-1
5.47
2.36
19.7
72.5
69.9
19.3
2.41
8.43
50.0
0
25.0
25.0
0
0
100
0
78.6
14.3
7.14
0
F.
% TCF-1+PD-1+ of KR+CD8+
50
40
30
20
10
0
S.c. Tumour
Liver
iLN
hLN

Figure 5.15. Stem-like CD8 T cells egress liver tumours.

C57BL/6 Kaede mice (9-12 weeks) were injected with 2.0 x10^5 MC38-OVA subcutaneously and intrahepatically, or subcutaneously only. Liver tumours were photoconverted day 12 post-injection through a limited abdominal incision, and tissues collected 24 hours after. All data shown are from two independent experiments. All graphs show the median value with IQR. Statistical significance was determined using a Kruskal-Wallis multiple comparison with post-hoc Dunn's correction.

A. Flow cytometry plots demonstrating Kaede red expression in the CD3 T cell population in different tissues. The plots are from the same mouse (with liver tumours) 24 hours post-photoconversion of the liver tumour immune compartment.
B. Flow cytometry plots of CD8+ cells among migratory KR+ CD3 T cells in different tissues. The plots are from the same mouse (with liver tumours) 24 hours post-photoconversion of the liver tumour immune compartment. Order of tissues same as A.
C. The percentage of Kaede red+ CD3 cells in different peripheral tissues 24 hours following photoconversion.
D. The percentage of CD8+ cells in the Kaede red CD3 population in different peripheral tissues 24 hours following photoconversion.
E. Flow cytometry plots of TCF-1 and PD-1 expression among migratory KR+ CD8+ T cells in different tissues. The plots are from the same mouse (with liver tumours) 24 hours post-photoconversion of the liver tumour immune compartment.
F. The percentage of TCF-1+ PD-1+ cells in the Kaede red+ CD8+ population in different peripheral tissues 24 hours following photoconversion.

tumours was carried out. C57BL/6 mice were injected with MC38-OVA subcutaneously, prior to intraperitoneal injection of either isotype, or anti-CD4, or anti-CD8 antibodies (10 mg/kg) on day 6. The size of subcutaneous tumours was measured on day 6, 10 and 12, and tumours, lymph nodes and blood samples collected on day 12. The subcutaneous tumours in the 'CD8 depleted' group grew the fastest and weighed the most, with the 'CD4 depleted' group showed the slowest growth and tumours of the lowest weight (Fig. 5.16A-B). Flow cytometry analyses of the tumour and dLN T cell populations confirmed that there was highly effective depletion of CD4 and CD8 T cells in their respective treatment groups, with near complete depletion achieved at day 12 (Fig. 5.16C-H). Further evidence of effective depletion in the blood samples is shown in the Appendix 5.5.

The same experimental set up was then applied to the dual liver and subcutaneous tumour model, with depleting antibodies administered on day 6, and tissues collected on day 12. The effect of depletion on the size of the liver tumour was not significant at day 12, with the CD8-depleted group demonstrating a slight increase in the size of liver tumours (Fig. 5.17A-B). Highly effective depletion of CD4 and CD8 T cells was observed within the liver tumours themselves according to the treatment group (Fig. 5.17C-D). The effect of depleting CD4+ and CD8+ T cells on the subcutaneous tumour was then examined. The group in which there was CD4 depletion had the smallest subcutaneous tumours, and CD8 depletion conversely resulted in the largest tumours (Fig. 5.17E-G). However, the increase in size of the subcutaneous tumour in the CD8 depleted group, nor the decrease seen in the CD4 depleted group, was statistically significant compared to the isotype control. Phenotypic analyses of the subcutaneous tumour immune infiltrate again demonstrated

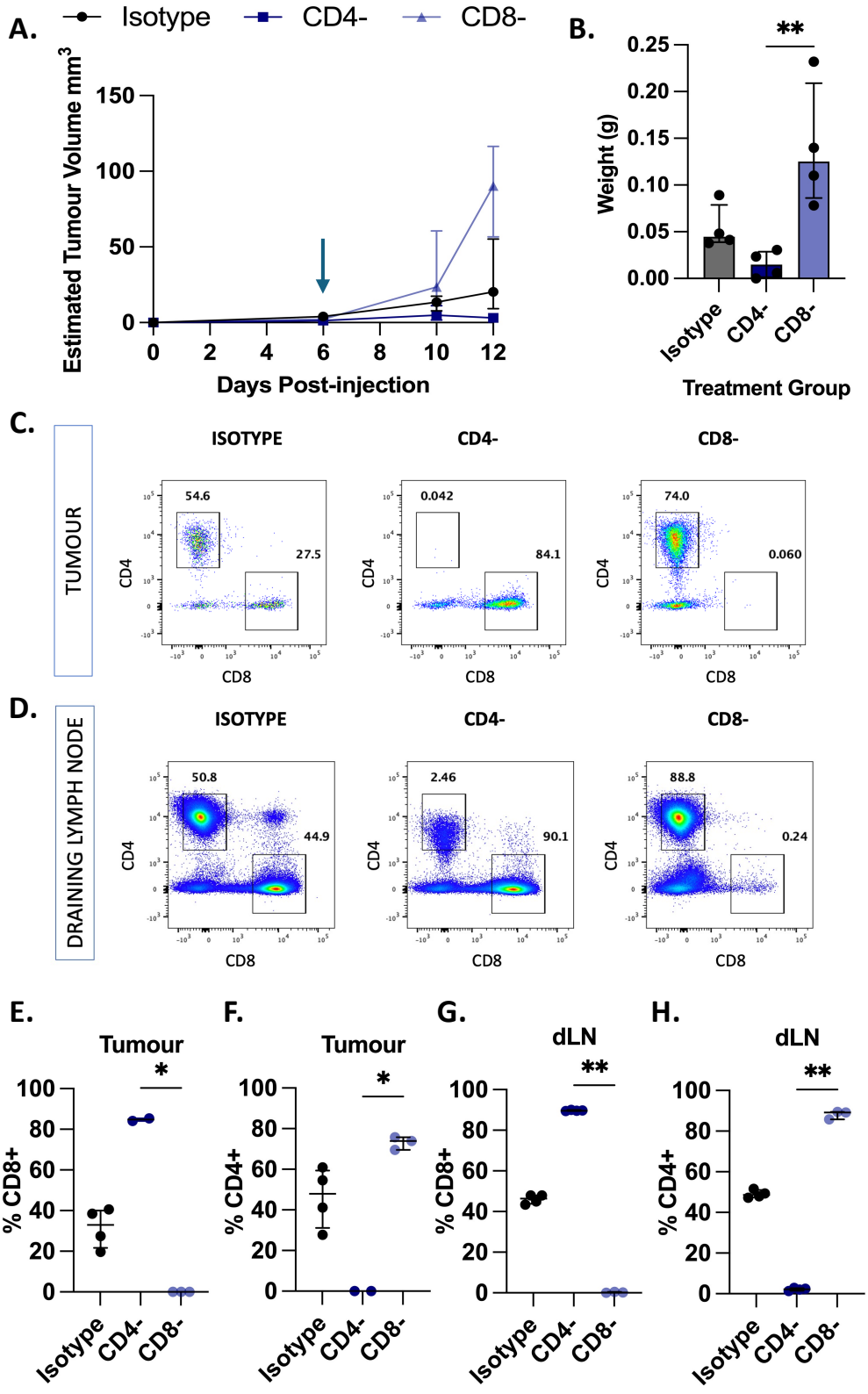

A.
Isotype
CD4-
CD8-
Estimated Tumour Volume mm3
150
100
50
0
0
2
4
6
8
10
12
Days Post-injection
B.
**
0.25
0.20
0.15
0.10
0.05
0.00
Weight (g)
Isotype
CD4-
CD8-
Treatment Group
C.
TUMOUR
ISOTYPE
CD4-
CD8-
54.6
27.5
0.042
84.1
74.0
0.060
CD4
CD8
D.
DRAINING LYMPH NODE
ISOTYPE
CD4-
CD8-
50.8
44.9
2.46
90.1
88.8
0.24
CD4
CD8
E.
Tumour
*
% CD8+
F.
Tumour
*
% CD4+
G.
dLN
**
% CD8+
H.
dLN
**
% CD4+
100
80
60
40
20
0
Isotype
CD4-
CD8-

Figure 5.16. Establishing *in vivo* depletion of CD4 and CD8 T cells.

C57BL/6 mice (9 weeks) were injected with 2.5 x10^5 MC38-OVA subcutaneously. A single 200 µg dose of depleting CD4, CD8 or isotype antibody diluted in 200 µl (10 mg/kg body weight) was injected intraperitoneally on day 6 after tumour implantation. Tissues were harvested on day 12 post-injection. All data shown are from one experiment. All graphs show the median value with IQR. Statistical significance was determined using a Kruskal-Wallis multiple comparison with post-hoc Dunn's correction. ** = p < 0.05, ** = p < 0.01.*

A. Growth curves plotting estimated tumour volume based on measurements taken on day 5, 10 and 12. The median and IQR for each of the three treatment groups is plotted. Arrow indicates the day of antibody administration.
B. Tumour weight (g) for each of the treatment groups.
C. Flow cytometry plots demonstrating the expression of CD4 and CD8 in live CD45+ CD11B- B220- CD3+ cells (pre-gated) in subcutaneous tumours. Representative tumour samples from isotype, CD4 depleted and CD8 depleted (left to right) are shown.
D. Flow cytometry plots demonstrating the expression of CD4 and CD8 in live CD45+ CD11B- B220- CD3+ cells (pre-gated) in dLNs. Representative tumour samples from isotype, CD4 depleted and CD8 depleted (left to right) are shown.
E. The percentage of CD3+ cells that are CD8+ in tumour samples from the three different treatment groups.
F. The percentage of CD3+ cells that are CD4+ in tumour samples from the three different treatment groups.
G. The percentage of CD3+ cells that are CD8+ in tumour dLN samples from the three different treatment groups.
H. The percentage of CD3+ cells that are CD4+ in tumour dLN samples from the three different treatment groups.

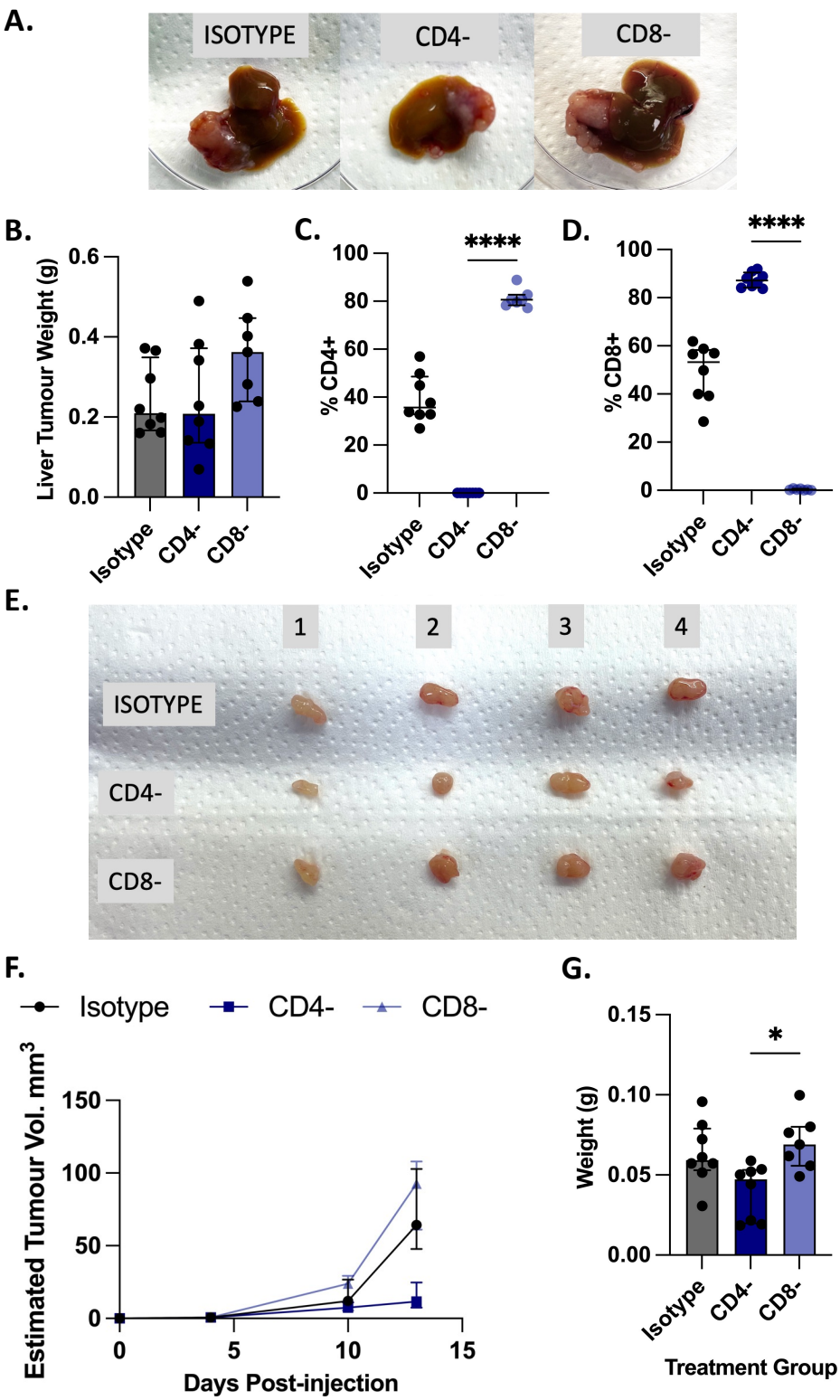

A.
ISOTYPE
CD4-
CD8-
B.
Liver Tumour Weight (g)
0.6
0.4
0.2
0.0
Isotype
CD4-
CD8-
C.
****
% CD4+
100
80
60
40
20
0
Isotype
CD4-
CD8-
D.
****
% CD8+
100
80
60
40
20
0
Isotype
CD4-
CD8-
E.
1
2
3
4
ISOTYPE
CD4-
CD8-
F.
Isotype
CD4-
CD8-
Estimated Tumour Vol. mm3
150
100
50
0
0
5
10
15
Days Post-injection
G.
*
Weight (g)
0.15
0.10
0.05
0.00
Isotype
CD4-
CD8-
Treatment Group

Figure 5.17. Depletion of CD4 and CD8 T cells in the dual liver/s.c. tumour model- impact on tumour growth.

BALB/c mice (10-12 weeks) were injected with 2.0 x10^5 CT26 subcutaneously and intrahepatically. A single 200 µg dose of depleting CD4, CD8 or isotype antibody diluted in 200 µl (10 mg/kg body weight) was injected intraperitoneally on day 6 after tumour implantation. Tissues were harvested on day 12 post-injection. All data shown are from two experiments. All graphs show the median value with IQR. Statistical significance was determined using a Kruskal-Wallis multiple comparison with post-hoc Dunn's correction. ** = p < 0.05, ** = p < 0.01, *** = p < 0.001, **** = p < 0.0001.*

A. Images of the CT26 liver tumours and surrounding liver tissue from mice treated with isotype, depleting CD4, or depleting CD8 antibody (from left to right).
B. The weight (g) of liver tumours in different treatment groups.
C. The proportion of CD3 T cells that are CD4+ in liver tumours in different treatment groups.
D. The proportion of CD3 T cells that are CD8+ in liver tumours in different treatment groups.
E. Image of the CT26 subcutaneous tumours from mice treated with isotype, depleting CD4, or depleting CD8 antibody (from top to bottom rows).
F. Growth curves showing the estimated tumour volume, from measurements taken on day 6, 10 and 12.
G. The weight (g) of CT26 s.c. tumours in each of the three treatment groups.

effective depletion of the targeted populations within the tumour (Fig. 5.18A-C). Finally, focus was shifted to the CD8 T cell population of those mice in which CD4 T cells were depleted, to examine whether overt phenotypic differences were evident compared with the isotype treated group. A higher proportion of the intratumoural CD8 T cells within the subcutaneous tumours of the CD4 depleted group expressed CX3CR1, consistent with an intermediate exhausted phenotype and superior effector function, alongside increased expression of PD-1 and TOX (Fig. 5.18D-F).(160, 348, 349) In CD4 depleted subcutaneous tumours there was an expansion of TOX+ PD-1+ cells, consistent with an expanded exhausted T cell population (Fig. 5.18G-H). Since most of this population expressed CX3CR1 (Fig. 5.18I-J) they likely retained effector functions, unlike terminally exhausted CD8 T cells that lack CX3CR1, contributing to better tumour control. In summary, these data are consistent with CD8 T cell mediated control of tumour growth as expected. It is noteworthy that depletion of CD4 T cells after 6 days of tumour implantation, when help to the CD8 T cell response has likely occurred, resulted in an enhanced CD8 T cell response. While further experiments are required to definitively test why this occurs, it is tempting to speculate that the absence or loss of regulatory CD4 T cells is one approach to overcome the suppressive effect of liver tumours.

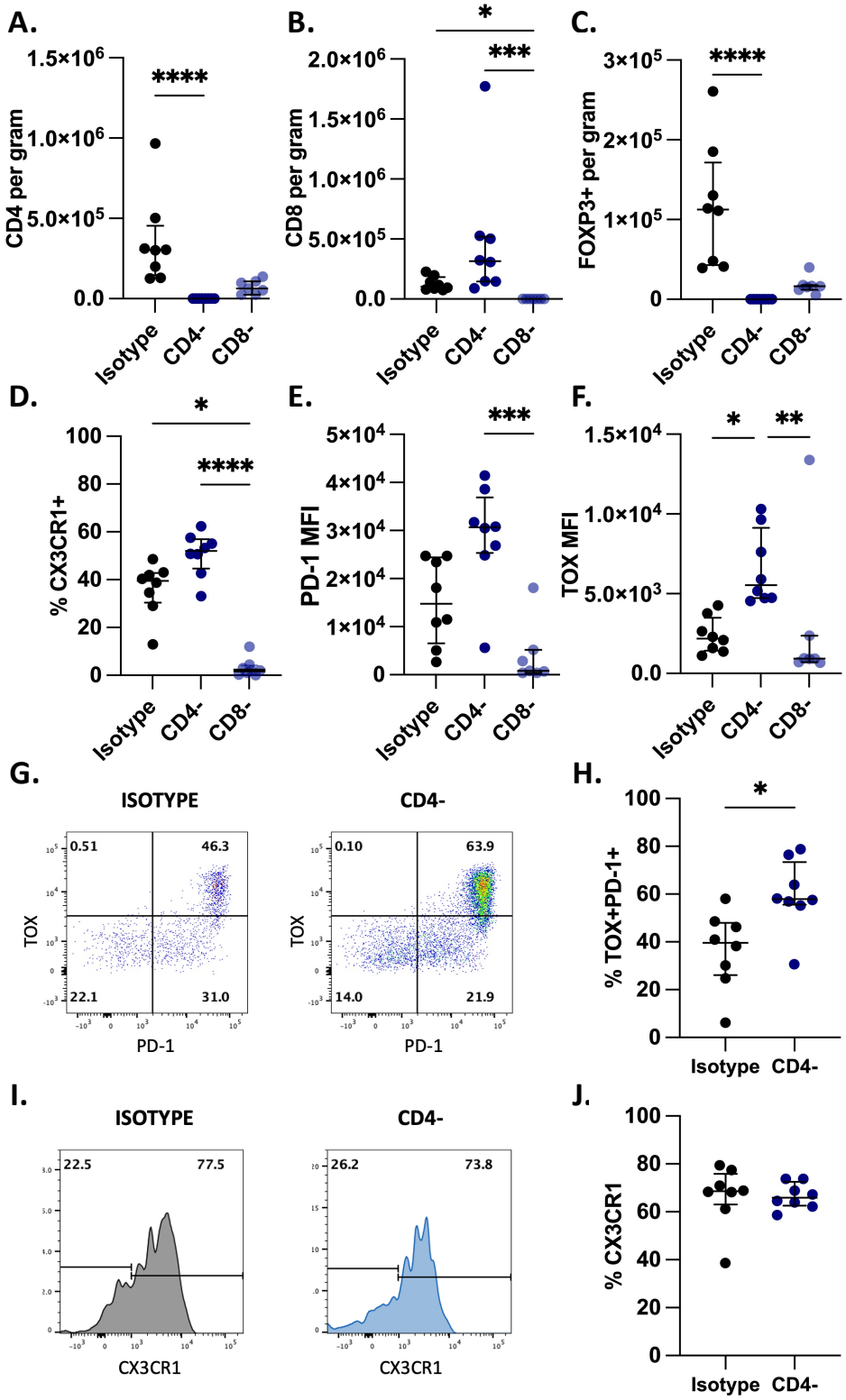

A.
B.
C.
D.
E.
F.
G.
H.
I.
J.
CD4 per gram
CD8 per gram
FOXP3+ per gram
% CX3CR1+
PD-1 MFI
TOX MFI
% TOX+PD-1+
% CX3CR1
Isotype
CD4-
CD8-
ISOTYPE
CD4-
TOX
PD-1
CX3CR1
0.51
46.3
22.1
31.0
0.10
63.9
14.0
21.9
22.5
77.5
26.2
73.8

Figure 5.18. Depletion of CD4 and CD8 T cells in the dual liver/s.c. tumour model- impact on immune populations in the s.c. tumour.

BALB/c mice (10-12 weeks) were injected with 2.0 x10^5 CT26 subcutaneously and intrahepatically. A single 200 µg dose of depleting CD4, CD8 or isotype antibody diluted in 200 µl (10 mg/kg body weight) was injected intraperitoneally on day 6 after tumour implantation. Tissues were harvested on day 12 post-injection. All data shown are from two experiments. All graphs show the median value with IQR. Statistical significance was determined using a Kruskal-Wallis with post-hoc Dunn's correction for multiple comparisons, and in the case of two column analysis a Mann-Whitney test was used. ** = p < 0.05, ** = p < 0.01, *** = p < 0.001, **** = p < 0.0001.*

A. The number of CD4+ cells per gram of s.c. tumour in different treatment groups.
B. The number of CD8+ cells per gram of s.c. tumour in different treatment groups.
C. The number of FOXP3+ CD4+ cells per gram of s.c. tumour in different treatment groups.
D. The percentage of CD8 T cells that are CX3CR1+ in the s.c. tumours in different treatment groups.
E. The MFI of PD-1 in the CD8 population of s.c. tumours in different treatment groups.
F. The MFI of TOX in the CD8 population of s.c. tumours in different treatment groups.
G. Flow cytometry plots demonstrating the TOX and PD-1 expression in the CD8 population of s.c. tumours in different treatment groups. Representative tumours from each group are shown.
H. The proportion of CD8 T cells that are TOX+ PD-1+ in the s.c. tumours in different treatment groups.
I. Histograms demonstrating CX3CR1 expression in the TOX+ PD-1+ CD8 T cell population of s.c. tumours in different treatment groups. Representative tumours from each group are shown.
J. The percentage of TOX+ PD-1+ CD8 T cells that are CX3CR1+ in the s.c. tumours in different treatment groups.

5.3. Summary

In this chapter, building on the liver tumour model developed in Chapter 4, I established an *in vivo* dual liver and subcutaneous tumour model to recapitulate the systemic suppressive effect of liver tumours on the anti-tumour immune response. Having validated the systemic suppression reported in other studies, I performed initial experiments investigating the migration of T cells between the two tumour sites, an approach never before undertaken and also assessed the impact of depleting CD4 or CD8 T cells on tumour control. The key findings from this chapter are summarised in Figure 5.19.

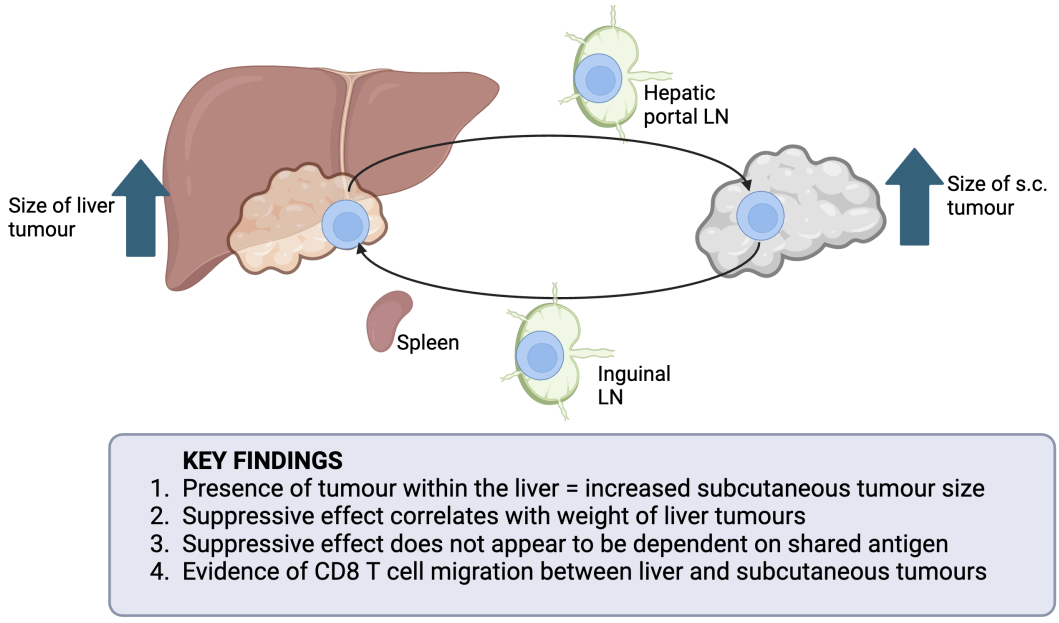


Figure 5.19. Illustration of Chapter 5 findings.

In this chapter the suppressive effect of liver tumours on the systemic anti-tumour immune response was explored. The main findings are summarised in the graphic. Created using Biorender.com.

5.3.1. Exhaustion is rapidly established in the intratumoural CD8 population of liver tumours

Initially, it was important to define how, or if, the intratumoural CD8 compartment differed between liver tumours and subcutaneous tumours generated from implantation of the same cell line at different anatomical sites. We had not observed overt differences when cell lines were implanted into the colon but, given the reported resistance of liver tumours to ICB we anticipated differences in the T cell response when tumours were implanted into the liver. The data demonstrated that implanted liver tumours clearly contain an exhausted T cell population, similar to that seen in the subcutaneous tumour model. There were marginally less stem-like CD8 T cells within liver tumours, and an increase in the proportion of exhausted CD8 T cells defined by PD-1 and TOX expression, but these were relatively modest differences and the main CD8 T cell populations identified at other sites were present within the liver tumours. Examining when exhausted T cell populations became established in the tumours, liver tumours at day 7 after implantation appeared to contain more exhausted CD8 T cells, evidenced by higher PD-1 expression compared to subcutaneous tumours. However, liver tumours were also larger at day 7 than subcutaneous controls in the same experiment, likely due to more rapid vascularisation. Thus, whether differences in the T cell compartment simply reflect more rapid tumour growth, rather than location specific effects, remains unclear. Future experiments titrating the number of tumour cells injected into the liver would help resolve this.

5.3.2. Dual liver and subcutaneous tumour models can be used to investigate systemic suppression of the anti-cancer immune response

The dual liver and subcutaneous model was first trialled with anti-PD-L1 treatment, to ensure that the presence of liver tumours impeded the immune response to ICB within subcutaneous tumours, as previously described.(265, 266) However, in our hands, the suppressive effect of liver tumours was not only observable in the response to anti-PD-L1 therapy, it was found that the subcutaneous tumours in mice bearing liver tumours were significantly bigger at baseline in the absence of intervention. This observation was not made by the two papers utilising this model.(265, 266) However, considering that anti-PD-L1 treatment supports reinvigoration of the anti-tumour T cell response, mechanisms that drive the systemic suppression of T cells would logically operate whether immune checkpoints are targeted or not. Potentially, treatment with ICB simply amplifies these effects. Identification of the impact of liver tumours on the anti-tumour T cell response in the absence of therapeutic intervention may reflect the care taken in establishing the model and measuring tumour growth. An interesting further potential difference to published data was the observation that the suppression of the response in the subcutaneous tumour could be linked to the size or burden of the liver tumour. In contrast to the studies by Lee *et al.* and Yu *et al.,* who both observed that suppression was dependent upon the same cell line being implanted intraheptically and subcutaneously, in our hands, pairing B16 subcutaneous tumours with MC38-OVA liver tumours, resulted in larger tumour growth than when paired with B16 liver tumours. While the data is preliminary at this stage and needs further experiments to test this, including experiments

that better control for the different growth rates of different cell lines within the liver, these data do question which mechanisms are key to driving systemic suppression.

A further interesting observation was that the presence of tumour within the liver resulted in changes in the immune environment in an anatomically distinct lobe. A clear exhausted CD8 T cell compartment was present in the 'healthy' liver lobe of animals with liver tumours, this population was not evident in those with subcutaneous tumours only. While this may reflect dissemination of the tumour from the initial site of implantation, the impact of this was minimised through selection of an anatomically distinct lobe with separate vasculature and no gross signs of disease. Follow up experiments exploring changes in the T cell response at other sites in the liver, as well as in peripheral tissues, need to be performed to further develop this observation.

5.3.3. Novel *in vivo* tumour labelling can be used to assess immune trafficking between tumours

The Kaede tumour photolabelling approach can be used to temporally label intratumoural immune populations and monitor their subsequent migration to the periphery, including to distal tumours. Labelling of the immune compartment in pre-clinical models of multi-site disease is completely novel within the group and was first explored in the dual flank subcutaneous model in Chapter 3. In this chapter, photolabelling was used in the context of the dual liver/subcutaneous tumour model, which has not previously been described. First, through labelling of the subcutaneous tumour, it was confirmed that the presence of liver tumour did not appear to influence immune infiltration into the subcutaneous

tumour, at least within the time frame and populations assessed here. It will be important to repeat these experiments and assess the ingress of other T cells and also innate populations. The migration of T cells from the subcutaneous tumour to the periphery was evident, including a population of stem-like CD8 T cells; though the number of these cells found to have migrated to the liver tumour and background liver was minimal. These data are consistent with the subcutaneous labelling in Chapter 3, reinforcing the observation that there is systemic dissemination of the stem-like CD8 population.

Photolabelling of the liver tumour immune compartment, outlined in Chapter 4, was used to investigate the trafficking of immune cells from hepatic tumours. In the instance of liver tumours complete photolabelling of the immune compartment was not achieved, likely due to the larger size of these tumours, or potentially cellular density within the liver. However, immune cell egress from the tumours was still evident and initial data identified both DC and T cell migration from liver tumours to the hepatic portal lymph node. Further, migration of T cell populations from the liver tumour to the subcutaneous tumour was observed. Finally, a stem-like CD8 compartment migrating from liver tumours was identifiable within the hepatic portal lymph node and peripheral lymphoid tissue, again consistent with the idea of a circulatory stem-like compartment. Key further studies using photolabelling of the liver tumour would better determine the phenotype of migratory T cells, particularly amongst the CD4 T cell compartment which accounted for more than 50% of the migratory T cells. It is also important to consider the potential dissemination of other (non-T cell) immune populations between the tumour sites, experiments which were not feasible within the time frame of this project. Detailed insight into precisely how

systemic suppression is mediated by liver tumours will undoubtedly be aided by better understanding of the immune cell dynamics at both tumour sites as well as intertumour trafficking.

5.3.4. The cellular basis of systemic suppression of the anti-tumour immune response by liver tumours

Following the data revealing migration of lymphocyte populations between liver tumour and subcutaneous tumour, and vice versa, depletion of CD4 and CD8 T cell responses was used to better understand if either population was required for tumour control in the dual liver/subcutaneous model. Depletion of either lymphocyte population did not significantly alter the size of the liver tumour but had a more marked effect on the size of the subcutaneous tumour. CD4 depletion resulted in the smallest subcutaneous tumours, and CD8 depletion the largest, though neither of these changes were statistically significant compared to the isotype control given the relatively small group sizes in this complex model. Ideally these experiments would have been extended over more days with the aim of teasing out effects on tumour growth, however, this timeline was chosen to ensure that the tumours were able to establish prior to therapeutic intervention at day 6; and day 12 was chosen due to welfare concerns surrounding tumour burden in the CD8 group. If the growth kinetics of liver tumours was slowed, for example through titrating the number of tumour cells implanted, it might have resulted in significant differences over a prolonged period. Of course, a dependency on CD8 T cells for tumour control is not a surprising result. Of more potential relevance was the impact of depleting CD4 T cells, indicating that regulatory T cell populations actively hindered the systemic anti-tumour response.

The lack of effective treatments for liver metastases were highlighted above and demand the use of better pre-clinical models to try and identify the therapeutically targetable mechanisms to aid cancer patients. While CD4 T cell depletion is clearly not a viable treatment option, identification of ways to selectively target Tregs in the liver or perhaps regulatory T cells that egress the liver and operate systemically, may prove to be more appropriate approaches.

Chapter 6

Discussion

6.1. Overview

The overarching aim of this work was to better understand the CD8 T cell response in pre-clinical models of colorectal cancer and metastatic disease, with a particular focus on the T cell dynamics that underpin these responses. Initial experiments used subcutaneous implantation of CRC cell lines into Kaede mice to facilitate a detailed interrogation of how the CD8 T cell population changed over time within the tumour. Using scRNA-seq and flow cytometry, a clear stem-like CD8 population within our CRC models was identified and characterised, building on studies in the lab that were published near the start of this project.(286) Across multiple experiments, my studies provided a detailed analysis of which cells are retained in the tumour and which egress, revealing that although a TCF-1+ PD-1+ stem-like compartment is retained in tumours for at least several days, a proportion of these cells continually traffic from the tumour to the dLN and beyond to peripheral lymphoid tissues. Using a dual flank model then allowed for the direct tracking of T cells between tumour sites as well as the peripheral lymphoid compartment. While migration of CD8 T cells between the two subcutaneous tumours was minimal, there was strong evidence that a circulatory 'tumour-experienced' CD8 T cell population developed and some of these possessed a stem-like phenotype that we further validated using phenotypic markers established during the study.

Orthotopic tumours were then established to better model primary and metastatic disease in patients. Endoscopy-guided injection of CT26 cell lines into the colon wall allowed for a more anatomically relevant model of primary CRC. Whilst the use of direct injection of

CT26 and MC38-OVA cells into the liver lobe was developed to model the major site of CRC metastasis. Interestingly, the phenotype and spatial organisation of the intratumoural CD8 T cell compartment appeared to be consistent regardless of the site of tumour implantation. At all sites, the injected cell line resulted in a rapidly growing tumour, densely packed with cancer cells. Novel methods to photolabel tumours within both orthotopic sites were successfully developed, allowing for the study of immune cell migration as established for subcutaneous tumours. Importantly, there was evidence of systemic dissemination of a stem-like CD8 population from both colon and liver tumours, providing further proof that this compartment is dynamic and may be involved in providing systemic protection.

Finally, using the model of CRC liver metastasis developed earlier, a dual liver and subcutaneous tumour model was set up to aid in the study of the systemic suppressive effect of liver metastases that has been described in both pre-clinical models and cancer patients treated with ICB.(266) Building on published data that demonstrated that the presence of liver tumour limits the response to ICB in an anatomically distinct subcutaneous tumour, in our hands we observed the same effect in the CT26 model.(265, 266) Further to this, we observed the systemic immune suppressive effect of liver metastases did not only apply in the context of the response to ICB, but demonstrated that liver tumours license subcutaneous tumours to grow larger in the absence of therapeutic intervention. In addition, the presence of tumour within one liver lobe resulted in changes to the CD8 population in other liver lobes that were not implanted with tumour cells. Photolabelling of both liver and subcutaneous tumours in this setting allowed cell traffic

between the two sites to be assessed for the first time, and we were able to confirm that intertumoural migration of CD8 T cells occurred in this model. Ultimately, this work led to the development of a model that facilitates better understanding of how liver metastases impact the systemic anti-tumour immune response.

6.1.1. The dynamics of the stem-like CD8 response in cancer

The stem-like CD8 population is thought to be integral in sustaining the CD8 T cell compartment in settings of T cell exhaustion, such as chronic infection and cancer, and is thought to be clinically important as it underlies the proliferative burst following ICB.(149, 158, 160, 161) Much of the initial characterisation of this population was carried out in murine LCMV models.(158, 160, 348) This model of chronic infection mirrors the prolonged exposure to antigen in cancer, though the antigen is distributed systemically due to the manner in which mice are infected and viral tropism. Thus, there are likely limits to which observations on immune cell dynamics in LCMV infection are consistent with cancer models where antigen must be more localised. Whilst recent studies have brought to light the role of the stem-like CD8 compartment in the anti-tumour response, a comprehensive and sufficiently granular scRNA-seq dataset in mice has not been published, while existing datasets clearly don't segregate different TCF-1+ CD8 T cell populations.(301) Our lab produced a pre-clinical tumour scRNA-seq dataset that enabled the identification of this subset both within the primary tumour mass and tumour dLN. This unbiased characterisation then facilitated a more robust assessment of the phenotype of this subpopulation at the protein level by flow cytometry. This stem-like CD8 compartment comprised a discrete, but small population within the PD-1+ intratumoural CD8 T cell pool

across multiple CRC models (CT26 and MC38-OVA) implanted in multiple sites (subcutaneous, colon, and liver). The proportion of these cells was notably consistent across the models.

Currently, the migratory potential of the stem-like CD8 subset and how this population is established is not clear from the literature. Data from the lab demonstrated TCF-1+ PD-1+ CD8 T cell egress from the tumour to the dLN utilising the Kaede tumour photolabelling approach.(286) Building on from this, novel application of tumour photolabelling to colon and liver tumours confirmed that there is a prominent population of Kaede red+ stem-like CD8 T cells migrating from these tumours to the dLN. Therefore, this behavioural property is not specific to the subcutaneous tumour model but appears to exist regardless of anatomical placement of the tumour. In addition, the experiments in this thesis analysed peripheral tissues beyond the dLN to assess the migration of this population systemically. Consistently, there was proof of stem-like CD8 T cell dissemination to peripheral lymphoid tissues which had not previously been shown. Finally, photolabelling of the dLN itself, provided evidence that a limited number of stem-like CD8 T cells migrate back into the tumour; though, these cells were of a seemingly more immature phenotype, being PD-1 intermediate rather than PD-1 high. Whether the stem-like compartment contains further differentiation states remains unresolved. In our hands PD-1 expression clearly changed with time in the tumour, for example newly entering TCF-1+ PD-1+ cells expressed lower levels of PD-1 than retained TCF-1+ PD-1+ cells, but the functional relevance is unclear. Changes to inhibitory receptor expression, likely related to TCR signalling, are insufficient at this stage to really denote distinct states.

Studies of the stem-like CD8 population in the setting of chronic viral infection have suggested that this compartment is lymphoid tissue-resident.(149, 290) However, as highlighted earlier, antigen is present systemically in viral infection models and will likely influence the establishment and migration of this population. Studies of the location of stem-like CD8 T cells within tumours have demonstrated their distribution with APCs and alongside tumour vasculature and lymphatics.(288, 291) Cellular traffic between the LN and tumour has been suggested, but not directly assessed, within the existing literature.(106, 292, 293) In this thesis, by direct labelling of CD8 T cells within the tumour and dLN, the stem-like CD8 T cell population was demonstrated to be migratory between these two sites. Our data support the hypothesis that stem-like CD8 T cells within the dLN are able to traffic to the tumour, with a PD-1 low immature phenotype, before some further 'maturation' within the tumour environment. This model helps account for the local expansion of intratumoural exhausted CD8 T cells, whilst providing an explanation for the preservation of a stem-like phenotype in the face of continued antigen exposure within the tumour. Whether a fraction of this population retains migratory capacity and is able to again re-circulate from the tumour, remains uncertain. Further investigation of the stem-like cells that egress the tumour may reveal whether this represents a specific subset of this population; other than upregulation of PD-1 and NKG2A upon entry, we have not yet clearly identified changes relating to the population that egresses the tumour. Overall, the data in this thesis and within the existing literature supports the idea of a migratory and dynamic stem-like CD8 population, in contrast to the more resident stem-like CD8 T cells found in the context of LCMV infection.(149)

6.1.2. Modelling colorectal cancer and metastatic disease

Pre-clinical tumour models have been critical in advancing the field of tumour immunology. The implantation of tumour cell lines subcutaneously has formed the basis of much of the work done in the murine pre-clinical setting. Despite the utility of these models, there are critical limitations. Firstly, these models lack the relevant anatomical context for the study of most cancers, and in the study of immune cell dynamics and migration, vasculature and lymphatic drainage are essential components. In this work we probed whether the implantation of tumour cell lines within different sites altered the nature of the anti-tumour CD8 response. CRC cell lines were successfully implanted within the colon wall and intrahepatically, and interestingly, the phenotype nor spatial organisation of intratumoural CD8 populations was markedly altered by the location of tumour growth. Clear evidence of CD8 T cell infiltration into the tumour mass was found consistently across subcutaneous, colon and liver tumours; in this way our models do not recapitulate the immune excluded landscape of pMMR CRC, representing the predominant subtype of CRC clinically.(250, 251, 330)

Another key issue with subcutaneous tumour models that this work aimed to address, is the modelling of metastatic disease, which is a fundamental issue in the treatment of CRC.(258, 259) Initially a simplified model of multi-site disease was set up, in which CRC cell lines were injected into opposite flanks within Kaede transgenic mice, this presented a unique opportunity to directly study the immune cell traffic between tumours at anatomically distinct sites. There was found to be minimal migration of the T cells between

the two subcutaneous tumour sites, however, this may be due to the limited immature vasculature of subcutaneous tumours limiting cellular traffic and infiltration. Building on from this, I sought to improve this model of CRC metastasis by incorporating the liver tumour model established, injecting CRC cell lines into the liver and subcutaneously. The liver represents the main site of CRC metastasis and is a poor prognostic indicator, so modelling the effect of disease at this site on peripheral tumours is clinically important.(258, 260) Using novel tumour photolabelling approaches, CD8 T cell migration between liver tumour and subcutaneous tumour was captured, providing a direct cellular link between the immune compartments within two anatomically distinct tumours. Currently this model uses simultaneous injection of tumour cell lines intrahepatically and subcutaneously, sequential implantation of the 'primary' (subcutaneous) tumour followed by the 'metastasis' (liver tumour) may change the response. Further to this, the most anatomically accurate model would involve implantation of cell lines in the wall of the colon followed by the liver. Both of these approaches are feasible given the techniques developed during the course of this thesis.

Ultimately, subcutaneous tumour models fall short in accurately predicting the response to treatment in the clinic. The models developed throughout this thesis, highlight that improving pre-clinical tumour models likely goes beyond anatomical location. An underlying reason for the homogeneity in the intratumoural CD8 phenotype across the models used here may be the underdeveloped TME. Utilising models that better consider the TME may better reflect the response to treatment in clinic.(50, 53) For example, a direct link has been made between increasing CAFs within the subcutaneous MC38 model

and a decreased response to ICB.(50) A key outcome of this thesis was the development of models that enable immune cell trafficking between multiple tumour sites to be directly assessed. Improving pre-clinical tumour models available will aid in a more accurate understanding of the mechanisms behind the anti-tumour immune response, and eventually in the development of better therapeutic interventions.

6.1.3. Systemic suppression of anti-tumour immunity by hepatic metastases in CRC

Metastatic disease poses one of the greatest clinical challenges in the treatment of CRC.(258, 259) Liver metastases result in poorer therapeutic responses than other sites of metastasis, such as lung, and this is not only specific to CRC.(260-264) Treatment failure in patients with liver metastases results in progression of disease not only within the liver, but systemically.(260, 261) This phenomenon has been reproduced in pre-clinical dual liver and subcutaneous tumour models, with previously ICB-responsive subcutaneous tumours becoming unresponsive to treatment in the presence of liver tumours.(265, 266) Both papers mentioned examined liver tumour-mediated immune suppression in the context of treatment with ICB, suggesting two distinct mechanisms underlying this effect.(265, 266) Yu *et al.* suggest that liver-resident macrophages are responsible for removing circulating antigen-specific T cells.(265) Lee *et al.* reported that the presence of tumour antigen within the liver led to a change in the activation state of regulatory T cells.(266) In this thesis using the CT26 CRC cell line, we first confirmed that indeed the response to anti-PD-L1 in subcutaneous tumours was eliminated in mice bearing liver tumours. However, the liver tumour-mediated suppression of the immune response within the subcutaneous tumour was also evident in the absence of ICB. Whether the suppression of the response to ICB

required shared antigen between the two tumour sites was unclear, as both papers used the same tumour cell line injected intrahepatically and subcutaneously.(265, 266) Interestingly, data collected here suggest that the magnitude of the liver tumour burden, rather than shared antigen, dictated the degree of immune suppression within the distal tumour in the absence of ICB. However, as this data was from a pilot experiment the growth of MC38-OVA and B16 cell lines within the liver varied considerably, and titration of cell numbers is needed to produce liver tumours of a consistent size between the two groups. In an initial study of the role of CD4 and CD8 T cell populations, it was demonstrated that depletion of CD4 T cell populations resulted in smaller subcutaneous tumours; hinting that regulatory T cell populations might be impeding the systemic anti-tumour response. However, more work is required to confirm this effect in other models and unpick exactly how this is mediated. The size of the liver tumour may well impact regulatory cells in the adaptive arm of the immune system or influence innate populations that are proportional to tumour size. Understanding the mechanisms behind the systemic suppression of the anti-tumour immune response by liver metastases could result in targeted immunotherapies for patients with the worst prognoses.

6.2. Limitations & Future Work

6.2.1. Defining the stem-like CD8 compartment in pre-clinical tumour models

This work has provided a more detailed phenotypic description, through both scRNA-seq and flow cytometry, of the stem-like CD8 population within pre-clinical tumour models. In addition, new insight was provided into the dynamics and migration of this compartment in a direct manner using the Kaede tumour photolabelling model. Unfortunately, the functional importance of the migratory stem-like population was not explored given the time frame. Firstly, showing the proliferation and altered migration of this population in response to treatment with ICB, would add to the literature surrounding the role of the stem-like compartment in the therapeutic response.(148) A second, though technically challenging way of demonstrating the functionality of the migratory stem-like CD8 compartment is via *in vivo* transfer experiments. However, due to the small number of circulatory Kaede red+ stem-like CD8 T cells, sorting for this population to gather significant numbers for transfer could generate the greatest barrier. A way of bypassing this could be to pool multiple lymph nodes and enrich for CD8 T cells (see Chapter 2 for method), prior to then sorting for Kaede red+ TCF-1+ PD-1+ cells. Whether this approach would generate sufficient numbers for an effect post-transfer is uncertain.

6.2.2. Improving orthotopic tumour models

An issue, not limited to our tumour models, is the short time frame in which *in vivo* pre-clinical tumour experiments are conducted. Within each of the models mentioned in this thesis, titration of cell numbers, to enable the minimum number of cells to be injected

whilst also balancing this to ensure they are not cleared by the immune system before a tumour is established, would facilitate in prolonging the experimental window. A longer experimental time frame would enable both different dosing regimens to be applied and assist in observing longer term impacts on immune populations, both clear merits. These titration experiments will have to be performed not only for each site but for each cell line, due to each having unique growth kinetics, demonstrated by the variation in the growth of B16 and MC38-OVA cell lines injected intrahepatically in Chapter 5. Another means of achieving slowed growth is to use tumour organoid models rather than cell lines, these models have slower growth kinetics in general.(324, 331, 332) Within my time in the lab, I additionally cultured 'AKPT' organoids (provided by Sansom Lab, CRUK Scotland Institute) and successfully injected them within the colon wall. These organoids are generated from the tumours of $Villin^{CreER}$ $Apc^{fl/+}$ $Kras^{G12D/+}$ $P53^{fl/fl}$ $Tgfbr1^{fl/fl}$ mice.(324) The resultant tumours within the colon wall, when excised a month after injection, had not yet reached the size of CT26 tumours grown in two weeks (Appendix 6.1), indicating a much slower rate of growth *in vivo*. However, organoids cannot be counted in the same way that cell lines can be, and so ensuring consistency between experiments could present a challenge. In sum, there are several methods to aid in prolonging the experimental window, which would prove invaluable in modelling the immune response to therapy.

Within our multiple tumour models, dual subcutaneous or dual liver and subcutaneous models, staggered implantation of tumours may be an interesting model development. Currently, the peripheral subcutaneous tumour is injected simultaneously with the liver or contralateral subcutaneous tumour. This makes it difficult to ascribe primary and

secondary tumours, as is the case in true metastatic disease. Observing the impact of this sequential implantation on the anti-tumour immune response could be an important improvement to modelling disease. Organoid models, mentioned above, result in natural metastatic deposits and although not conducive to the photolabelling approaches developed here, provide a superior method of modelling metastatic disease.(331, 332)

The cell line models utilised throughout this thesis result in tumours with an underdeveloped TME.(50) Hence, the perturbations in the TME caused by therapeutic interventions are fundamentally lacking. The role of immune cell populations outside of the CD8 T cell response was not fully examined within this work, and as mentioned previously, phenotyping of both innate and regulatory populations is necessary. Non-immune cell populations, such as stromal cells, that have been shown to interact with and influence the immune response within CRC, were also outside of the scope of this work.(52) CAFs, which have been shown to modify the response to ICB, are essentially absent from subcutaneous tumour models.(50, 53) To better model this in future, the co-injection of fibroblasts alongside tumour cell lines is being set up within the lab.(50) Alternatively, the AKPT organoid model mentioned earlier has also been shown to contain CAFs and is sensitive to TGFβ inhibition, likely at least in part through targeting of CAFs.(324) Crucially, future models must find ways of incorporating a study of the TME, as it is clear that this impacts upon the response to treatment and vice versa.(50, 53)

Finally, further work into improving the photolabelling approaches, within both the colon and liver tumour models, could allow for the dynamics of cell entry into these tumours to

be elucidated. In the experiments presented in this thesis, only partial labelling of colon and liver tumours was achieved and so entry of Kaede green cells into the tumours was rendered meaningless. As mentioned previously within this chapter, slowing the growth of tumours within these sites may provide an obvious yet effective means of improving photoconversion. The photolabelling of smaller tumours results in more complete labelling of the intratumoural immune compartment. Another issue is, despite effectively capturing the migration via lymphatics within this model, migration within the vasculature is not studied. Particularly within the new liver model, tumours demonstrate enhanced vascularisation compared to subcutaneously implanted tumours, and hence capturing immune cell migration within the vasculature could be important. A way of studying this is through the i.v. injection of fluorescently labelled CD45 antibody (see Chapter 3) at the same time as tumour photoconversion. Hence, cells that were within the tumour vasculature at the time of photoconversion can be identified as double positive for Kaede red and i.v. CD45 antibody, allowing for the migration of these cells to be assessed.

6.2.3. Investigating the systemic suppressive effect of liver metastasis

An essential initial experiment required within the dual liver and subcutaneous tumour model is the titration of cell numbers implanted within the liver site. Unfortunately, due to the short time frame of this PhD, set up experiments were limited in order to progress the project. However, this is important to control for tumour growth differences, and enable experimental time frames to be extended beyond 14 days. In the pilot experiment examining whether the suppressive effect of liver tumours is dependent on shared tumour antigen, MC38-OVA and B16 liver tumours grew at differing rates; thus, to robustly test

that inhibition is due to liver tumour burden rather than antigen specificity, tumour growth must be comparable between the two groups. Of course, larger tumours may underlie the suppressive effect seen in the absence of treatment, but shared antigen between tumour sites could be key in the diminished response to ICB seen both in this thesis and within the literature.(265, 266) A future experiment would likely involve examining the effect of ICB in the setting of liver and subcutaneous tumours with shared antigen and no shared antigen, having better synchronised the growth of different tumour cell lines in the liver.

Key to understanding the systemic suppressive effect of liver metastases on immune populations within the subcutaneous site is a more thorough analysis of its immune compartment. Within the current analysis the phenotype of the intratumoural CD8 T cell population does not look to be altered, however, this is only according to the limited parameters chosen here; with the addition of functional markers and looking later in the response by using longer 48- and 72-hour photoconversion time points, we may find that differences exist. In addition, other immune populations were outside the scope of this work, but clearly a thorough characterisation of CD4 and DC populations are needed. Bulk RNA-seq may aid in providing a broad initial view of immune populations within the subcutaneous sample and capture changes in specific pathways. This would be a more affordable initial experiment that might then support subsequent scRNA-seq experiments to capture changes in specific cell types thought to contribute to potential mechanisms.

Two distinct mechanisms underlying the systemic suppressive effect of liver metastases have been proposed within the literature. Utilising the models developed in this work, the

reported mechanisms can be investigated further. Yu *et al.* explain the systemic suppression through depletion of the tumour antigen-specific CD8 T cell compartment.(265) To clarify whether this is occurring within our models, the antigen-specific CD8 T cell response within the MC38-OVA tumour model can be assessed, in addition looking for changes in the phenotype of these cells. In the work presented in Chapter 3, no significant loss of the CD8 compartment within the liver tumour nor systemically was observed. However, enumeration of OVA-specific CD8 T cells both within the tumour and systemically could be helpful in confirming that this effect is not apparent within our tumour models. To build on the data presented by Lee *et al.,* the new photolabelling approach within the context of the dual liver and subcutaneous tumour model will allow more detailed examination of what lymphocyte and non-lymphocyte subsets egress, or are unable to egress, the photolabelled liver. As mentioned earlier, CD4 T cells represent a key population to phenotype and characterise the migration of within the dual liver and subcutaneous tumour model.(266) Tracking the migration of antigen-specific regulatory T cell populations has been established within the lab by Suaad Idris, and this could be combined with photolabelling of the immune compartment of liver tumours;(350) enabling the effect of liver metastases on regulatory T cell migration to be assessed. This would extend observations by Lee *et al.* to the peripheral regulatory T cell compartment.(266)

6.3. Concluding Remarks

Overall, these studies have provided new insight into the migratory potential of the stem-like CD8 population in tumours. The generation of new pre-clinical models to study immune cell migration, including colon and liver tumour photolabelling approaches, confirmed that the dissemination of stem-like CD8 T cells was not a phenomenon limited to subcutaneous tumours. Establishing dual flank, and dual liver and subcutaneous tumour models on a Kaede background facilitated the study of how intratumoural immune populations at anatomically distinct sites interact; showing limited traffic between two subcutaneous tumours, but clear migration between tumours implanted in the liver and subcutaneously. Finally, utilising the dual liver and subcutaneous tumour model, initial investigations into the mechanism behind the systemic immune suppressive effect of liver metastases were carried out.

Papers arising from this PhD

Lee, C.Y.C., Kennedy, B.C., Richoz, N. *et al.* Tumour-retained activated CCR7+ dendritic cells are heterogeneous and regulate local anti-tumour cytolytic activity. *Nat Commun* **15**, 682 (2024). https://doi.org/10.1038/s41467-024-44787-1

Kennedy BC, Dean I, Withers DR. Migration of stem-like CD8 T cells between tissue microenvironments underpins successful anti-tumour immune responses. *Discov Immunol*. 2023 Feb 18;2(1):kyad004. doi: 10.1093/discim/kyad004.

Dean I, Kennedy BC, Li Z, Berditchevski F, Withers DR. Protocol for transcutaneous tumor photolabeling to track immune cells in vivo using Kaede mice. STAR Protoc. 2024 Jun 21;5(2):102956. doi: 10.1016/j.xpro.2024.102956.

References

1. CRUK. Cancer Incidence Statistics for United Kingdom. 2021. [Internet]. Available from: https://www.cancerresearchuk.org/health-professional/cancer-statistics/incidence. (21/07/2023).
2. CRUK. Cancer Mortality Statistics for United Kingdom. 2020. [Internet]. Available from: https://www.cancerresearchuk.org/health-professional/cancer-statistics/mortality.21/07/2023.
3. CRUK. Cancer Incidence Statistics Worldwide. 2022. [Internet]. Available from: https://www.cancerresearchuk.org/health-professional/cancer-statistics/worldwide-cancer/incidence.
4. CRUK. Cancer Mortality Statistics Worldwide. 2022. [Internet]. Available from: https://www.cancerresearchuk.org/health-professional/cancer-statistics/worldwide-cancer/mortality. (21/07/2023).
5. Steeg PS. Tumor metastasis: mechanistic insights and clinical challenges. Nature Medicine. 2006;12(8):895-904.
6. Dillekås H, Rogers MS, Straume O. Are 90% of deaths from cancer caused by metastases? Cancer Med. 2019;8(12):5574-6.
7. Press release: The Nobel Prize in Physiology or Medicine 2018. [press release]. 2018-10-01.
8. Turcotte S, Rosenberg SA. Immunotherapy for Metastatic Solid Cancers. Advances in Surgery. 2011;45(1):341-60.
9. Schaller J, Agudo J. Metastatic Colonization: Escaping Immune Surveillance. Cancers (Basel). 2020;12(11).
10. Martínez-Jiménez F, Priestley P, Shale C, Baber J, Rozemuller E, Cuppen E. Genetic immune escape landscape in primary and metastatic cancer. Nature Genetics. 2023;55(5):820-31.
11. Ehrlich P. On the current state of carcinoma research. Contributions to experimental pathology and chemotherapy. 1909;5:273-90.
12. Ludwik Gross MD. Intradermal Immunization of C3H Mice against a Sarcoma That Originated in an Animal of the Same Line. Cancer Res. 1943;3(4):326–33.
13. Clowes G. Further evidence of immunity against cancer in mice after spontaneous recovery. Med News.87:968-71.
14. Foley EJ. Antigenic properties of methylcholanthrene-induced tumors in mice of the strain of origin. Cancer Res. 1953;13(12):835-7.
15. Burnet FM. The concept of immunological surveillance. Prog Exp Tumor Res. 1970;13:1-27.
16. Shankaran V, Ikeda H, Bruce AT, White JM, Swanson PE, Old LJ, et al. IFNγ and lymphocytes prevent primary tumour development and shape tumour immunogenicity. Nature. 2001;410(6832):1107-11.
17. Smyth MJ, Crowe NY, Godfrey DI. NK cells and NKT cells collaborate in host protection from methylcholanthrene-induced fibrosarcoma. Int Immunol. 2001;13(4):459-63.
18. Girardi M, Oppenheim DE, Steele CR, Lewis JM, Glusac E, Filler R, et al. Regulation of cutaneous malignancy by gammadelta T cells. Science. 2001;294(5542):605-9.
19. Street SE, Cretney E, Smyth MJ. Perforin and interferon-gamma activities independently control tumor initiation, growth, and metastasis. Blood. 2001;97(1):192-7.

20. Dighe AS, Richards E, Old LJ, Schreiber RD. Enhanced in vivo growth and resistance to rejection of tumor cells expressing dominant negative IFN gamma receptors. Immunity. 1994;1(6):447-56.
21. Russell JH, Ley TJ. Lymphocyte-mediated cytotoxicity. Annu Rev Immunol. 2002;20:323-70.
22. Vajdic CM, van Leeuwen MT. Cancer incidence and risk factors after solid organ transplantation. Int J Cancer. 2009;125(8):1747-54.
23. Pham SM, Kormos RL, Landreneau RJ, Kawai A, Gonzalez-Cancel I, Hardesty RL, et al. Solid tumors after heart transplantation: lethality of lung cancer. Ann Thorac Surg. 1995;60(6):1623-6.
24. Birkeland SA, Storm HH, Lamm LU, Barlow L, Blohmé I, Forsberg B, et al. Cancer risk after renal transplantation in the Nordic countries, 1964-1986. Int J Cancer. 1995;60(2):183-9.
25. Penn I. Malignant melanoma in organ allograft recipients. Transplantation. 1996;61(2):274-8.
26. Sheil AG. Cancer after transplantation. World J Surg. 1986;10(3):389-96.
27. Gatti RA, Good RA. Occurrence of malignancy in immunodeficiency diseases. A literature review. Cancer. 1971;28(1):89-98.
28. Dunn GP, Bruce AT, Ikeda H, Old LJ, Schreiber RD. Cancer immunoediting: from immunosurveillance to tumor escape. Nat Immunol. 2002;3(11):991-8.
29. Jang G-Y, Lee Jw, Kim YS, Lee SE, Han HD, Hong K-J, et al. Interactions between tumor-derived proteins and Toll-like receptors. Experimental & Molecular Medicine. 2020;52(12):1926-35.
30. Bromberg JF, Horvath CM, Wen Z, Schreiber RD, Darnell JE, Jr. Transcriptionally active Stat1 is required for the antiproliferative effects of both interferon alpha and interferon gamma. Proc Natl Acad Sci U S A. 1996;93(15):7673-8.
31. Cole KE, Strick CA, Paradis TJ, Ogborne KT, Loetscher M, Gladue RP, et al. Interferon-inducible T cell alpha chemoattractant (I-TAC): a novel non-ELR CXC chemokine with potent activity on activated T cells through selective high affinity binding to CXCR3. J Exp Med. 1998;187(12):2009-21.
32. Luster AD, Ravetch JV. Biochemical characterization of a gamma interferon-inducible cytokine (IP-10). J Exp Med. 1987;166(4):1084-97.
33. Woo SR, Fuertes MB, Corrales L, Spranger S, Furdyna MJ, Leung MY, et al. STING-dependent cytosolic DNA sensing mediates innate immune recognition of immunogenic tumors. Immunity. 2014;41(5):830-42.
34. Fuertes MB, Kacha AK, Kline J, Woo SR, Kranz DM, Murphy KM, et al. Host type I IFN signals are required for antitumor CD8+ T cell responses through CD8{alpha}+ dendritic cells. J Exp Med. 2011;208(10):2005-16.
35. Hanahan D, Weinberg RA. The hallmarks of cancer. Cell. 2000;100(1):57-70.
36. Hanahan D, Weinberg RA. Hallmarks of cancer: the next generation. Cell. 2011;144(5):646-74.
37. Ostrand-Rosenberg S, Sinha P. Myeloid-derived suppressor cells: linking inflammation and cancer. J Immunol. 2009;182(8):4499-506.

38. Togashi Y, Shitara K, Nishikawa H. Regulatory T cells in cancer immunosuppression — implications for anticancer therapy. Nature Reviews Clinical Oncology. 2019;16(6):356-71.
39. Yang L, Pang Y, Moses HL. TGF-beta and immune cells: an important regulatory axis in the tumor microenvironment and progression. Trends Immunol. 2010;31(6):220-7.
40. Hanahan D. Hallmarks of Cancer: New Dimensions. Cancer Discov. 2022;12(1):31-46.
41. Iwai Y, Ishida M, Tanaka Y, Okazaki T, Honjo T, Minato N. Involvement of PD-L1 on tumor cells in the escape from host immune system and tumor immunotherapy by PD-L1 blockade. Proc Natl Acad Sci U S A. 2002;99(19):12293-7.
42. Leach DR, Krummel MF, Allison JP. Enhancement of antitumor immunity by CTLA-4 blockade. Science. 1996;271(5256):1734-6.
43. Liu S, Galat V, Galat Y, Lee YKA, Wainwright D, Wu J. NK cell-based cancer immunotherapy: from basic biology to clinical development. Journal of Hematology & Oncology. 2021;14(1):7.
44. Raskov H, Orhan A, Christensen JP, Gögenur I. Cytotoxic CD8+ T cells in cancer and cancer immunotherapy. British Journal of Cancer. 2021;124(2):359-67.
45. Duan Z, Luo Y. Targeting macrophages in cancer immunotherapy. Signal Transduction and Targeted Therapy. 2021;6(1):127.
46. Wculek SK, Cueto FJ, Mujal AM, Melero I, Krummel MF, Sancho D. Dendritic cells in cancer immunology and immunotherapy. Nature Reviews Immunology. 2020;20(1):7-24.
47. Tay RE, Richardson EK, Toh HC. Revisiting the role of CD4+ T cells in cancer immunotherapy—new insights into old paradigms. Cancer Gene Therapy. 2021;28(1):5-17.
48. Quail DF, Amulic B, Aziz M, Barnes BJ, Eruslanov E, Fridlender ZG, et al. Neutrophil phenotypes and functions in cancer: A consensus statement. J Exp Med. 2022;219(6).
49. Yang Y, Li C, Liu T, Dai X, Bazhin AV. Myeloid-Derived Suppressor Cells in Tumors: From Mechanisms to Antigen Specificity and Microenvironmental Regulation. Frontiers in Immunology. 2020;11.
50. Ford K, Hanley CJ, Mellone M, Szyndralewiez C, Heitz F, Wiesel P, et al. NOX4 Inhibition Potentiates Immunotherapy by Overcoming Cancer-Associated Fibroblast-Mediated CD8 T-cell Exclusion from Tumors. Cancer Res. 2020;80(9):1846-60.
51. Liu T, Han C, Wang S, Fang P, Ma Z, Xu L, et al. Cancer-associated fibroblasts: an emerging target of anti-cancer immunotherapy. Journal of Hematology & Oncology. 2019;12(1):86.
52. Qi J, Sun H, Zhang Y, Wang Z, Xun Z, Li Z, et al. Single-cell and spatial analysis reveal interaction of FAP(+) fibroblasts and SPP1(+) macrophages in colorectal cancer. Nat Commun. 2022;13(1):1742.
53. Sahai E, Astsaturov I, Cukierman E, DeNardo DG, Egeblad M, Evans RM, et al. A framework for advancing our understanding of cancer-associated fibroblasts. Nature Reviews Cancer. 2020;20(3):174-86.
54. Galon J, Costes A, Sanchez-Cabo F, Kirilovsky A, Mlecnik B, Lagorce-Pagès C, et al. Type, density, and location of immune cells within human colorectal tumors predict clinical outcome. Science. 2006;313(5795):1960-4.

55. Li F, Li C, Cai X, Xie Z, Zhou L, Cheng B, et al. The association between CD8+ tumor-infiltrating lymphocytes and the clinical outcome of cancer immunotherapy: A systematic review and meta-analysis. eClinicalMedicine. 2021;41.
56. Zhang L, Conejo-Garcia JR, Katsaros D, Gimotty PA, Massobrio M, Regnani G, et al. Intratumoral T cells, recurrence, and survival in epithelial ovarian cancer. N Engl J Med. 2003;348(3):203-13.
57. Salgado R, Denkert C, Demaria S, Sirtaine N, Klauschen F, Pruneri G, et al. The evaluation of tumor-infiltrating lymphocytes (TILs) in breast cancer: recommendations by an International TILs Working Group 2014. Ann Oncol. 2015;26(2):259-71.
58. Leffers N, Gooden MJM, de Jong RA, Hoogeboom B-N, ten Hoor KA, Hollema H, et al. Prognostic significance of tumor-infiltrating T-lymphocytes in primary and metastatic lesions of advanced stage ovarian cancer. Cancer Immunology, Immunotherapy. 2009;58(3):449-59.
59. Azimi F, Scolyer RA, Rumcheva P, Moncrieff M, Murali R, McCarthy SW, et al. Tumor-infiltrating lymphocyte grade is an independent predictor of sentinel lymph node status and survival in patients with cutaneous melanoma. J Clin Oncol. 2012;30(21):2678-83.
60. Liu S, Lachapelle J, Leung S, Gao D, Foulkes WD, Nielsen TO. CD8+ lymphocyte infiltration is an independent favorable prognostic indicator in basal-like breast cancer. Breast Cancer Research. 2012;14(2):R48.
61. Martin MD, Badovinac VP. Defining Memory CD8 T Cell. Frontiers in Immunology. 2018;9.
62. Mempel TR, Henrickson SE, von Andrian UH. T-cell priming by dendritic cells in lymph nodes occurs in three distinct phases. Nature. 2004;427(6970):154-9.
63. Celluzzi CM, Mayordomo JI, Storkus WJ, Lotze MT, Falo LD, Jr. Peptide-pulsed dendritic cells induce antigen-specific CTL-mediated protective tumor immunity. J Exp Med. 1996;183(1):283-7.
64. Roberts EW, Broz ML, Binnewies M, Headley MB, Nelson AE, Wolf DM, et al. Critical Role for CD103(+)/CD141(+) Dendritic Cells Bearing CCR7 for Tumor Antigen Trafficking and Priming of T Cell Immunity in Melanoma. Cancer Cell. 2016;30(2):324-36.
65. Nelson DJ, Mukherjee S, Bundell C, Fisher S, van Hagen D, Robinson B. Tumor progression despite efficient tumor antigen cross-presentation and effective "arming" of tumor antigen-specific CTL. J Immunol. 2001;166(9):5557-66.
66. Nguyen LT, Elford AR, Murakami K, Garza KM, Schoenberger SP, Odermatt B, et al. Tumor growth enhances cross-presentation leading to limited T cell activation without tolerance. J Exp Med. 2002;195(4):423-35.
67. Binnewies M, Roberts EW, Kersten K, Chan V, Fearon DF, Merad M, et al. Understanding the tumor immune microenvironment (TIME) for effective therapy. Nat Med. 2018;24(5):541-50.
68. Thompson ED, Enriquez HL, Fu YX, Engelhard VH. Tumor masses support naive T cell infiltration, activation, and differentiation into effectors. J Exp Med. 2010;207(8):1791-804.
69. Bai XF, Gao JX, Liu J, Wen J, Zheng P, Liu Y. On the site and mode of antigen presentation for the initiation of clonal expansion of CD8 T cells specific for a natural tumor antigen. Cancer Res. 2001;61(18):6860-7.

70. von Andrian UH, Mackay CR. T-cell function and migration. Two sides of the same coin. N Engl J Med. 2000;343(14):1020-34.
71. Yu P, Lee Y, Liu W, Chin RK, Wang J, Wang Y, et al. Priming of naive T cells inside tumors leads to eradication of established tumors. Nature Immunology. 2004;5(2):141-9.
72. Michea P, Noël F, Zakine E, Czerwinska U, Sirven P, Abouzid O, et al. Adjustment of dendritic cells to the breast-cancer microenvironment is subset specific. Nature Immunology. 2018;19(8):885-97.
73. Böttcher JP, Bonavita E, Chakravarty P, Blees H, Cabeza-Cabrerizo M, Sammicheli S, et al. NK Cells Stimulate Recruitment of cDC1 into the Tumor Microenvironment Promoting Cancer Immune Control. Cell. 2018;172(5):1022-37.e14.
74. Barry KC, Hsu J, Broz ML, Cueto FJ, Binnewies M, Combes AJ, et al. A natural killer–dendritic cell axis defines checkpoint therapy–responsive tumor microenvironments. Nature Medicine. 2018;24(8):1178-91.
75. Rakoff-Nahoum S, Medzhitov R. Toll-like receptors and cancer. Nat Rev Cancer. 2009;9(1):57-63.
76. Bracci L, Schiavoni G, Sistigu A, Belardelli F. Immune-based mechanisms of cytotoxic chemotherapy: implications for the design of novel and rationale-based combined treatments against cancer. Cell Death Differ. 2014;21(1):15-25.
77. Förster R, Schubel A, Breitfeld D, Kremmer E, Renner-Müller I, Wolf E, et al. CCR7 coordinates the primary immune response by establishing functional microenvironments in secondary lymphoid organs. Cell. 1999;99(1):23-33.
78. Ohl L, Mohaupt M, Czeloth N, Hintzen G, Kiafard Z, Zwirner J, et al. CCR7 governs skin dendritic cell migration under inflammatory and steady-state conditions. Immunity. 2004;21(2):279-88.
79. van der Bruggen P, Traversari C, Chomez P, Lurquin C, De Plaen E, Van den Eynde B, et al. A gene encoding an antigen recognized by cytolytic T lymphocytes on a human melanoma. Science. 1991;254(5038):1643-7.
80. Alexandrov LB, Kim J, Haradhvala NJ, Huang MN, Tian Ng AW, Wu Y, et al. The repertoire of mutational signatures in human cancer. Nature. 2020;578(7793):94-101.
81. Yarchoan M, Hopkins A, Jaffee EM. Tumor Mutational Burden and Response Rate to PD-1 Inhibition. N Engl J Med. 2017;377(25):2500-1.
82. Maier B, Leader AM, Chen ST, Tung N, Chang C, LeBerichel J, et al. A conserved dendritic-cell regulatory program limits antitumour immunity. Nature. 2020;580(7802):257-62.
83. Lee CYC, Kennedy BC, Richoz N, Dean I, Tuong ZK, Gaspal F, et al. Tumour-retained activated CCR7+ dendritic cells are heterogeneous and regulate local anti-tumour cytolytic activity. Nature Communications. 2024;15(1):682.
84. Anderson G, Hare KJ, Jenkinson EJ. Positive selection of thymocytes: the long and winding road. Immunol Today. 1999;20(10):463-8.
85. Zhan Y, Purton JF, Godfrey DI, Cole TJ, Heath WR, Lew AM. Without peripheral interference, thymic deletion is mediated in a cohort of double-positive cells without classical activation. Proc Natl Acad Sci U S A. 2003;100(3):1197-202.
86. Sant'Angelo DB, Janeway CA, Jr. Negative selection of thymocytes expressing the D10 TCR. Proc Natl Acad Sci U S A. 2002;99(10):6931-6.

87. Goldman KP, Park CS, Kim M, Matzinger P, Anderson CC. Thymic cortical epithelium induces self tolerance. Eur J Immunol. 2005;35(3):709-17.
88. Baldwin KK, Trenchak BP, Altman JD, Davis MM. Negative selection of T cells occurs throughout thymic development. J Immunol. 1999;163(2):689-98.
89. Surh CD, Sprent J. T-cell apoptosis detected in situ during positive and negative selection in the thymus. Nature. 1994;372(6501):100-3.
90. Alarcón B, Gil D, Delgado P, Schamel WW. Initiation of TCR signaling: regulation within CD3 dimers. Immunol Rev. 2003;191:38-46.
91. Seliger B, Ritz U, Abele R, Bock M, Tampé R, Sutter G, et al. Immune escape of melanoma: first evidence of structural alterations in two distinct components of the MHC class I antigen processing pathway. Cancer Res. 2001;61(24):8647-50.
92. Maleno I, Cabrera CM, Cabrera T, Paco L, López-Nevot MA, Collado A, et al. Distribution of HLA class I altered phenotypes in colorectal carcinomas: high frequency of HLA haplotype loss associated with loss of heterozygosity in chromosome region 6p21. Immunogenetics. 2004;56(4):244-53.
93. June CH, Ledbetter JA, Linsley PS, Thompson CB. Role of the CD28 receptor in T-cell activation. Immunol Today. 1990;11(6):211-6.
94. Jenkins MK, Ashwell JD, Schwartz RH. Allogeneic non-T spleen cells restore the responsiveness of normal T cell clones stimulated with antigen and chemically modified antigen-presenting cells. J Immunol. 1988;140(10):3324-30.
95. Chen L, Flies DB. Molecular mechanisms of T cell co-stimulation and co-inhibition. Nature Reviews Immunology. 2013;13(4):227-42.
96. Bullock TN, Yagita H. Induction of CD70 on dendritic cells through CD40 or TLR stimulation contributes to the development of CD8+ T cell responses in the absence of CD4+ T cells. J Immunol. 2005;174(2):710-7.
97. Prilliman KR, Lemmens EE, Palioungas G, Wolfe TG, Allison JP, Sharpe AH, et al. Cutting edge: a crucial role for B7-CD28 in transmitting T help from APC to CTL. J Immunol. 2002;169(8):4094-7.
98. Schluns KS, Williams K, Ma A, Zheng XX, Lefrançois L. Cutting edge: requirement for IL-15 in the generation of primary and memory antigen-specific CD8 T cells. J Immunol. 2002;168(10):4827-31.
99. Curtsinger JM, Schmidt CS, Mondino A, Lins DC, Kedl RM, Jenkins MK, et al. Inflammatory cytokines provide a third signal for activation of naive CD4+ and CD8+ T cells. J Immunol. 1999;162(6):3256-62.
100. Wiesel M, Kratky W, Oxenius A. Type I IFN substitutes for T cell help during viral infections. J Immunol. 2011;186(2):754-63.
101. Schulz O, Edwards AD, Schito M, Aliberti J, Manickasingham S, Sher A, et al. CD40 triggering of heterodimeric IL-12 p70 production by dendritic cells in vivo requires a microbial priming signal. Immunity. 2000;13(4):453-62.
102. Agarwal P, Raghavan A, Nandiwada SL, Curtsinger JM, Bohjanen PR, Mueller DL, et al. Gene regulation and chromatin remodeling by IL-12 and type I IFN in programming for CD8 T cell effector function and memory. J Immunol. 2009;183(3):1695-704.
103. Curtsinger JM, Agarwal P, Lins DC, Mescher MF. Autocrine IFN-γ promotes naive CD8 T cell differentiation and synergizes with IFN-α to stimulate strong function. J Immunol. 2012;189(2):659-68.

104. Harding FA, McArthur JG, Gross JA, Raulet DH, Allison JP. CD28-mediated signalling co-stimulates murine T cells and prevents induction of anergy in T-cell clones. Nature. 1992;356(6370):607-9.
105. Schwartz RH. A cell culture model for T lymphocyte clonal anergy. Science. 1990;248(4961):1349-56.
106. Prokhnevska N, Cardenas MA, Valanparambil RM, Sobierajska E, Barwick BG, Jansen C, et al. CD8(+) T cell activation in cancer comprises an initial activation phase in lymph nodes followed by effector differentiation within the tumor. Immunity. 2023;56(1):107-24.e5.
107. Testi R, Phillips JH, Lanier LL. T cell activation via Leu-23 (CD69). J Immunol. 1989;143(4):1123-8.
108. Miyawaki T, Uehara T, Nibu R, Tsuji T, Yachie A, Yonehara S, et al. Differential expression of apoptosis-related Fas antigen on lymphocyte subpopulations in human peripheral blood. J Immunol. 1992;149(11):3753-8.
109. Sullivan BM, Juedes A, Szabo SJ, von Herrath M, Glimcher LH. Antigen-driven effector CD8 T cell function regulated by T-bet. Proc Natl Acad Sci U S A. 2003;100(26):15818-23.
110. Pearce EL, Mullen AC, Martins GA, Krawczyk CM, Hutchins AS, Zediak VP, et al. Control of effector CD8+ T cell function by the transcription factor Eomesodermin. Science. 2003;302(5647):1041-3.
111. Kägi D, Ledermann B, Bürki K, Seiler P, Odermatt B, Olsen KJ, et al. Cytotoxicity mediated by T cells and natural killer cells is greatly impaired in perforin-deficient mice. Nature. 1994;369(6475):31-7.
112. Shresta S, MacIvor DM, Heusel JW, Russell JH, Ley TJ. Natural killer and lymphokine-activated killer cells require granzyme B for the rapid induction of apoptosis in susceptible target cells. Proc Natl Acad Sci U S A. 1995;92(12):5679-83.
113. Rouvier E, Luciani MF, Golstein P. Fas involvement in Ca(2+)-independent T cell-mediated cytotoxicity. J Exp Med. 1993;177(1):195-200.
114. Algeciras-Schimnich A, Pietras EM, Barnhart BC, Legembre P, Vijayan S, Holbeck SL, et al. Two CD95 tumor classes with different sensitivities to antitumor drugs. Proc Natl Acad Sci U S A. 2003;100(20):11445-50.
115. Ivanov VN, Ronai Z, Hei TK. Opposite roles of FAP-1 and dynamin in the regulation of Fas (CD95) translocation to the cell surface and susceptibility to Fas ligand-mediated apoptosis. J Biol Chem. 2006;281(3):1840-52.
116. Tourneur L, Mistou S, Michiels FM, Devauchelle V, Renia L, Feunteun J, et al. Loss of FADD protein expression results in a biased Fas-signaling pathway and correlates with the development of tumoral status in thyroid follicular cells. Oncogene. 2003;22(18):2795-804.
117. Teitz T, Wei T, Valentine MB, Vanin EF, Grenet J, Valentine VA, et al. Caspase 8 is deleted or silenced preferentially in childhood neuroblastomas with amplification of MYCN. Nat Med. 2000;6(5):529-35.
118. O'Connell J, O'Sullivan GC, Collins JK, Shanahan F. The Fas counterattack: Fas-mediated T cell killing by colon cancer cells expressing Fas ligand. J Exp Med. 1996;184(3):1075-82.

119. Nathan CF, Murray HW, Wiebe ME, Rubin BY. Identification of interferon-gamma as the lymphokine that activates human macrophage oxidative metabolism and antimicrobial activity. J Exp Med. 1983;158(3):670-89.
120. Shirayoshi Y, Burke PA, Appella E, Ozato K. Interferon-induced transcription of a major histocompatibility class I gene accompanies binding of inducible nuclear factors to the interferon consensus sequence. Proc Natl Acad Sci U S A. 1988;85(16):5884-8.
121. Coussens LM, Werb Z. Inflammation and cancer. Nature. 2002;420(6917):860-7.
122. Hanada T, Kobayashi T, Chinen T, Saeki K, Takaki H, Koga K, et al. IFNgamma-dependent, spontaneous development of colorectal carcinomas in SOCS1-deficient mice. J Exp Med. 2006;203(6):1391-7.
123. Abiko K, Matsumura N, Hamanishi J, Horikawa N, Murakami R, Yamaguchi K, et al. IFN-γ from lymphocytes induces PD-L1 expression and promotes progression of ovarian cancer. Br J Cancer. 2015;112(9):1501-9.
124. Spranger S, Spaapen RM, Zha Y, Williams J, Meng Y, Ha TT, et al. Up-regulation of PD-L1, IDO, and T(regs) in the melanoma tumor microenvironment is driven by CD8(+) T cells. Sci Transl Med. 2013;5(200):200ra116.
125. Zajac AJ, Blattman JN, Murali-Krishna K, Sourdive DJ, Suresh M, Altman JD, et al. Viral immune evasion due to persistence of activated T cells without effector function. J Exp Med. 1998;188(12):2205-13.
126. Moskophidis D, Lechner F, Pircher H, Zinkernagel RM. Virus persistence in acutely infected immunocompetent mice by exhaustion of antiviral cytotoxic effector T cells. Nature. 1993;362(6422):758-61.
127. Gallimore A, Glithero A, Godkin A, Tissot AC, Plückthun A, Elliott T, et al. Induction and exhaustion of lymphocytic choriomeningitis virus-specific cytotoxic T lymphocytes visualized using soluble tetrameric major histocompatibility complex class I-peptide complexes. J Exp Med. 1998;187(9):1383-93.
128. Blackburn SD, Shin H, Haining WN, Zou T, Workman CJ, Polley A, et al. Coregulation of CD8+ T cell exhaustion by multiple inhibitory receptors during chronic viral infection. Nat Immunol. 2009;10(1):29-37.
129. Nakamoto N, Kaplan DE, Coleclough J, Li Y, Valiga ME, Kaminski M, et al. Functional Restoration of HCV-Specific CD8 T Cells by PD-1 Blockade Is Defined by PD-1 Expression and Compartmentalization. Gastroenterology. 2008;134(7):1927-37.e2.
130. Day CL, Kaufmann DE, Kiepiela P, Brown JA, Moodley ES, Reddy S, et al. PD-1 expression on HIV-specific T cells is associated with T-cell exhaustion and disease progression. Nature. 2006;443(7109):350-4.
131. Velu V, Kannanganat S, Ibegbu C, Chennareddi L, Villinger F, Freeman Gordon J, et al. Elevated Expression Levels of Inhibitory Receptor Programmed Death 1 on Simian Immunodeficiency Virus-Specific CD8 T Cells during Chronic Infection but Not after Vaccination. Journal of Virology. 2007;81(11):5819-28.
132. Wherry EJ. T cell exhaustion. Nature Immunology. 2011;12(6):492-9.
133. Scott AC, Dündar F, Zumbo P, Chandran SS, Klebanoff CA, Shakiba M, et al. TOX is a critical regulator of tumour-specific T cell differentiation. Nature. 2019;571(7764):270-4.

134. Khan O, Giles JR, McDonald S, Manne S, Ngiow SF, Patel KP, et al. TOX transcriptionally and epigenetically programs CD8(+) T cell exhaustion. Nature. 2019;571(7764):211-8.
135. Abdel-Hakeem MS, Manne S, Beltra J-C, Stelekati E, Chen Z, Nzingha K, et al. Epigenetic scarring of exhausted T cells hinders memory differentiation upon eliminating chronic antigenic stimulation. Nature Immunology. 2021;22(8):1008-19.
136. Li J, He Y, Hao J, Ni L, Dong C. High Levels of Eomes Promote Exhaustion of Anti-tumor CD8(+) T Cells. Front Immunol. 2018;9:2981.
137. Shin H, Blackburn SD, Intlekofer AM, Kao C, Angelosanto JM, Reiner SL, et al. A Role for the Transcriptional Repressor Blimp-1 in CD8+ T Cell Exhaustion during Chronic Viral Infection. Immunity. 2009;31(2):309-20.
138. Richter K, Brocker T, Oxenius A. Antigen amount dictates CD8+ T-cell exhaustion during chronic viral infection irrespective of the type of antigen presenting cell. Eur J Immunol. 2012;42(9):2290-304.
139. Wherry EJ, Blattman JN, Murali-Krishna K, van der Most R, Ahmed R. Viral persistence alters CD8 T-cell immunodominance and tissue distribution and results in distinct stages of functional impairment. J Virol. 2003;77(8):4911-27.
140. Mueller SN, Ahmed R. High antigen levels are the cause of T cell exhaustion during chronic viral infection. Proc Natl Acad Sci U S A. 2009;106(21):8623-8.
141. Utzschneider DT, Alfei F, Roelli P, Barras D, Chennupati V, Darbre S, et al. High antigen levels induce an exhausted phenotype in a chronic infection without impairing T cell expansion and survival. J Exp Med. 2016;213(9):1819-34.
142. Bucks CM, Norton JA, Boesteanu AC, Mueller YM, Katsikis PD. Chronic antigen stimulation alone is sufficient to drive CD8+ T cell exhaustion. J Immunol. 2009;182(11):6697-708.
143. Matloubian M, Concepcion RJ, Ahmed R. CD4+ T cells are required to sustain CD8+ cytotoxic T-cell responses during chronic viral infection. J Virol. 1994;68(12):8056-63.
144. Brooks DG, Ha SJ, Elsaesser H, Sharpe AH, Freeman GJ, Oldstone MB. IL-10 and PD-L1 operate through distinct pathways to suppress T-cell activity during persistent viral infection. Proc Natl Acad Sci U S A. 2008;105(51):20428-33.
145. Brooks DG, Trifilo MJ, Edelmann KH, Teyton L, McGavern DB, Oldstone MB. Interleukin-10 determines viral clearance or persistence in vivo. Nat Med. 2006;12(11):1301-9.
146. Ejrnaes M, Filippi CM, Martinic MM, Ling EM, Togher LM, Crotty S, et al. Resolution of a chronic viral infection after interleukin-10 receptor blockade. J Exp Med. 2006;203(11):2461-72.
147. Tinoco R, Alcalde V, Yang Y, Sauer K, Zuniga EI. Cell-intrinsic transforming growth factor-beta signaling mediates virus-specific CD8+ T cell deletion and viral persistence in vivo. Immunity. 2009;31(1):145-57.
148. Siddiqui I, Schaeuble K, Chennupati V, Fuertes Marraco SA, Calderon-Copete S, Pais Ferreira D, et al. Intratumoral Tcf1(+)PD-1(+)CD8(+) T Cells with Stem-like Properties Promote Tumor Control in Response to Vaccination and Checkpoint Blockade Immunotherapy. Immunity. 2019;50(1):195-211.e10.

149. Im SJ, Hashimoto M, Gerner MY, Lee J, Kissick HT, Burger MC, et al. Defining CD8+ T cells that provide the proliferative burst after PD-1 therapy. Nature. 2016;537(7620):417-21.
150. Baitsch L, Baumgaertner P, Devêvre E, Raghav SK, Legat A, Barba L, et al. Exhaustion of tumor-specific CD8$^+$ T cells in metastases from melanoma patients. J Clin Invest. 2011;121(6):2350-60.
151. Ahmadzadeh M, Johnson LA, Heemskerk B, Wunderlich JR, Dudley ME, White DE, et al. Tumor antigen-specific CD8 T cells infiltrating the tumor express high levels of PD-1 and are functionally impaired. Blood. 2009;114(8):1537-44.
152. Kamphorst AO, Pillai RN, Yang S, Nasti TH, Akondy RS, Wieland A, et al. Proliferation of PD-1+ CD8 T cells in peripheral blood after PD-1-targeted therapy in lung cancer patients. Proc Natl Acad Sci U S A. 2017;114(19):4993-8.
153. Kurtulus S, Madi A, Escobar G, Klapholz M, Nyman J, Christian E, et al. Checkpoint Blockade Immunotherapy Induces Dynamic Changes in PD-1(-)CD8(+) Tumor-Infiltrating T Cells. Immunity. 2019;50(1):181-94.e6.
154. Mognol GP, Spreafico R, Wong V, Scott-Browne JP, Togher S, Hoffmann A, et al. Exhaustion-associated regulatory regions in CD8(+) tumor-infiltrating T cells. Proc Natl Acad Sci U S A. 2017;114(13):E2776-e85.
155. Pauken KE, Sammons MA, Odorizzi PM, Manne S, Godec J, Khan O, et al. Epigenetic stability of exhausted T cells limits durability of reinvigoration by PD-1 blockade. Science. 2016;354(6316):1160-5.
156. Pritykin Y, van der Veeken J, Pine AR, Zhong Y, Sahin M, Mazutis L, et al. A unified atlas of CD8 T cell dysfunctional states in cancer and infection. Mol Cell. 2021;81(11):2477-93.e10.
157. Utzschneider DT, Legat A, Fuertes Marraco SA, Carrié L, Luescher I, Speiser DE, et al. T cells maintain an exhausted phenotype after antigen withdrawal and population reexpansion. Nat Immunol. 2013;14(6):603-10.
158. Utzschneider DT, Charmoy M, Chennupati V, Pousse L, Ferreira DP, Calderon-Copete S, et al. T Cell Factor 1-Expressing Memory-like CD8(+) T Cells Sustain the Immune Response to Chronic Viral Infections. Immunity. 2016;45(2):415-27.
159. Brummelman J, Mazza EMC, Alvisi G, Colombo FS, Grilli A, Mikulak J, et al. High-dimensional single cell analysis identifies stem-like cytotoxic CD8(+) T cells infiltrating human tumors. J Exp Med. 2018;215(10):2520-35.
160. Utzschneider DT, Gabriel SS, Chisanga D, Gloury R, Gubser PM, Vasanthakumar A, et al. Early precursor T cells establish and propagate T cell exhaustion in chronic infection. Nature Immunology. 2020;21(10):1256-66.
161. Sade-Feldman M, Yizhak K, Bjorgaard SL, Ray JP, de Boer CG, Jenkins RW, et al. Defining T Cell States Associated with Response to Checkpoint Immunotherapy in Melanoma. Cell. 2018;175(4):998-1013.e20.
162. NICE. Nivolumab [Specialist drug]. BNF. [Internet]. Available from: https://bnf.nice.org.uk/drugs/nivolumab-specialist-drug/. (31/08/2023).
163. NICE. Pembrolizumab [Specialist drug]. BNF. [Internet]. Available from: https://bnf.nice.org.uk/drugs/pembrolizumab-specialist-drug/. (31/08/2023).
164. NICE. Ipilimumab [Specialist drug]. BNF. [Internet]. Available from: https://bnf.nice.org.uk/drugs/ipilimumab-specialist-drug/. (31/08/2023).

165. Sharma P, Allison JP. Immune checkpoint targeting in cancer therapy: toward combination strategies with curative potential. Cell. 2015;161(2):205-14.
166. Klein C, Waldhauer I, Nicolini VG, Freimoser-Grundschober A, Nayak T, Vugts DJ, et al. Cergutuzumab amunaleukin (CEA-IL2v), a CEA-targeted IL-2 variant-based immunocytokine for combination cancer immunotherapy: Overcoming limitations of aldesleukin and conventional IL-2-based immunocytokines. Oncoimmunology. 2017;6(3):e1277306.
167. Klebanoff CA, Finkelstein SE, Surman DR, Lichtman MK, Gattinoni L, Theoret MR, et al. IL-15 enhances the in vivo antitumor activity of tumor-reactive CD8+ T cells. Proc Natl Acad Sci U S A. 2004;101(7):1969-74.
168. Kennedy MK, Glaccum M, Brown SN, Butz EA, Viney JL, Embers M, et al. Reversible defects in natural killer and memory CD8 T cell lineages in interleukin 15-deficient mice. J Exp Med. 2000;191(5):771-80.
169. Di Scala M, Gil-Fariña I, Olagüe C, Vales A, Sobrevals L, Fortes P, et al. Identification of IFN-γ-producing T cells as the main mediators of the side effects associated to mouse interleukin-15 sustained exposure. Oncotarget. 2016;7(31):49008-26.
170. Ibe S, Qin Z, Schüler T, Preiss S, Blankenstein T. Tumor rejection by disturbing tumor stroma cell interactions. J Exp Med. 2001;194(11):1549-59.
171. Brunda MJ, Luistro L, Warrier RR, Wright RB, Hubbard BR, Murphy M, et al. Antitumor and antimetastatic activity of interleukin 12 against murine tumors. J Exp Med. 1993;178(4):1223-30.
172. Montfort A, Filleron T, Virazels M, Dufau C, Milhès J, Pagès C, et al. Combining Nivolumab and Ipilimumab with Infliximab or Certolizumab in Patients with Advanced Melanoma: First Results of a Phase Ib Clinical Trial. Clin Cancer Res. 2021;27(4):1037-47.
173. Cho BC, Kim TM, Vicente D, Felip E, Lee DH, Lee KH, et al. Two-year follow-up of bintrafusp alfa, a bifunctional fusion protein targeting TGF-β and PD-L1, for second-line (2L) treatment of non-small cell lung cancer (NSCLC). Journal of Clinical Oncology. 2020;38(15_suppl):9558-.
174. Strauss J, Gatti-Mays ME, Cho BC, Hill A, Salas S, McClay E, et al. Bintrafusp alfa, a bifunctional fusion protein targeting TGF-β and PD-L1, in patients with human papillomavirus-associated malignancies. J Immunother Cancer. 2020;8(2).
175. Zheng L, Fisher G, Miller RE, Peschon J, Lynch DH, Lenardo MJ. Induction of apoptosis in mature T cells by tumour necrosis factor. Nature. 1995;377(6547):348-51.
176. Bertrand F, Montfort A, Marcheteau E, Imbert C, Gilhodes J, Filleron T, et al. TNFα blockade overcomes resistance to anti-PD-1 in experimental melanoma. Nat Commun. 2017;8(1):2256.
177. Shull MM, Ormsby I, Kier AB, Pawlowski S, Diebold RJ, Yin M, et al. Targeted disruption of the mouse transforming growth factor-beta 1 gene results in multifocal inflammatory disease. Nature. 1992;359(6397):693-9.
178. Gorelik L, Flavell RA. Immune-mediated eradication of tumors through the blockade of transforming growth factor-beta signaling in T cells. Nat Med. 2001;7(10):1118-22.

179. Park JH, Rivière I, Gonen M, Wang X, Sénéchal B, Curran KJ, et al. Long-Term Follow-up of CD19 CAR Therapy in Acute Lymphoblastic Leukemia. N Engl J Med. 2018;378(5):449-59.
180. Maude SL, Laetsch TW, Buechner J, Rives S, Boyer M, Bittencourt H, et al. Tisagenlecleucel in Children and Young Adults with B-Cell Lymphoblastic Leukemia. N Engl J Med. 2018;378(5):439-48.
181. Besser MJ, Shapira-Frommer R, Treves AJ, Zippel D, Itzhaki O, Hershkovitz L, et al. Clinical responses in a phase II study using adoptive transfer of short-term cultured tumor infiltration lymphocytes in metastatic melanoma patients. Clin Cancer Res. 2010;16(9):2646-55.
182. Rosenberg SA, Yang JC, Sherry RM, Kammula US, Hughes MS, Phan GQ, et al. Durable complete responses in heavily pretreated patients with metastatic melanoma using T-cell transfer immunotherapy. Clin Cancer Res. 2011;17(13):4550-7.
183. Zhang P, Zhang G, Wan X. Challenges and new technologies in adoptive cell therapy. Journal of Hematology & Oncology. 2023;16(1):97.
184. Coulie PG, Van den Eynde BJ, van der Bruggen P, Boon T. Tumour antigens recognized by T lymphocytes: at the core of cancer immunotherapy. Nat Rev Cancer. 2014;14(2):135-46.
185. Melero I, Gaudernack G, Gerritsen W, Huber C, Parmiani G, Scholl S, et al. Therapeutic vaccines for cancer: an overview of clinical trials. Nat Rev Clin Oncol. 2014;11(9):509-24.
186. Blass E, Ott PA. Advances in the development of personalized neoantigen-based therapeutic cancer vaccines. Nat Rev Clin Oncol. 2021;18(4):215-29.
187. The problem with neoantigen prediction. Nature Biotechnology. 2017;35(2):97-.
188. Liu J, Fu M, Wang M, Wan D, Wei Y, Wei X. Cancer vaccines as promising immuno-therapeutics: platforms and current progress. Journal of Hematology & Oncology. 2022;15(1):28.
189. Ishida Y, Agata Y, Shibahara K, Honjo T. Induced expression of PD-1, a novel member of the immunoglobulin gene superfamily, upon programmed cell death. Embo j. 1992;11(11):3887-95.
190. Walunas TL, Bakker CY, Bluestone JA. CTLA-4 ligation blocks CD28-dependent T cell activation. J Exp Med. 1996;183(6):2541-50.
191. NICE. Atezolizumab [Specialist drug]. BNF. [Internet]. Available from: https://bnf.nice.org.uk/drugs/atezolizumab-specialist-drug/.
192. Tawbi HA, Schadendorf D, Lipson EJ, Ascierto PA, Matamala L, Castillo Gutiérrez E, et al. Relatlimab and Nivolumab versus Nivolumab in Untreated Advanced Melanoma. N Engl J Med. 2022;386(1):24-34.
193. Marin-Acevedo JA, Kimbrough EO, Lou Y. Next generation of immune checkpoint inhibitors and beyond. Journal of Hematology & Oncology. 2021;14(1):45.
194. NICE. Pembrolizumab plus chemotherapy for untreated, triple-negative, locally recurrent unresectable or metastatic breast cancer. Technology appraisal guidance [TA801]. 2022. Available from: https://www.nice.org.uk/guidance/ta801. (07/10/23).
195. NICE. Pembrolizumab plus chemotherapy with or without bevacizumab for persistent, recurrent or metastatic cervical cancer. Technology appraisal guidance [TA885]. 2023. Available from: https://www.nice.org.uk/guidance/ta885.07/10/23.

196. NICE. Nivolumab with ipilimumab and chemotherapy for untreated metastatic non-small-cell lung cancer. Technology appraisal guidance [TA724]. 2021. Available from: https://www.nice.org.uk/guidance/ta724. (07/10/23).
197. NICE. Nivolumab–relatlimab for untreated unresectable or metastatic melanoma in people 12 years and over. Technology appraisal guidance [TA950]. Available from: https://www.nice.org.uk/guidance/ta950.
198. Rudin CM, Liu SV, Soo RA, Lu S, Hong MH, Lee JS, et al. SKYSCRAPER-02: Tiragolumab in Combination With Atezolizumab Plus Chemotherapy in Untreated Extensive-Stage Small-Cell Lung Cancer. J Clin Oncol. 2024;42(3):324-35.
199. Zeidan AM, Giagounidis A, Sekeres MA, Xiao Z, Sanz GF, Hoef MV, et al. STIMULUS-MDS2 design and rationale: a phase III trial with the anti-TIM-3 sabatolimab (MBG453) + azacitidine in higher risk MDS and CMML-2. Future Oncol. 2023;19(9):631-42.
200. Patel SP, Alonso-Gordoa T, Banerjee S, Wang D, Naidoo J, Standifer NE, et al. Phase 1/2 study of monalizumab plus durvalumab in patients with advanced solid tumors. J Immunother Cancer. 2024;12(2).
201. Hansen AR, Stanton TS, Hong MH, Cohen EEW, Mehanna HM, Chisamore MJ, et al. INDUCE-3: A randomized, double-blind study of GSK3359609 (GSK609), an inducible T-cell co-stimulatory (ICOS) agonist antibody, plus pembrolizumab (PE) versus placebo (PL) plus PE for first-line treatment of PD-L1-positive recurrent/metastatic head and neck squamous cell carcinoma (R/M HNSCC). Journal of Clinical Oncology. 2020;38(15_suppl):TPS6591-TPS.
202. Schilder RJ, Powderly JD, Park H, Bilen MA, McKean M, May R, et al. Phase Ia dose-escalation study of the anti-BTLA antibody icatolimab as a monotherapy in patients with advanced solid tumor. Journal of Clinical Oncology. 2022;40(16_suppl):2643-.
203. Ming Z. Tumor mutation burden for predicting immune checkpoint blockade response: the more, the better. Journal for ImmunoTherapy of Cancer. 2022;10(1):e003087.
204. Niknafs N, Balan A, Cherry C, Hummelink K, Monkhorst K, Shao XM, et al. Persistent mutation burden drives sustained anti-tumor immune responses. Nature Medicine. 2023;29(2):440-9.
205. Snyder A, Makarov V, Merghoub T, Yuan J, Zaretsky JM, Desrichard A, et al. Genetic basis for clinical response to CTLA-4 blockade in melanoma. N Engl J Med. 2014;371(23):2189-99.
206. Goodman AM, Kato S, Bazhenova L, Patel SP, Frampton GM, Miller V, et al. Tumor Mutational Burden as an Independent Predictor of Response to Immunotherapy in Diverse Cancers. Mol Cancer Ther. 2017;16(11):2598-608.
207. Cristescu R, Mogg R, Ayers M, Albright A, Murphy E, Yearley J, et al. Pan-tumor genomic biomarkers for PD-1 checkpoint blockade-based immunotherapy. Science. 2018;362(6411).
208. McGranahan N, Swanton C. Biological and therapeutic impact of intratumor heterogeneity in cancer evolution. Cancer Cell. 2015;27(1):15-26.
209. Cornel AM, Mimpen IL, Nierkens S. MHC Class I Downregulation in Cancer: Underlying Mechanisms and Potential Targets for Cancer Immunotherapy. Cancers (Basel). 2020;12(7).

210. Benitez R, Godelaine D, Lopez-Nevot MA, Brasseur F, Jiménez P, Marchand M, et al. Mutations of the beta2-microglobulin gene result in a lack of HLA class I molecules on melanoma cells of two patients immunized with MAGE peptides. Tissue Antigens. 1998;52(6):520-9.
211. Watson NF, Ramage JM, Madjd Z, Spendlove I, Ellis IO, Scholefield JH, et al. Immunosurveillance is active in colorectal cancer as downregulation but not complete loss of MHC class I expression correlates with a poor prognosis. Int J Cancer. 2006;118(1):6-10.
212. Turcotte S, Katz SC, Shia J, Jarnagin WR, Kingham TP, Allen PJ, et al. Tumor MHC class I expression improves the prognostic value of T-cell density in resected colorectal liver metastases. Cancer Immunol Res. 2014;2(6):530-7.
213. Simpson JA, Al-Attar A, Watson NF, Scholefield JH, Ilyas M, Durrant LG. Intratumoral T cell infiltration, MHC class I and STAT1 as biomarkers of good prognosis in colorectal cancer. Gut. 2010;59(7):926-33.
214. Wang MM, Coupland SE, Aittokallio T, Figueiredo CR. Resistance to immune checkpoint therapies by tumour-induced T-cell desertification and exclusion: key mechanisms, prognostication and new therapeutic opportunities. British Journal of Cancer. 2023.
215. Yin Z, Li C, Wang J, Xue L. Myeloid-derived suppressor cells: Roles in the tumor microenvironment and tumor radiotherapy. Int J Cancer. 2019;144(5):933-46.
216. Tanaka A, Sakaguchi S. Targeting Treg cells in cancer immunotherapy. Eur J Immunol. 2019;49(8):1140-6.
217. Reynolds LM, Ding J, Taylor JR, Lohman K, Soranzo N, de la Fuente A, et al. Transcriptomic profiles of aging in purified human immune cells. BMC Genomics. 2015;16(1):333.
218. Yousefzadeh MJ, Zhao J, Bukata C, Wade EA, McGowan SJ, Angelini LA, et al. Tissue specificity of senescent cell accumulation during physiologic and accelerated aging of mice. Aging Cell. 2020;19(3):e13094.
219. Sivan A, Corrales L, Hubert N, Williams JB, Aquino-Michaels K, Earley ZM, et al. Commensal Bifidobacterium promotes antitumor immunity and facilitates anti–PD-L1 efficacy. Science. 2015;350(6264):1084-9.
220. Li X, Zhang S, Guo G, Han J, Yu J. Gut microbiome in modulating immune checkpoint inhibitors. eBioMedicine. 2022;82.
221. Hodi FS, Chiarion-Sileni V, Gonzalez R, Grob JJ, Rutkowski P, Cowey CL, et al. Nivolumab plus ipilimumab or nivolumab alone versus ipilimumab alone in advanced melanoma (CheckMate 067): 4-year outcomes of a multicentre, randomised, phase 3 trial. Lancet Oncol. 2018;19(11):1480-92.
222. Galluzzi L, Vitale I, Warren S, Adjemian S, Agostinis P, Martinez AB, et al. Consensus guidelines for the definition, detection and interpretation of immunogenic cell death. J Immunother Cancer. 2020;8(1).
223. Gravett AM, Trautwein N, Stevanović S, Dalgleish AG, Copier J. Gemcitabine alters the proteasome composition and immunopeptidome of tumour cells. Oncoimmunology. 2018;7(6):e1438107.
224. Zhou J, Wang G, Chen Y, Wang H, Hua Y, Cai Z. Immunogenic cell death in cancer therapy: Present and emerging inducers. J Cell Mol Med. 2019;23(8):4854-65.

225. Kho VM, Mekers VE, Span PN, Bussink J, Adema GJ. Radiotherapy and cGAS/STING signaling: Impact on MDSCs in the tumor microenvironment. Cell Immunol. 2021;362:104298.
226. Zhang Md J, Zhang Md L, Yang Md Y, Liu Md Q, Ma Md H, Huang Md A, et al. Polymorphonuclear-MDSCs Facilitate Tumor Regrowth After Radiation by Suppressing CD8(+) T Cells. Int J Radiat Oncol Biol Phys. 2021;109(5):1533-46.
227. Basu A, Hoerning A, Datta D, Edelbauer M, Stack MP, Calzadilla K, et al. Cutting edge: Vascular endothelial growth factor-mediated signaling in human CD45RO+ CD4+ T cells promotes Akt and ERK activation and costimulates IFN-gamma production. J Immunol. 2010;184(2):545-9.
228. Gabrilovich DI, Chen HL, Girgis KR, Cunningham HT, Meny GM, Nadaf S, et al. Production of vascular endothelial growth factor by human tumors inhibits the functional maturation of dendritic cells. Nat Med. 1996;2(10):1096-103.
229. Paz-Ares L, Kim TM, Vicente D, Felip E, Lee DH, Lee KH, et al. Bintrafusp Alfa, a Bifunctional Fusion Protein Targeting TGF-β and PD-L1, in Second-Line Treatment of Patients With NSCLC: Results From an Expansion Cohort of a Phase 1 Trial. J Thorac Oncol. 2020;15(7):1210-22.
230. Liu B, Kong L, Han K, Hong H, Marcus WD, Chen X, et al. A Novel Fusion of ALT-803 (Interleukin (IL)-15 Superagonist) with an Antibody Demonstrates Antigen-specific Antitumor Responses. J Biol Chem. 2016;291(46):23869-81.
231. Cherkassky L, Morello A, Villena-Vargas J, Feng Y, Dimitrov DS, Jones DR, et al. Human CAR T cells with cell-intrinsic PD-1 checkpoint blockade resist tumor-mediated inhibition. J Clin Invest. 2016;126(8):3130-44.
232. Postow MA, Chesney J, Pavlick AC, Robert C, Grossmann K, McDermott D, et al. Nivolumab and Ipilimumab versus Ipilimumab in Untreated Melanoma. New England Journal of Medicine. 2015;372(21):2006-17.
233. Hand TW, Morre M, Kaech SM. Expression of IL-7 receptor alpha is necessary but not sufficient for the formation of memory CD8 T cells during viral infection. Proc Natl Acad Sci U S A. 2007;104(28):11730-5.
234. Berard M, Brandt K, Paus SB, Tough DF. IL-15 Promotes the Survival of Naive and Memory Phenotype CD8 T Cells. The Journal of Immunology. 2003;170(10):5018.
235. Veiga-Fernandes H, Walter U, Bourgeois C, McLean A, Rocha B. Response of naïve and memory CD8+ T cells to antigen stimulation in vivo. Nature Immunology. 2000;1(1):47-53.
236. Sallusto F, Lenig D, Förster R, Lipp M, Lanzavecchia A. Two subsets of memory T lymphocytes with distinct homing potentials and effector functions. Nature. 1999;401(6754):708-12.
237. Jiang X, Clark RA, Liu L, Wagers AJ, Fuhlbrigge RC, Kupper TS. Skin infection generates non-migratory memory CD8+ TRM cells providing global skin immunity. Nature. 2012;483(7388):227-31.
238. Shin H, Wherry EJ. CD8 T cell dysfunction during chronic viral infection. Curr Opin Immunol. 2007;19(4):408-15.
239. Spitzer MH, Carmi Y, Reticker-Flynn NE, Kwek SS, Madhireddy D, Martins MM, et al. Systemic Immunity Is Required for Effective Cancer Immunotherapy. Cell. 2017;168(3):487-502.e15.

240. Huang Q, Wu X, Wang Z, Chen X, Wang L, Lu Y, et al. The primordial differentiation of tumor-specific memory CD8(+) T cells as bona fide responders to PD-1/PD-L1 blockade in draining lymph nodes. Cell. 2022;185(22):4049-66.e25.
241. Djenidi F, Adam J, Goubar A, Durgeau A, Meurice G, de Montpréville V, et al. CD8+CD103+ Tumor–Infiltrating Lymphocytes Are Tumor-Specific Tissue-Resident Memory T Cells and a Prognostic Factor for Survival in Lung Cancer Patients. The Journal of Immunology. 2015;194(7):3475.
242. Wang Z-Q, Milne K, Derocher H, Webb JR, Nelson BH, Watson PH. CD103 and Intratumoral Immune Response in Breast Cancer. Clinical Cancer Research. 2016;22(24):6290-7.
243. Workel HH, Komdeur FL, Wouters MCA, Plat A, Klip HG, Eggink FA, et al. CD103 defines intraepithelial CD8+ PD1+ tumour-infiltrating lymphocytes of prognostic significance in endometrial adenocarcinoma. European Journal of Cancer. 2016;60:1-11.
244. Clarke J, Panwar B, Madrigal A, Singh D, Gujar R, Wood O, et al. Single-cell transcriptomic analysis of tissue-resident memory T cells in human lung cancer. J Exp Med. 2019;216(9):2128-49.
245. Beura LK, Wijeyesinghe S, Thompson EA, Macchietto MG, Rosato PC, Pierson MJ, et al. T Cells in Nonlymphoid Tissues Give Rise to Lymph-Node-Resident Memory T Cells. Immunity. 2018;48(2):327-38.e5.
246. CRUK. Bowel Cancer Statistics. 2022. [Internet]. Available from: https://www.cancerresearchuk.org/health-professional/cancer-statistics/statistics-by-cancer-type/bowel-cancer#heading-Five. (20/09/23).
247. National Cancer Registration and Analysis Service. Chemotherapy, Radiotherapy and Surgical Tumour Resections in England. [Internet]. Available from: https://www.cancerdata.nhs.uk/treatments. (19/09/23).
248. Fearon ER, Vogelstein B. A genetic model for colorectal tumorigenesis. Cell. 1990;61(5):759-67.
249. Guinney J, Dienstmann R, Wang X, de Reyniès A, Schlicker A, Soneson C, et al. The consensus molecular subtypes of colorectal cancer. Nat Med. 2015;21(11):1350-6.
250. Le DT, Uram JN, Wang H, Bartlett BR, Kemberling H, Eyring AD, et al. PD-1 Blockade in Tumors with Mismatch-Repair Deficiency. N Engl J Med. 2015;372(26):2509-20.
251. Verschoor YL, van den Berg J, Beets G, Sikorska K, Aalbers A, van Lent A, et al. Neoadjuvant nivolumab, ipilimumab, and celecoxib in MMR-proficient and MMR-deficient colon cancers: Final clinical analysis of the NICHE study. Journal of Clinical Oncology. 2022;40(16_suppl):3511-.
252. Chalabi M, Fanchi LF, Dijkstra KK, Van den Berg JG, Aalbers AG, Sikorska K, et al. Neoadjuvant immunotherapy leads to pathological responses in MMR-proficient and MMR-deficient early-stage colon cancers. Nat Med. 2020;26(4):566-76.
253. CRUK. TNM Staging. [Internet]. Available from: https://www.cancerresearchuk.org/about-cancer/bowel-cancer/stages-types-and-grades/TNM-staging. (19/09/23).
254. Pagès F, Mlecnik B, Marliot F, Bindea G, Ou FS, Bifulco C, et al. International validation of the consensus Immunoscore for the classification of colon cancer: a prognostic and accuracy study. Lancet. 2018;391(10135):2128-39.

255. Torre LA, Bray F, Siegel RL, Ferlay J, Lortet-Tieulent J, Jemal A. Global cancer statistics, 2012. CA Cancer J Clin. 2015;65(2):87-108.
256. McPhail S, Johnson S, Greenberg D, Peake M, Rous B. Stage at diagnosis and early mortality from cancer in England. British Journal of Cancer. 2015;112(1):S108-S15.
257. van der Geest LG, Lam-Boer J, Koopman M, Verhoef C, Elferink MA, de Wilt JH. Nationwide trends in incidence, treatment and survival of colorectal cancer patients with synchronous metastases. Clin Exp Metastasis. 2015;32(5):457-65.
258. Riihimäki M, Hemminki A, Sundquist J, Hemminki K. Patterns of metastasis in colon and rectal cancer. Sci Rep. 2016;6:29765.
259. Manfredi S, Lepage C, Hatem C, Coatmeur O, Faivre J, Bouvier A-M. Epidemiology and Management of Liver Metastases From Colorectal Cancer. Annals of Surgery. 2006;244(2).
260. Mettu NB, Ou FS, Zemla TJ, Halfdanarson TR, Lenz HJ, Breakstone RA, et al. Assessment of Capecitabine and Bevacizumab With or Without Atezolizumab for the Treatment of Refractory Metastatic Colorectal Cancer: A Randomized Clinical Trial. JAMA Netw Open. 2022;5(2):e2149040.
261. Fukuoka S, Hara H, Takahashi N, Kojima T, Kawazoe A, Asayama M, et al. Regorafenib Plus Nivolumab in Patients With Advanced Gastric or Colorectal Cancer: An Open-Label, Dose-Escalation, and Dose-Expansion Phase Ib Trial (REGONIVO, EPOC1603). J Clin Oncol. 2020;38(18):2053-61.
262. Pires da Silva I, Lo S, Quek C, Gonzalez M, Carlino MS, Long GV, et al. Site-specific response patterns, pseudoprogression, and acquired resistance in patients with melanoma treated with ipilimumab combined with anti-PD-1 therapy. Cancer. 2020;126(1):86-97.
263. Tumeh PC, Hellmann MD, Hamid O, Tsai KK, Loo KL, Gubens MA, et al. Liver Metastasis and Treatment Outcome with Anti-PD-1 Monoclonal Antibody in Patients with Melanoma and NSCLC. Cancer Immunol Res. 2017;5(5):417-24.
264. Schmid S, Diem S, Li Q, Krapf M, Flatz L, Leschka S, et al. Organ-specific response to nivolumab in patients with non-small cell lung cancer (NSCLC). Cancer Immunol Immunother. 2018;67(12):1825-32.
265. Yu J, Green MD, Li S, Sun Y, Journey SN, Choi JE, et al. Liver metastasis restrains immunotherapy efficacy via macrophage-mediated T cell elimination. Nature Medicine. 2021;27(1):152-64.
266. Lee JC, Mehdizadeh S, Smith J, Young A, Mufazalov IA, Mowery CT, et al. Regulatory T cell control of systemic immunity and immunotherapy response in liver metastasis. Sci Immunol. 2020;5(52).
267. Maughan TS, Adams RA, Smith CG, Meade AM, Seymour MT, Wilson RH, et al. Addition of cetuximab to oxaliplatin-based first-line combination chemotherapy for treatment of advanced colorectal cancer: results of the randomised phase 3 MRC COIN trial. Lancet. 2011;377(9783):2103-14.
268. Pembrolizumab for untreated metastatic colorectal cancer with high microsatellite instability or mismatch repair deficiency. Technology appraisal guidance [TA709]. 2021. Available from: https://www.nice.org.uk/guidance/ta709/chapter/1-Recommendations. (01/10/2023).

269. Chen EX, Jonker DJ, Loree JM, Kennecke HF, Berry SR, Couture F, et al. Effect of Combined Immune Checkpoint Inhibition vs Best Supportive Care Alone in Patients With Advanced Colorectal Cancer: The Canadian Cancer Trials Group CO.26 Study. JAMA Oncol. 2020;6(6):831-8.
270. Ree AH, Hamre H, Kersten C, Hofsli E, Guren MG, Sorbye H, et al. Repeat sequential oxaliplatin-based chemotherapy (FLOX) and nivolumab versus FLOX alone as first-line treatment of microsatellite-stable (MSS) metastatic colorectal cancer (mCRC): Initial results from the randomized METIMMOX study. Journal of Clinical Oncology. 2021;39(15_suppl):3556-.
271. van den Eynde M, Huyghe N, Sinapi I, De Cuyper A, Verstraelen E, Goffette P, et al. 635P Avelumab (AVE) combined with cetuximab (CET) and irinotecan (IRI) for the treatment of refractory microsatellite stable (MSS) metastatic colorectal cancer (mCRC): The AVETUXIRI phase II study. Annals of Oncology. 2023;34:S450.
272. Mettu NB, Ou F-S, Zemla TJ, Halfdanarson TR, Lenz H-J, Breakstone RA, et al. Assessment of Capecitabine and Bevacizumab With or Without Atezolizumab for the Treatment of Refractory Metastatic Colorectal Cancer: A Randomized Clinical Trial. JAMA Network Open. 2022;5(2):e2149040-e.
273. Antoniotti C, Rossini D, Pietrantonio F, Salvatore L, Marmorino F, Ambrosini M, et al. FOLFOXIRI plus bevacizumab and atezolizumab as upfront treatment of unresectable metastatic colorectal cancer (mCRC): Updated and overall survival results of the phase II randomized AtezoTRIBE study. Journal of Clinical Oncology. 2023;41(16_suppl):3500-.
274. Lenz HJ, Parikh A, Spigel DR, Cohn AL, Yoshino T, Kochenderfer M, et al. Modified FOLFOX6 plus bevacizumab with and without nivolumab for first-line treatment of metastatic colorectal cancer: phase 2 results from the CheckMate 9X8 randomized clinical trial. J Immunother Cancer. 2024;12(3).
275. Cousin S, Metges JP, Bellera CA, Guégan JP, Adenis A, Gomez-Roca CA, et al. REGOMUNE: A phase II study of regorafenib plus avelumab in solid tumors—Results of the oesophageal or gastric carcinoma (OGC) cohort. Journal of Clinical Oncology. 2022;40(16_suppl):4060-.
276. Gomez-Roca C, Yanez E, Im S-A, Castanon Alvarez E, Senellart H, Doherty M, et al. LEAP-005: A phase II multicohort study of lenvatinib plus pembrolizumab in patients with previously treated selected solid tumors—Results from the colorectal cancer cohort. Journal of Clinical Oncology. 2021;39(3_suppl):94-.
277. Lee MS, Loehrer PJ, Imanirad I, Cohen S, Ciombor KK, Moore DT, et al. Phase II study of ipilimumab, nivolumab, and panitumumab in patients with KRAS/NRAS/BRAF wild-type (WT) microsatellite stable (MSS) metastatic colorectal cancer (mCRC). Journal of Clinical Oncology. 2021;39(3_suppl):7-.
278. Kim T, Taieb J, Passhak M, Kim T, Kim S, Geva R, et al. P-81 Phase 3 study of MK4280A (coformulated favezelimab and pembrolizumab) versus standard of care in previously treated PD-L1–positive metastatic colorectal cancer (mCRC). Annals of Oncology. 2022;33:S277.
279. Houston SA, Cerovic V, Thomson C, Brewer J, Mowat AM, Milling S. The lymph nodes draining the small intestine and colon are anatomically separate and immunologically distinct. Mucosal Immunology. 2016;9(2):468-78.

280. Zheng M, Yu J, Tian Z. Characterization of the liver-draining lymph nodes in mice and their role in mounting regional immunity to HBV. Cellular & Molecular Immunology. 2013;10(2):143-50.
281. FlowJo™ Software [software application] Version 10. Becton, Dickinson and Company; 2021.
282. GraphPad Prism version 9.0.0 for Mac, GraphPad Software, San Diego, California USA, www.graphpad.com.
283. Gosselin RD. Guidelines on statistics for researchers using laboratory animals: the essentials. Lab Anim. 2019;53(1):28-42.
284. Wherry EJ, Barber DL, Kaech SM, Blattman JN, Ahmed R. Antigen-independent memory CD8 T cells do not develop during chronic viral infection. Proc Natl Acad Sci U S A. 2004;101(45):16004-9.
285. Gehring AJ, Ho ZZ, Tan AT, Aung MO, Lee KH, Tan KC, et al. Profile of tumor antigen-specific CD8 T cells in patients with hepatitis B virus-related hepatocellular carcinoma. Gastroenterology. 2009;137(2):682-90.
286. Li Z, Tuong ZK, Dean I, Willis C, Gaspal F, Fiancette R, et al. In vivo labeling reveals continuous trafficking of TCF-1+ T cells between tumor and lymphoid tissue. J Exp Med. 2022;219(6).
287. Kallies A, Zehn D, Utzschneider DT. Precursor exhausted T cells: key to successful immunotherapy? Nature Reviews Immunology. 2020;20(2):128-36.
288. Jansen CS, Prokhnevska N, Master VA, Sanda MG, Carlisle JW, Bilen MA, et al. An intra-tumoral niche maintains and differentiates stem-like CD8 T cells. Nature. 2019;576(7787):465-70.
289. Tsui C, Kretschmer L, Rapelius S, Gabriel SS, Chisanga D, Knöpper K, et al. MYB orchestrates T cell exhaustion and response to checkpoint inhibition. Nature. 2022;609(7926):354-60.
290. Dähling S, Mansilla AM, Knöpper K, Grafen A, Utzschneider DT, Ugur M, et al. Type 1 conventional dendritic cells maintain and guide the differentiation of precursors of exhausted T cells in distinct cellular niches. Immunity. 2022;55(4):656-70.e8.
291. Hua Y, Vella G, Rambow F, Allen E, Antoranz Martinez A, Duhamel M, et al. Cancer immunotherapies transition endothelial cells into HEVs that generate TCF1(+) T lymphocyte niches through a feed-forward loop. Cancer Cell. 2022;40(12):1600-18.e10.
292. Dammeijer F, van Gulijk M, Mulder EE, Lukkes M, Klaase L, van den Bosch T, et al. The PD-1/PD-L1-Checkpoint Restrains T cell Immunity in Tumor-Draining Lymph Nodes. Cancer Cell. 2020;38(5):685-700.e8.
293. Connolly KA, Kuchroo M, Venkat A, Khatun A, Wang J, William I, et al. A reservoir of stem-like CD8(+) T cells in the tumor-draining lymph node preserves the ongoing antitumor immune response. Sci Immunol. 2021;6(64):eabg7836.
294. Mizuno H, Mal TK, Tong KI, Ando R, Furuta T, Ikura M, et al. Photo-induced peptide cleavage in the green-to-red conversion of a fluorescent protein. Mol Cell. 2003;12(4):1051-8.
295. Tomura M, Yoshida N, Tanaka J, Karasawa S, Miwa Y, Miyawaki A, et al. Monitoring cellular movement *in vivo* with photoconvertible fluorescence protein "Kaede" transgenic mice. Proceedings of the National Academy of Sciences. 2008;105(31):10871.

296. Tomura M, Honda T, Tanizaki H, Otsuka A, Egawa G, Tokura Y, et al. Activated regulatory T cells are the major T cell type emigrating from the skin during a cutaneous immune response in mice. J Clin Invest. 2010;120(3):883-93.
297. Tomura M, Hata A, Matsuoka S, Shand FHW, Nakanishi Y, Ikebuchi R, et al. Tracking and quantification of dendritic cell migration and antigen trafficking between the skin and lymph nodes. Scientific Reports. 2014;4(1):6030.
298. Marriott CL, Dutton EE, Tomura M, Withers DR. Retention of Ag-specific memory CD4(+) T cells in the draining lymph node indicates lymphoid tissue resident memory populations. European journal of immunology. 2017;47(5):860-71.
299. van Montfoort N, Borst L, Korrer MJ, Sluijter M, Marijt KA, Santegoets SJ, et al. NKG2A Blockade Potentiates CD8 T Cell Immunity Induced by Cancer Vaccines. Cell. 2018;175(7):1744-55.e15.
300. Beltra JC, Manne S, Abdel-Hakeem MS, Kurachi M, Giles JR, Chen Z, et al. Developmental Relationships of Four Exhausted CD8(+) T Cell Subsets Reveals Underlying Transcriptional and Epigenetic Landscape Control Mechanisms. Immunity. 2020;52(5):825-41.e8.
301. Singer M, Wang C, Cong L, Marjanovic ND, Kowalczyk MS, Zhang H, et al. A Distinct Gene Module for Dysfunction Uncoupled from Activation in Tumor-Infiltrating T Cells. Cell. 2016;166(6):1500-11.e9.
302. Dean I, Lee CYC, Tuong ZK, Li Z, Tibbitt CA, Willis C, et al. Rapid functional impairment of natural killer cells following tumor entry limits anti-tumor immunity. Nature Communications. 2024;15(1):683.
303. Giles JR, Globig AM, Kaech SM, Wherry EJ. CD8(+) T cells in the cancer-immunity cycle. Immunity. 2023;56(10):2231-53.
304. Li Y, Ge J, Zhao X, Xu M, Gou M, Xie B, et al. Cell autonomous expression of BCL6 is required to maintain lineage identity of mouse CCR6+ ILC3s. J Exp Med. 2023;220(4).
305. Snipstad S, Bremnes F, Dehli Haugum M, Sulheim E. Characterization of immune cell populations in syngeneic murine tumor models. Cancer Med. 2023;12(10):11589-601.
306. Meininger I, Carrasco A, Rao A, Soini T, Kokkinou E, Mjösberg J. Tissue-Specific Features of Innate Lymphoid Cells. Trends Immunol. 2020;41(10):902-17.
307. Devaud C, Westwood JA, John LB, Flynn JK, Paquet-Fifield S, Duong CP, et al. Tissues in different anatomical sites can sculpt and vary the tumor microenvironment to affect responses to therapy. Mol Ther. 2014;22(1):18-27.
308. Eruslanov EB, Singhal S, Albelda SM. Mouse versus Human Neutrophils in Cancer: A Major Knowledge Gap. Trends Cancer. 2017;3(2):149-60.
309. Zhong W, Myers JS, Wang F, Wang K, Lucas J, Rosfjord E, et al. Comparison of the molecular and cellular phenotypes of common mouse syngeneic models with human tumors. BMC Genomics. 2020;21(1):2.
310. Le CT, Murphy WJ. Moving forward to address key unanswered questions on targeting PD-1/PD-L1 in cancer: limitations in preclinical models and the need to incorporate human modifying factors. Journal for ImmunoTherapy of Cancer. 2019;7(1):291.
311. Golovko D, Kedrin D, Yilmaz Ö H, Roper J. Colorectal cancer models for novel drug discovery. Expert Opin Drug Discov. 2015;10(11):1217-29.

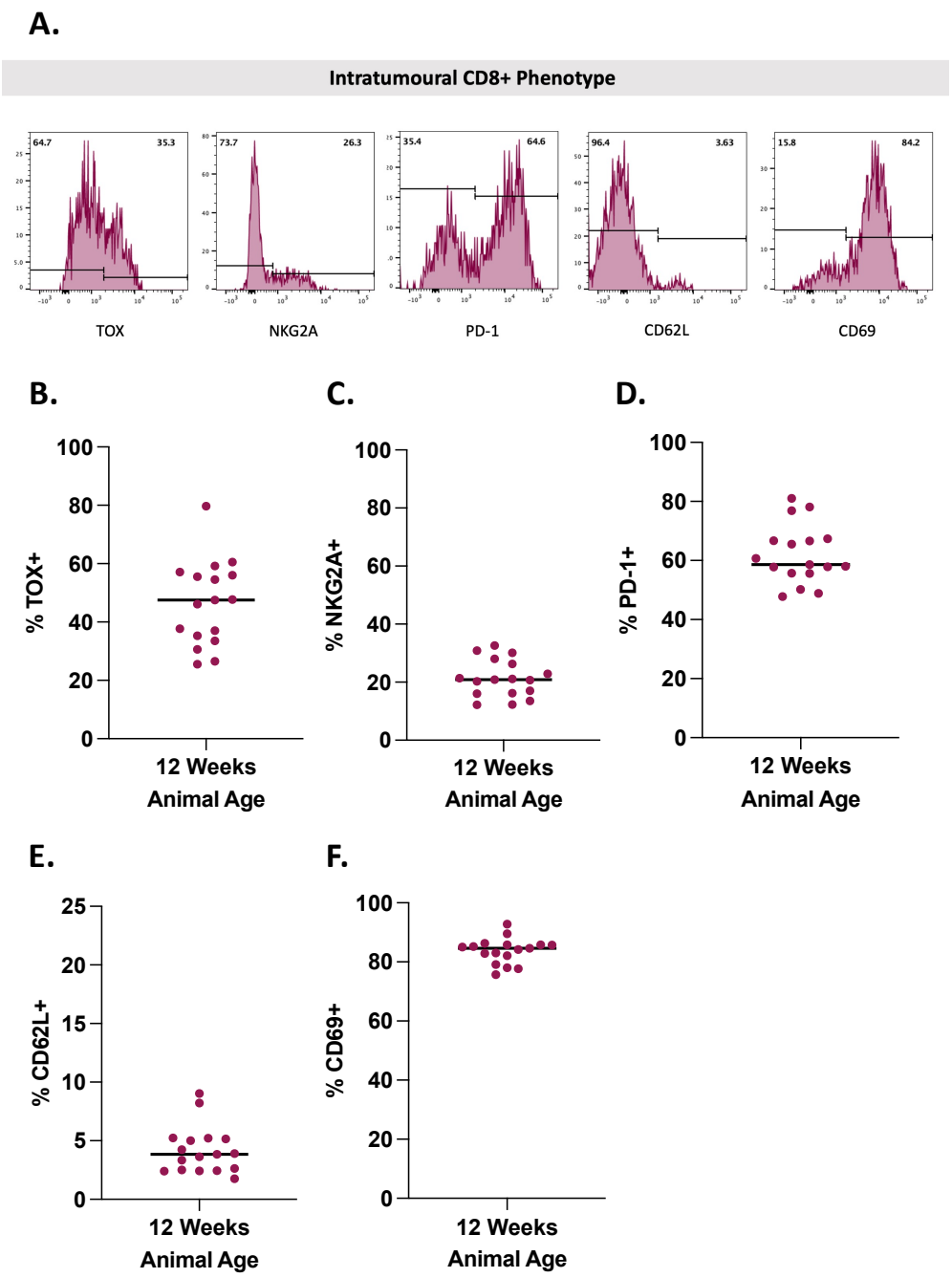
312. Hanahan D, Folkman J. Patterns and emerging mechanisms of the angiogenic switch during tumorigenesis. Cell. 1996;86(3):353-64.
313. Gee MS, Procopio WN, Makonnen S, Feldman MD, Yeilding NM, Lee WM. Tumor vessel development and maturation impose limits on the effectiveness of anti-vascular therapy. Am J Pathol. 2003;162(1):183-93.
314. Falk P. Differences in vascular pattern between the spontaneous and the transplanted C3H mouse mammary carcinoma. Eur J Cancer Clin Oncol. 1982;18(2):155-65.
315. Farsaci B, Donahue RN, Coplin MA, Grenga I, Lepone LM, Molinolo AA, et al. Immune consequences of decreasing tumor vasculature with antiangiogenic tyrosine kinase inhibitors in combination with therapeutic vaccines. Cancer Immunol Res. 2014;2(11):1090-102.
316. Bürtin F, Mullins CS, Linnebacher M. Mouse models of colorectal cancer: Past, present and future perspectives. World J Gastroenterol. 2020;26(13):1394-426.
317. Zhao X, Li L, Starr TK, Subramanian S. Tumor location impacts immune response in mouse models of colon cancer. Oncotarget. 2017;8(33):54775-87.
318. Zhang Y, Davis C, Ryan J, Janney C, Peña MM. Development and characterization of a reliable mouse model of colorectal cancer metastasis to the liver. Clin Exp Metastasis. 2013;30(7):903-18.
319. Goddard ET, Fischer J, Schedin P. A Portal Vein Injection Model to Study Liver Metastasis of Breast Cancer. J Vis Exp. 2016(118).
320. Soares KC, Foley K, Olino K, Leubner A, Mayo SC, Jain A, et al. A preclinical murine model of hepatic metastases. J Vis Exp. 2014(91):51677.
321. Ho WW, Gomes-Santos IL, Aoki S, Datta M, Kawaguchi K, Talele NP, et al. Dendritic cell paucity in mismatch repair-proficient colorectal cancer liver metastases limits immune checkpoint blockade efficacy. Proc Natl Acad Sci U S A. 2021;118(45).
322. Chen C, Neumann J, Kühn F, Lee SML, Drefs M, Andrassy J, et al. Establishment of an Endoscopy-Guided Minimally Invasive Orthotopic Mouse Model of Colorectal Cancer. Cancers (Basel). 2020;12(10).
323. Evans JP, Winiarski BK, Sutton PA, Ressel L, Duckworth CA, Pritchard DM, et al. Development of an orthotopic syngeneic murine model of colorectal cancer for use in translational research. Lab Anim. 2019;53(6):598-609.
324. Tauriello DVF, Palomo-Ponce S, Stork D, Berenguer-Llergo A, Badia-Ramentol J, Iglesias M, et al. TGFβ drives immune evasion in genetically reconstituted colon cancer metastasis. Nature. 2018;554(7693):538-43.
325. Perkin Elmer. IVIS Spectrum In Vivo Imaging System. [Web page]. Available from: https://www.perkinelmer.com/uk/product/ivis-instrument-spectrum-120v-andor-c-124262.
326. Lucas B, White AJ, Parnell SM, Henley PM, Jenkinson WE, Anderson G. Progressive Changes in CXCR4 Expression That Define Thymocyte Positive Selection Are Dispensable For Both Innate and Conventional αβT-cell Development. Sci Rep. 2017;7(1):5068.
327. Agudo J, Ruzo A, Park ES, Sweeney R, Kana V, Wu M, et al. GFP-specific CD8 T cells enable targeted cell depletion and visualization of T-cell interactions. Nat Biotechnol. 2015;33(12):1287-92.

328. Eggert T, Greten TF. Tumor regulation of the tissue environment in the liver. Pharmacol Ther. 2017;173:47-57.
329. Khan O, Giles JR, McDonald S, Manne S, Ngiow SF, Patel KP, et al. TOX transcriptionally and epigenetically programs CD8+ T cell exhaustion. Nature. 2019;571(7764):211-8.
330. Galon J, Bruni D. Approaches to treat immune hot, altered and cold tumours with combination immunotherapies. Nature Reviews Drug Discovery. 2019;18(3):197-218.
331. Jackstadt R, van Hooff SR, Leach JD, Cortes-Lavaud X, Lohuis JO, Ridgway RA, et al. Epithelial NOTCH Signaling Rewires the Tumor Microenvironment of Colorectal Cancer to Drive Poor-Prognosis Subtypes and Metastasis. Cancer Cell. 2019;36(3):319-36.e7.
332. O'Rourke KP, Loizou E, Livshits G, Schatoff EM, Baslan T, Manchado E, et al. Transplantation of engineered organoids enables rapid generation of metastatic mouse models of colorectal cancer. Nat Biotechnol. 2017;35(6):577-82.
333. Londoño MC, Rimola A, O'Grady J, Sanchez-Fueyo A. Immunosuppression minimization vs. complete drug withdrawal in liver transplantation. J Hepatol. 2013;59(4):872-9.
334. Gabrilovich DI, Nagaraj S. Myeloid-derived suppressor cells as regulators of the immune system. Nat Rev Immunol. 2009;9(3):162-74.
335. De Creus A, Abe M, Lau AH, Hackstein H, Raimondi G, Thomson AW. Low TLR4 expression by liver dendritic cells correlates with reduced capacity to activate allogeneic T cells in response to endotoxin. J Immunol. 2005;174(4):2037-45.
336. Knolle PA, Uhrig A, Hegenbarth S, Löser E, Schmitt E, Gerken G, et al. IL-10 down-regulates T cell activation by antigen-presenting liver sinusoidal endothelial cells through decreased antigen uptake via the mannose receptor and lowered surface expression of accessory molecules. Clin Exp Immunol. 1998;114(3):427-33.
337. Knolle P, Schlaak J, Uhrig A, Kempf P, Meyer zum Büschenfelde KH, Gerken G. Human Kupffer cells secrete IL-10 in response to lipopolysaccharide (LPS) challenge. J Hepatol. 1995;22(2):226-9.
338. Robinson MW, Harmon C, O'Farrelly C. Liver immunology and its role in inflammation and homeostasis. Cellular & Molecular Immunology. 2016;13(3):267-76.
339. Mühlbauer M, Fleck M, Schütz C, Weiss T, Froh M, Blank C, et al. PD-L1 is induced in hepatocytes by viral infection and by interferon-α and -γ and mediates T cell apoptosis. Journal of Hepatology. 2006;45(4):520-8.
340. Lau AH, Thomson AW. Dendritic cells and immune regulation in the liver. Gut. 2003;52(2):307-14.
341. Bamboat ZM, Stableford JA, Plitas G, Burt BM, Nguyen HM, Welles AP, et al. Human liver dendritic cells promote T cell hyporesponsiveness. J Immunol. 2009;182(4):1901-11.
342. Morelli AE, O'Connell PJ, Khanna A, Logar AJ, Lu L, Thomson AW. Preferential induction of Th1 responses by functionally mature hepatic (CD8alpha- and CD8alpha+) dendritic cells: association with conversion from liver transplant tolerance to acute rejection. Transplantation. 2000;69(12):2647-57.
343. Sebode M, Peiseler M, Franke B, Schwinge D, Schoknecht T, Wortmann F, et al. Reduced FOXP3(+) regulatory T cells in patients with primary sclerosing cholangitis are associated with IL2RA gene polymorphisms. J Hepatol. 2014;60(5):1010-6.

344. Gao Q, Qiu SJ, Fan J, Zhou J, Wang XY, Xiao YS, et al. Intratumoral balance of regulatory and cytotoxic T cells is associated with prognosis of hepatocellular carcinoma after resection. J Clin Oncol. 2007;25(18):2586-93.
345. Sun CM, Hall JA, Blank RB, Bouladoux N, Oukka M, Mora JR, et al. Small intestine lamina propria dendritic cells promote de novo generation of Foxp3 T reg cells via retinoic acid. J Exp Med. 2007;204(8):1775-85.
346. Diehl L, Schurich A, Grochtmann R, Hegenbarth S, Chen L, Knolle PA. Tolerogenic maturation of liver sinusoidal endothelial cells promotes B7-homolog 1-dependent CD8+ T cell tolerance. Hepatology. 2008;47(1):296-305.
347. Carambia A, Freund B, Schwinge D, Heine M, Laschtowitz A, Huber S, et al. TGF-β-dependent induction of $CD4^+CD25^+Foxp3^+$ Tregs by liver sinusoidal endothelial cells. J Hepatol. 2014;61(3):594-9.
348. Hudson WH, Gensheimer J, Hashimoto M, Wieland A, Valanparambil RM, Li P, et al. Proliferating Transitory T Cells with an Effector-like Transcriptional Signature Emerge from PD-1(+) Stem-like CD8(+) T Cells during Chronic Infection. Immunity. 2019;51(6):1043-58.e4.
349. Zander R, Schauder D, Xin G, Nguyen C, Wu X, Zajac A, et al. CD4(+) T Cell Help Is Required for the Formation of a Cytolytic CD8(+) T Cell Subset that Protects against Chronic Infection and Cancer. Immunity. 2019;51(6):1028-42.e4.
350. Magen A, Nie J, Ciucci T, Tamoutounour S, Zhao Y, Mehta M, et al. Single-Cell Profiling Defines Transcriptomic Signatures Specific to Tumor-Reactive versus Virus-Responsive CD4(+) T Cells. Cell Rep. 2019;29(10):3019-32.e6.

Appendix

Chapter 3

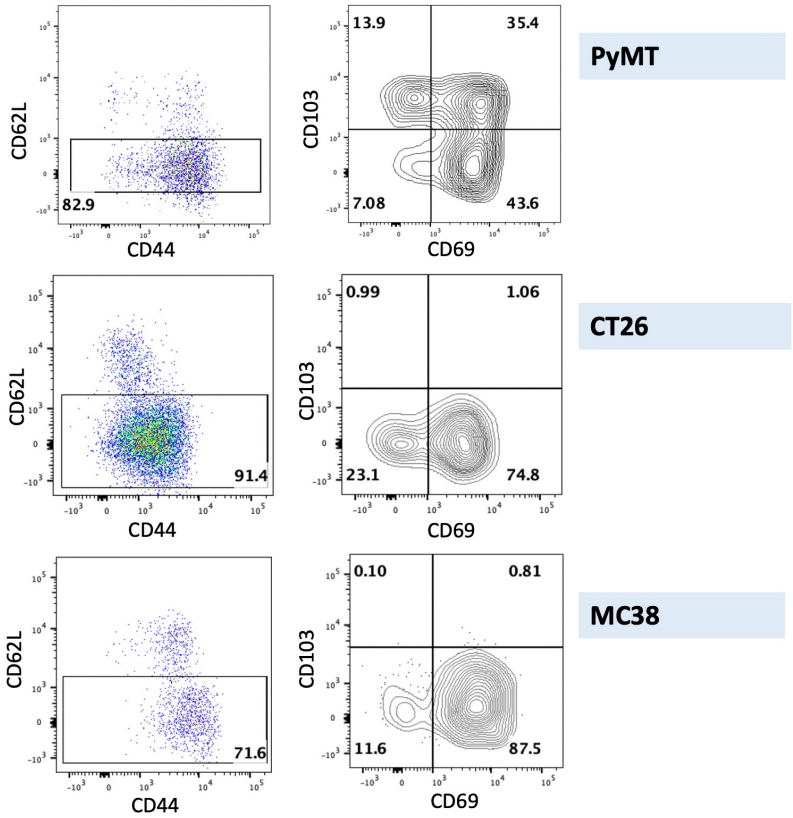

A.
Intratumoural CD8+ Phenotype
64.7
35.3
73.7
26.3
35.4
64.6
96.4
3.63
15.8
84.2
TOX
NKG2A
PD-1
CD62L
CD69
B.
% TOX+
12 Weeks
Animal Age
C.
% NKG2A+
12 Weeks
Animal Age
D.
% PD-1+
12 Weeks
Animal Age
E.
% CD62L+
12 Weeks
Animal Age
F.
% CD69+
12 Weeks
Animal Age

Appendix 3.1. Phenotype of the CD8 T cell population in spontaneous PyMT tumour model.

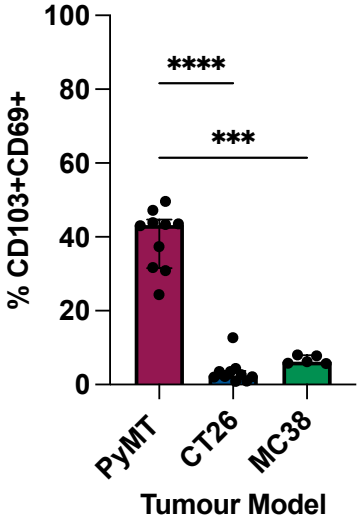
To generate the MMTV-PyMT model on a Kaede background, F1 mice resulting from crossing PyMT+ male mice with Kaede female mice were used, in which tumours typically appeared within 11-14 weeks. Tumours were collected when animals were 10-13 weeks old. Cells were isolated from subcutaneous tumours as per methods. All data shown are from two independent experiments. All graphs show the median value.

A. Histograms demonstrating the MFI of TOX, NKG2A, PD-1, CD62L, and CD69 in the total CD8+ population in a representative PyMT tumour sample collected when the animal spontaneously developed mammary tumours at around 12 weeks of age.
B. The percentage of TOX+ CD8 T cells in PyMT tumours.
C. The percentage of NKG2A+ CD8 T cells in PyMT tumours.
D. The percentage of PD-1+ CD8 T cells in PyMT tumours.
E. The percentage of CD62L+ CD8 T cells in PyMT tumours.
F. The percentage of CD69+ CD8 T cells in PyMT tumours.

A.


CD62L
CD44
82.9
CD103
CD69
13.9
35.4
7.08
43.6
PyMT
CD62L
CD44
91.4
CD103
CD69
0.99
1.06
23.1
74.8
CT26
CD62L
CD44
71.6
CD103
CD69
0.10
0.81
11.6
87.5
MC38

B.

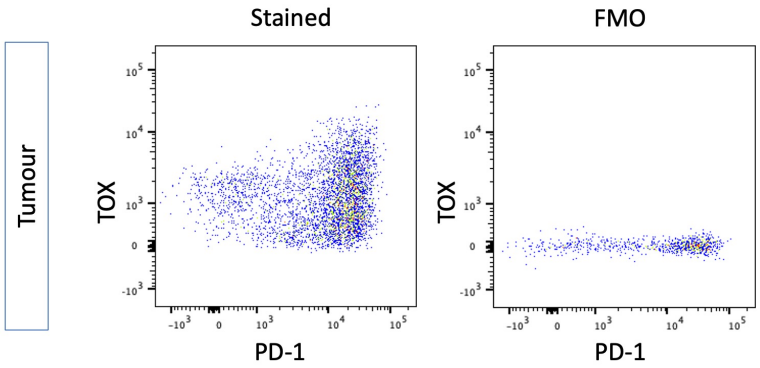

% CD103+CD69+
100
80
60
40
20
0
****
***
PyMT
CT26
MC38
Tumour Model

Appendix 3.2. The tissue resident memory CD8 population is absent in implanted CT26 and MC38-OVA tumours but present in primary PyMT tumours.

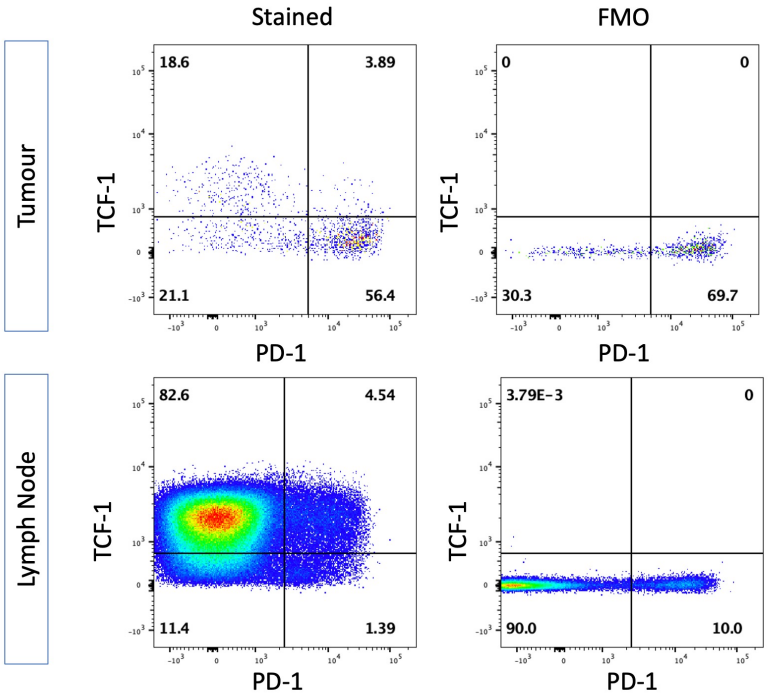
The graph shown in 'B' represents the collective data from three independent CT26, two MC38-OVA, and two PyMT experiments. The graph demonstrates median and IQR. Statistical significance was determined with a Kruskal-Wallis multiple comparison. ** = $p < 0.05$, ** = $p < 0.01$, *** = $p < 0.001$, **** = $p < 0.0001$*

A. Flow cytometry plots from three different tumour models, PyMT (top row), CT26 (middle row), MC38 (bottom row) pre-gated on live CD45+ CD11b- CD11c- B220- CD3+ CD8+ T cells. The left-hand plot shows how the CD8+ population was gated on CD62L- cells. The right-hand plot demonstrates the expression of CD103 and CD69, the top right-hand quadrant represents the Trm population.
B. The percentage of intratumoural CD8+ CD62L- cells that are a Trm phenotype (CD69+ CD103+) in three different tumour models.

A.


Stained
FMO
Tumour
TOX
PD-1
TOX
PD-1

B.

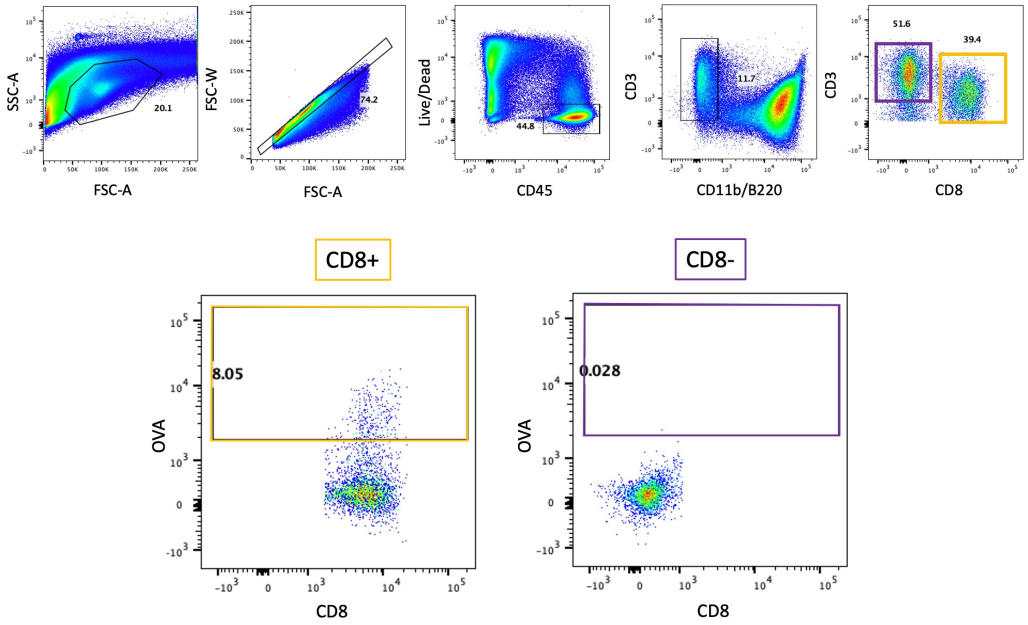

Stained
FMO
Tumour
18.6
3.89
21.1
56.4
TCF-1
PD-1
0
0
30.3
69.7
TCF-1
PD-1
Lymph Node
82.6
4.54
11.4
1.39
TCF-1
PD-1
3.79E-3
0
90.0
10.0
TCF-1
PD-1

Appendix 3.3. FMO and isotype controls for TCF-1, TOX intracellular stains.

C57BL/6 mice (6-9 weeks) were injected subcutaneously with 2.5 x10^5 MC38-OVA cells. Representative tumour and dLN samples are shown. Plots shown population pre-gated on live CD45+CD11b-CD11c-B220-CD3+CD8+ cells.

A. Flow cytometry plot demonstrating TOX expression alongside PD-1, within a stained tumour sample (left) and TOX FMO (right).
B. Flow cytometry plot demonstrating TCF-1 expression alongside PD-1, within a stained sample (left) and isotype control (right), in a tumour (top row) and dLN (bottom row).

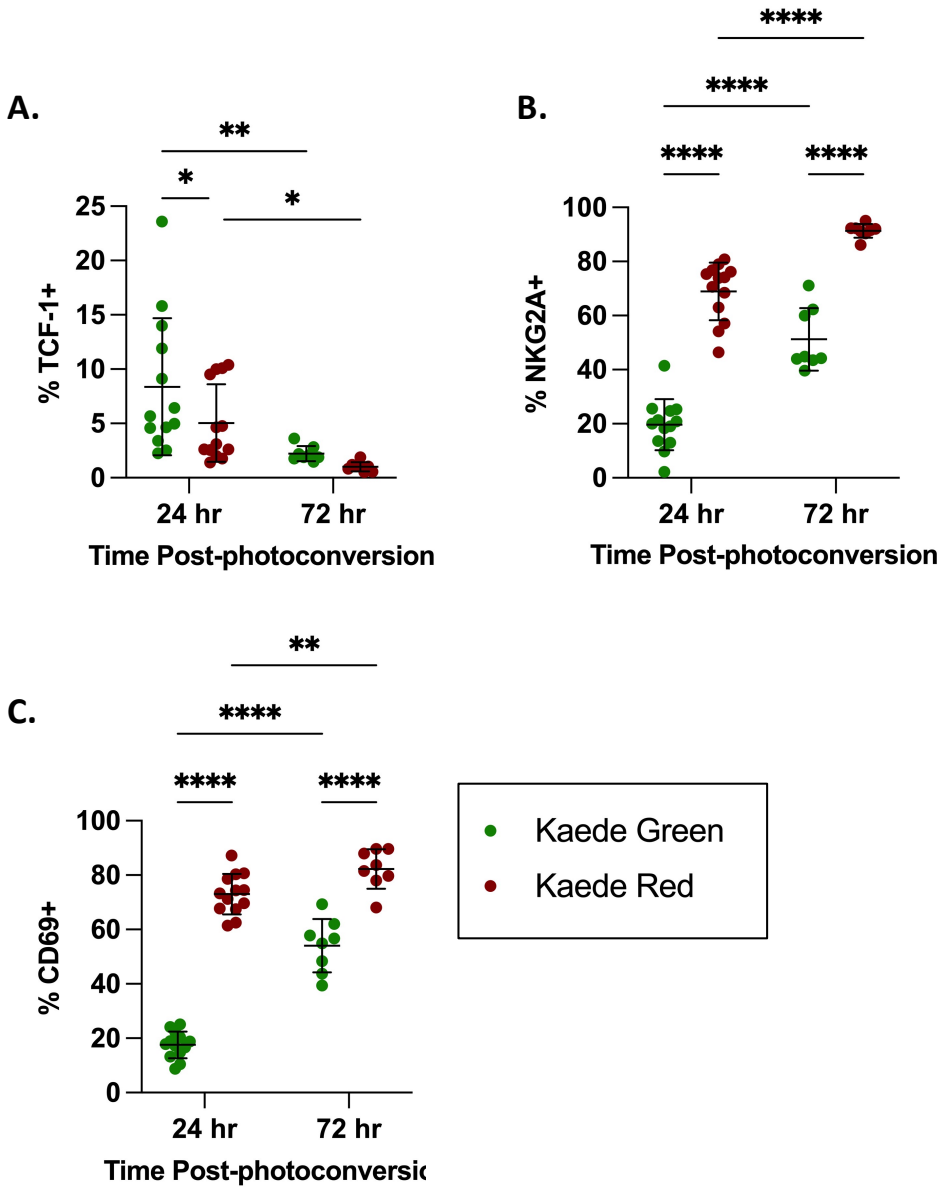
A.


SSC-A
FSC-A
20.1
FSC-W
FSC-A
74.2
Live/Dead
CD45
44.8
CD3
CD11b/B220
11.7
CD3
CD8
51.6
39.4
CD8+
CD8-
OVA
CD8
8.05
OVA
CD8
0.028

Appendix 3.4. Validation of OVA tetramer staining.

C57BL/6 mice (6-9 weeks) were injected with 2.5 x10^5 MC38-OVA cells subcutaneously. A representative tumour sample is shown.

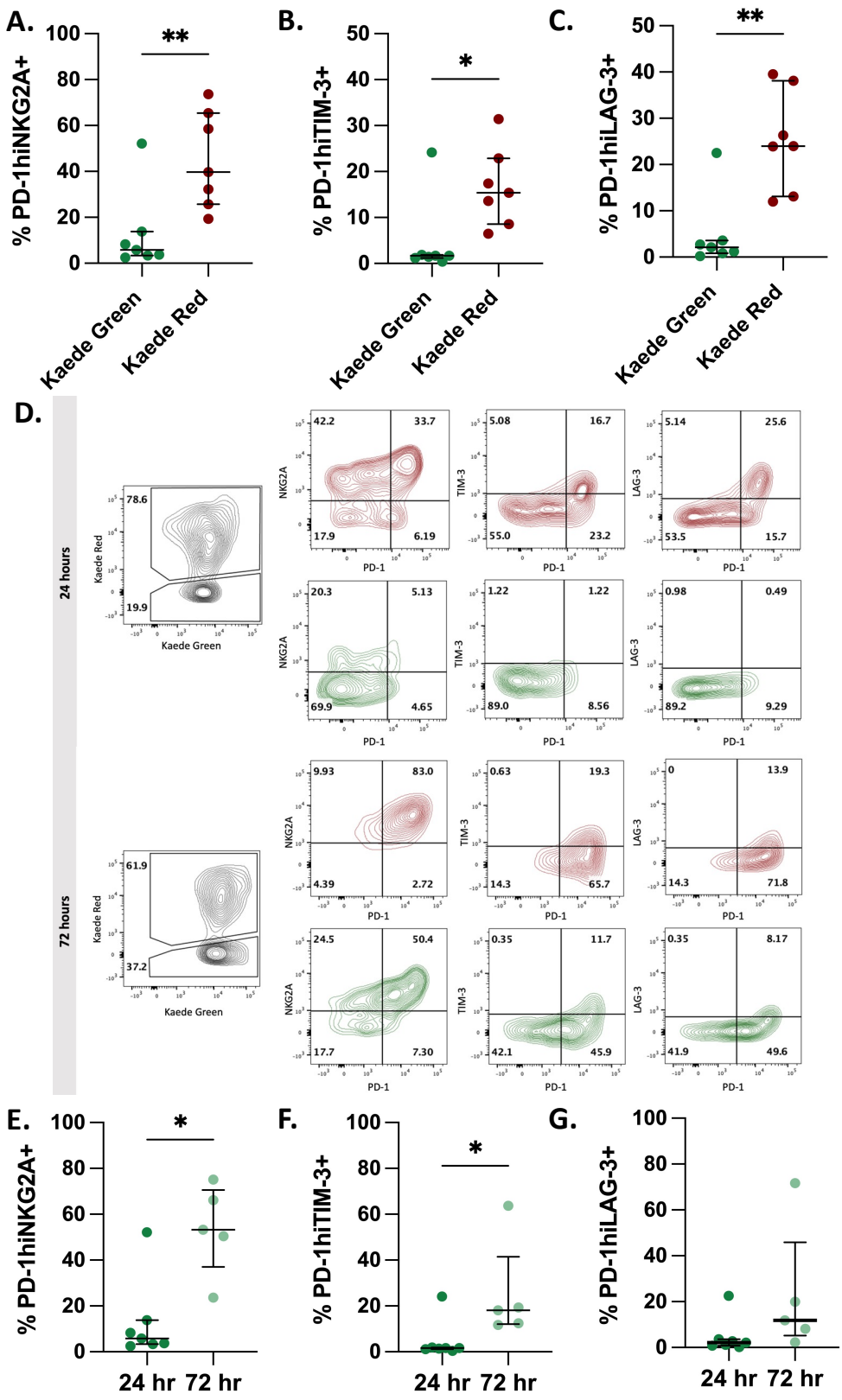
A. Flow cytometry plots demonstrating the gating and staining for OVA+ cells in CD8+ T cells and CD8- T cells (acting as control).


A.
**
*
*
25
20
15
10
5
0
% TCF-1+
24 hr
72 hr
Time Post-photoconversion
B.
****
****
****
****
100
80
60
40
20
0
% NKG2A+
24 hr
72 hr
Time Post-photoconversion
C.
**
****
****
****
100
80
60
40
20
0
% CD69+
24 hr
72 hr
Time Post-photoconversio
Kaede Green
Kaede Red

Appendix 3.5. Phenotype of the total CD8 T cell intratumoural population in subcutaneous CT26 tumour models over time- further quantitation.

BALB/c Kaede mice (6-9 weeks) were injected with 2.5 x10^5 CT26 cells subcutaneously. Tumours were photoconverted on day 11 post-injection, and tissues collected on day 12 or day 14. All data shown are from three independent experiments. All graphs show the mean ± SD. Statistical significance was determined using a two-way ANOVA , 4 family comparison, Fisher's LSD test. ** = p < 0.05, ** = p < 0.01, *** = p< 0.001, **** = p< 0.0001*

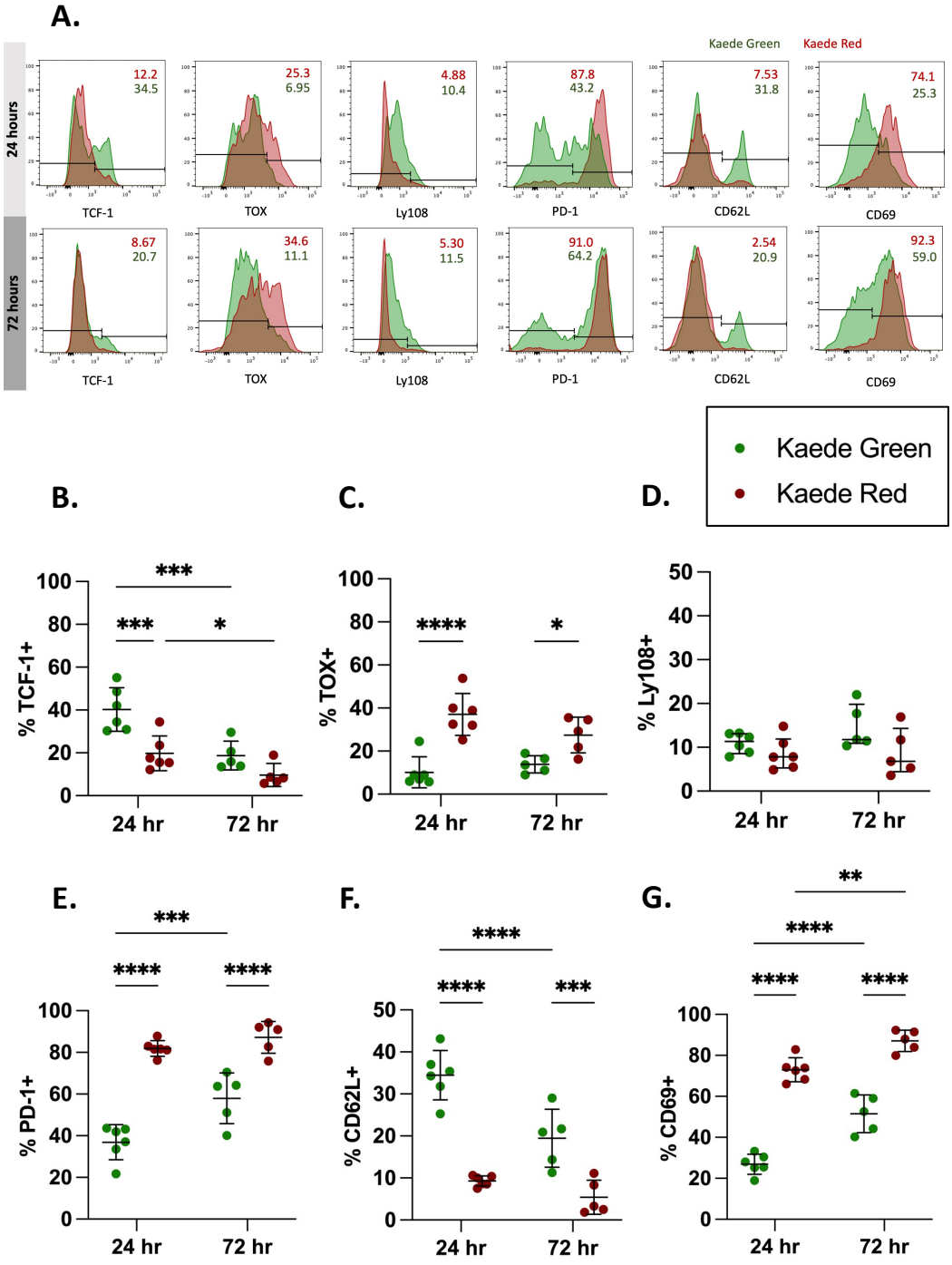
A. The percentage of intratumoural CD8+ Kaede red and green cells positive for TCF-1 expression at 24 and 72 hours after photo-conversion.
B. The percentage of intratumoural CD8+ Kaede red and green cells positive for NKG2A expression at 24 and 72 hours after photo-conversion.
C. The percentage of intratumoural CD8+ Kaede red and green cells positive for CD69 expression at 24 and 72 hours after photo-conversion.


A.
% PD-1hiNKG2A+
100
80
60
40
20
0
**
Kaede Green
Kaede Red
B.
% PD-1hiTIM-3+
50
40
30
20
10
0
*
Kaede Green
Kaede Red
C.
% PD-1hiLAG-3+
50
40
30
20
10
0
**
Kaede Green
Kaede Red
D.
24 hours
72 hours
Kaede Red
Kaede Green
78.6
19.9
61.9
37.2
NKG2A
TIM-3
LAG-3
PD-1
42.2
33.7
17.9
6.19
5.08
16.7
55.0
23.2
5.14
25.6
53.5
15.7
20.3
5.13
69.9
4.65
1.22
1.22
89.0
8.56
0.98
0.49
89.2
9.29
9.93
83.0
4.39
2.72
0.63
19.3
14.3
65.7
0
13.9
14.3
71.8
24.5
50.4
17.7
7.30
0.35
11.7
42.1
45.9
0.35
8.17
41.9
49.6
E.
% PD-1hiNKG2A+
100
80
60
40
20
0
*
24 hr
72 hr
F.
% PD-1hiTIM-3+
100
80
60
40
20
0
*
24 hr
72 hr
G.
% PD-1hiLAG-3+
100
80
60
40
20
0
24 hr
72 hr

Appendix 3.6. Characterising the co-expression of inhibitory receptors on CD8 T cells in subcutaneous tumour models over time.

BALB/c Kaede mice (6-9 weeks) were injected with 2.0 x10^5 CT26 cells subcutaneously. Tumours were photoconverted on day 11 post-injection, and tissues collected on day 12 or day 14. All CT26 data shown are from two independent experiments. All graphs show the median and IQR. Statistical significance was determined using a Mann-Whitney test. ** = $p < 0.05$, ** = $p < 0.01$*

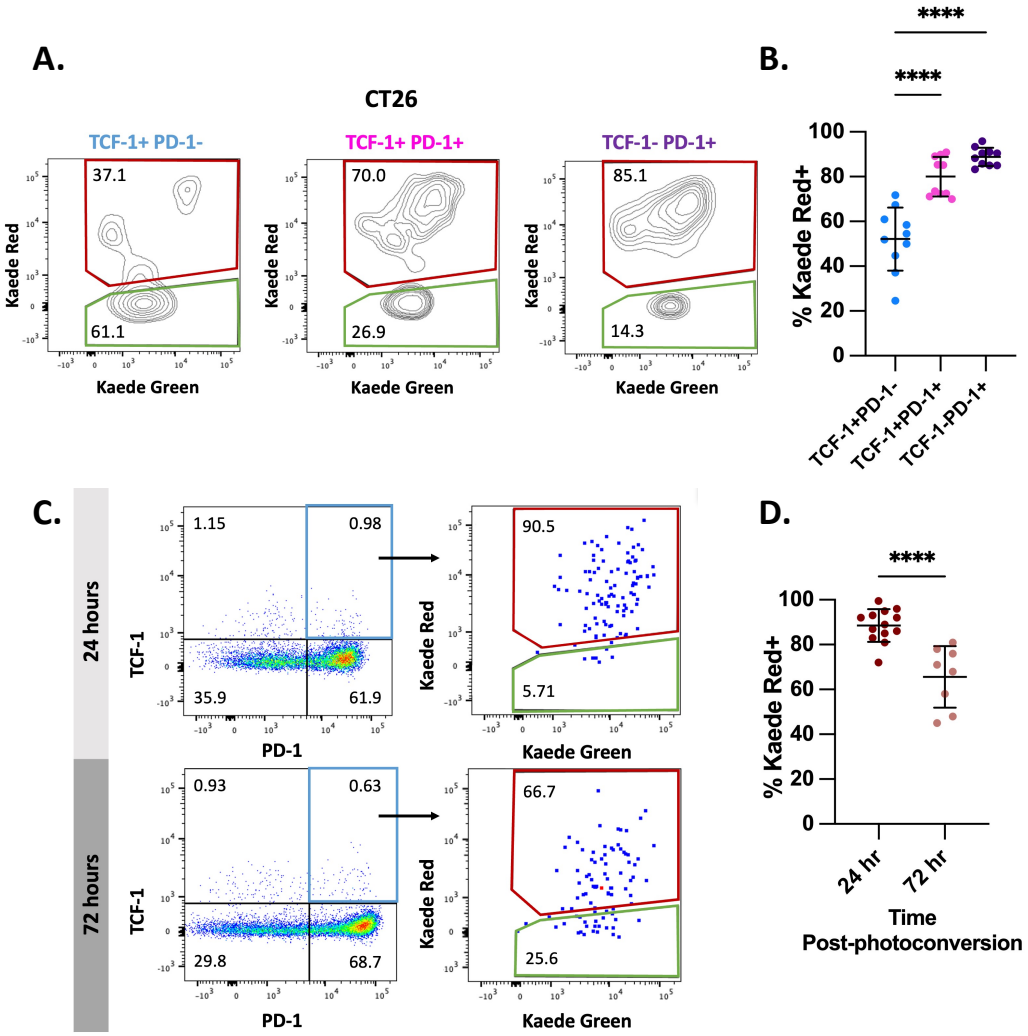
A. The percentage of intratumoural Kaede red+ and Kaede green+ CD8+ cells PD-1hi NKG2A+ at 24 after photo-conversion.
B. The percentage of intratumoural Kaede red+ and Kaede green+ CD8+ cells PD-1hi TIM-3+ at 24 after photo-conversion.
C. The percentage of intratumoural Kaede red+ and Kaede green+ CD8+ cells PD-1hi LAG-3+ at 24 after photo-conversion.
D. Flow cytometry plots demonstrating the differences in co-expression of the co-inhibitory receptors NKG2A, TIM-3, and LAG-3 with PD-1 between intratumoural Kaede red and Kaede green CD8 populations at 24 and 72 hours following photoconversion. The red contour plots demonstrate co-inhibitory receptor expression in Kaede red+ CD8 T cells and the green contour plots Kaede green+ CD8 T cells. The flow plots are from a representative CT26 tumour sample at 24 and 72 hours following photoconversion.
E. The percentage of intratumoural Kaede green+ CD8+ cells PD-1hi NKG2A+ at 24 and 72 hours after photo-conversion.
F. The percentage of intratumoural Kaede green+ CD8+ cells PD-1hi TIM-3+ at 24 and 72 hours after photo-conversion.
G. The percentage of intratumoural Kaede green+ CD8+ cells PD-1hi LAG-3+ at 24 and 72 hours after photo-conversion.


A.
Kaede Green
Kaede Red
24 hours
72 hours
12.2
34.5
TCF-1
25.3
6.95
TOX
4.88
10.4
Ly108
87.8
43.2
PD-1
7.53
31.8
CD62L
74.1
25.3
CD69
8.67
20.7
TCF-1
34.6
11.1
TOX
5.30
11.5
Ly108
91.0
64.2
PD-1
2.54
20.9
CD62L
92.3
59.0
CD69
Kaede Green
Kaede Red
B.
% TCF-1+
C.
% TOX+
D.
% Ly108+
E.
% PD-1+
F.
% CD62L+
G.
% CD69+
24 hr
72 hr

Appendix 3.7. Phenotype of the CD8 T cell intratumoural population in subcutaneous tumour models over time in MC38-OVA model.

C57BL/6 Kaede mice (6-9 weeks) were injected with 2.5 x10^5 MC38-OVA cells subcutaneously. Tumours were photoconverted on day 11 post-injection, and tissues collected on day 12 or day 14. All MC38-OVA data shown are from two independent experiments. All graphs show the mean ± SD. Statistical significance was determined using a two-way ANOVA , 4 family comparison, Fisher's LSD test. ** = p < 0.05, ** = p < 0.01, *** = p< 0.001, **** = p< 0.0001*

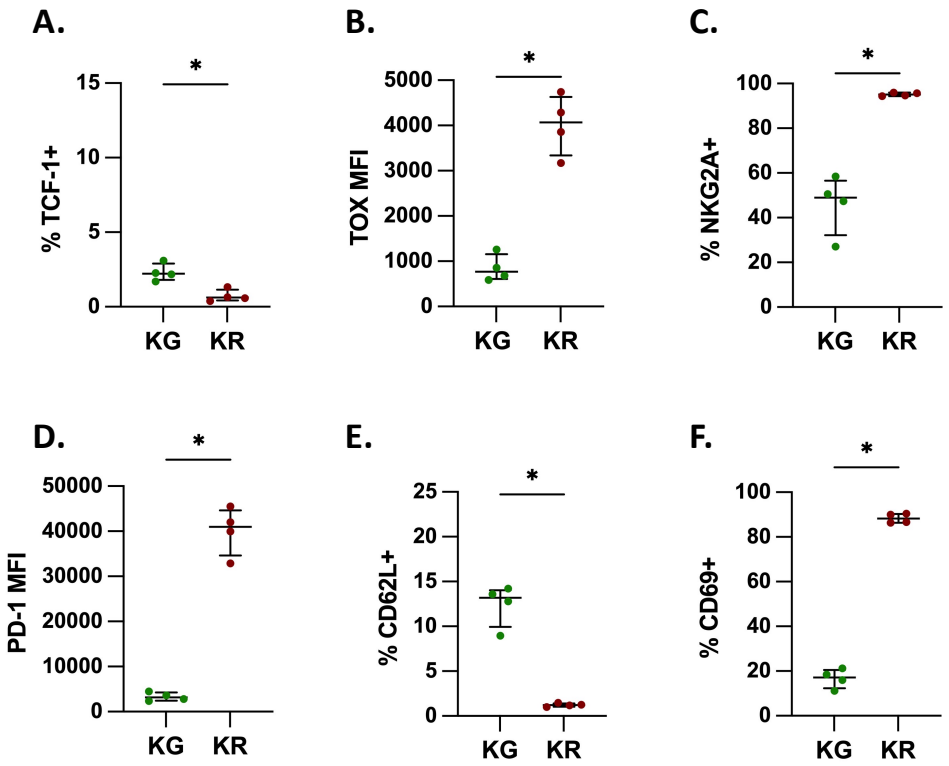
A. Histograms demonstrating the expression of TCF-1, TOX, Ly108, PD-1, CD62L, and CD69 in the Kaede green+ (green) and Kaede red+ (red) CD8 T cell population in a representative MC38-OVA tumour sample 24hrs (top row) and 72hrs (bottom row) following photoconversion.
B. The percentage of intratumoural CD8+ Kaede red and green cells that are TCF-1+ at 24 and 72 hours after photo-conversion.
C. The percentage of intratumoural CD8+ Kaede red and green cells that are TOX+ at 24 and 72 hours after photo-conversion.
D. The percentage of intratumoural CD8+ Kaede red and green cells that are Ly108+ at 24 and 72 hours after photo-conversion.
E. The percentage of intratumoural CD8+ Kaede red and green cells that are PD-1+ at 24 and 72 hours after photo-conversion.
F. The percentage of intratumoural CD8+ Kaede red and green cells that are CD62L+ at 24 and 72 hours after photo-conversion.
G. The percentage of intratumoural CD8+ Kaede red and green cells that are CD69+ at 24 and 72 hours after photo-conversion.


A.
CT26
TCF-1+ PD-1-
TCF-1+ PD-1+
TCF-1- PD-1+
37.1
61.1
70.0
26.9
85.1
14.3
Kaede Red
Kaede Green
B.
****
****
% Kaede Red+
TCF-1+PD-1-
TCF-1+PD-1+
TCF-1-PD-1+
C.
24 hours
72 hours
TCF-1
PD-1
1.15
0.98
35.9
61.9
0.93
0.63
29.8
68.7
Kaede Red
Kaede Green
90.5
5.71
66.7
25.6
D.
****
% Kaede Red+
24 hr
72 hr
Time
Post-photoconversion

Appendix 3.8. Phenotyping the intratumoural stem-like CD8 population over time.

BALB/c Kaede mice (6-9 weeks) were injected with 2.0 x10^5 CT26 cells subcutaneously. Tumours were photoconverted on day 11 post-injection, and tissues collected on day 12 or day 14. All CT26 data shown are from three independent experiments. All graphs show the mean ± SD. In the case of two-column analysis statistical significance was determined using an unpaired *t* test. In the case of multiple column analysis statistical significance was determined with an ordinary one-way ANOVA with a Tukey's multiple comparison post-hoc test. ** = p < 0.05, ** = p < 0.01, *** = p < 0.001, **** = p < 0.0001*

A. Flow cytometry plots showing Kaede expression in the TCF-1+ PD-1- CD8 population (left), the TCF-1+ PD-1+ CD8 population (centre), and the TCF-1- PD-1+ CD8 population (right). Data shown are from a representative CT26 tumour 24 hours following photoconversion.
B. The percentage of Kaede red+ cells based on expression of TCF-1 and PD-1 at 24 hours following photoconversion of CT26 tumours.
C. Flow cytometry plots showing Kaede expression (right plot) in the TCF-1+ PD-1+ CD8 population highlighted (blue) in the left-hand flow plot at 24 and 72 hours following photoconversion. Data shown are from representative CT26 tumours at each time point.
D. The percentage of Kaede red+ cells in the TCF-1+ PD-1+ CD8 population at 24 and 72 hours following photoconversion of CT26 tumours.


A.
% TCF-1+
15
10
5
0
*
KG
KR
B.
TOX MFI
5000
4000
3000
2000
1000
0
*
KG
KR
C.
% NKG2A+
100
80
60
40
20
0
*
KG
KR
D.
PD-1 MFI
50000
40000
30000
20000
10000
0
*
KG
KR
E.
% CD62L+
25
20
15
10
5
0
*
KG
KR
F.
% CD69+
100
80
60
40
20
0
*
KG
KR

Appendix 3.9. Phenotype of CD8 T cells entering the tumour within 5 hours of photoconversion.

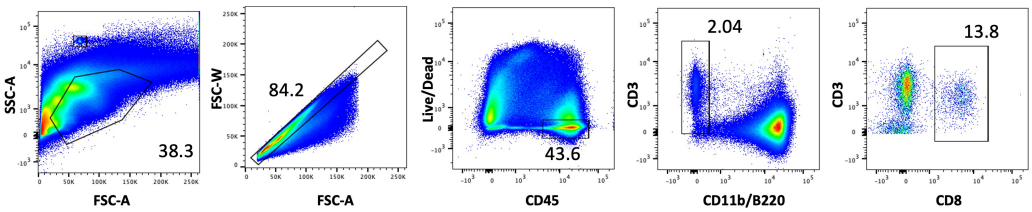
BALB/c Kaede mice (6-9 weeks) were injected with 2.5 x10^5 CT26 cells subcutaneously. Subcutaneous tumours were photoconverted at day 11 post-injection, and tissue collected 5 hours following the procedure. All CT26 data shown are from two independent experiments. All graphs show the median and IQR. Statistical significance was determined using a Mann-Whitney test. ** = $p < 0.05$*

A. The percentage of KR and KG CD8 T cells that were TCF-1+ 5 hours after photoconversion.
B. The MFI of TOX in KR and KG CD8 T cells 5 hours after photoconversion.
C. The percentage of KR and KG CD8 T cells that were NKG2A+ 5 hours after photoconversion.
D. The MFI of PD-1 in KR and KG CD8 T cells 5 hours after photoconversion.
E. The percentage of KR and KG CD8 T cells that were CD62L+ 5 hours after photoconversion.
F. The percentage of KR and KG CD8 T cells that were CD69+ 5 hours after photoconversion.

Appendix

Chapter 4

A.

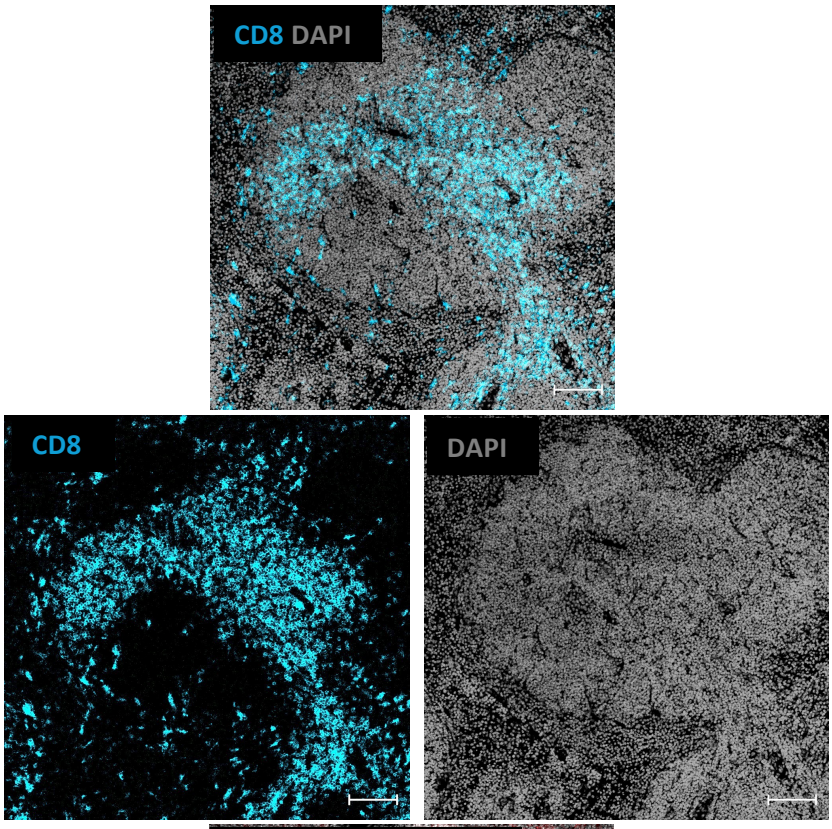

SSC-A
FSC-A
38.3
FSC-W
FSC-A
84.2
Live/Dead
CD45
43.6
CD3
CD11b/B220
2.04
CD3
CD8
13.8

Appendix 4.1. Gating strategy used to identify CD8 T cells within colon tumours.

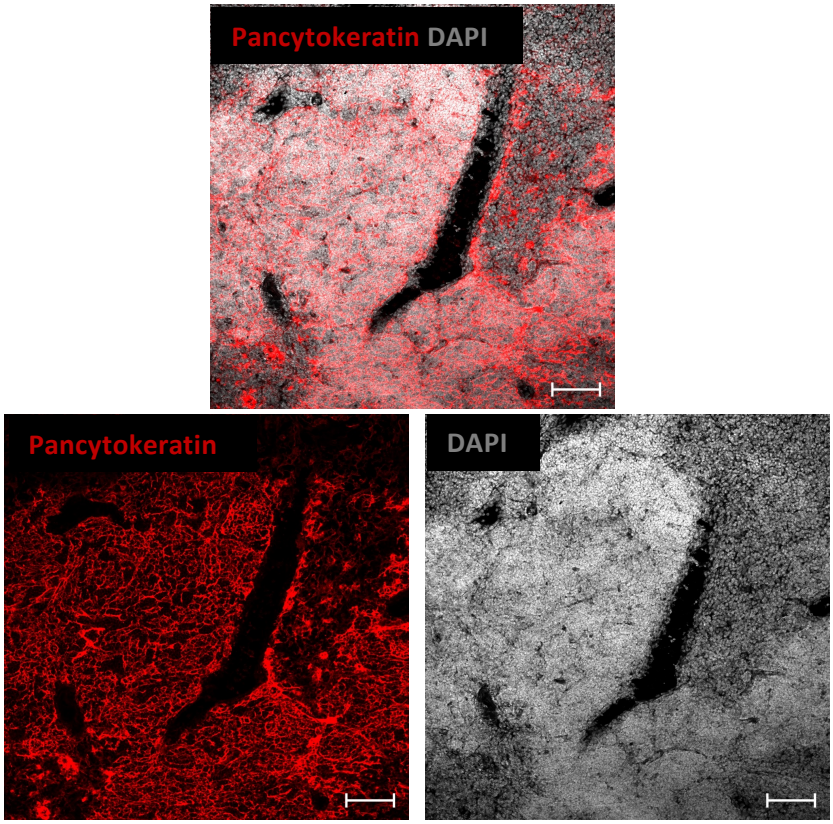
BALB/c Kaede mice (8-10 weeks) were injected with 5 x10^5 CT26 WT cells into the colon wall. Colon tumours were collected at day 14 post-injection.

A. Gating strategy used to define the CD8+ T cell population in colon tumours. Representative flow cytometry plots from CT26 WT colon tumour harvested day 14 post-injection.

A.


CD8 DAPI
CD8
DAPI

B.

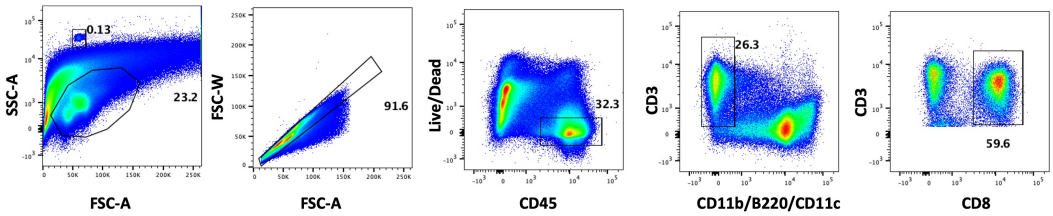

Pancytokeratin DAPI
Pancytokeratin
DAPI

Appendix 4.2. Microscopy controls for CD8 and pancytokeratin stain.

Microscopy controls (n=2). Representative images selected. All scale bars represent 100µm.

A. CD8 positive control. x25 of spleen. DAPI is shown is grey and CD8 in cyan.
B. Pancytokeratin positive control. x25 of thymus. DAPI is shown in grey and pancytokeratin in red.

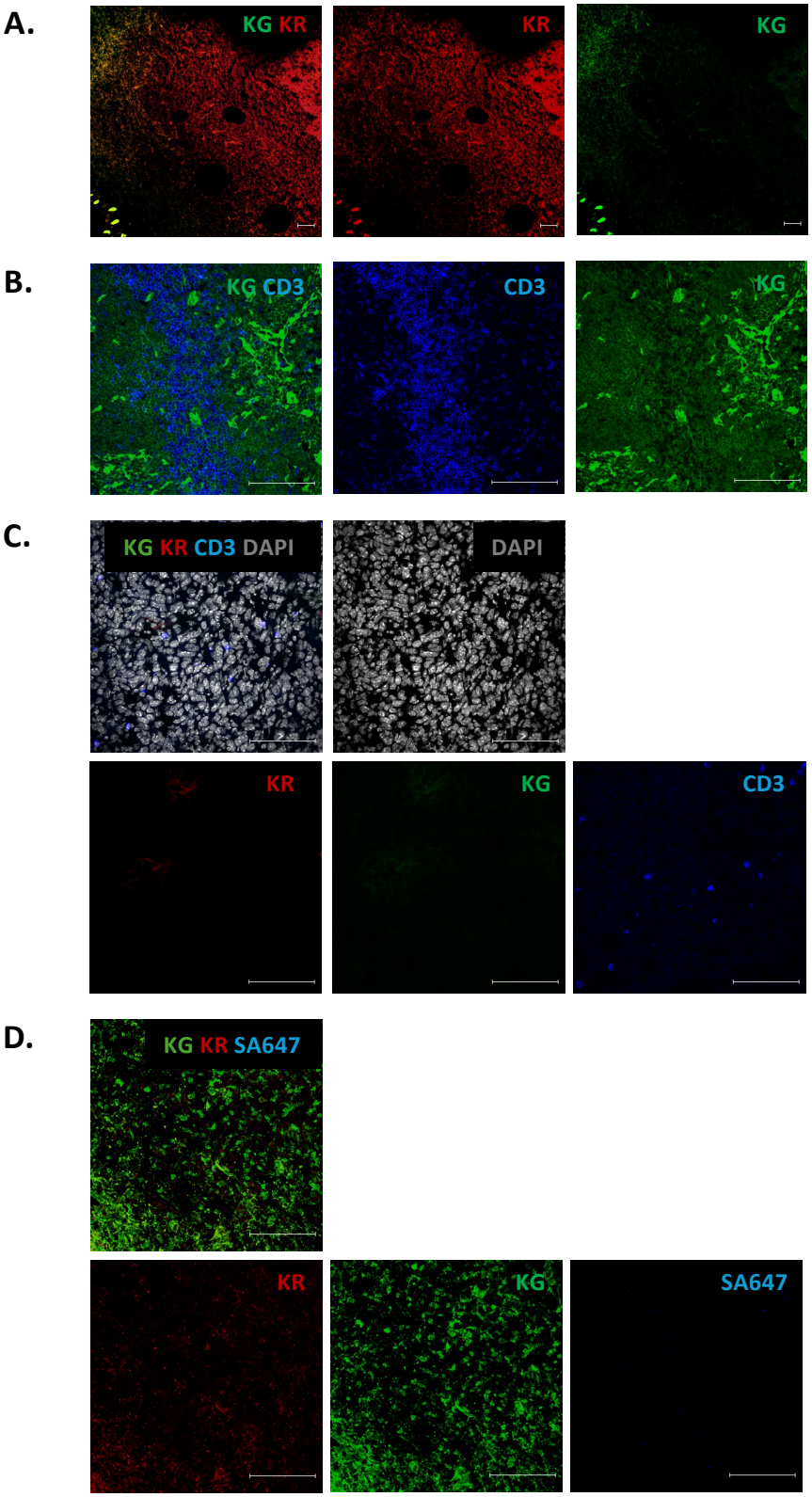
A.


SSC-A
FSC-A
0.13
23.2
FSC-W
FSC-A
91.6
Live/Dead
CD45
32.3
CD3
CD11b/B220/CD11c
26.3
CD3
CD8
59.6

Appendix 4.3. Gating strategy used to identify CD8 T cells within liver tumours.

BALB/C Kaede mice (12 weeks) were injected with 2.5 x10^5 CT26 GFP Luc tumour cells in 30% Matrigel or PBS into the liver. Tissues were collected on day 14 post injection of tumour cell lines.

A. Gating strategy used to define the CD8+ T cell population in liver tumours. Representative flow cytometry plots from CT26 liver tumour harvested day 14 post-injection.


A.
KG KR
KR
KG
B.
KG CD3
CD3
KG
C.
KG KR CD3 DAPI
DAPI
KR
KG
CD3
D.
KG KR SA647
KR
KG
SA647

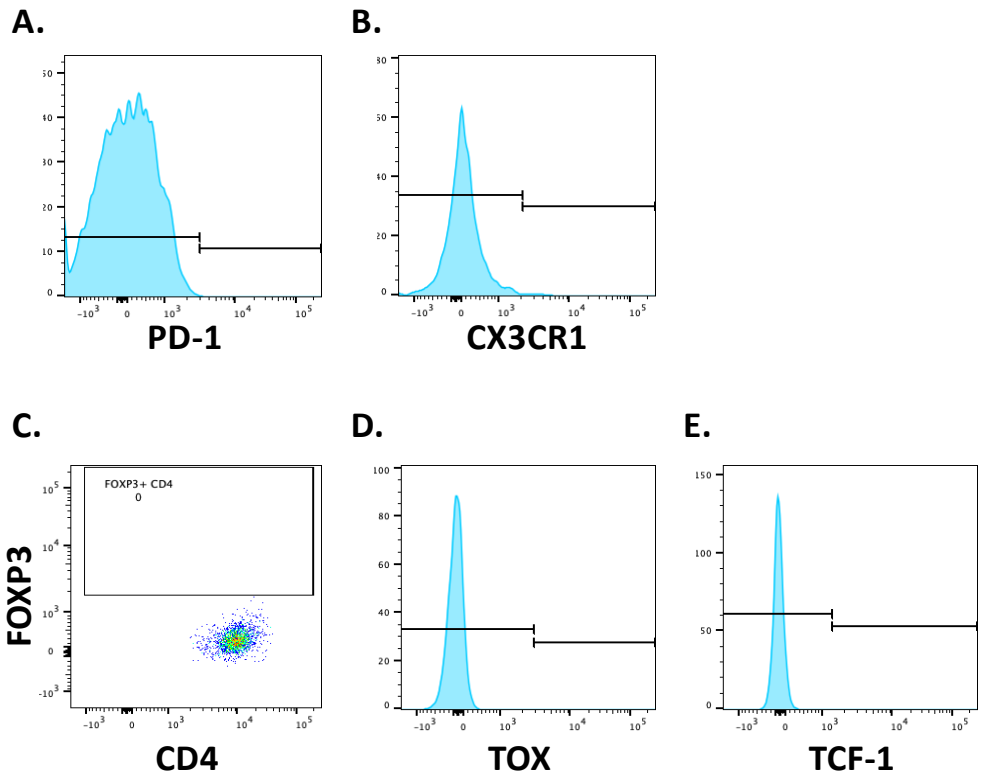
Appendix 4.4. Microscopy controls for photoconverted tumours.

Microscopy controls (n=2). Kaede green is shown in green, Kaede red in red, CD3/SA647 in blue, and DAPI in grey. Representative images selected. All scale bars represent 100µm.

A. Kaede red positive control. x25 of Kaede dLN photoconverted *ex vivo*.
B. Kaede green & CD3 positive control. x40 of Kaede dLN stained with CD3.
C. Kaede green and red negative control. x40 of s.c. tumour from WT (non-Kaede) mouse fully stained for CD3.
D. CD3 biotin negative control. x40 of photoconverted s.c. tumour from a Kaede mouse stained with SA 647 only (minus CD3 biotin).

Appendix

Chapter 5

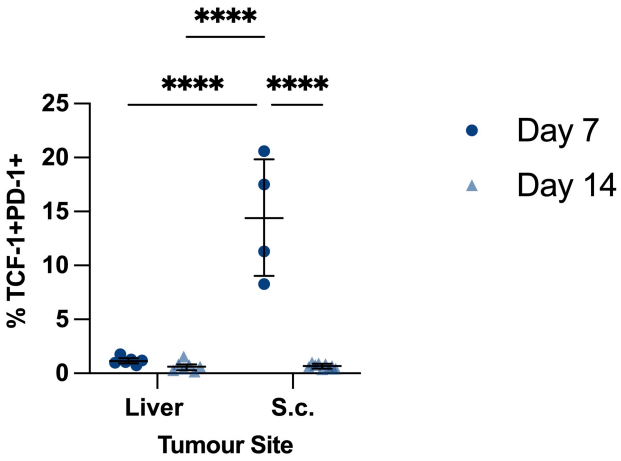

A.
B.
PD-1
CX3CR1
C.
D.
E.
FOXP3+ CD4
0
FOXP3
CD4
TOX
TCF-1

Appendix 5.1. FMO and isotype controls for PD-1, CX3CR1, FOXP3, TOX, TCF-1.

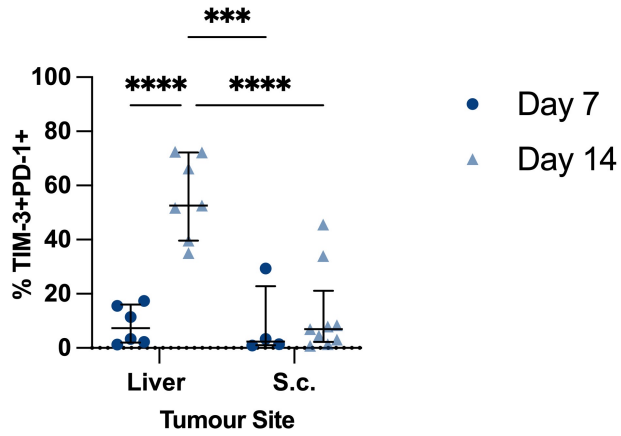
C57BL/6 mice (9-12 weeks) were injected with subcutaneous tumours. All MC38-OVA data shown are from subcutaneous tumours stained in different experiments. All plots shown are pre-gated on live CD45+ CD11b- CD11c- B220-CD3+ CD8+ cells.

A. Histogram demonstrating PD-1 expression in isotype control.
B. Histogram demonstrating CX3CR1 expression in FMO.
C. Flow cytometry plot demonstrating FOXP3 expression in FMO.
D. Histogram demonstrating TOX expression in FMO.
E. Histogram demonstrating TCF-1 expression in isotype control.

A.


****
****
****
% TCF-1+PD-1+
25
20
15
10
5
0
Liver
S.c.
Tumour Site
Day 7
Day 14

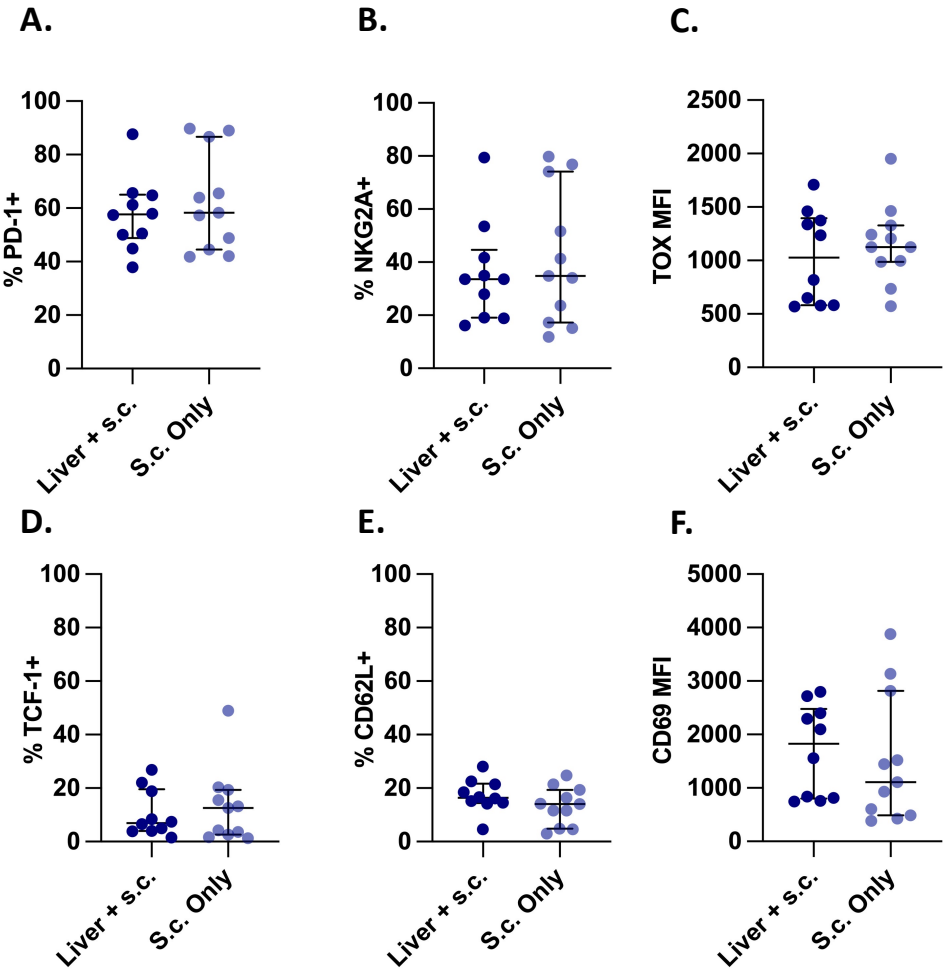
B.


***
****
****
% TIM-3+PD-1+
100
80
60
40
20
0
Liver
S.c.
Tumour Site
Day 7
Day 14

Appendix 5.2. Comparison of exhausted CD8 T cell populations in liver tumours at day 7 and 14 -further enumeration.

BALB/c mice (9- 12 weeks) were injected with 2.0 x10^5 CT26 WT cells subcutaneously or intrahepatically. Tissues were harvested on day 7 or day 14 post-injection. All data shown are from two independent experiments. All graphs show the mean ± SD. Statistical significance was determined using a 2-way ANOVA with Tukey's correction for multiple comparison. ** = p < 0.05, ** = p < 0.01, *** = p < 0.001, **** = p < 0.0001*

A. The percentage of CD8+ T cells that are TCF-1+ PD-1+ at day 7 and day 14 post-injection in liver tumours and s.c. tumours.
B. The percentage of CD8+ T cells that are TIM-3+ PD-1+ at day 7 and day 14 post-injection in liver tumours and s.c. tumours.

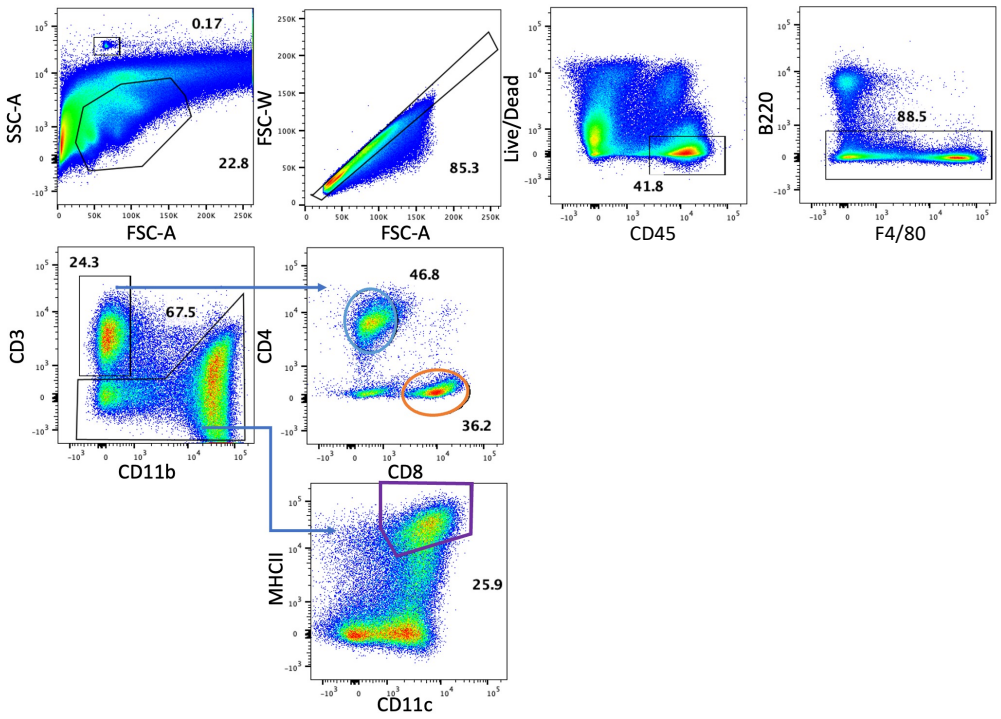

A.
% PD-1+
100
80
60
40
20
0
Liver + s.c.
S.c. Only
B.
% NKG2A+
100
80
60
40
20
0
Liver + s.c.
S.c. Only
C.
TOX MFI
2500
2000
1500
1000
500
0
Liver + s.c.
S.c. Only
D.
% TCF-1+
100
80
60
40
20
0
Liver + s.c.
S.c. Only
E.
% CD62L+
100
80
60
40
20
0
Liver + s.c.
S.c. Only
F.
CD69 MFI
5000
4000
3000
2000
1000
0
Liver + s.c.
S.c. Only

Appendix 5.3. Comparison of CD8 T cell populations within tumours implanted intrahepatically versus subcutaneously – further enumeration.

BALB/c mice were injected with 2.0 x10^5 CT26 WT subcutaneously and intrahepatically, or subcutaneously only, between 9-12 weeks of age. Tissues were harvested on day 12 post-injection. Cells were isolated from tumours as per methods. All data shown above are from two independent experiments. All graphs show the median and IQR. Statistical significance was determined using a Mann-Whitney test.

A. The percentage of CD8+ T cells that are PD-1+ at day 12 post-injection in subcutaneous tumours of mice with or without liver tumours.
B. The percentage of CD8+ T cells that are NKG2A+ at day 12 post-injection in subcutaneous tumours of mice with or without liver tumours.
C. The MFI of TOX in CD8+ T cells at day 12 post injection in subcutaneous tumours of mice with or without liver tumours.
D. The percentage of CD8+ T cells that are TCF-1+ at day 12 post-injection in subcutaneous tumours of mice with or without liver tumours.
E. The percentage of CD8+ T cells that are CD62L+ at day 12 post-injection in subcutaneous tumours of mice with or without liver tumours.
F. The MFI of CD69 in CD8+ T cells at day 12 post injection in subcutaneous tumours of mice with or without liver tumours.

A.

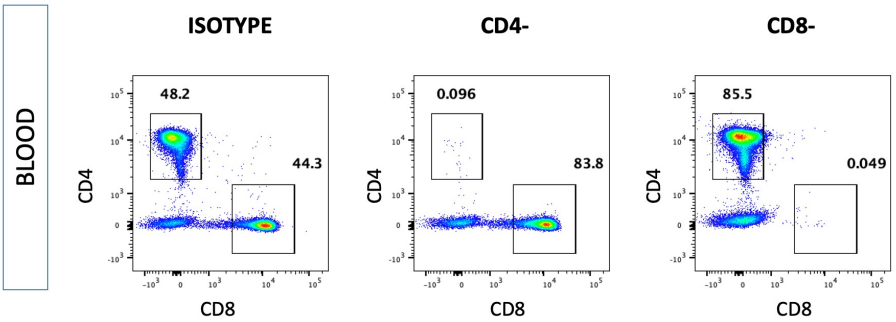

SSC-A
FSC-A
0.17
22.8
FSC-W
FSC-A
85.3
Live/Dead
CD45
41.8
B220
F4/80
88.5
CD3
CD11b
24.3
67.5
CD4
CD8
46.8
36.2
MHCII
CD11c
25.9

Appendix 5.4. Establishing a dual liver + flank subcutaneous tumour model to understand the migration of CD8 T cells from liver tumour to subcutaneous tumour.

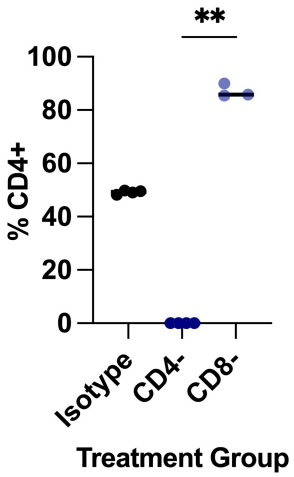
BALB/c Kaede mice (9-12 weeks) were injected with 2.0 x10^5 CT26 WT subcutaneously and intrahepatically, or subcutaneously only. Liver tumours were photoconverted day 12 post-injection through a limited abdominal incision, and tissues collected 24 hours after.

A. Flow cytometry plots demonstrating the initial gating used to define CD4, CD8 and DC populations in tumour samples. The plots are from the same mouse 24 hours post-photoconversion.

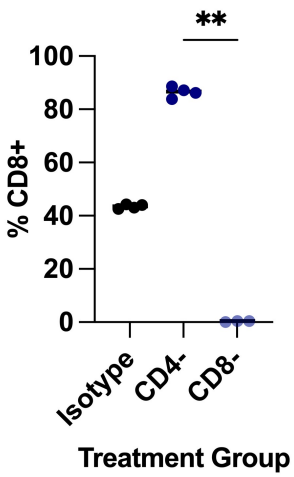
A.


BLOOD
ISOTYPE
CD4-
CD8-
48.2
44.3
0.096
83.8
85.5
0.049
CD4
CD8

B.


**
100
80
60
40
20
0
% CD4+
Isotype
CD4-
CD8-
Treatment Group

C.


**
100
80
60
40
20
0
% CD8+
Isotype
CD4-
CD8-
Treatment Group

Appendix 5.5. Establishing *in vivo* depletion of CD4 and CD8 T cells –further validation using blood samples.

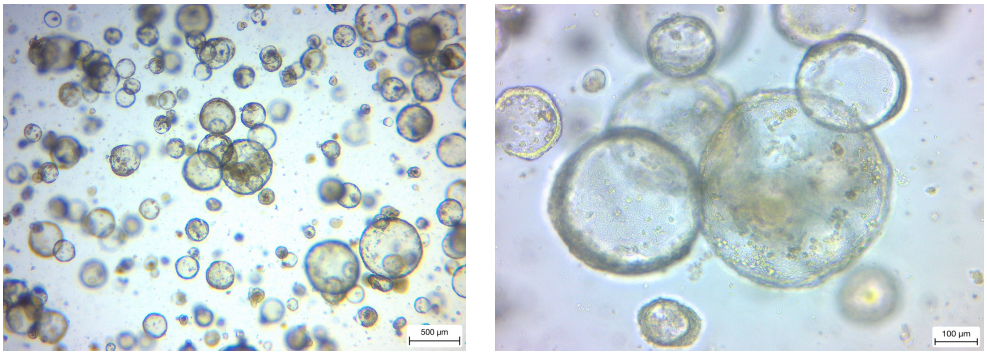
C57BL/6 mice (9 weeks) were injected with 2.5 x10^5 MC38-OVA subcutaneously. A single 200 µg dose of depleting CD4, CD8 or isotype antibody diluted in 200 µl (10 mg/kg body weight) was injected intraperitoneally on day 6 after tumour implantation. Tissues were harvested on day 12 post-injection. Cells were isolated from the blood. All data shown is from one experiment. All graphs show the median value. Statistical significance was determined using a Kruskal-Wallis with post-hoc Dunn's correction for multiple comparisons. ** = p < 0.05, ** = p < 0.01.*

A. Flow cytometry plots demonstrating the expression of CD4 and CD8 in live CD45+ CD11B- B220- CD3+ cells (pre-gated) in the blood. Representative samples from isotype, CD4 depleted and CD8 depleted (left to right) are shown.
B. The percentage of CD3+ cells that are CD4+ in blood samples from the three different treatment groups.
C. The percentage of CD3+ cells that are CD8+ in blood samples from the three different treatment groups.

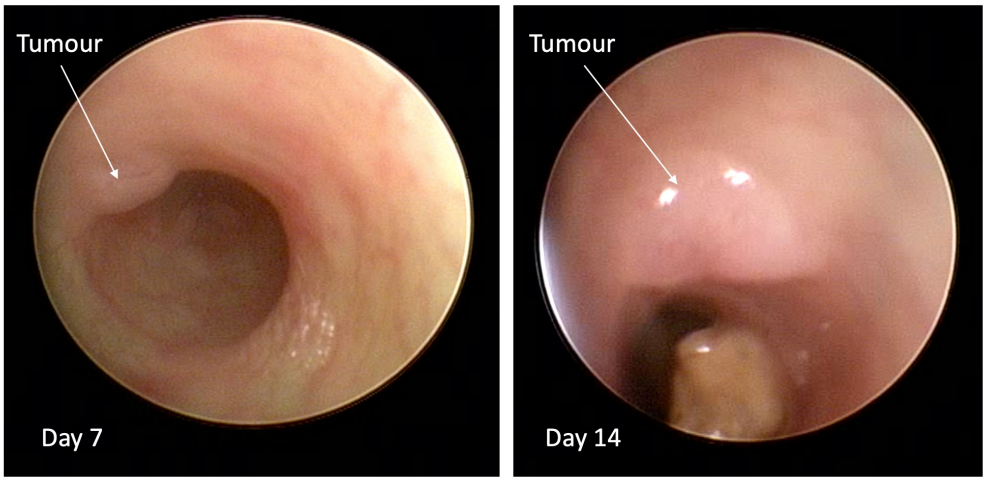
Appendix

Chapter 6

A.



B.



Appendix 6.1. Injection of AKPT organoids into the colon wall as a further orthotopic colorectal cancer model.

In the pilot experiment for injection of AKPT organoids into the colon wall, organoids were implanted in 12-week-old Kaede mice. All the data shown is from one pilot experiment.

A. Images of AKPT organoids in Matrigel Growth Factor Reduced Basement Membrane Matrix, at 2.5x (left) and 10x (right) magnification.
B. AKPT tumour growth *in situ* after organoid implantation into the colon. The left-hand panel demonstrates tumour growth at day 7 and right-hand panel day 14. Images were taken using a Karl Storz Endoskope with multi-purpose rigid telescope. AKPT organoids were implanted in 10-week-old C57BL/6 Kaede mice.